

# The University of Sheffield



## The Use of Multilevel Power Converter Technology in Aerospace Starter-Generator Systems

Richard Haydn Williams

A thesis submitted for the degree of PhD  
in the Department of Electronic and  
Electrical Engineering, The University  
of Sheffield, December 2012.

# Abstract

This thesis investigates how a back-to-back connected, 5-level, diode-clamped multilevel inverter may be applied in an aerospace Starter / Generator (S/G) system. The performance of the proposed system is investigated with both wound field (WF) and permanent magnet (PM) synchronous machines. Control techniques are investigated to improve the waveform quality at the machine side. Also the grid interfacing of the converter is considered to make the system more resilient to AC distribution bus distortion.

Aerospace generators are typically low inductance machines owing to the need to regulate the back-emf at the high rated speed, reduce stator losses and to increase power density. However, the driving of low inductance synchronous machines with a two level inverter results in a high level of current ripple at the same frequency as the converter switching frequency. A high level of current ripple increases losses in both the converter and machine necessitating additional heatsinking/cooling. The high ripple also results in increased radiated and conducted EMI. Additional filtering/shielding is therefore required to protect other vulnerable systems in the vicinity. The stability of the converter's controller may be adversely affected by a high level of current ripple. This instability can lead to the increased production of low order harmonic in the current waveform.

The effect of interfacing a two-level inverter to an aircraft's AC distribution bus must also be considered. Power quality standards require the converter to draw a high quality sinusoidal current from the grid and introduce minimal distortion onto the voltage waveform. In order to reduce the current ripple in the machine windings and to ensure the distortion at the grid connection is within the governed limit, it is customary to use increased passive filtering and/or raise the converter switching frequency. Both of which incur a weight penalty. This study sought to investigate how a multilevel converter may be used as an alternative approach to this problem. The stepped PWM waveform produced by a multilevel converter offers superior harmonic performance and may therefore require reduced amounts of passive filtering whilst still producing a high quality waveform.

The performance of the converter is initially demonstrated experimentally upon a PMSM. This is considered relevant as future 'embedded' S/Gs are likely to be PMSM due to the robust rotor structure and high power density. Performance is verified experimentally using a dynamometer test rig. The dynamometer is controlled to provide a rudimentary model of

a gas turbine in both starting and generating mode. It is therefore possible to load the S/G in a similar manner to a real world application and provide realistic testing data.

The converter is then applied to a WFSM. WFSMs are the industry norm for aerospace generators and it is this machine topology that is used as the S/G in Trent 1000 engine. Converter performance with a WFSM must therefore be assessed if this study is to be considered relevant. The excitation of the machine is investigated to ensure that the machine may be driven in motoring mode from zero speed and to maximise the available torque throughout the starting sequence. The excitation is then used to regulate the back-emf during generating mode. The same dynamometer test rig is used to provide full system test experimental data.

Predictive control is then investigated to obtain a further reduction in waveform distortion in the stator current. Predictive control utilises a mathematical model of the load to predict the converter output voltage required in the next PWM period to minimise the current error. The estimated switching vector may then be applied in the next modulation period. This is shown to provide a substantial reduction in THD throughout both modes of operation. A reduction in THD in a real-world application would provide lower losses in both the machine and converter. The heatsinking/cooling arrangement may be reduced giving a possible weight reduction.

In the final stage of this study, the control and synchronisation of the grid connected inverter is investigated. Aerospace power converters are required by the standards to function under distorted grid conditions. In this study a review is conducted into the competing grid synchronisation methods, to determine which is the most suitable to accommodate the heavily unbalanced grid waveforms commonly found on an aircraft distribution bus. A virtual-flux estimator is identified as the most promising technique as it eliminates the three voltage transducers at the grid connection. This not only makes the converter more resilient to grid distortion but may also increase the converter's reliability as three essential components have been removed. The system is assessed in both simulation and hardware. The level of grid distortion applied to the grid waveform is the maximum permissible according to the aerospace power quality standards. The system performance is satisfactory, maintaining synchronisation with the grid with minimal error despite the heavily unbalanced supply.

# Acknowledgement

First and foremost, I wish to express my gratitude to my supervisors, Dr Martin P Foster and Dr Dave A Stone, and colleague Dr Stephen Minshull.

Secondly I wish to acknowledge my parents for the opportunities they have afforded me.

I also wish to thank all those present in the Sheffield UTC office for making my period of study so enjoyable. Special thanks to Dr Keir Douglas Wilkie, for aiding in the production of this study in the latter stages.

A special note to my partner, Dr N. Finn, for maintaining patience during the writing-up stage.

This work was kindly supported financially by the EPSRC and Rolls-Royce, through their University Technology Centre structure.

Finally, to everyone who was forced to proof-read the original manuscript, I apologise!

## Publications

R. H. Williams, D. A. Stone, M. P. Foster, S. R. Minshull, "Back-to-Back Connected Multilevel Converters for Aerospace Starter-Generator Applications," Power Conversion Intelligent Motion Conference, Nuremburg, Germany, pp. 352-357, 2011.

R. H. Williams, D. A. Stone, M. P. Foster, S. R. Minshull, "Utilizing Existing Aircraft Wound Field Generators for Starter-Generators," 8<sup>th</sup> International Conference on Power Electronics, Jeju, South Korea, pp. 691-696, 2011.

R.H. Williams, D. A. Stone, M. P. Foster, S. R. Minshull, "Reduction of Passive Filtering in Aerospace Starter/Generator Systems Using a Multilevel Converter with Predictive Current Control," Power Electronics Machines and Drives Conference, Bristol, UK2012.

R.H. Williams, D. A. Stone, M. P. Foster, S. R. Minshull, "The Use of Virtual Flux Estimation in Aerospace Starter-Generator Systems," International Symposium on Power Electronics, Electrical Drives, Automation and Motion, Sorrento, Italy, pp. 426-431, 2012.

# Table of Contents

Abstract.....	1
Acknowledgement .....	3
Publications.....	4
Nomenclature .....	9
Table of Figures.....	12
1 Introduction .....	17
1.1 Motivation and Objectives.....	18
1.2 Thesis Outline.....	19
2 Aerospace Systems .....	20
2.1 Introduction .....	20
2.2 Power Generation and Distribution.....	20
2.2.1 Aerospace Generators .....	23
2.2.2 Future Aerospace Generators.....	24
2.2.3 Power Quality Standards and Filtering .....	27
2.3 Aerospace Power Conversion .....	32
2.4 Engine Starting Systems.....	35
2.5 Conclusion.....	35
2.6 References .....	37
3 Power Converter Topologies .....	39
3.1 Introduction .....	39
3.2 Multilevel Power Converter Topologies .....	40
3.2.1 Cascaded H-Bridge Converter .....	49
3.2.2 Flying Capacitor Converter.....	50
3.2.3 Diode Clamped Converter.....	51
3.3 Competing Power Converter Topologies.....	57

3.3.1	Matrix Converter.....	57
3.4	Conclusion.....	60
3.5	References .....	62
4	Power Converter Modulation Techniques.....	65
4.1	Introduction .....	65
4.2	Space Vector Control .....	65
4.3	Selective Harmonic Elimination .....	66
4.4	Sinusoidal PWM .....	67
4.5	Space Vector PWM .....	70
4.5.1	GH Transformation and Reflection into the First Sextant .....	72
4.5.2	Calculation of Duty Cycles and Vector Sequencing.....	77
4.5.3	Capacitor Voltage Balancing .....	78
4.5.4	Device Switching Frequency Minimisation .....	81
4.5.5	Complete Algorithm.....	82
4.6	Conclusion.....	83
4.7	References .....	85
5	Development of a PM Starter/Generator System .....	87
5.1	Introduction .....	87
5.2	Vector Control of the Converter .....	90
5.2.1	Machine Connected Inverter Controller .....	90
5.2.2	Grid Connected Inverter Controller (AFE).....	102
5.3	Test Setup .....	108
5.3.1	PM S/G Test Machine.....	114
5.4	Experimental Results .....	114
5.4.1	Initial Testing Results .....	114
5.4.2	Full System Testing.....	116

5.5	Conclusion.....	119
5.6	References .....	122
6	Utilisation of Wound Field Synchronous Machines .....	125
6.1	Introduction .....	125
6.2	System Development.....	126
6.3	Exciter Mapping .....	130
6.3.1	Excitation During Starting Mode.....	133
6.3.2	Excitation During Generating Mode .....	136
6.4	Test Setup .....	137
6.5	Results.....	138
6.6	Conclusion.....	141
6.7	References .....	144
7	Implementation of Predictive Current Control.....	145
7.1	Introduction .....	145
7.2	Application of Predictive Control to Multilevel Converters.....	149
7.3	Control Algorithm Development.....	150
7.4	Results.....	154
7.5	Conclusion.....	158
7.6	References .....	160
8	Grid Interface .....	162
8.1	Introduction .....	162
8.2	Grid Interface Techniques.....	163
8.3	Virtual Flux Estimation .....	165
8.4	Implementation of VF Estimator with Space Vector Modulator .....	167
8.5	Simulation Results.....	169
8.5.1	Balanced Grid Conditions.....	170

8.5.2	Unbalanced Grid Conditions .....	173
8.6	Experimental Results .....	177
8.6.1	Balanced Phase Conditions .....	177
8.6.2	Distorted Phase Conditions.....	179
8.7	Conclusion.....	181
8.8	References .....	182
9	Conclusion.....	184
10	Future Work.....	189
	Appendix A.....	190
	Appendix B.....	192
	Appendix C.....	193
	Appendix D.....	194
	Appendix E .....	197

## Nomenclature

AFE	Active Front End
APU	Auxiliary Power Unit
ATRU	Auto Transformer Rectifier Unit
BTB	Bus Tie Breaker
CF	Constant Frequency
CSD	Constant Speed Drive
DPC	Direct Power Control
DSC	Direct Speed Control
FOC	Field Orientated Controller
GCU	Generator Control Unit
HBPC	Hysteresis Based Predictive Control
HP	High Pressure
IDG	Integrated Drive Generator
IGBT	Insulated Gate Bipolar Transistor
IPM	Intelligent Power Modules
IPMSM	Interior Permanent Magnet Synchronous Machine
IP	Intermediate Pressure

LP	Low Pressure
MMF	Magnetomotive Force
MEAI	More Electric Aircraft Initiative
MPC	Model Predictive Controller
MTPAC	Maximum Torque Per Ampere Control
MTTF	Mean Time To Failure
NI	National Instruments
NPC	Neural Point Clamped
NTV	Nearest Three Vector
PLL	Phase Locked Loop
PM	Permanent Magnet
PMSM	Permanent Magnet Synchronous Machine
PWM	Pulse Width Modulation
SFB	Specific Fuel Burn
SHE	Selective Harmonic Elimination
SPWM	Sinusoidal Pulse Width Modulation
SR	Switched Reluctance Machine
S/G	Starter/Generator
SV	Space Vector

SVPWM	Space Vector Pulse Width Modulation
THD	Total Harmonic Distortion
TRU	Transformer Rectifier Unit
UAV	Unmanned Air Vehicle
UDF	Unity Displacement Factor
VF	Virtual Flux
VFOC	Virtual Flux Orientated Control
VFVA	Variable Frequency Variable Amplitude
VOC	Voltage Orientated Control
VSCF	Variable Speed Constant Frequency
WF	Wound Field
WFSM	Wound Field Synchronous Machine

## Table of Figures

Figure 2-1: Twin engine aircraft power network.....	22
Figure 2-2: Wound field synchronous machine.....	23
Figure 2-3: Generator arrangement for a three shaft engine. ....	25
Figure 2-4: Turbine including HP Starter/Generator and LP generator.....	25
Figure 2-5: Spectrum envelope for 400 Hz system under normal operating conditions (MIL-STD-704F).....	28
Figure 2-6: Variable Speed Constant Frequency Converter.....	32
Figure 2-7: Cycloconverter.....	33
Figure 2-8: Twelve Pulse Transformer Rectifier Unit.....	34
Figure 3-1: (a) Generic multilevel inverter, (b) Stepped waveform.....	40
Figure 3-2: Power converter output waveforms, line-line voltages (a) Two level, (b) Three level, (c) Five level.....	42
Figure 3-3: Power converter output spectrum (a) Two level, (b) Three level, (c) Five level.	43
Figure 3-4: Cascaded H-bridge converter schematics (a) Three-level, (b) Nine-level. ....	49
Figure 3-5: Flying capacitor clamped converter schematics (a) Three-level, (b) Five-level...	50
Figure 3-6: Diode-clamped converter schematics (a) Neutral point clamped, (b) Five-level. ....	52
Figure 3-7: Back-to-back connected, five-level, diode-clamped inverters. ....	53
Figure 3-8: Schematic for a 3x3 matrix converter. ....	58
Figure 3-9: Bidirectional switch configurations, (a) Diode bridge, (b) Switch Cell. ....	58
Figure 3-10: Two stage, three-level matrix converter. ....	59
Figure 4-1: Modulation methods grouped according to switching frequency [4.1].....	65
Figure 4-2: Selective harmonic elimination. ....	67
Figure 4-3: Carrier and reference signals.....	68

Figure 4-4: Output of modulator. ....	68
Figure 4-5: Five level SPWM waveforms.....	69
Figure 4-6: Three-level SV diagram.....	71
Figure 4-7: SV diagram showing gh transformation, (a) Reference vector in 2nd sextant, (b) Reference vector in 3rd sextant.....	73
Figure 4-8: Five-level SV diagram, Sextant 1.....	74
Figure 4-9: Five-level SV diagram over modulation limit.....	74
Figure 4-10: Vector sequence. ....	77
Figure 4-11: Location of capacitor and mid-point currents in a 5-level inverter.....	80
Figure 4-12: Complete SV algorithm.....	83
Figure 5-1: Three-axis winding transformed into two axis representation. ....	91
Figure 5-2: Rotating dq reference frame with respect to $\alpha\beta$ stationery frame.....	92
Figure 5-3: DQ axis in relationship to three-phase, salient PMSM rotor.....	92
Figure 5-4: Two-level, motor connected inverter.....	95
Figure 5-5: Decoupled inverter controller. ....	96
Figure 5-6: Inverter controller during starting mode. ....	102
Figure 5-7: Inverter controller during generation mode. ....	102
Figure 5-8: Two level, grid connected inverter.....	103
Figure 5-9: Decoupled AFE controller.....	105
Figure 5-10: Three-phase, software based PLL.....	106
Figure 5-11: AFE controller during starting mode. ....	107
Figure 5-12: AFE controller during generation mode. ....	108
Figure 5-13: Test cell.....	110
Figure 5-14: LabView control program panel.....	110
Figure 5-15: Block diagram of test rig.....	111
Figure 5-16: Torque-speed profile of dynamometer during starting mode.....	112

Figure 5-17: Complete dynamometer torque speed profile. ....	113
Figure 5-18: Starting mode current waveforms (a) AFE, (b) Inverter. ....	115
Figure 5-19: Generating mode waveforms (a) AFE, (b) Inverter. ....	115
Figure 5-20: DC link under fluctuating machine speed conditions. ....	116
Figure 5-21: Complete test waveforms. ....	118
Figure 6-1: WFSM rotor. ....	127
Figure 6-2: Fixed frequency S/G system (a) Starting mode, (b) Generating mode. ....	128
Figure 6-3: Trent 1000 S/G system (a) Starting mode, (b) Generating mode. ....	130
Figure 6-4: WFSM mounted to dynamometer. ....	131
Figure 6-5: Rolls-Royce Artouste engine. ....	132
Figure 6-6: WFSM Tc under DC excitation. ....	133
Figure 6-7: WFSM Tc under AC excitation. ....	134
Figure 6-8: Torque Constant as a function of excitation and speed. ....	135
Figure 6-9: Optimum excitation frequency. ....	135
Figure 6-10: Measured back-EMF as excitation and machine speed vary. ....	136
Figure 6-11: Experimental test setup. ....	137
Figure 6-12: Starting mode waveforms, Upper waveform- AFE, Lower waveform- Inverter. ....	138
Figure 6-13: Generating mode waveforms (a) AFE, (b) Inverter. ....	139
Figure 6-14: Full S/G profile testing. ....	140
Figure 7-1: Hysteresis controller. ....	146
Figure 7-2: Hysteresis control, reference vector and corresponding boundary circle. ....	146
Figure 7-3: Model Predictive Controller block diagram. ....	148
Figure 7-4: Control system block diagram. ....	154
Figure 7-5: Starting mode stator current, (a) Conventional control, (b) Predictive control. ....	155

Figure 7-6: Starting mode current spectrum (a) Conventional control, (b) Predictive Control .....	155
Figure 7-7: THD measured as a function of machine speed. ....	156
Figure 7-8: Generating mode waveforms, (a) Conventional control, (b) Predictive control. .....	157
Figure 7-9: THD measured in the stator as a function of current driven into the utility network. ....	158
Figure 8-1: Virtual flux block diagram. ....	166
Figure 8-2: AFE controller incorporating VF estimator. ....	169
Figure 8-3: Estimated and actual grid angle under balanced conditions during starting mode. ....	170
Figure 8-4: Starting mode (a) Line current waveforms, (b) Real and reactive power. ....	170
Figure 8-5 Starting mode (a) DC link voltage, (b) Capacitor voltages. ....	171
Figure 8-6: Estimated and actual grid angle under balanced conditions during generating mode. ....	172
Figure 8-7: Generating mode (a) Line current waveforms, (b) Real and reactive power. ...	172
Figure 8-8: Distorted grid voltage waveform during starting mode. ....	173
Figure 8-9: Estimated and actual grid angle under distorted conditions during starting mode. ....	173
Figure 8-10: Starting mode (a) Line current waveforms, (b) Real and reactive power. ....	174
Figure 8-11: Starting mode (a) DC link voltage, (b) Capacitor voltages. ....	174
Figure 8-12: Estimated and actual grid angle under distorted conditions during generating mode. ....	176
Figure 8-13: Generating mode (a) Line current waveforms, (b) Real and reactive power. .	176
Figure 8-14: Grid angle (a) Estimated, (b) Actual. ....	177
Figure 8-15: Current drawn from the grid. ....	178
Figure 8-16: Grid angle under distorted conditions (a) Estimated, (b) Actual. ....	179
Figure 8-17: Current drawn from grid under distorted grid conditions. ....	179

Figure 0-1: Test rig. ....	190
Figure 0-2: Control board.....	191

# 1 Introduction

The application of power electronics in the aerospace environment is becoming an increasingly important area, both in industry and academia. Due to the safety critical nature of aerospace the uptake of power electronics in this industry has historically been limited, with preference being given to pneumatic, hydraulic or mechanical systems where possible.

However, over the past decade, it has been noted by engine and aircraft manufacturers that the use of electrical systems to replace these mechanical systems brings a host of advantages including; reduction in weight, increased flexibility, lower maintenance schedule and an improved Specific Fuel Burn (SFB). The replacement of traditionally mechanical system with electrical has been termed the More Electric Aircraft Initiative (MEAI) and is a trend seen across the industry. The MEAI has greatly increased the interest in aircraft power electronics as it is seen as a key, enabling technology.

Outside of industry in the academic world, the potential for aerospace power electronics is providing new and diverse research avenues due to the complex, constrained and often hostile environment which ensures there are many challenges and obstacles to be overcome. As such there are now many institutions and individuals focusing their research efforts on aerospace power electronics.

In the latest generation of aircraft such as the Boeing 787 (B787), there has been a dramatic increase in the level of electrical power consumption compared to previous generations of aircraft. This is to be expected in MEA architectures with the replacement of mechanical systems with electrical. For example the bleed air system used traditionally to provide de-icing and to drive the cabin air conditioning system has been removed from the Trent 1000, as used on the B787, and replaced with electrical systems. This provides a substantial improvement in engine efficiency and a weight reduction. However the electrical power requirements are increased greatly, up to an unprecedented 1 MW in the case of the B787.

This increase in power requirements has made the design of the aircraft's generation system an important research area. There have been many different solutions proposed and these are reviewed in subsequent chapters. One bi-product of the increase in installed electrical generation capacity, is the fact that the generators are now of sufficient size for starting the engines in addition to performing their normal generating duties. This is a major advantage to aircraft and engine manufacturers as it allows the elimination of the complex and heavy mechanical starting system.

A power converter is required in order to use an electrical machine as a starter/generator. At the start of this thesis the common power converter topologies normally employed in S/G systems are reviewed. These are generally based around the industry standard, six switch inverter. This topology suffers from a substantial amount of harmonic distortion in the output necessitating large amounts of passive filtering to produce acceptable waveforms. Large amounts of filtering incur a substantial weight penalty which is a severe limitation in an aerospace application.

It is well documented in the literature that multilevel converters can be used to great effect in drive and grid interfacing applications to reduce the amount of filtering required. This is as a result of the high quality waveform these converters produce. The purpose of this study is to investigate if a multilevel power converter may be used in an aerospace S/G system.

## 1.1 Motivation and Objectives

The primary motivation of this thesis is the application of a multilevel converter in an aerospace S/G system. If successful and this technology were applied to future engine starting systems, it is hoped that a reduction in the required level of passive filtering would result both at machine and distribution bus terminals.

The key objectives are therefore:

- **Identify what is required of a power converter in a S/G system.**
- **Evaluate the available power converter topologies and select which is most appropriate for this application.**
- **Validate the converter performance with typical aerospace S/G machines operating under realistic conditions.**

- **Consider the grid interfacing of the power converter to the aircraft's distribution network.**

## 1.2 Thesis Outline

In Chapter 2 a brief review of a typical aircraft electrical generation and distribution network is provided. Following this is a literature review covering current and potential future aircraft S/G machine and converter topologies. The various power quality standards governing aircraft electrical systems are then described.

Chapter 3 provides a review of the various multilevel and other competing power converter topologies suitable for use in a S/G system. The topologies are compared to find the most suitable for this application. In Chapter 4 a review of power converter control and modulation strategies is conducted. Emphasis is placed on what capabilities the selected control strategy must provide in this challenging and unique application.

In Chapter 5 the selected converter topology and controller are applied to a PM S/G system. The vector control of the machine is examined in detail. The test rig used throughout this study is described with emphasis on how it provides a realistic test platform. Experimental results are included to validate the proposed system.

In Chapter 6 the developed system is applied to a WFSM S/G. The excitation conditions are first examined to enable this machine to be used in this manner. Experimental results are provided to demonstrate satisfactory system performance.

Chapter 7 investigates control techniques to further improve the harmonic performance of the converter. Experimental results are provided to compare the new controller against the industry standard.

The grid interfacing of the converter to an aircraft's electrical network is explored in Chapter 8. Emphasis is placed on making the converter resilient to the level of electrical distortion typically encountered in a real application.

In Chapters 9 and 10 this study is concluded and recommendations made for future work to compliment this study.

## 2 Aerospace Systems

### 2.1 Introduction

This chapter provides a description of a typical aircraft's electrical network and engine starting systems. Both power generation and distribution is examined as well as the standards to which any installed system must comply. This is considered necessary as the nature of the existing power network will govern how the developed S/G system is interfaced, as well as influencing it's design. Current and future generators are examined, and the suitability of each topology for incorporation in a S/G system discussed.

The power converters typically found in aerospace power systems are then documented. This is important for two reasons; firstly any novel system proposed in this study must provide clear advantages over the existing technology, secondly a significant portion of the load upon a S/G system during generation mode is likely to be other power converters. It is essential that consideration is given in the design of the S/G system to the non-linear nature of these power converter loads.

For completeness, existing engine starting methods are listed and described. It is hoped that the starting method proposed in this study may with further development provide both a net weight reduction and increased functionality compared to these established methods.

### 2.2 Power Generation and Distribution

A twin engine aircraft's power network may be divided into the main and backup network. Both networks have a generator coupled to each engine. A description of generator topologies commonly found upon aircraft is provided in Section 2.2.1. A backup network is required to provide a high level of redundancy [2.1] in the system. In addition to the two main engines, a smaller gas turbine called the Auxiliary Power Unit (APU) which is typically located at the rear of the aircraft, also has a small generator. The APU is installed to

provide compressed air for starting the main engines and electrical power for the galley when the main engines are off [2.2].

Traditionally the main network is formed by two isolated three phase AC buses, one running down each side of the aircraft [2.1,2.2]. To produce the fixed frequency supply required the generators must be driven at a constant speed which is determined by the number of pole pairs present in the stator winding. The generator cannot be directly coupled to the turbine's shaft. This is because the turbine's rotational velocity is typically substantially higher ( $\approx 30,000$ - $50,000$  rpm in the compressor) than the generator's rated speed ( $\approx 6000$  rpm) [2.3], also the speed fluctuates during operation. To overcome this the generator is coupled to the shaft by a Constant Speed Drive (CSD) [2.1,2.2]. The CSD is a gearbox that ensures the generator rotates at constant velocity regardless of engine speed. Typically the generator and CSD are packaged together in an Integrated Drive Generator (IDG) [2.1,2.2,2.4].

Each main generator, supplies the AC bus running down its respective side of the aircraft. Isolation is maintained between the buses to avoid the need for synchronisation. In the event of an electrical fault upon the main bus, power may be routed using Bus Tie Breakers (BTBs) from the functioning bus [2.1,2.2]. This provides additional electrical redundancy.

Unlike on the main network, the backup generators rotate at a speed that fluctuates with the engine shaft speed, therefore producing a Variable Frequency, Variable Amplitude (VFVA) output. A power converter is employed to take this VFVA supply and produce the fixed amplitude, fixed frequency supply required by the network. This is termed a Variable Speed Constant Frequency (VSCF) converter and is discussed in Section 2.3.

With the exception of the A380 and B787, in most large civil aircraft the main power network is a constant 400 Hz, 115 V<sub>LL</sub> as stipulated in the standards [2.5,2.6]. In addition to the main network, a 28 V AC network and 28 V DC link is also provided on some aircraft [2.2,2.5]. The DC link is supplied by Transformer Rectifier Units (TRU) [2.4,2.5] or from the aircraft's battery bank when the main engines are off.

A simplified diagram of a twin engine aircraft's power network is provided in Figure 2-1 [2.1,2.2]. It is apparent from this figure how transfer buses and BTBs may be used to route either the main or backup bus onto the opposing main distribution bus in the event of a

fault. There is therefore a high level of redundancy in this system. Most aircraft also feature an external power socket. The airports shore supply can therefore be used to supply all galley requirements when the main engines and APU are off.

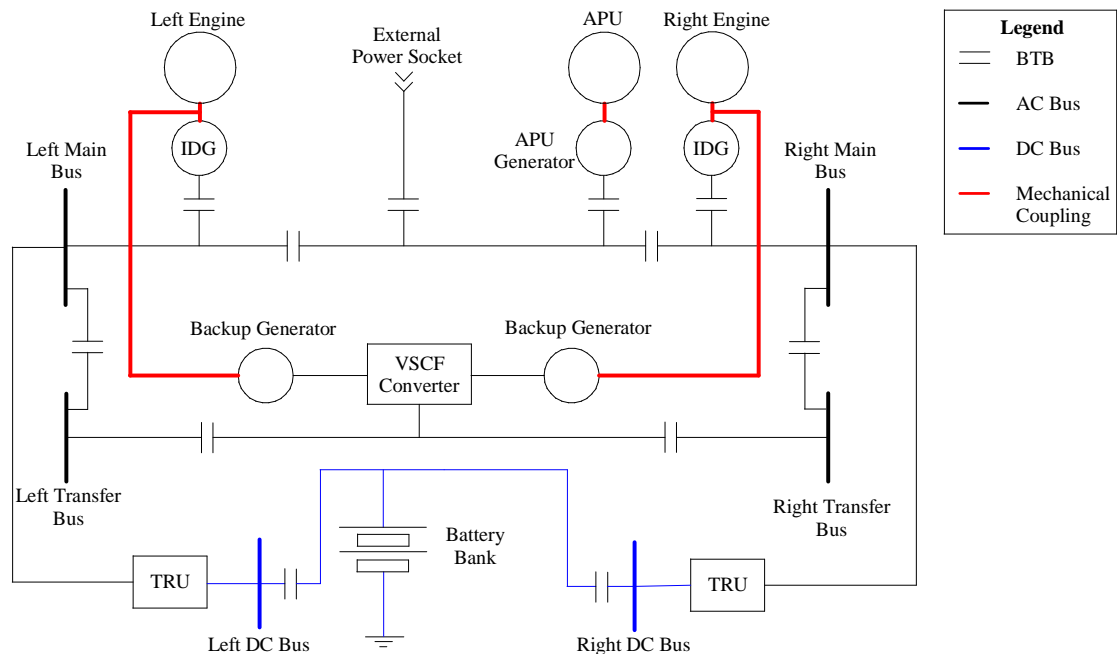


Figure 2-1: Twin engine aircraft power network.

The Airbus A380 is the first generation of MEA in the sense that its electrical system differs from the conventional power network described previously. The CSD has been removed from the IDG, thus the generator output frequency varies with turbine speed in the range 360-800 Hz [2.4,2.7,2.8]. This is a benefit as CSDs feature complex and heavy hydraulics to produce a constant speed output. The CSD also imposes a heavy maintenance schedule upon the aircraft owner/operator. One drawback of this arrangement is the necessity to ensure that all electrical loads across the aircraft are capable of utilising this variable frequency supply. A more complex power converter stage may therefore be required at the input for some loads.

An even more complex electrical system than that shown in Figure 2-1 is employed in the B787. The aircraft distributes AC power at 235 V and 115 V, whilst DC power is distributed at 270 V and 28 V. As in the A380, variable frequency generators are used to avoid the need for an IDG. AC power is delivered both as both variable frequency and fixed frequency

(400 Hz). The fixed frequency supply is reserved for frequency sensitive loads and is obtained using solid state power converters.

### 2.2.1 Aerospace Generators

Main generators are typically Wound Field Synchronous Machines (WFSM) [2.2,2.9,2.4,2.10], a block diagram of this topology is presented in Figure 2-2. The WFSM has three constituent stages [2.2,2.10] all built around the same shaft; these include a small Permanent Magnet (PM) generator, a rotating transformer with a rotor mounted diode rectifier connected to the secondary winding and a large Wound Field (WF) generator.

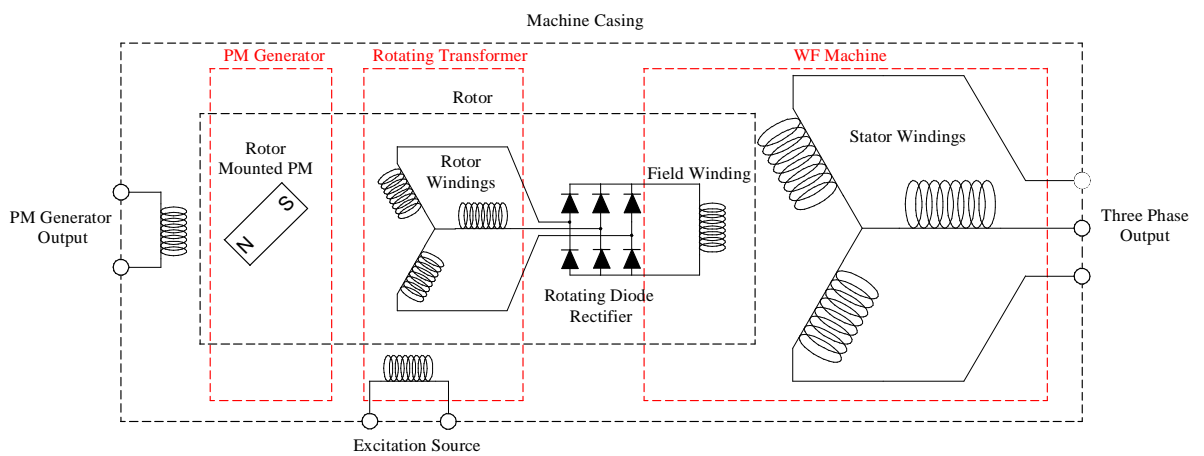


**Figure 2-2: Wound field synchronous machine.**

The field winding produces the magnetic field required to induce electrical power in the stator. Thus the three phase output is proportional to the magnitude of the current flowing through the field winding. This is of major benefit to aircraft electrical system designers. Control of the field current provides simple regulation of the output voltage magnitude regardless of fluctuations in electrical loading or engine speed. This negates the need for a power converter on the machine output to produce the fixed amplitude voltage required by the distribution bus [2.4]. Control of the field current also provides unsurpassed fault tolerance. In the event of a fault the field current can be removed/reduced to limit the current. A Generator Control Unit (GCU) is employed to produce the required field current to regulate the stator output.

The purpose of the rotating transformer and diode rectifier is to supply the field winding without resorting to a slip rings and brushes arrangement [2.2]. A DC excitation source is applied across the exciter winding (primary). A current is induced in the rotor winding (secondary) due to the relative motion between it and the stationary excitation winding. This rotor winding current is rectified and used to supply the field winding.

The PM generator is present to provide power for excitation at engine start-up. As the generator accelerates a small electrical output is produced by the PM machine, this is used to supply the GCU in order to produce an initial electrical output on the stator. The PM machine is sometimes referred to as the pilot generator. Once the APU has reached operational speed, some of the stator output is fed back to supply the GCU.

### **2.2.2 Future Aerospace Generators**

In subsequent generations of the MEA the required electrical generating capacity is predicted to increase substantially [2.4]. This is intuitive considering that as existing mechanical/pneumatic/hydraulic systems are replaced with electrical motors/actuators the net electricity consumed across the aircraft will invariably increase.

It is documented in the literature [2.3,2.4,2.11] that the loading placed upon an engine due to electrical generation may become too large to place upon just one of the engine's shafts. In the case of a two spool engine it may be necessary to drive generators from both the Low Pressure (LP) and High Pressure (HP) shafts. As the HP and LP shafts operate at different speeds, a power converter may be required at the generator output to condition the electrical power such that it may be distributed on a common bus, if air-framers wish to persist with this form of power distribution. This system is highlighted in Figure 2-3 but this time showing the structure for an engine with an additional Intermediate Pressure (IP) shaft and corresponding generator.

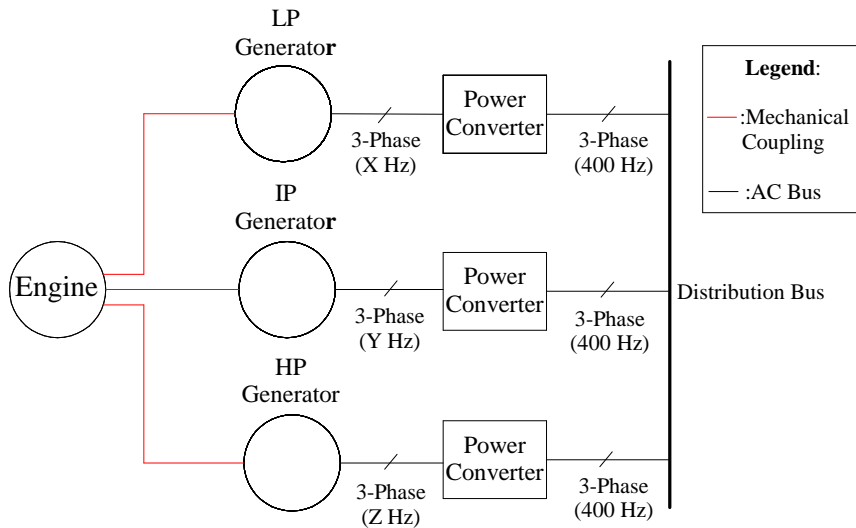


Figure 2-3: Generator arrangement for a three shaft engine.

In order for manufacturers to incorporate one/two additional generators into the engine without incurring a significant weight gain, it has been widely proposed in the literature [2.3,2.4,2.12] and in industry that the machines should be embedded within the engine (Figure 2-4) [2.12]. Here the machine is built directly around the shaft inside the engine. This would mean the CSD is no longer required therefore saving weight and reducing mechanical coupling complexity.

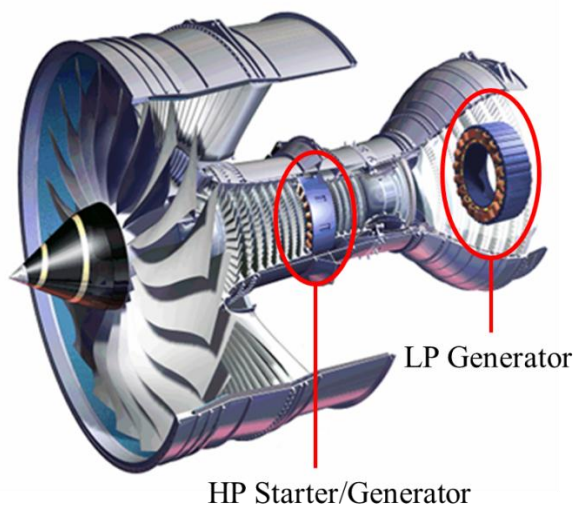


Figure 2-4: Turbine including HP Starter/Generator and LP generator.

However an embedded machine would be required to operate in a hostile environment, rotating at shaft speed within the engine's high ambient temperature. The two most likely machine topologies for this application would be PM synchronous (PMSM) and Switched Reluctance (SR) [2.3,2.4,2.12,2.13]. Both topologies have a relatively simple and robust rotor, which makes these designs more resilient to the embedded operating conditions when compared to a WFSM with its complex rotor structure.

SR and PMSM aerospace generators are also likely to provide superior power density when compared to the equivalent WFSM case. Neither SR nor PMSMs require the small PM pilot generator, exciter windings and rotating diode rectifier. In addition the GCU may be removed. However PMSM machines do not have the fault tolerance property of the WF topology. This is likely to necessitate additional protection at the generator terminals, or perhaps in the PM case an increased synchronous reactance, to limit the potential fault current. An increase in synchronous reactance however is not desirable as it will result in increased machine losses and a reduction in the Power Factor (PF). This is because the VA rating of the machine must be increased to achieve the same level of real power, resulting in a higher current magnitude. This increases losses in both the converter and the machine. This will necessitate a higher power converter in the case of a S/G system. This thesis concerns itself only with the power converter design necessary for a synchronous machine S/G and is therefore not applicable to a SR system.

To accommodate multiple generators within the confined space of an engine it will be essential that the machines are of high power density design. The power density of the machine may be increased by pushing the PF towards unity. This can be achieved by reducing the synchronous reactance, resulting in a low inductance machine. Unfortunately if as a consequence of reducing the synchronous reactance the stator current waveform's harmonic spectrum deteriorates, losses in the rotor will increase substantially. Rotor losses in an embedded machine are problematic due to the inaccessible and hostile location. This makes cooling the rotor difficult. It is hoped that the topology proposed in this study may go some way to enabling the synchronous reactance to be reduced, whilst still producing a sufficiently high waveform quality such that rotor losses do not increase. This will afford aerospace machine designers the flexibility to pursue greater power density free from the limitations imposed by the power converter.

### 2.2.3 Power Quality Standards and Filtering

Like all aircraft systems, power converters are subject to extensive legislation to ensure safe operation. Although this body of work is an investigation into the feasibility of using the multilevel topology within a S/G system and is not aimed at producing an industry standard device ready for implementation within the aircraft, it is important that the relevant standards are examined to ensure there is no clause that the chosen topology could not theoretically meet.

A S/G system has two distinct modes of operation, during the starting procedure the power converter must draw electrical power from the grid and therefore acts as a load upon the system. Once the engine has been started, the power converter draws electrical power from the generator to place onto the grid, in this mode the system acts as a supply.

Table 2-1 [2.5,2.6] provides the steady state characteristics to which an aircraft's 400 Hz supply must comply. The output of the S/G system under normal generating operation must therefore comply with these limits. The definitions from [2.6] for some of these characteristics are provided below.

- **Voltage modulation** is defined as the variation of the AC voltage and is calculated as the difference between the maximum and minimum values that occur in a one second period.
- **Distortion factor** is the ratio of the AC distortion to the rms value of the fundamental component.
- **Frequency modulation** is the difference between the maximum and minimum frequency values that occur in a one minute period.
- **Distortion spectrum** quantifies the distortion in an AC system in terms of the amplitude of each frequency component.

Steady State Characteristics	Limits
Steady State Voltage	108-118 V (rms)
Voltage Unbalance	$\leq 3$ V (rms)
Voltage Modulation	$\leq 2$ V (rms)
Distortion Factor	$\leq 0.05$
DC Component	+ 0.1 to - 0.1 V
Steady State Frequency	393 to 407 Hz
Frequency Modulation	4 Hz
Spectrum Envelope	See Figure 2-5

Table 2-1: Normal operating limits for a 400 Hz system.

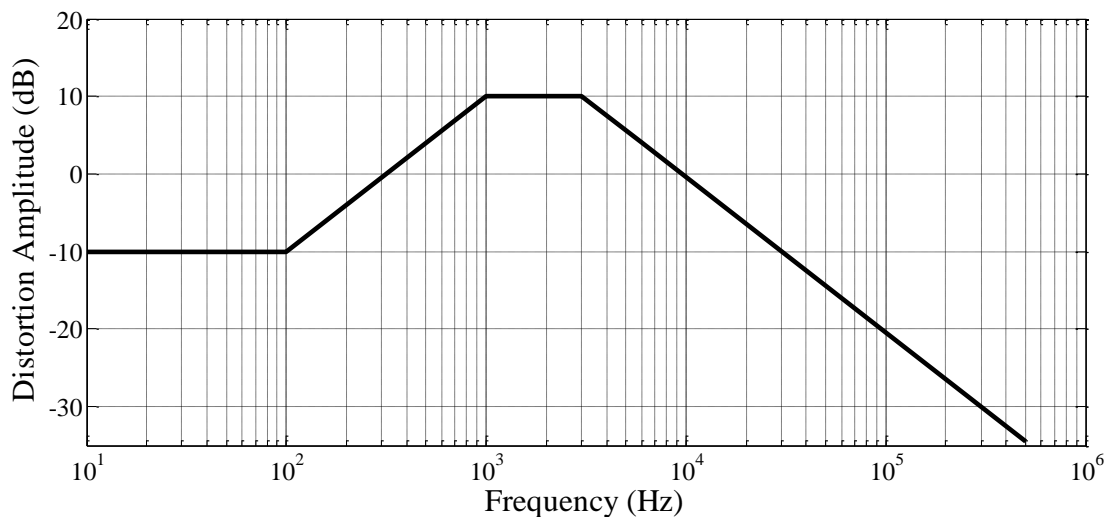


Figure 2-5: Spectrum envelope for 400 Hz system under normal operating conditions (MIL-STD-704F).

The limits provided in Table 2-1 govern performance in a fixed frequency system. Additional standards exist governing the behaviour of variable frequency distribution

networks such as those on modern large civil aircraft such as the A380 or B787. These standards are not reviewed as the assumption made throughout this study was that a fixed frequency distribution bus is used. This assumption has been made as this study focuses on the design of a back-to-back power converter which connects the S/G to the distribution bus. It would be contrived to have a fully rated power converter and then distribute at a variable frequency thus complicating the grid interfacing of all connected loads.

In the case of a back-to-back connected aerospace power converter the limits provided in Table 2-1 particularly the spectrum limits will partly size the grid side filter. In addition the filter size will also be determined by performance requirements under fault conditions. To comply with these limits 3<sup>rd</sup> order LCL filters are typically used in preference to second order (LC) and first order choke filters. Third order filters are preferred as the 60 dB/decade roll-off is substantially greater than the roll-off for the harmonic limits in standard. Thus, a lower switching frequency may be employed minimising converter losses whilst still meeting the harmonic standard. It has also been suggested [2.14] that by adopting a higher order filter much smaller inductor values may be used. This provides a total filter net weight reduction when compared to a comparable lower order filter achieving similar harmonic attenuation. However the greater harmonic attenuation of the higher order filter comes at the cost of an increased component count. As with all higher order filters, there is a need to consider damping to safeguard stability.

The performance of electrical loads upon the distribution network is also governed by the power quality standards. This does not impact on the performance requirements of the power converter during starting mode as the standards make allowances for the degradation of power quality during an electrical start. However for a real world application when designing the grid interfacing inverter's controller and filter, the non-uniform currents drawn by the bus connected loads during generation mode must be considered to guarantee satisfactory converter performance.

It is considered unfeasible for a PhD study to perform a full aircraft electrical network simulation to examine the effect of all the non-linear loads. It would require industrially sensitive data from the airframer which is not available to this study. Instead a brief review of allowable load characteristics is provided to give a snapshot of the kind of non-uniformity the generation system can be expected to encounter. In Section 8 performance under simple distorted load conditions is examined.

For electrical loads exceeding 30 kVA, the characteristic limits are provided in Table 2-2 [2.5,2.6]. Where  $I_{fund}$  represents the amplitude of the fundamental component of the load current, and load unbalance is defined as the ratio of the highest and lowest phase loads [2.6].

Load Characteristic	Limits
Load Unbalance	3.33%
Power Factor	Unity to 0.85 lagging
Spectrum Envelope	See Table 2-3

**Table 2-2: Characteristics for loads exceeding 30 kVA.**

Harmonic Order	Limits
$3^{rd}, 5^{th}, 7^{th}$	$0.02 * I_{fund}$
Odd Triplen Harmonics	$0.1 * I_{fund} / n$
Odd Non-Triplen Harmonics (11,13)	$0.03 * I_{fund}$
Odd Non-Triplen Harmonics (17,19)	$0.04 * I_{fund}$
Odd Non-Triplen Harmonics (23,25)	$0.03 * I_{fund}$
Odd Non-Triplen Harmonics (29,31,35,37)	$0.3 * I_{fund} / n$
Even Harmonics (2,4)	$0.01 * I_{fund} / n$
Even Harmonics (>4)	$0.0025 * I_{fund}$
Subharmonics and Interharmonics	$0.001 * I_{fund}$

**Table 2-3: Current harmonic limits for three phase loads greater than 5 kVA.**

Standards [2.15,2.16] are also imposed on the performance and design of power converters for use in the aerospace environment. Key points from [2.11,2.13] which are likely to effect the design of a S/G system are summarised in Table 2-4.

	<b>Clause</b>	<b>Standard</b>	<b>Specification</b>
1	Shelf Life	[2.16]	The power converter must have a minimum shelf life of 20 years.
2	Altitude	[2.16]	The power converter must continue to function at altitudes up to 21,300 meters.
3	Efficiency	[2.15]	The power converter must operate with an efficiency greater than 65%.
4	Fault Tolerance	[2.15]	The power converter must be capable of producing 150% rated output for 10 seconds and 300% rated output for 5 seconds.
5	Overhauls	[2.15]	The power converter must be capable of a minimum 3000 hours of operation between overhauls.
6	Start-up	[2.15]	The converter must reach a steady state output within 1 second of start-up.
7	Ripple	[2.15]	The power converter must not produce a ripple greater than 2 V peak-peak at the output.

**Table 2-4: Standards governing power converter performance.**

The clauses provided in Table 2-4 are likely to impose restrictions on the design of the power converter for a S/G application. For instance the fault tolerance clause will mean both the converter and filter would need to be sized not for the nominal power but for fault conditions. The efficiency clause may limit the choice of some topologies owing to high losses.

Crucially the shelf life and performance at altitude precludes the use of electrolytic capacitors in aerospace. The performance of electrolytic capacitors is also compromised at

the elevated temperatures which are likely to be found in future aircraft power systems with the deployment of wide band semiconductors. Electrolytic is normally the capacitor technology of choice in industry to achieve high levels of bulk energy storage efficiently and cheaply. As these are not available in aerospace other technologies such as ceramic or polymer film have been explored. Unfortunately the energy density achievable with these technologies is lower when compared to electrolytic. The effect is to discourage the use of large amounts of bulk energy storage in aerospace due to the inherent weight penalties. This has resulted in great interest in bulk-storage-less topologies such as the matrix converter (discussed in Section 3.3.1).

## 2.3 Aerospace Power Conversion

The most commonplace power converter found in aerospace is the VSCF. This converter has found limited use on the main distribution network and is primarily used on the backup network. The backup PM generators fitted to each engine on the B777 and B737 [2.1,2.9], are used in the event of a fault to supply the VSCF. The VSCF first rectifies the VF PMSM output, then inverts this to a constant 400 Hz, 115 V<sub>rms</sub> line-line output. The VSCF is formed by a two back-back, six switch inverters connected using a common DC link [2.1]. Capacitors upon the DC link are used to decouple the two inverters, and IGBTs are used for the switching devices. The VSCF power circuit is shown in Figure 2-6.

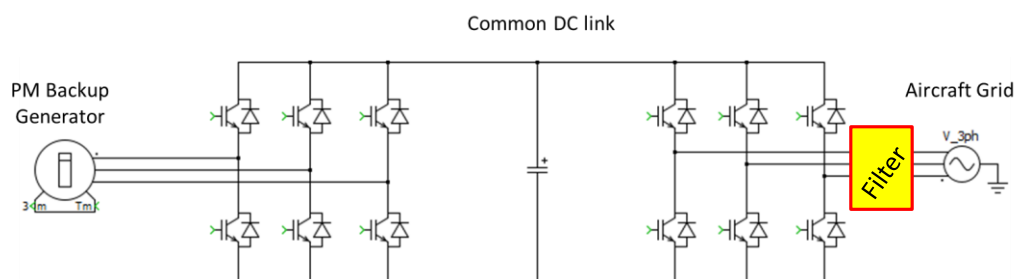


**Figure 2-6: Variable Speed Constant Frequency Converter**

The uptake of the VSCF in the main power distribution network has been limited in civil aviation. The reliability of the VSCF drive is not considered to rival that of an IDG. Use of VSCFs in defence aerospace is not known by the author at the time of writing.

Aircraft and particularly engine manufacturers pursuit of an all-electric starter-generator does necessitate the use of some solid state power conversion in the main power path in

future aircraft. At present the VSCF must be considered the most mature technology with semiconductor manufacturers producing packaged, six switch Intelligent Power Modules (IPM). The use of this topology is therefore greatly simplified. There are a number of well documented limitations of this circuit which are discussed in Section 3. It is the objective of this study to examine alternative topologies to the VSCF for use in future S/G systems. As the most mature technology the two-level VSCF is the benchmark against which alternative topologies must be compared.

An alternative method to the IDG or VSCF to obtain a Constant Frequency (CF) bus from a generator connected to a variable speed shaft is to use a cycloconverter. This method has been adopted in a number of military applications [2.9]. The cycloconverter works using an array of switches to electronically commutate the three-phase, variable frequency generator output, to produce the required constant frequency supply to the bus [2.17]. It therefore has similarities to the matrix converter discussed in Section 3.3.1.

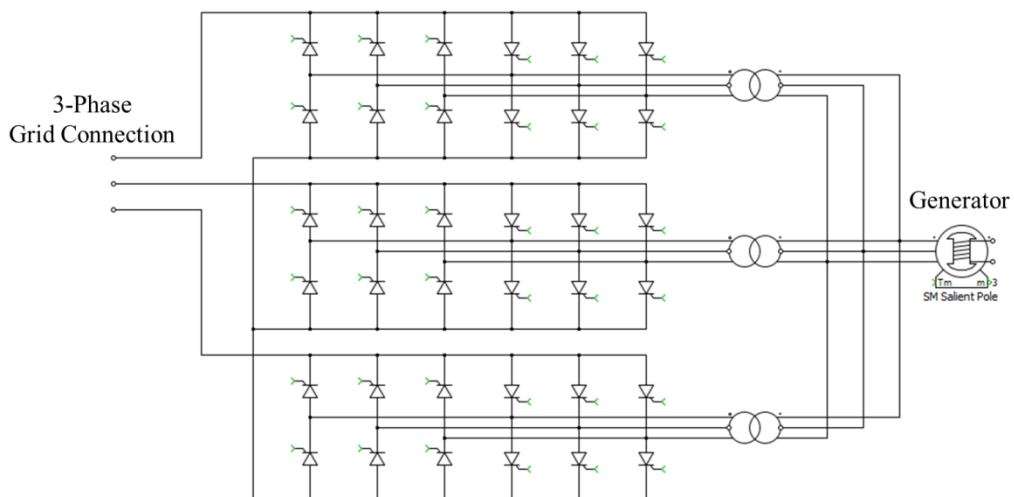


**Figure 2-7: Cycloconverter.**

From a generator system perspective the cycloconverter has a number of advantages. Firstly there is no large DC link energy storage. This is likely to reduce the converter volume substantially and also limit the potential fault current. The switches are also naturally commutating which reduces both the switching losses and gate drive complexity.

From a S/G system perspective the major disadvantage of the cycloconverter is the requirement for the input frequency to be substantially greater than the output frequency

for normal operation of the converter. The generator output frequency would therefore need to be a lot higher than the grid frequency, and would also prevent starting operation from a fixed frequency bus. The cycloconverter is therefore not considered applicable to a S/G system.

The major power converter topologies found on aircraft is the Transformer Rectifier Unit (TRU) and the Auto Transformer Rectifier Unit (ATRU). TRUs are used to produce the DC distribution buses found in both modern and older aircraft electrical architectures, and also to supply some large loads. Numerous configurations exist, all though feature some form of phase shifting transformer/autotransformer to obtain the high pulse number typically required to comply with power quality standards, then multiple bridge rectifiers with the outputs connected in either series or parallel. Either line or force commutated devices may be used depending on the application and the level of output regulation required. The force commutated variant being preferred if control is required over the output voltage. An example 12-pulse TRU is shown, however 18 and 24 pulse variants are also commonplace [2.18]. An interphase reactor would also normally be included in a 12-pulse rectifier to guarantee current sharing between bridges if they were instead connected in parallel.

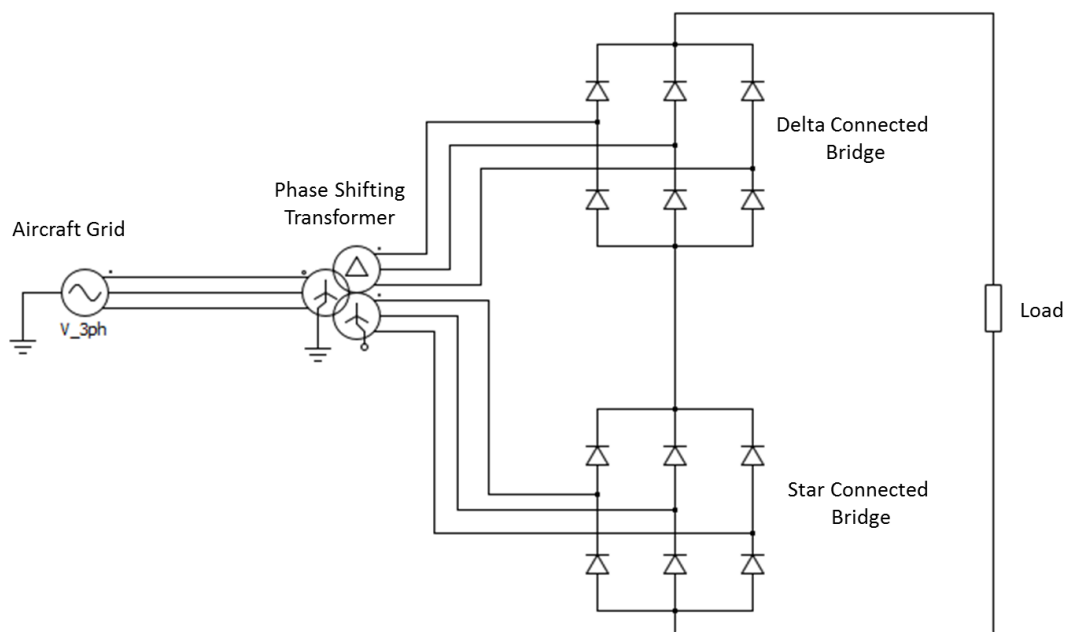


**Figure 2-8: Twelve Pulse Transformer Rectifier Unit.**

Although TRUs are not suitable for use in S/G systems as they do not provide bidirectional power flow a description has been included in this study as they are likely to make up a

significant portion of the load upon the grid facing inverter during generation mode. The non-linear nature of a TRU results in a distorted current waveform. The converter controller must therefore be adapted to function under this non-ideal electrical loading.

## 2.4 Engine Starting Systems

There are a number of different industry standard engine starting systems. The method used depends on the engine size, configuration and application. For small engines such as turboprops or APUs, a DC electric starter motor is typically employed supplied by the aircraft's battery bank. The starter motor is coupled to the engine shaft through the auxiliary gear box.

The majority of medium/large civil engines are started using a pneumatic starter. Compressed air typically bled from the APU is used to drive an air turbine mechanically coupled to the engine shaft through a clutch [2.19]. In the case of a two spooled engine the starting system is typically coupled solely to the HP shaft.

In some aircraft the starter turbine is instead driven by a fuel cartridge. The combustion of the cartridge accelerates both the starter turbine and the engine HP shaft to sufficient speed whereby it can be ignited.

The first generation of large civil engines which feature an electric start option is now in-flight. In the case of the Trent 1000 and GENx engines, the WFSM generator is temporarily driven as a starter motor using an inverter. Upon completion of the starting cycle, breakers are used to disconnect the inverter from the machine, and instead connect the distribution bus directly to the generator. This results in the frequency wild distribution system outlined in Section 2.2.

## 2.5 Conclusion

This chapter initially focused on the electrical network found in a typical aircraft using fixed frequency distribution. The main and backup networks were identified along with the numerous normally isolated distribution buses. This defines the architecture an all-electric S/G system must fit into.

Current and future aerospace generator topologies were then examined. Likely candidate machines for a S/G were identified and in subsequent chapters the systems necessary to utilise these topologies in this mode is discussed.

The standards governing aircraft power quality and power converter design was then introduced. Though the purpose of this study is not to produce an industry standard system, it is important to consider the relevant legislation to ensure that it does not influence topology selection.

Finally existing aerospace power converters and engine starting systems were reviewed. This puts the proposed system developed in this study into perspective with the industry standard.

## 2.6 References

- [2.1] L. Andrade, C. Tenning, "Design of the Boeing 777 Electric System," IEEE National Aerospace and Electronics Conference, Dayton, Ohio, Vol. 3, pp.1281-1290, 1992.
- [2.2] E. H. J. Pallet, "Aircraft Electrical Systems," Longman, 1987.
- [2.3] A. J. Mitcham, J. J. A. Cullen, "Permanent Magnet Generator Options for the More Electric Aircraft," Power Electronics Machines and Drives Conference (PEMD), Bath, UK, pp. 241-245, 2002.
- [2.4] C. R. Avery, S. G. Burrow, P. H. Mellor, "Electrical Generation and Distribution for the More Electric Aircraft," Universities Power Engineering Conference, Brighton, UK, 2007, pp.1007-1012.
- [2.5] E. Matheson, K. Karimi, "Power Quality Specification Development for More Electric Airplane Architecture," Power Systems Conference, Florida, USA, 2002.
- [2.6] Department of Defence Interface Standard: Aircraft Electrical Power Characteristics, MIL-STD-704F, 2004.
- [2.7] J. Chang, A. Wang, "New VF-Power System Architecture and Evaluation for Future Aircraft," IEEE Transactions on Aerospace and Electronic Systems, Vol. 42, April, 2006, pp. 527-539.
- [2.8] J. Chang, "Outlook of Roles and Necessities of Power Electronics for VF-Power System of Future Large Aircraft," International Conference on Electrical Machines and Systems, Wuhan, China, 2008, pp. 1190-1195.
- [2.9] I. Moir, A. Seabridge, "Aircraft Systems: Mechanical, Electrical and Avionics Subsystems Integration," Professional Engineering Publishing Ltd, 2001.
- [2.10] M. E. Elbuluk, M. D. Kankam, "Potential Starter/Generator Technologies for Future Aerospace Applications," IEEE AES Systems Magazine, pp.24-31, 2007.

- [2.11] M. J. Provost, "The More Electric Aero-Engine: A General Overview from an Engine Manufacturer," Power Electronics Machines and Drives Conference (PEMD), Bath, UK, pp. 246-251, 2002.
- [2.12] D. J. Powell, G. W. Jewell, J. D. Ede, D. Howell, "An Integrated Starter/Generator for a Large Civil Aero-Engine," International Energy Conference and Exhibit, AIAA, San Francisco, USA, 2005.
- [2.13] J. D. Ede, G. W. Jewell, K. Attallah, D. J. Powell, J. J. A. Cullen, A. Mitcham, "Design of a 250kW, Fault Tolerant PM Generator for the More Electric Aircraft," International Energy Conference and Exhibit, AIAA, San Francisco, USA, 2005.
- [2.14] M. Liserre, F. Blaabjerg, S. Hansen, "Design and Control of an LCL-Filter-Based Three-Phase Active Rectifier," IEEE Trans. Industry Applications, Vol. 41, September, pp. 1281-1291, 2005.
- [2.15] BS 2G 169:1971, Specification for static inverters.
- [2.16] BS G 249:1993, Specification for solid-state remote power controllers – General Requirements.
- [2.17] T. H. Barton, "Rectifiers Cycloconverters and AC Controllers," Oxford Science Publications, 1994.
- [2.18] Ismael Araujo-Vargas, "High Performance Rectification for Future Power Networks," Ph.D. Thesis, University of Manchester, 2007.
- [2.19] Ronald D. Flack, "Fundamentals of Jet Propulsion with Applications," Cambridge University Press, 2005.

## 3 Power Converter Topologies

### 3.1 Introduction

The objective of this chapter is to select the best suited converter topology for further development into a novel *S/G* system. The key requirements were developed in the previous chapter:

- Capable of bidirectional power flow.
- Suitable for driving a synchronous machine in starting and generating modes.
- Provide excellent power quality at the grid connection without resorting to copious amounts of filtering.
- Minimise harmonic current flow at the machine side therefore reducing machine losses.
- Power density should be considered from the outset.

The field of multilevel converters has received considerable attention in the literature for use in applications demanding some of the aforementioned attributes. It is therefore the objective of this study to determine if and how such a converter topology could be applied in this application.

The chapter initially provides a review of the basic concept of multilevel power conversion and the associated advantages. This includes a comparison between the outputs of converters with different numbers of levels. The most prominent converter topologies documented in the literature are then examined. For each topology a critical assessment is made upon the suitability for the given application.

Also pertinent modifications to the main three topologies are discussed to see what benefits to this study they provide. Finally other converter topologies which do not fall under the broad multilevel category are reviewed. Attention is focused on topologies that

have received a large amount of attention from the aerospace industry, to see if they have any usefulness in this study.

The chapter is then concluded by comparing all topologies to see which is deemed the most appropriate. The selected topology is then carried forward for the development discussed in the remaining chapters.

### 3.2 Multilevel Power Converter Topologies

The term “multilevel” is applied to a converter which has the ability to produce a stepped output waveform through the selective addition of several discrete voltage levels. Practically, this usually consists of a number of separate DC sources which may be summed at the output node using complex switching routines. A block diagram of a generic  $n$ -level converter and a characteristic stepped output waveform is provided in Figure 3-1 [3.1,3.2].

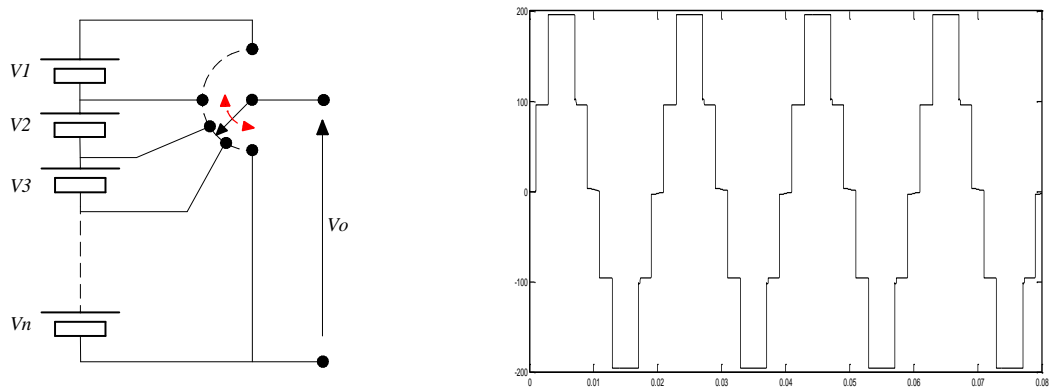


Figure 3-1: (a) Generic multilevel inverter, (b) Stepped waveform.

Multilevel converters initially found prominence where megawatt applications necessitated the connection of power converters to medium-voltage grids (up to 6.9 kV) [3.2,3.3]. The series connection of the power switches which is common in all multilevel converter topologies enables a DC link to be used which is greater than the break down voltage of an individual transistor.

In more recent literature, it is well documented how multilevel converters have been deployed in low voltage applications [3.4] where the transistor breakdown voltage is not a concern for the designer. These applications provide the system designer with additional advantages when compared to a conventional 2-level converter.

The most prominent advantage with regards to this study is an improvement in the spectrum of the output. For generic multilevel waveforms, the Total Harmonic Distortion (THD) of the output voltage waveform decreases as the number of converter levels increases. This can be observed in Figure 3-2 and Figure 3-3 where the line-line voltage waveform and spectrum are provided respectively for two, three and five-level converters obtained from simulation. To generate Figure 3-2, a high frequency PWM scheme was used. In all three cases a PWM carrier frequency of 24 kHz. The improvements in the output spectrum associated with both PWM controllers and multilevel converters are therefore achieved. A complete description of converter modulation strategies is provided in Chapter 4.

For clarity the procedure used throughout this thesis for calculating THD is shown in (3.0). Here, X is the variable for which the THD is to be calculated, this would typically be current or voltage. In (3.0),  $X_{WF}$  and  $X_{F1}$  denote the waveform rms value and the fundamental harmonic rms value respectively.

$$THD(\%) = \frac{X_{WF} - X_{F1}}{X_{F1}} * 100\% \quad (3.0)$$

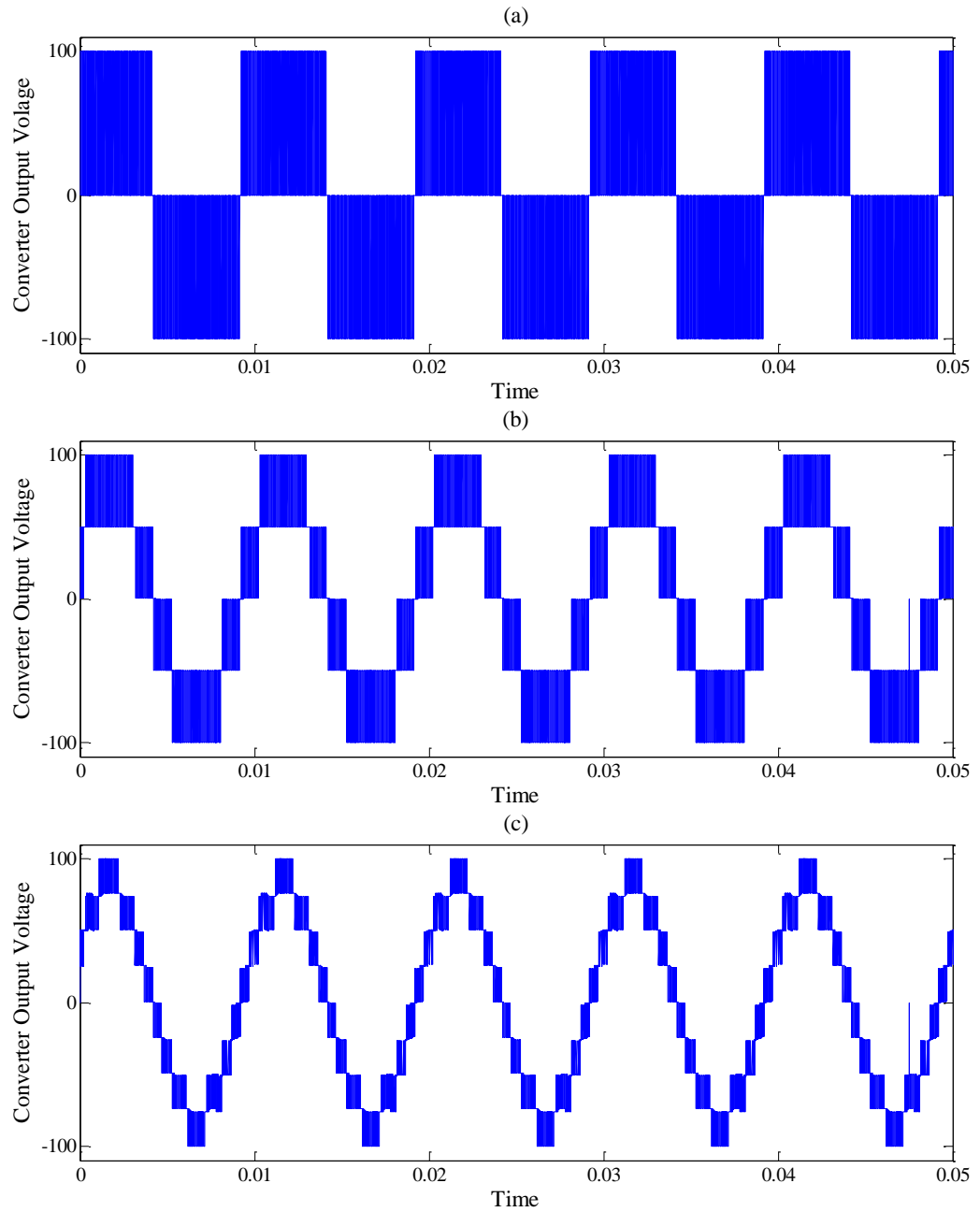
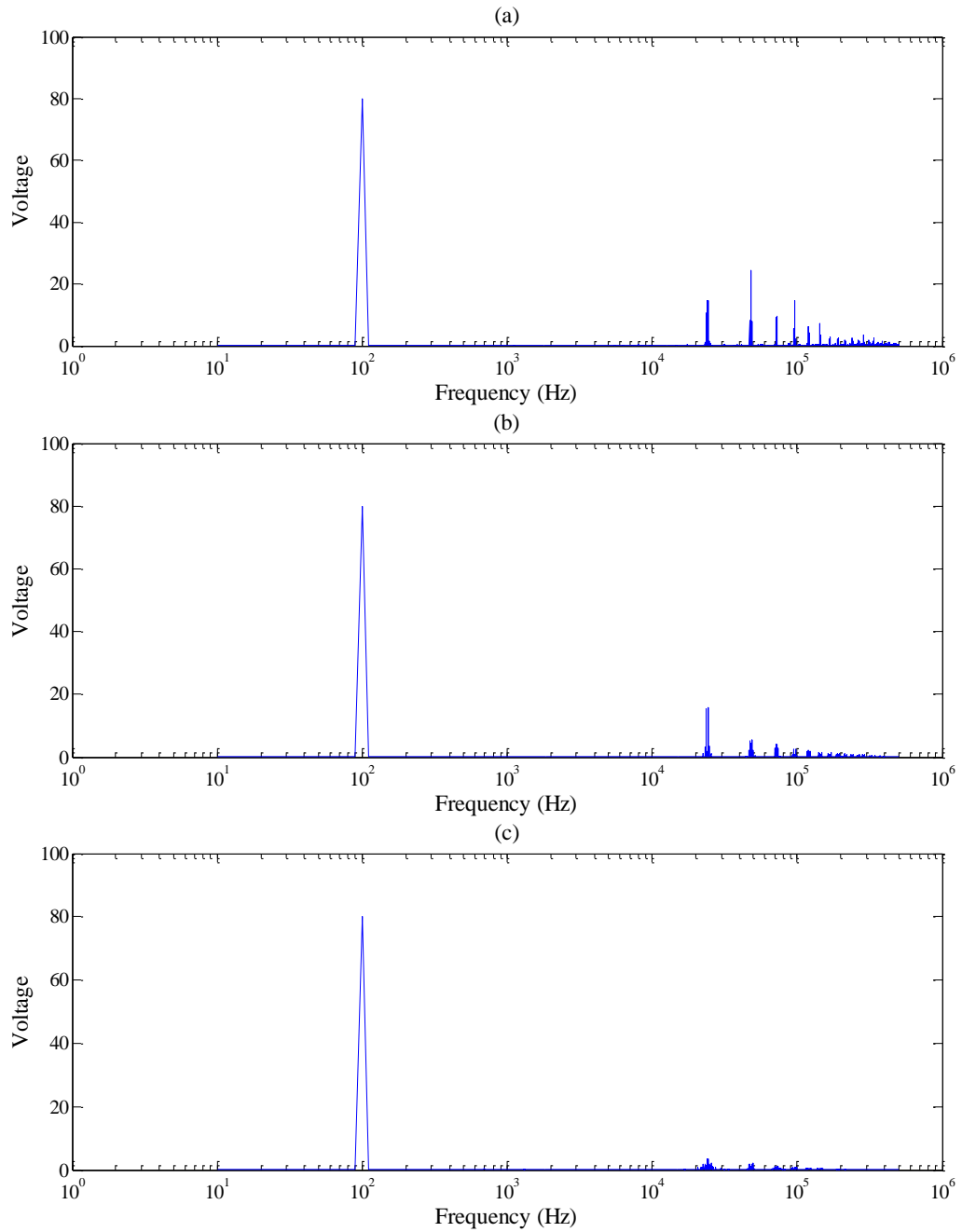


Figure 3-2: Power converter output waveforms, line-line voltages (a) Two level, (b) Three level, (c) Five level.



**Figure 3-3: Power converter output spectrum (a) Two level, (b) Three level, (c) Five level.**

The THD for each of the three waveforms was measured at 77 %, 38 % and 17 % for the two, three and five level converters respectively. The improvement in the measured THD is primarily because of the lower  $\Delta V$  in the stepped PWM waveform. For instance, in the two level waveform the  $\Delta V$  seen in the line-line voltage for one PWM period is 100 V. By contrast in the three and five level topologies the  $\Delta V$  in the output is 50 V and 25 V respectively.

The improvement in the quality of the converter output voltage provides several advantages. The ripple (and thus THD) in the converter output voltage is reduced.

Further advantages of utilising multilevel converters in low voltage applications include:

- **Reduction of the common mode voltage in the output.**

It is well documented in the literature [3.5] how the use of a voltage source converter switched at high frequency typically generates a substantial common mode voltage ( $V_{com}$ ) across the load. Common mode voltage is that induced across the load with respect to the ground. In a motor application some degree of  $V_{com}$  may normally be measured between the rotor and stator and is therefore directly across the bearings. In some circumstances  $V_{com}$  can reach sufficient magnitude that it exceeds the dielectric breakdown voltage of the bearing grease leading to current flow [3.5,3.6]. It is now accepted that this in some circumstances bearing currents leads to the early failure of the bearing.

In future, embedded generator designs eliminating bearing currents will be imperative from a safety perspective. In an embedded design with generators built around one or more of the engine shafts, any common mode voltage is likely to induce currents in the main shaft bearings. Manufacturers will not tolerate any degradation of such a critical component, a failure of which would be catastrophic. In addition, high common mode voltages in some circumstances may lead to the degradation of the winding insulation. This process could ultimately lead to winding-to-winding, or winding-to-earth faults which would lead to an electrical failure.

The use of a multilevel converter provides the designer with the flexibility to partially or completely eliminate common mode voltages [3.5,3.6]. Common mode voltages can be completely eliminated by selecting switching states which result in a constant  $V_{com}$ . This technique is documented in [3.5,3.10] where it is noted that whilst it is possible to completely eliminate any high frequency variation in  $V_{com}$ , this in practice severely limits the available switching vectors (see Section 4) and also reduces the maximum converter output voltage. In the case of a three-level inverter, employing a common mode elimination modulation strategy would result in a two-level operation. If the strategy was applied to a five-level inverter, a three-level output would be achieved.

As this thesis is primarily a feasibility study into the use of a multilevel converter in a S/G system a detailed examination of the level of common mode voltage attenuation required in a practical system is considered beyond the scope of this study. It is simply noted that a multilevel converter's modulation strategy may be adapted using the referenced techniques such that the level of common-mode filtering may be reduced in a practical application.

- **Possible increase in converter efficiency.**

The transistors in multilevel converters need to have substantially lower blocking voltages when compared to those in a two level inverter of equivalent power and voltage rating. This enables transistors with superior switching and on-state characteristics to be used [3.7], however this is mitigated by the fact that there are more switches. As total converter losses are dominated by device losses, in some applications the use of a multilevel converter may result in an improvement in the converter efficiency. This is ultimately application specific and will depend on factors such as required switching frequency, DC link voltage and available devices. A thorough loss review would therefore be required in each new application to determine the optimal solution.

- **Reduction in switching frequency.**

The improvement in the output waveform quality provides the flexibility to reduce the converter switching frequency when compared to a comparable two level system whilst still complying with the relevant power quality standards. Reducing the switching frequency in most applications will curtail the converter switching losses. This is likely to be a major benefit to engine manufacturers such as Rolls-Royce. Current starting systems are fuel cooled, along with many other mechanical subsystems as well as the engine oil. The cooling capacity of the engine's fuel is quickly becoming a depleted resource with so many systems reliant on it. The available cooling capacity in a system is limited by the maximum permissible temperature of the fuel.

The cooling demands are likely to get worse with More Electric Aircraft due to the increased electrical take-off power from the engine. Eventually it is likely that bleed air from the bypass will be required to meet the increased cooling requirements. However this increases the drag coefficient of the engine therefore reducing the efficiency of the whole

aircraft. Any means of reducing the cooling requirements of the electrical systems is therefore a benefit to both engine manufacturers and aircraft operators.

- **Reduced converter peak current rating**

The reduced  $\Delta V$  in the output spectrum results in a proportional reduction in the peak-peak value of current ripple. This reduces the required semiconductor pulsed current rating for a given rms current rating. In some applications this may enable lower current rated devices to be used with superior switching characteristics.

A reduction in the peak-peak ripple is of great benefit in a S/G system during starting mode. At low speeds the back-emf is negligible meaning the entire converter output voltage is across the stator winding impedance. The current ripple at this point is therefore at its maximum and any method to reduce it is a benefit.

It has been documented in the literature that by reducing the output ripple, the stall-torque rating of the drive is effectively increased. This may be a benefit in some aerospace applications depending on whether the drive is sized for starting or generating mode. The S/G units for large civil engines are sized for generating mode as the aircraft's power requirements are substantially larger than the power required for starting. However this may not be the case in smaller engines for regional or corporate aircraft. In this case an increase in stall torque would be a great advantage.

The increase in stall torque occurs because with the reduction of the current ripple, comes the opportunity to push the maximum peak DC output current closer to the rated current of the devices. With a two level converter the DC output current with zero back-emf is normally limited by the inverter's repetitive pulsed current rating. This can be overcome by increasing the switching frequency, however this is not always possible in large drives.

The disadvantages of adopting a multilevel converter for this application must also be considered.

- **Increased converter cost.**

Regardless of the multilevel topology selected for this application, it is likely to result in a substantially more complex converter. The complexity is increased both in the number of active devices, the converter layout (bus-bar designs) and the control. Increased converter complexity will ultimately result in a more costly solution when compared to a comparable two-level system. The increased converter cost due to the higher number of devices required may be slightly offset by the reduced switch voltage rating, therefore each individual device is likely to be cheaper. Performing a cost analysis for a suitably rated multilevel S/G converter ready for off-the-shelf implementation within an aircraft is considered beyond the scope of this thesis, particularly because it would require access to sensitive industrial information. However such a preliminary cost study would need to be conducted if a manufacturer was to consider the potential for a multilevel converter to be used in a S/G system.

The cost of a suitably rated medium-power multilevel converter particularly the neutral point clamped topology is likely to fall considerably as manufacturers release custom modules to fit this purpose [3.8,3.9]. A three-level inverter in a modular format will greatly reduce the converter layout complexity from a converter manufacturer's perspective and may also reduce the total system cost. This may eventually swing the cost-vs-complexity argument in favour of the multilevel converter.

- **Possible impact on converter reliability.**

Electrical system reliability is of paramount importance in the field of aircraft power electronics. Reference [3.10] describes the procedure for estimating the reliability of power electronic systems for use in US military aircraft. Similar standards exist governing the reliability of power electronic systems for use in civil aviation. One of the key approaches for estimating power system reliability is to calculate the Mean Time To Failure (MTTF). Reference [3.10] provides the standard approach to calculating the MTTF. All possible failure methods are identified and the probability of each occurring calculated. The probability of each failure method may then be combined to provide a figure for the overall

reliability of the system. One of the dominant fault mechanisms in a power converter would be the destruction of a switching device. The probability of a switching device failure is estimated by calculating the electrical “stress” under normal operating conditions which is then used to calculate the MTTF for that device [3.10].

Due to the greatly increased complexity and number of switching devices the reliability of multilevel converters is considered to be poor when compared to the classical two-level inverter. The converter inherently has a greater number of components leading to an increased number of possible failure mechanisms which in turn has a detrimental effect on the estimated MTTF. Concerns over reliability have hindered the uptake of this technology by the aerospace industry.

Certain topologies though may offer the opportunity to offset the increased number of failure mechanisms by having switching devices operating under greatly reduced electrical stress. For instance in the five-level diode clamped inverter discussed in Section 3.2.3, the main switching devices whilst carrying the full line current, are only subject to a fraction of the DC link voltage. Assuming equally rated devices are used, these transistors are under substantially lower electrical stress when compared to the equivalent devices in the two-level inverter. In the diode-clamped case the MTTF for each device is therefore likely to be larger.

The use of multilevel topologies may also become more attractive to manufacturers with the release of dedicated modules as the devices are contained within a more predictable and defined environment. Parasitic components such as stray inductance which with discrete components result in increased electrical stress, are minimised in the modular arrangement. Device heatsinking is also better defined and more consistent. Increased device manufacturer data is also available for modules making it possible to more accurately define key reliability parameters. The electrical stress upon fast switching IGBTs is influenced by stray inductance in the circuit. The data is provided by module manufacturers, but is hard to estimate if the converter is manufactured from discrete devices. The use of topologies such as the diode-clamped inverter with reduced device electrical stress available in a well-defined modular format is likely to appeal to aerospace manufacturers in the future looking to overcome the limitations of existing power converter systems without compromising reliability.

A brief description of the three major multilevel converter topologies is now provided.

### 3.2.1 Cascaded H-Bridge Converter

The cascaded H-bridge converter consists of the series connection of  $n$  H-bridges, where each bridge is supplied with its own isolated source [2.1,2.2]. In Figure 3-4 the schematics are provided for the single phase configuration of five and nine level cascaded H-bridge converters. The output of individual cell's may take the value of  $+V_{dc}$ ,  $-V_{dc}$ , or  $0V$ . The converter output voltage ( $V_o$ ) is formed by the summation of each cell's output [2.1,2.2].

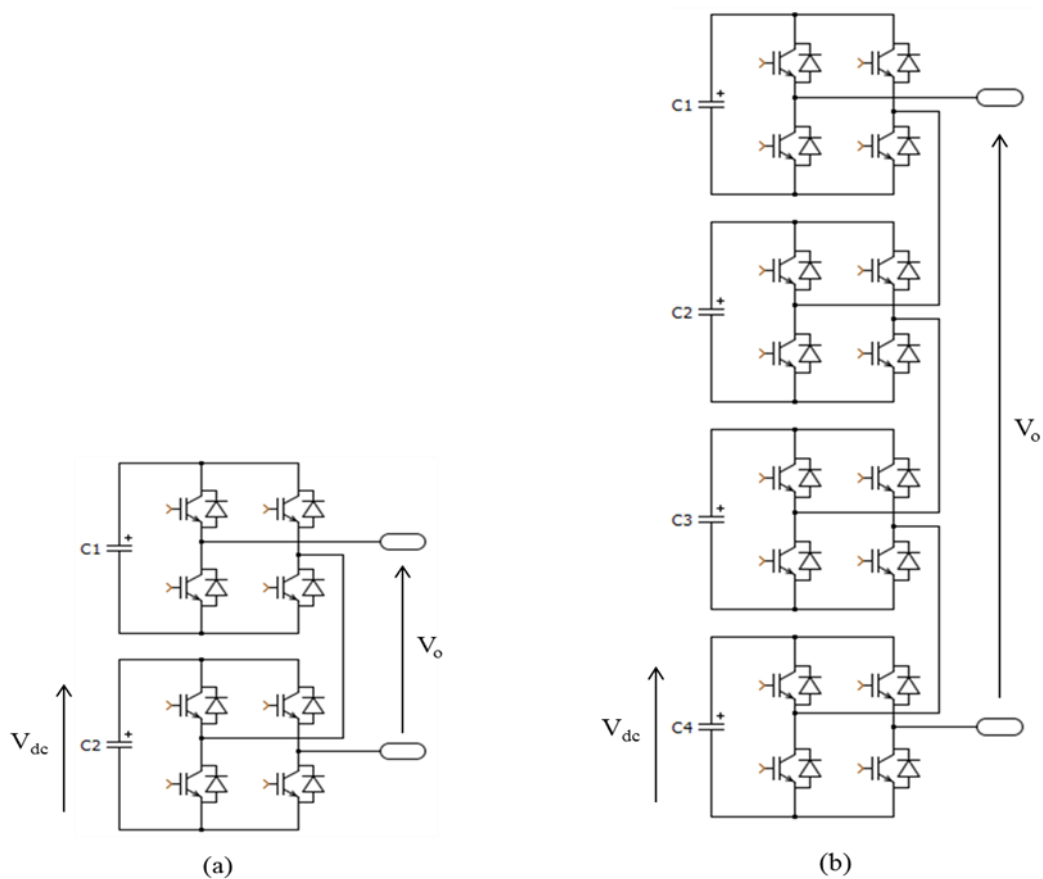


Figure 3-4: Cascaded H-bridge converter schematics (a) Three-level, (b) Nine-level.

The major disadvantage of this topology from this study's perspective is the requirement of one isolated DC source for each H-bridge. This could be achieved by inserting a multi-winding transformer between the machine and grid terminals. However one of the objectives of this study is to minimise passive filtering and magnetic component

requirements due to the weight implications. The inclusion of a transformer with a similar rating to the machine is therefore not acceptable. The cascaded H-bridge inverter is therefore far better suited to applications where isolated DC sources are already available; for instance the grid interfacing of arrays of photovoltaic cells, or the driving of traction motors from a battery bank [3.3].

### 3.2.2 Flying Capacitor Converter

Figure 3-5 provides the schematics for the single phase configurations of the three-level and five-level, flying capacitor converters. Unlike the diode-clamped configuration mentioned before, and to be discussed in Section 3.2.3, voltage clamping is achieved using the capacitors [3.3].

In Figure 3-5 the series connection of multiple capacitors is used to denote that each capacitor has an equal voltage rating. Only one capacitor ( $C1$ ) is used for the lowest voltage level as it must only withstand  $V_{dc}/4$ . The series connection of  $C7, C8, C9, C10$  are used at the largest level as this capacitor chain must withstand the full the DC link voltage.

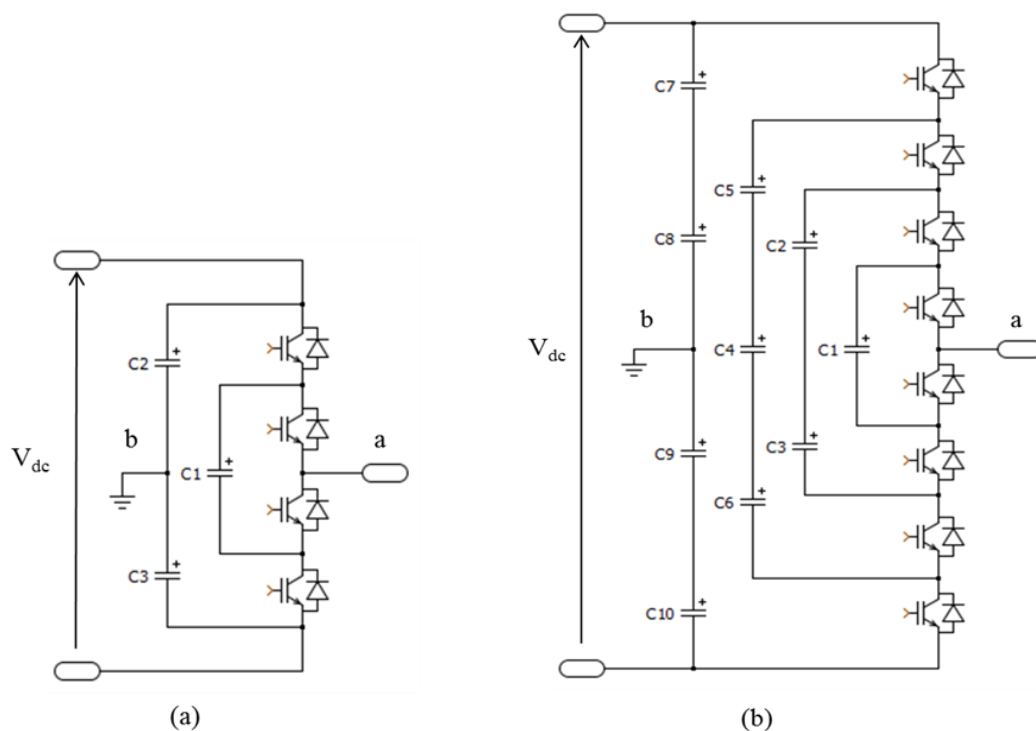


Figure 3-5: Flying capacitor clamped converter schematics (a) Three-level, (b) Five-level.

One advantage of the flying-capacitor converter is that it has phase redundant switching vectors, as opposed to the diode-clamped converter which only has line-line redundant vectors. This means in the flying capacitor case, different switch combinations can be used to produce the same phase output [3.11]. This is not the case for a diode-clamped inverter where the redundant vectors produce identical line-line voltages (assuming a three-phase configuration), but not identical phase outputs. This property of the flying-capacitor converter simplifies the balancing of the capacitor voltage levels as each redundant vector has a different effect on the movement of charge between the DC link capacitors. This means that a single-phase flying-capacitor inverter can achieve DC link balance, the same can only be achieved in the diode-clamped converter in a three-phase configuration. In Section 3.2.3 and 4, the concept of redundant switching vectors and balancing DC link capacitor voltages is explained in greater detail.

From an aerospace perspective the major disadvantage of the flying capacitor converter is the high capacitor requirements when compared to the diode clamped configuration. This is likely to result in a much heavier and bulkier converter when compared to a diode-clamped inverter of similar rating. The comparison between the capacitor and diode clamped topologies is continued in Section 3.2.3.

### **3.2.3 Diode Clamped Converter**

Figure 3-6 provides the schematics for the single phase configuration of the three-level and five-level, diode clamped converters. The three-level diode clamped inverter is also commonly termed the Neutral Point Clamped (NPC) converter [2.2].

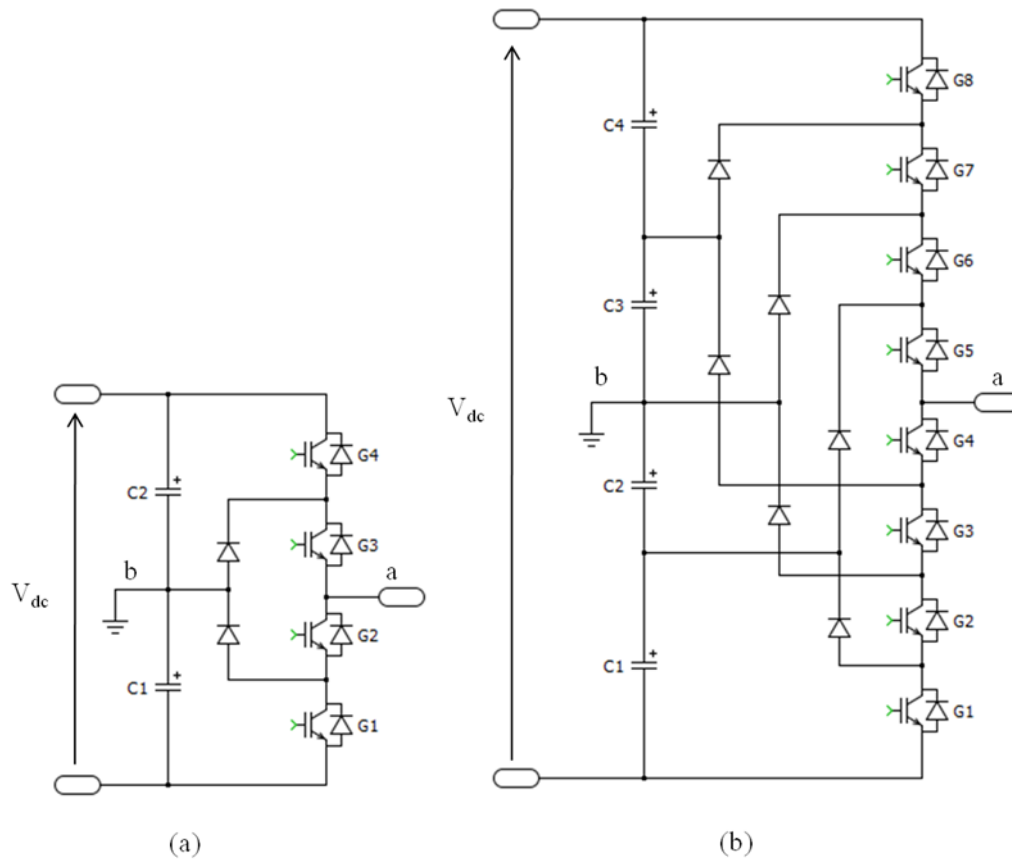


**Figure 3-6: Diode-clamped converter schematics (a) Neutral point clamped, (b) Five-level.**

In the NPC the midpoint between capacitors C1 and C2 is maintained at zero volts. The inclusion of the two additional switches when compared to a two-level inverter, mean the neutral point may be switched to the phase output [3.5], therefore providing this topology with the ability to select one of three output voltage states. The DC link is split equally between C1 and C2 to produce a two level bus. The additional components allow the output (measured between nodes *a* and *b*) to attain the values  $+V_{dc}/2$ ,  $-V_{dc}/2$  and  $0V$  assuming the voltages of C1 and C2 are equal.

The concept of diode-clamping to a DC link has been extended in the literature to a number of different converter levels. The multilevel DC bus can be formed using multiple isolated DC sources, or one source applied across a series connection of capacitors as is shown in the five level case in Figure 3-6.

The distribution of this voltage such that each capacitor has a voltage across it of  $V_{dc}/(n-1)$ , where *n* represents the number of levels, is termed capacitor “balancing”. It has been

extensively demonstrated in the literature that when the diode-clamped inverter is connected in a three-phase configuration, the use of “redundant” switching vectors in a PWM modulation strategy enables DC link capacitor balance to be achieved. Redundant switching vectors are where two or more inverter switch configurations produce the same line-line output voltage. Each redundant switching vector has a different effect on the flow of charge between the capacitors. By using a complex modulation strategy where the effect on the state of charge of each capacitor is estimated, the optimal redundant vectors may be selected which ensure all DC levels remain balanced. Unfortunately balance can only be achieved in the three-phase configuration fed from a single DC source, provided the converter modulation index remains below 0.5 [3.3]. The concept of balancing through the use of redundant vectors is discussed extensively in Section 4.

There has been a large amount of published literature [3.4, 3.12] on how the diode-clamped converter can be extended to make it more applicable for AC drive applications by the back-to-back connection of two inverters. This concept is illustrated in Figure 3-7 where the back-to-back connection of two, five level inverters is shown. The Active Front End (AFE) and inverter are the grid and machine side connected inverters respectively. (This inverter naming convention is used throughout this thesis).

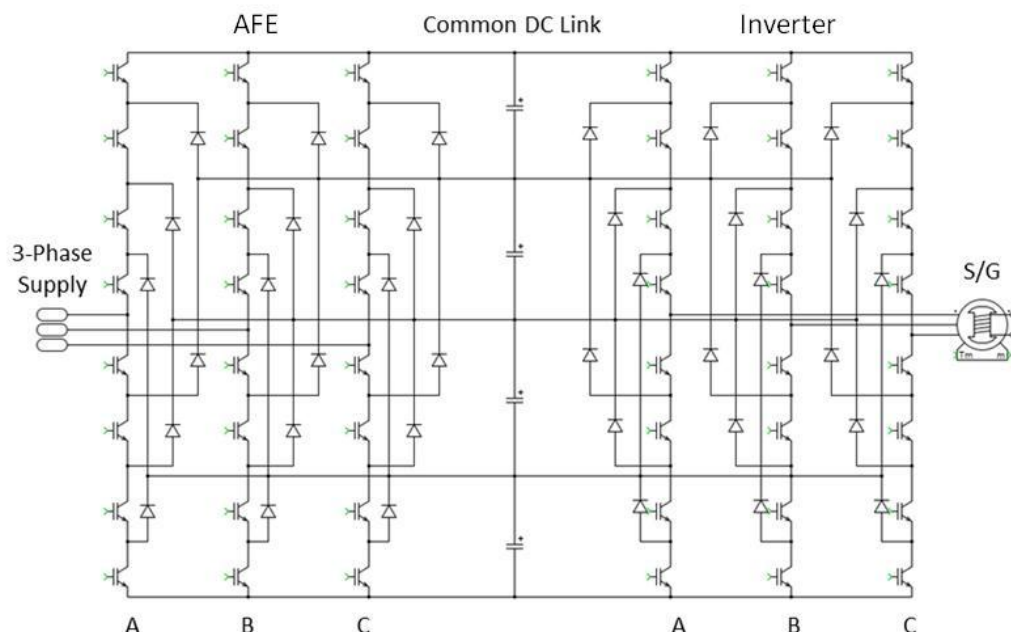


**Figure 3-7: Back-to-back connected, five-level, diode-clamped inverters.**

There are a number of benefits achieved through the interconnection of two inverters in this manner. It was previously mentioned that when using a three-phase, diode-clamped inverter supplied by a single DC source, DC-link capacitor balance can only be maintained using redundant switching vectors provided the modulation index remains below 0.5 [3.13]. It has also been demonstrated in the literature [3.12] that in the back-to-back connected case, balance can be maintained regardless of the modulation index [3.3].

In the author's opinion the back-to-back connected, diode-clamped topology is particularly applicable to motor drives and especially aerospace S/G systems. The reasons for this are outlined below:

- **Bidirectional Power Flow Capability.**

Bidirectional power flow in the power converter is considered essential if it is to be implemented within an aerospace S/G system. This study makes the assumption the power converter is permanently connected between the machine and grid terminals. During starting mode the power converter draws electrical power from the aircraft's distribution bus in order to drive the S/G in motoring mode and ultimately accelerate the engine to idle speed. Once this has been achieved the power converter reverses the direction of power flow, drawing electricity from the S/G to supply the aircraft's distribution bus connected loads.

In Chapter 6, alternative starting arrangements are discussed where the power converter is only connected to the S/G during starting mode. Under this arrangement the power converter does not require bidirectional power capabilities, however this is not the system addressed in this study.

- **Improvement in THD of the current seen at both the grid and machine terminals.**

The harmonic improvement benefits offered by a generic multilevel converter were discussed in Section 3.2. The need to ensure that power converters draw a high quality sinusoidal current with minimal distortion from the distribution bus in order to comply with power quality standards was documented in Section 2.2.3. The back-to-back connection of two multilevel converters ensures that the resulting improvement in waveform quality is apparent at the machine and grid terminals. This is a major benefit from an aerospace

perspective as the amount of filtering inductance required to meet the power quality standards at the grid terminals may be reduced. Whilst on the machine side the stator winding inductance may be used as the sole source of filtering. The back-to-back connection in a real world environment may therefore result in a net reduction in the amount of passive filtering required when compared to a two level system.

- **Voltage boost mode possible.**

As discussed in Chapter 2, frequency wild power distribution was adopted for use in the A380 and B787 to negate the need for a complex CSD arrangement. The natural progression from the view of an engine manufacture is to move to a completely embedded generator system. This will eliminate any mechanical coupling in the system, therefore giving the optimal solution from a weight perspective. The most likely machine topology candidate for such an embedded machine is the PMSM. Unlike the WFSM system used in B787, in the embedded PMSM case, the generator output at the machine terminals will fluctuate with engine speed and electrical loading. A power converter of some description is therefore likely to be essential at the generator output, to provide a constant frequency/voltage supply.

Back-to-back connected inverters make voltage boost mode possible. The variable amplitude, variable frequency output can be boosted by the AFE to provide a stable DC link voltage. This effectively decouples the voltage at the generator terminals from that at the grid terminals. Fluctuations in engine speed therefore do not effect/disrupt the grid voltage.

- **Improved harmonic performance when compared to the NPC.**

The NPC topology benefits from greatly reduced control complexity when compared to the five level configuration. At the time of writing it is also substantially easier to implement in hardware as several manufacturers now provide the NPC in a modular format. The five level configuration has the advantage in terms of harmonic performance as it has lower  $dV/dt$  at it's output. Therefore an output current waveform with a reduced THD is produced using the five-level converter when compared to the NPC. Also the NPC topology generates a high level of even order harmonic distortion in the output spectrum [3.14]. Aerospace power quality standards impose stringent limits on the level of even order

harmonics. The application of the NPC topology is therefore likely to necessitate additional filtering to curtail the amplitude of the odd order harmonics associated with AC network connected power converters, but also the even order harmonics that are a characteristic of this converter. As this study is focused on the minimization of passive filtering, the five-level topology is considered superior in this application.

- **Requires no isolated DC sources.**

As was discussed in Section 3.2.1, the cascaded-H bridge inverter requires isolated DC sources for each cell. A three-phase diode-clamped inverter would also require an isolated DC source for each one of the DC link levels if it was to be used with a modulation index above 0.5. These sources could be provided simply using transformer-rectifier units, however this solution would not provide bidirectional power flow capabilities. Transformer-rectifier units may also make the system prohibitively large and heavy. The back-to-back connection of diode clamped inverters overcomes this problem as it requires no isolated DC sources. Instead the inverters controller is modified to incorporate a closed loop, feedback controller to maintain the DC link level balance. Both inverter's controllers work to maintain this balance. No additional circuitry or transformers are required. Capacitor balancing is discussed in detail in Section 4.5.3.

The flying-capacitor converter described in Section 3.2.2 also has the ability to achieve DC link balance using redundant vectors. When compared to the diode-clamped converter, the flying capacitor configuration provides even greater flexibility as it can achieve balance in a single or three phase configuration [3.11]. However it is important to note that a S/G system will require the back-to-back connection of inverters to meet the bidirectional power flow requirement. In this configuration the flying-capacitor configuration provides no additional advantage in terms of balancing capabilities when compared to the diode-clamped inverter.

**Reduced number of DC link capacitors and lower voltage ratings.**

Although the flying-capacitor topology may also be used in a back-to-back configuration, the diode-clamped benefits from greatly reduced capacitor requirements. Five-level capacitor and diode clamped converters require five and four DC link capacitors respectively. Due the series connection of the capacitors in the diode-clamped inverter,

each capacitor only needs to be rated to  $V_{dc}/4$ . Conversely, in the capacitor clamped five level configuration, the higher rated series connected capacitor chains must withstand voltages of  $3*V_{dc}/4$  and  $V_{dc}/2$ .

This advantage comes at the expense of more diodes, however from a converter power density perspective more active components may be preferred over additional reactive components. Unlike the switches in the diode-clamped topology which operate under greatly reduced electrical stresses due to the reduced switch blocking voltage ( $V_{sw}$ ) (3.1), the diodes are subject to much higher voltages ( $V_{diode}$ ) (3.2) [3.3]. Although this may have some impact on converter reliability, it is the author's opinion that higher diode ratings are preferable in the aerospace environment to higher capacitor ratings. Aerospace systems are also typically low voltage, therefore limiting the required diode voltage rating to an acceptable figure.

$$V_{sw} = \frac{V_{dc}}{2 * (n - 1)} \quad (3.1)$$

$$V_{diode} = \frac{V_{dc}(n - 2)}{(n - 1)} \quad (3.2)$$

The reduction in both the quantity and the relative ratings of capacitors also make the diode-clamped inverter a more attractive solution when the stringent restrictions on the use of electrolytic capacitors in the aerospace environment are considered. This is due to the limited life time and poor performance of these capacitors under low atmospheric pressure conditions [3.15,3.16].

### 3.3 Competing Power Converter Topologies

#### 3.3.1 Matrix Converter

One topology of power converter that has received a lot of attention in recent years is the matrix converter [3.17]. The matrix converter consists of an array of force commutated, bidirectional switches. For a system with an input of  $p$  phases and an output of  $q$  phases, the converter is formed from an array of  $p \times q$  switches. In Figure 3-8 the schematic for a matrix converter is shown in a drive application, where the converter is connected to a 3-phase supply and is loaded by a three-phase motor. Two common methods of producing

the bidirectional switches necessary for a matrix converter are shown Figure 3-9, both using diodes and Insulated Gate Bipolar Transistors (IGBTs).

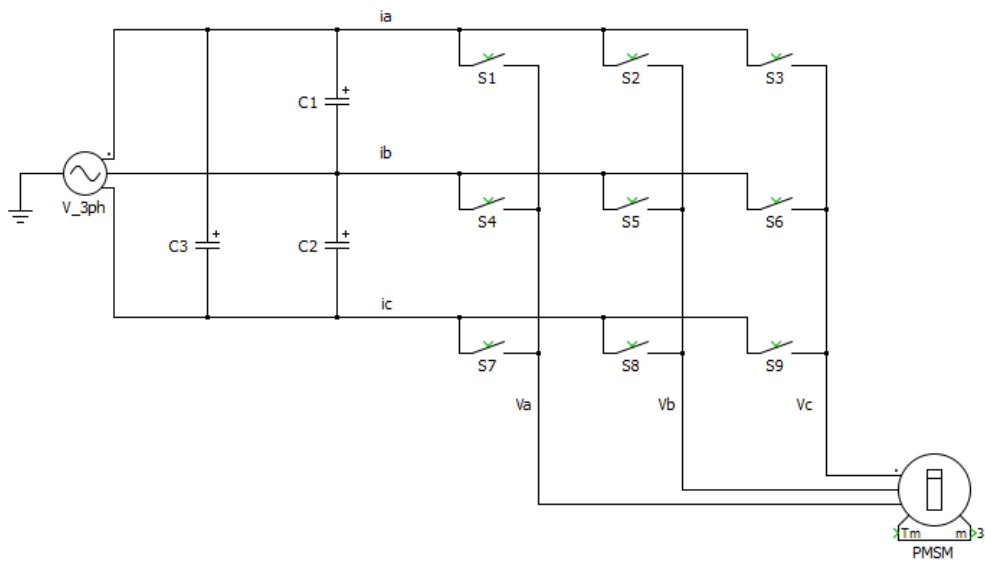


Figure 3-8: Schematic for a 3x3 matrix converter.

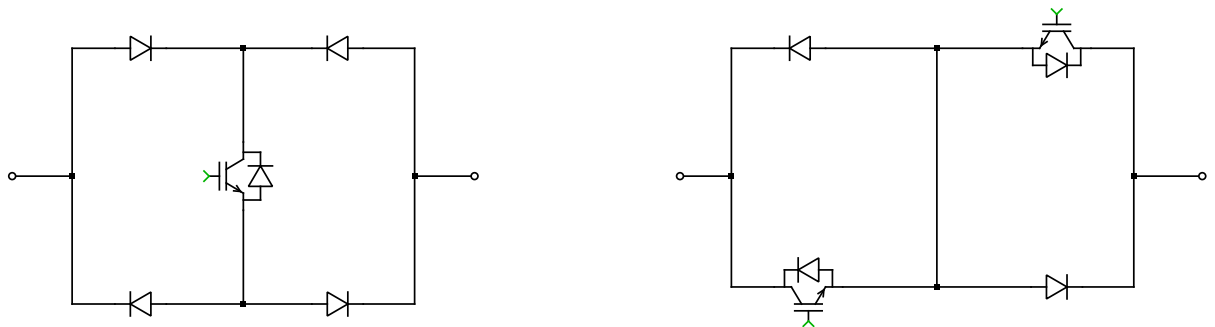


Figure 3-9: Bidirectional switch configurations, (a) Diode bridge, (b) Switch Cell.

In a drive application, the matrix converter offers the same benefits you would expect from a back-to-back connected power converter, such as sinusoidal input and output currents of Unity Displacement Factor (UDF), and the ability to support bi-directional power flow. However the major advantage this topology provides is the lack of bulk energy storage. This is a great benefit as the power density of the converter is increased due to the lack of bulky capacitors. The absence of capacitors has ensured the matrix converter is the subject of a large amount of research looking into the practical application of this topology in the aerospace environment [3.18,3.19]. Capacitors, especially electrolytics, are considered

large unreliable and both temperature and altitude dependant. Understandably aerospace manufacturers are keen to minimise their use.

The major down side of the matrix converter is the maximum theoretical voltage gain between the input and output of 0.87 [3.17,3.20], the converter can therefore not operate in boost mode. This stems from the fact that the output voltage waveform must stay within the input voltage waveform envelope. This imposes a severe limitation on the use of matrix converters in drive applications. Especially considering that the output voltage of the S/Gs (specifically in future systems employing PMSMs) varies as a function of both the machine speed and the electrical loading. Boost operation is therefore essential to ensure that the converter continues to function regardless of the operating conditions.

There has also been a significant amount of research conducted into hybrid power converter structures. The objective being to produce a converter with the direct energy transfer of a matrix converter but with the improved harmonic performance of the multilevel converter [3.21]. Numerous topologies have been proposed in the literature, shown in Figure 3-10 is the schematic for the combination of a matrix and NPC converters, this results in a two stage, three-level matrix converter.

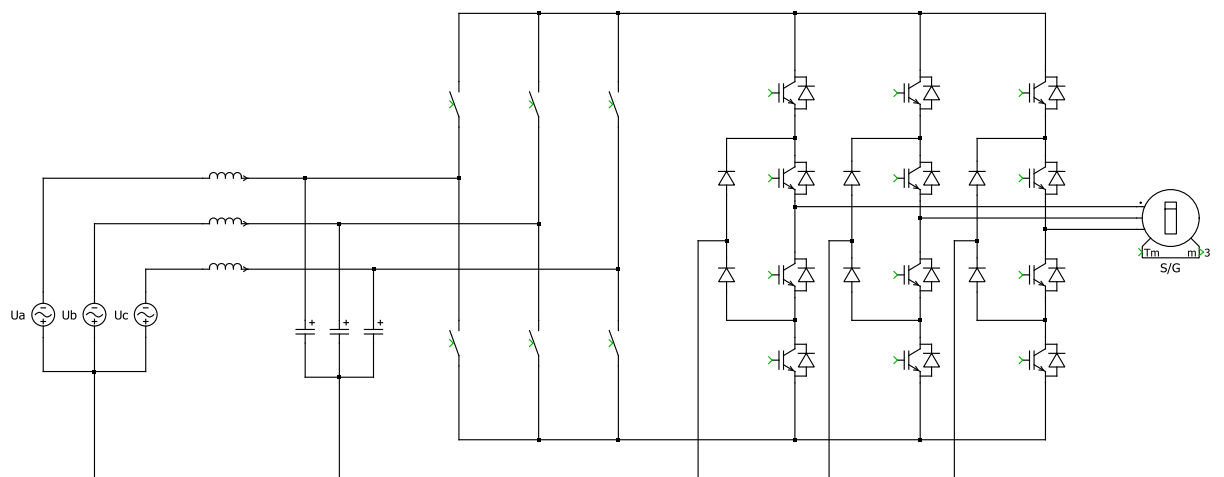


Figure 3-10: Two stage, three-level matrix converter.

In this configuration a three-to-two phase matrix converter is used to supply a NPC inverter. The mid-point of the NPC stage is clamped to the supply neutral to produce the third voltage level [3.21].

It is essential for an aerospace power converter to provide fault ride through capability. As such this capability is specified in the standards governing the performance and operation of aerospace power converters. The ride through capability of both conventional matrix converters and multilevel-hybrids is compromised by the absence of any DC link capacitance. Under fault conditions the converter output voltage is likely to collapse, disrupting the aircraft's distribution network [3.17]. For this reason, and also the reduced voltage gain, neither conventional matrix converters or hybrid converters are considered suitable for aerospace S/G systems at present.

### 3.4 Conclusion

This chapter has provided a review of the major multilevel converter topologies documented in the literature and also some other prominent designs, most notably the matrix converter. The objective is to select the most suited to an aerospace S/G system. The emphasis was placed on minimising the filtering requirements at the grid side and limiting harmonic distortion at the machine when compared to the industry standard, two-level inverter.

The cascaded H-bridge configuration was discounted quickly as it requires isolated DC sources. This could not easily be achieved as TRU units would not provide the required isolated, bidirectional sources. This topology could be used with a complex multi-winding transformer arrangement possibly utilising an active rectifier upon each winding to produce an isolated DC source. However this is unlikely to be an attractive solution from an aerospace perspective.

The flying capacitor topology was examined. This has the ability to self-balance the DC link meaning additional circuitry is not required. This is a major benefit, reducing both the weight and the complexity of the converter.

The diode-clamped inverter was discussed. The configuration is similar to the capacitor clamped variant, only diodes are used to clamp to a multilevel DC link rather than capacitors. The capacitor requirements are therefore reduced. Unfortunately the converter

can only achieve DC-link balance if the modulation index remains below 0.5. This severely limits the performance of the circuit in a practical application.

It was noted that self-balance can be achieved if two three-phase inverters are connected in a back-to-back configuration. This configuration is considered perfectly suited to a S/G system in an aircraft utilising fixed frequency distribution owing to the converter's frequency changing capabilities. The benefit of the multilevel output is also seen at both the machine and grid connections therefore achieving a possible reduction in grid side filtering and stator current ripple. Whilst the capacitor clamped inverter can also be operated in a back-to-back configuration the capacitor requirements are still likely to be bulky impacting power density.

Finally the matrix converter was examined. This topology is exciting from a power density perspective, in-part due to absence of any DC-link energy storage. This comes at the cost of only being able to operate in buck mode. This severely limits performance in a S/G system where the IDG has been removed resulting in a variable speed generator.

In conclusion, of the topologies reviewed the back-to-back connected diode-clamped converter is considered the most attractive for this application. In subsequent chapters the topology is developed for use in a S/G system.

### 3.5 References

- [3.1] J. Lai, F. Z. Peng, "Multilevel Converters – A New Breed of Power Converter," IEEE Transactions on Industry Applications, Vol. 32, No.3, pp. 509-517, May/June, 1996.
- [3.2] J. Rodriguez, J. Lai, F. Z. Peng, "Multilevel Inverters: A Survey of Topologies, Controls, and Applications," IEEE Transactions on Industrial Electronics, Vol. 49, No. 4, pp. 724-738, August, 2002.
- [3.3] J. Pou, "Modulation and Control of Three-Phase PWM Multilevel Converters," Ph.D. Dissertation, Universitat Politecnica De Catalunya, 2002.
- [3.4] S. R. Minshull, C. M. Bingham, D. A. Stone, M. P. Foster, "A Back to back Multilevel Converter for Driving Low Inductance Brushless AC Machines," Proc. Conference on Power Electronics and Applications, Aalborg, Denmark, pp. 1-9, 2007.
- [3.5] D. G. Holmes, T. A. Lipo, "Pulse Width Modulation for Power Converters: Principles and Practice," Wiley-Interscience, 2003.
- [3.6] H. Zhang, A. Jouanne, S. Dai, "Multilevel Inverter Modulation Schemes to Eliminate Common-Mode Voltages," IEEE Trans. Industry Applications, Vol. 36, No. 6, pp. 1645-1653, 2000.
- [3.7] R. Teichmann, S. Bernet, "A Comparison of Three-Level Converters Versus Two-Level Converters for Low-Voltage Drives, Traction, and Utility Applications," IEEE Trans. Industry Applications, Vol. 41, No. 3, pp. 855-865, 2005.
- [3.8] "SKiM 120GD176D", Semikron Datasheet, [www.semikron.com](http://www.semikron.com).
- [3.9] "F3L400R07ME4\_B22", Infineon Datasheet, [www.infineon.com](http://www.infineon.com).
- [3.10] Department of Defence Military Handbook: Reliability Prediction of Electronic Equipment, MIL-HDBK-217F, 1991.

- [3.11] M. H. Rashid, "Power Electronics Handbook," Academic Press, 2007.
- [3.12] M. Marchesoni, P. Tenca, "Diode-Clamped Multilevel Converters: A Practical Way to Balance DC-Link Voltages," IEEE Trans. Industrial Electronics, Vol. 49, No. 4, pp. 752-765, 2002.
- [3.13] M. Marchesoni, P. Tenca, "Theoretical and Practical Limits in Multilevel MPC Inverters with Passive Front Ends," European Conference on Power Electronics and Applications," Graz, Austria, 2001.
- [3.14] D. Feng, B. Wu, S. Wei, D. Xu, "Space Vector Modulation for Neutral Point Clamped Multilevel Inverter with Even Order Harmonic Elimination," CCECE, Toronto, Canada, 2004, pp. 1471-1475.
- [3.15] BS G 249:1993, Specification for solid-state remote power controllers – General Requirements.
- [3.16] "General Description of Aluminium Electrolytic Capacitors," Nichicon application note, [www.nichicon.co.jp](http://www.nichicon.co.jp).
- [3.17] P. W. Wheeler, J. Rodriguez, J. C. Clare, L. Empringham, A. Weinstein, "Matrix Converters: A Technology Review," IEEE Trans. on Industrial Electronics, Vol. 49, pp. 276-288, 2002.
- [3.18] M. Imayavaramban, P. W. Wheeler, "Avoiding Regeneration with a Matrix Converter Drive," Power Electronics Specialists Conference, Orlando Florida, pp. 2529-2534, 2007.
- [3.19] L. Lillo, L. Empringham, P. Wheeler, J. Clare, K. Bradley, "A 20 kW Matrix Converter Drive System for an Electro-Mechanical Aircraft (EMA) Actuator," European Conference on Power Electronics and Applications, Dresden, Germany, pp. 1-6, 2005.
- [3.20] A. Alesina, M. Venturini, "Analysis and Design of Optimum Amplitude Nine-Switch Direct AC-AC Converters," IEEE Trans. Power Electronics, Vol. 4, no. 1, pp. 101-112, 1989.

- [3.21] P.Wheeler, X. Lie, M. Y. Lee, L. Empringham, C. Klumpner, J. Clare, "A Review of Multi-level Matrix Converter Topologies," IET Conference on Power Electronics, Machines and Drives, York, UK, pp. 286-290, 2008.

## 4 Power Converter Modulation Techniques

### 4.1 Introduction

Having decided on a power converter topology, the modulation strategy must now be considered. Many different methods of modulation have been documented in the literature for use with multilevel converters. In [4.1] the authors group the different modulators together according to their relative switching frequencies (Figure 4-1). A description of each of the four main techniques is provided in this chapter. For each strategy it's applicability to this study is assessed. The most suitable strategy may therefore be selected.

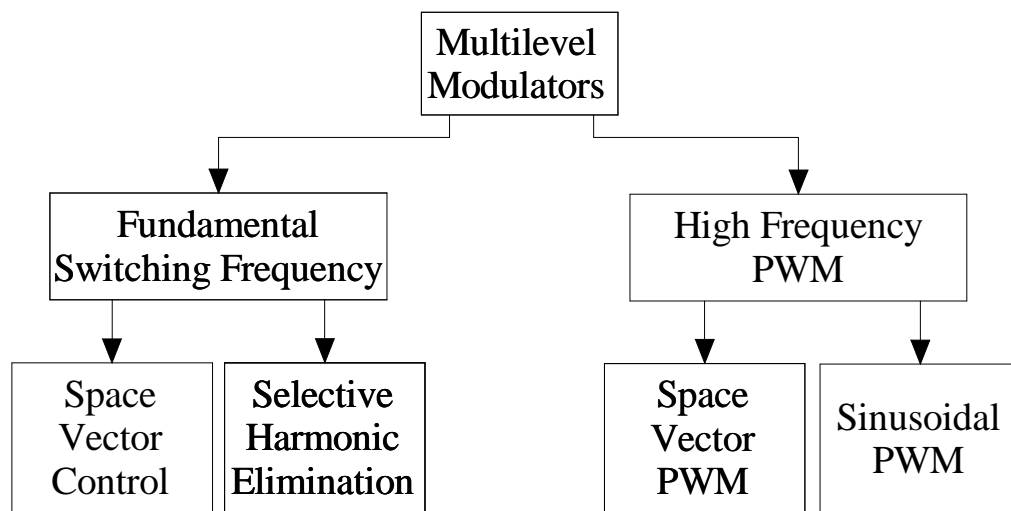


Figure 4-1: Modulation methods grouped according to switching frequency [4.1].

### 4.2 Space Vector Control

Space Vector (SV) control may be applied to a multilevel converter in much the same way as it is commonly used with two-level inverters. A converter's switching vectors may be

plotted on the SV plane along with the desired output reference vector. At the start of the modulation period the switching vector nearest the reference vector is selected for implementation. A full description of the SV plane, reference and switching vectors is provided in Section 4.5 where it is explained how it can be expanded to form a SV PWM strategy.

A SV modulation strategy when operated at fundamental frequency provides neither the harmonic performance nor the ability to balance the DC link capacitors required by this application. It was therefore not considered appropriate for this study.

### **4.3 Selective Harmonic Elimination**

A Selective Harmonic Elimination (SHE) modulation strategy may be applied to achieve improved harmonic performance at a low switching frequency when compared to SV modulation. The same stepped output waveform is produced by SHE as with SV modulation, but the angle between the discrete levels is controlled to achieve superior harmonic performance.

The output voltage waveform from a five-level inverter switching at fundamental frequency is shown in Figure 4-2. The conduction angles ( $\theta_1$  and  $\theta_2$  for the five-level case shown in Figure 4-2) may be controlled to either eliminate specific harmonics or reduce the THD across the spectrum. It is typical for the selection of  $\theta_1$  and  $\theta_2$  to be made to eliminate low order, high power harmonics [4.2]. In [4.2] the author provides a comprehensive description of the SHE technique and the necessary equations.

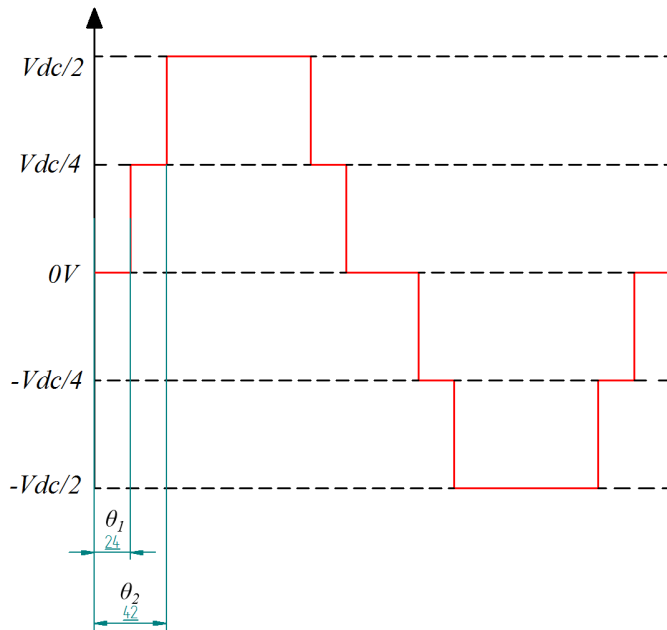


**Figure 4-2: Selective harmonic elimination.**

A SHE modulation strategy is not considered suitable for this study as the low switching frequency does not support capacitor balancing. The DC link would quickly become unbalanced leading to a poor quality output. The low switching frequency also results in poor harmonic performance across the spectrum. Additional passive filtering would therefore be required.

#### 4.4 Sinusoidal PWM

Sinusoidal PWM (SPWM) is the first of the two major high frequency modulation strategies considered in this study. It is first examined in the case of a three level inverter. The reference signal is compared with two identical but amplitude-offset, triangular carrier signals [4.1,4.2,4.3] (Figure 4-3). The frequency of the carriers equates to the converter switching frequency. The modulator output is clamped positive when the reference signal is greater than the positive carrier ( $C1$ ). The output is clamped negative when the reference is below the amplitude of the negative carrier ( $C2$ ). At all other times the output is clamped to the neutral point. The output of the SPWM block is shown in Figure 4-4.

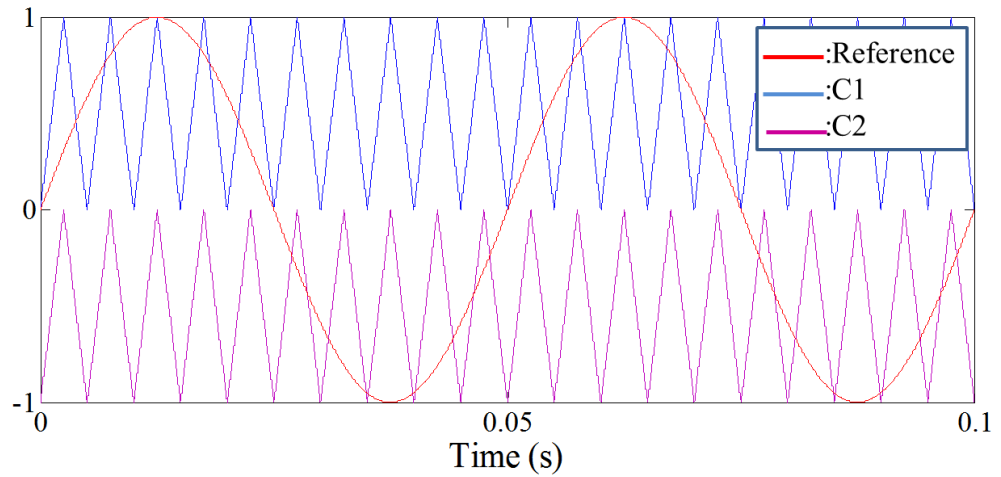


Figure 4-3: Carrier and reference signals.

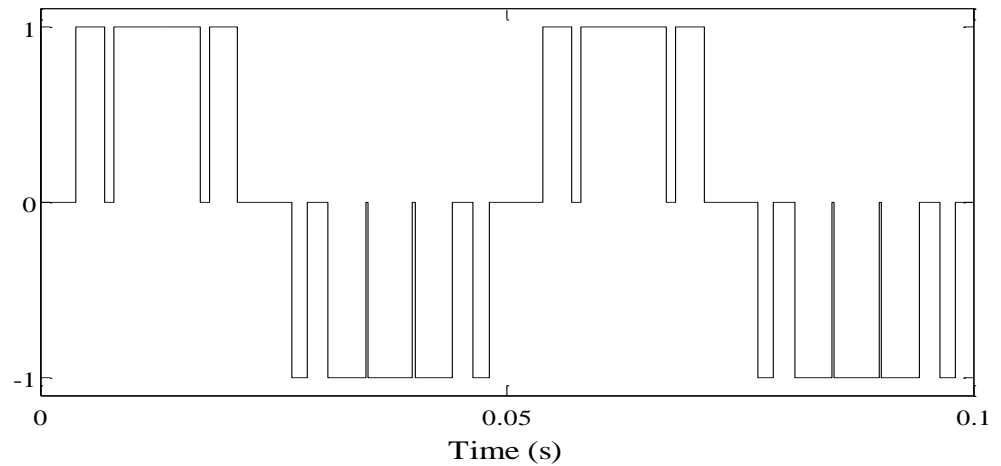
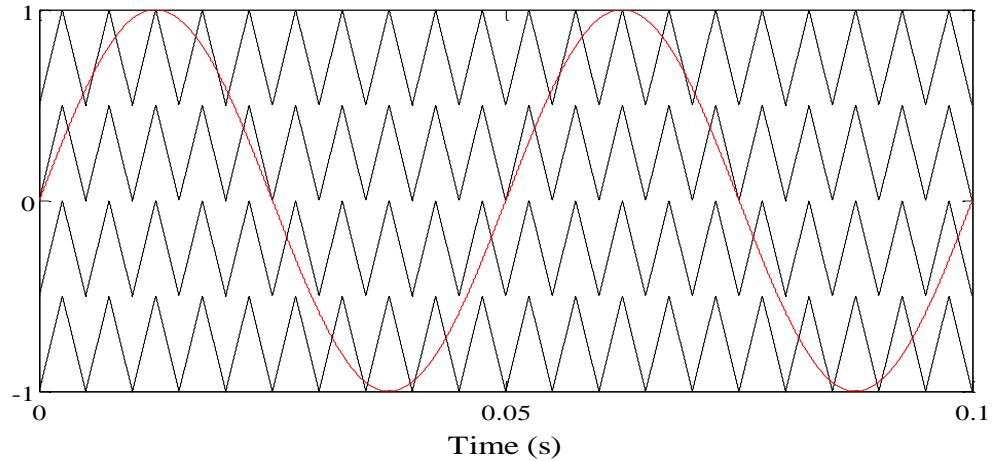


Figure 4-4: Output of modulator.

SPWM may be extended to higher order multilevel converters by using additional carrier signals [4.1,4.4]. As before, at the beginning of each modulation period each carrier is compared to the reference signal. For the positive carriers (located above 0V), the comparison returns either a 1 or 0 depending upon whether the reference is above or below the carrier respectively. For negative carriers, the comparisons return either a -1 or 0 dependent upon whether the reference is below or above the carrier respectively. The outputs from all comparisons are summed to determine the converter output voltage. The carrier waveforms for a 5 level converter are shown in Figure 4-5.



**Figure 4-5: Five level SPWM waveforms.**

There are a number of different subsets of SPWM for use in multilevel converters, which seek to reduce the harmonics in the output waveform by either phase-shifting or disposition of the carriers [4.1,4.4,4.5]. The three most well documented SPWM techniques are; Alternative Phase Opposition Disposition, Phase Opposition Disposition, Phase Disposition. A brief description of each technique is provided in [4.5]. The authors of [4.4, 4.5] conclude that for use with a three-phase diode-clamped inverter, phase disposition offers the highest quality line-line output waveform.

Recently work has been conducted into balancing of the capacitor voltages in the diode-clamped converter topology using SPWM [4.6,4.7,4.8,4.9]. Capacitor voltage balancing (discussed in Section 4.5.3) is a subject more closely associated with SVPWM. This area of research is still in it's infancy and there are therefore relatively few publications on the matter.

Unfortunately, SPWM offers poor utilisation of the DC link when compared to Space Vector PWM (discussed in Section 4.5). The maximum line-line output ( $\dot{V}_{LL}$ ) obtainable using SPWM avoiding over-modulation is given by (4.1). In comparison, a space vector strategy's maximum output voltage is increased by a factor of  $2/\sqrt{3}$ .

$$\dot{V}_{LL} = \frac{\sqrt{3}}{2\sqrt{2}} V_{dc} = 0.6123 V_{dc} \quad (4.1)$$

For a given application, utilising a SPWM modulation strategy would therefore necessitate a higher DC link voltage when compared to a SV modulator. Higher voltage DC link capacitors would be needed, which is likely to increase the volume and the weight of the power converter.

A higher DC link voltage would also adversely affect converter losses and reliability. An increase in the DC link voltage would increase converter switching losses, necessitating additional cooling. This would be disadvantageous in an aerospace system. According to the procedure described by the MIL-STDs, the devices would also be under increased electrical stress, which is likely to impact upon the converter mean-time-to failure. For these reasons SPWM was not selected for use in this study as it is likely to result in an unnecessarily large converter.

## 4.5 Space Vector PWM

Similarly to a two-level inverter, a multilevel inverter's switching states (vectors) may be plotted upon the stationary  $\alpha\beta$  domain (see Section 5.2) to form a Space Vector (SV) diagram. For example, the SV diagram for a three-level inverter is provided in Figure 4-6. Switching states exist and are labelled at the vertices of each triangle in Figure 4-6. Here, a vector of  $xyz$  provides the converter output voltages at phases a, b and c respectively should that vector be implemented. The vector notation used for the three-level inverter is provided in Table 4-1.

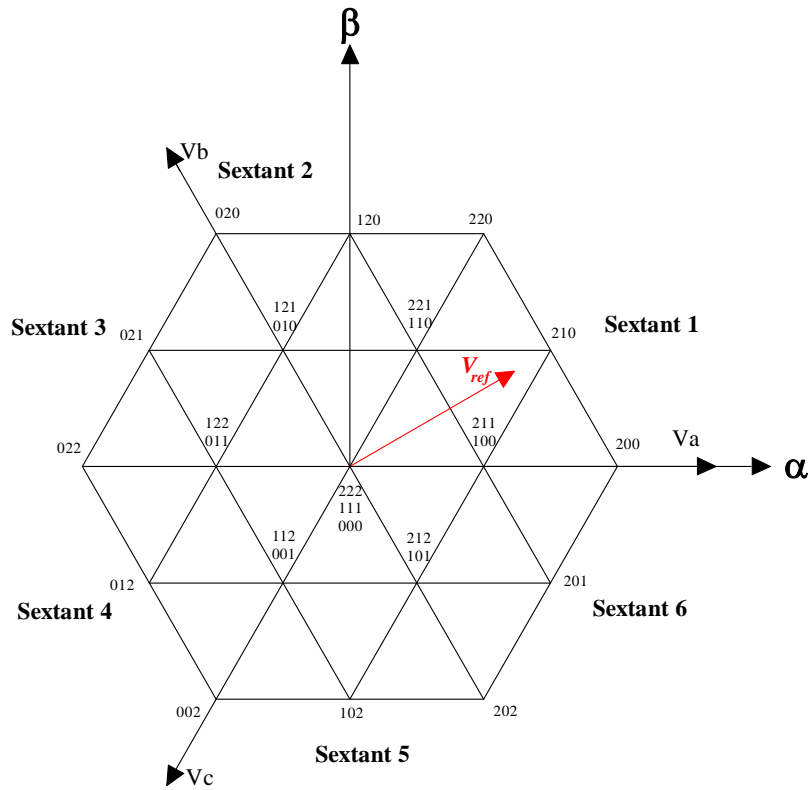


Figure 4-6: Three-level SV diagram.

Vector notation (xyz)	Phase output voltage
2	$V_{DC}$
1	$V_{dc}/2$
0	$0V$

Table 4-1: Vector notation for a three-level SV diagram.

Where two or more switching vectors exist which produce identical line-line voltage at the converter output, they are plotted in the same location upon the SV diagram. These vectors are called redundant switching states and are crucial to the balancing of the capacitor voltages in the DC link (see Section 4.5.3.)

The demand voltage vector ( $V_{ref}$ ) to be produced at the converter output is also plotted in Figure 4-6. This rotates around the diagram with the same frequency as the electrical

frequency of the motor/grid the inverter is connected to.  $V_{ref}$  is used to select the required switching vectors.

#### 4.5.1 GH Transformation and Reflection into the First Sextant

The implementation of a SVPWM can be computationally intensive and therefore problematic from a control system designer's perspective. The algorithm is typically performed using a DSP in real time, meaning there is only a short time window to calculate the necessary switching vector for implementation in the next PWM period. In addition to executing the SVPWM algorithm, the DSP is also tasked with performing other operations such as gathering data from ADCs, coordinate transforms and other control calculations for instance the various PI loops. This is especially true when SVPWM is applied to higher order multilevel converters as there are many more possible vectors to be considered, therefore increasing the computational load.

Overall converter efficiency must also be considered when designing the SVPWM algorithm. Multilevel converters are typically applied in medium/high-power applications, it is therefore beneficial to minimise the effective switching frequency in the devices to reduce the losses. This issue is specifically addressed in Section 4.5.3.

In [4.10,4.11] the author proposes an optimal SVPWM algorithm for multilevel converters which seeks to minimise both the computation load of the algorithm and also the effective switching frequency. For these reasons the scheme described in [4.10,4.11] is used during this study.

At the heart of the scheme is an alternative coordination transformation onto a non-orthogonal, stationary reference frame called the gh axis [4.10]. The g and h axes are located upon the SV diagram at zero and sixty degrees respectively. The algorithm takes advantage of the SV plane's symmetry to conduct all calculations within the first sextant. This is achieved by reflecting the reference vector produced by the vector controller into the first sextant if it initially resides in another sextant. This procedure is highlighted in Figure 4-7, where  $V_{ref}^1$  is the reflection into the first sextant. The transformation is provided (4.2).

The reflection into the first sextant, though simplifying the controller from the designer's perspective, does come at the cost of an increased computational load. As this was an

academic exercise, there was sufficient processing power available within the DSP for this not be a concern. However in an industrial application where processing power is limited, it may be preferable to conduct the SV modulation across the complete SV plane to reduce the computational intensity of the algorithm.

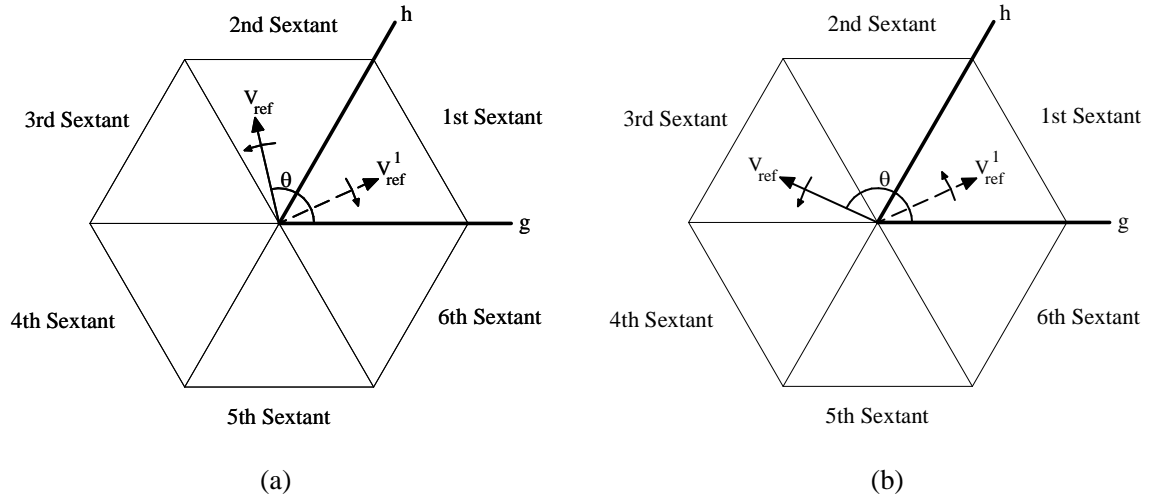


**Figure 4-7: SV diagram showing  $gh$  transformation, (a) Reference vector in 2nd sextant, (b) Reference vector in 3rd sextant.**

$$\begin{bmatrix} V_g \\ V_h \end{bmatrix} = \frac{\sqrt{2}}{V_{dc}/(n-1)} \begin{bmatrix} \sin(\theta + 2\pi/3) & \cos(\theta + 2\pi/3) \\ \sin(\theta) & \cos(\theta) \end{bmatrix} \begin{bmatrix} V_d \\ V_q \end{bmatrix} \quad (4.2)$$

The first sextant of a five-level SV diagram is shown in Figure 4-8. Also plotted is  $V_{ref}$  and its decomposition into the  $gh$  plain ( $V_g$  and  $V_h$ .) The first sextant is further divided into 16 triangular regions. In Figure 4-8 these are numbered in red. The SV modulator works by selecting the nearest three switching vectors to  $V_{ref}$  which are then used to synthesis the reference at the converter output.

The  $(n-1)/V_{dc}$  term in (4.2) scales the resultant vector to fit into SV diagram. In the five-level case this results in a vector with amplitude between 0-4. The amplitude of  $V_{ref}$  must therefore be constrained to avoid over modulation. The maximum permissible amplitude of  $V_{ref}$  to avoid entering the over modulation region is 3.464. This is highlighted in Figure 4-9.

This section discusses how the nearest three vectors to  $V_{ref}$  are selected for implementation, Section 4.5.2 examines how the duty cycles for each vector are calculated, whilst in Section 4.5.4 the ordering of the vectors is considered to minimise the switching frequency.

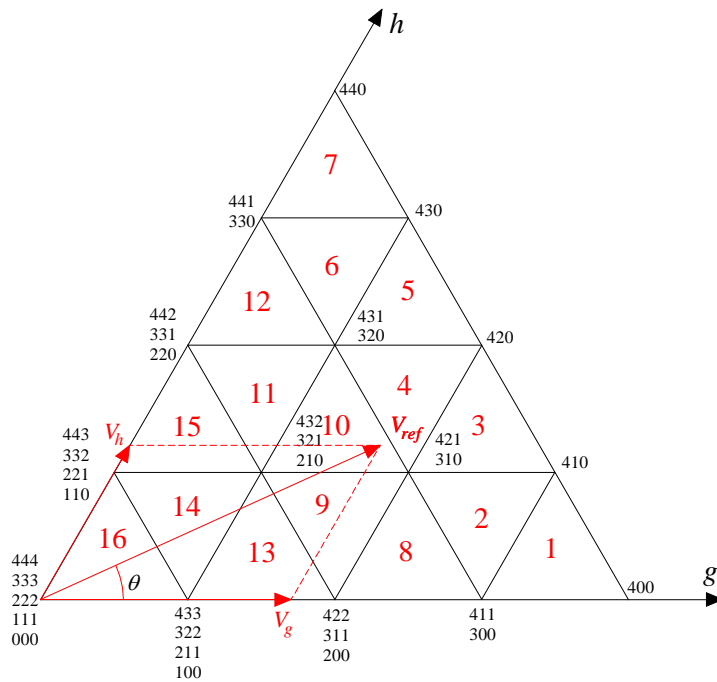


Figure 4-8: Five-level SV diagram, Sextant 1.

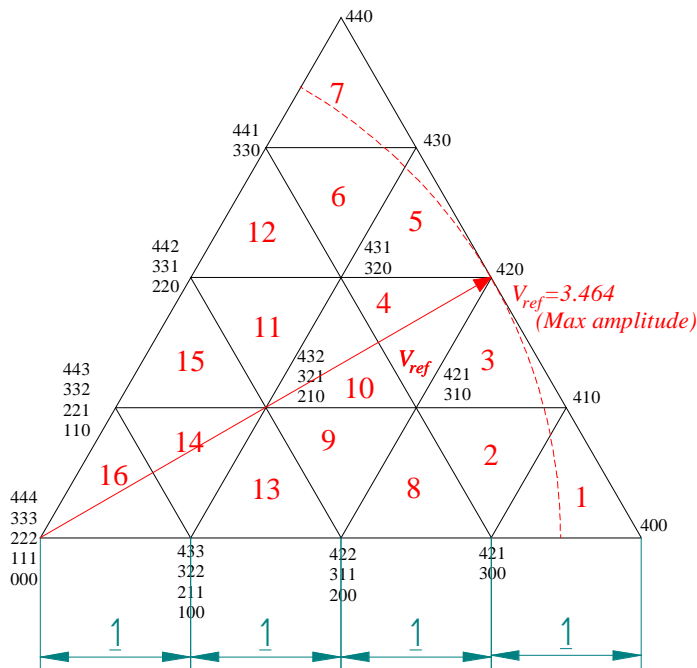


Figure 4-9: Five-level SV diagram over modulation limit.

The author of [4.10,4.11] simplifies the SV modulator through the use of a series of look up tables. Once  $V_g$  and  $V_h$  have been calculated using (4.2), it is necessary to determine what sextant  $V_{ref}$  resides in, and reflect it into the first sextant. Both operations are achieved using Table 4-2, where  $V_{g1}$  and  $V_{h1}$  are the g and h components of  $V_{ref}$  once it has been reflected into the first sextant.

gh Components	Sextant	Reflected Components in First Sextant
$V_g \geq 0 \quad V_h \geq 0$	1 <sup>st</sup>	$V_{g1} = V_g \quad V_{h1} = V_h$
$V_g < 0 \quad V_h \geq 0 \quad V_g + V_h \geq 0$	2 <sup>nd</sup>	$V_{g1} = -V_g \quad V_{h1} = V_g + V_h$
$V_g < 0 \quad V_h \geq 0 \quad V_g + V_h < 0$	3 <sup>rd</sup>	$V_{g1} = V_h \quad V_{h1} = -V_g - V_h$
$V_g < 0 \quad V_h < 0$	4 <sup>th</sup>	$V_{g1} = -V_h \quad V_{h1} = -V_g$
$V_g \geq 0 \quad V_h < 0 \quad V_g + V_h < 0$	5 <sup>th</sup>	$V_{g1} = -V_g - V_h \quad V_{h1} = V_g$
$V_g \geq 0 \quad V_h < 0 \quad V_g + V_h \geq 0$	6 <sup>th</sup>	$V_{g1} = V_g + V_h \quad V_{h1} = -V_h$

**Table 4-2: Reflection of reference vector into first sextant.**

It is now necessary to determine the region the reference lies in. This selects the nearest three vectors for the controller. This task is also achieved using a look-up table (Table 4-3) which reduces the processing load. Included in Table 4-3, is the determination of the duty ratio ( $d_{xyz}$ ), this is used in Section 4.5.2 to calculate the duty cycle for each of the selected vectors. For each region, Table 4-3 provides the duty ratios for each of the switching vectors at the vertices. Where the notation  $d_{xyz/\dots}$  is used, this denotes the duty ratio of redundant vectors. For clarity only one of the vectors is shown in the table.

Region	Vector Limits	Duty Ratio	Region	Vector Limits	Duty Ratio
16	$V_{g1} \leq 1$ $V_{h1} \leq 1$ $V_{g1} + V_{h2} \leq 1$	$d_{111/...} = 1 - V_{g1} - V_{h1}$ $d_{100/...} = V_{g1}$ $d_{110/...} = V_{h1}$	8	$2 < V_{g1} \leq 3$ $V_{h1} \leq 1$ $V_{g1} + V_{h2} \leq 3$	$d_{200/...} = 3 - V_{g1} - V_{h1}$ $d_{300/...} = V_{g1} - 2$ $d_{310/...} = V_{h1}$
15	$1 < V_{h1} \leq 2$ $V_{g1} \leq 1$ $V_{g1} + V_{h2} \leq 2$	$d_{110/...} = 2 - V_{g1} - V_{h1}$ $d_{100/...} = V_{g1}$ $d_{110/...} = 2 - V_{h1}$	7	$V_{g1} \leq 1$ $3 < V_{h1} \leq 4$ $V_{g1} + V_{h2} \leq 4$	$d_{440} = 1 - V_{g1}$ $d_{430} = 3 - V_{h1}$ $d_{441/...} = 4 - V_{h1} - V_{g1}$
14	$V_{g1} \leq 1$ $V_{h1} \leq 1$ $V_{g1} + V_{h2} > 1$	$d_{210/...} = V_{g1} + V_{h1} - 1$ $d_{100/...} = 1 - V_{h1}$ $d_{110/...} = 1 - V_{g1}$	6	$V_{g1} \leq 1$ $2 < V_{h1} \leq 3$ $V_{g1} + V_{h2} > 3$	$d_{441/...} = 1 - V_{g1}$ $d_{431/...} = 3 - V_{h1}$ $d_{430} = V_{h1} + V_{g1} - 3$
13	$1 < V_{g1} \leq 2$ $V_{h1} \leq 1$ $V_{g1} + V_{h2} \leq 2$	$d_{100/...} = 2 - V_{g1} - V_{h1}$ $d_{200/...} = V_{g1} - 1$ $d_{210/...} = V_{h1}$	5	$1 < V_{g1} \leq 2$ $2 < V_{h1} \leq 3$ $V_{g1} + V_{h2} \leq 4$	$d_{430} = V_{h1} - 2$ $d_{420} = V_{g1} - 1$ $d_{431/...} = 4 - V_{h1} - V_{g1}$
12	$V_{g1} \leq 1$ $2 < V_{h1} \leq 3$ $V_{g1} + V_{h2} \leq 3$	$d_{220/...} = 3 - V_{g1} - V_{h1}$ $d_{320/...} = V_{g1}$ $d_{330/...} = V_{h1} - 2$	4	$1 < V_{g1} \leq 2$ $1 < V_{h1} \leq 2$ $V_{g1} + V_{h2} > 3$	$d_{431/...} = 2 - V_{g1}$ $d_{421/...} = 2 - V_{h1}$ $d_{420} = V_{h1} + V_{g1} - 3$
11	$V_{g1} \leq 1$ $1 < V_{h1} \leq 2$ $V_{g1} + V_{h2} > 2$	$d_{320/...} = V_{g1} + V_{h1} - 2$ $d_{210/...} = 2 - V_{h1}$ $d_{220/...} = 1 - V_{g1}$	3	$2 < V_{g1} \leq 3$ $1 < V_{h1} \leq 2$ $V_{g1} + V_{h2} \leq 4$	$d_{420} = V_{h1} - 1$ $d_{410} = V_{g1} - 2$ $d_{421/...} = 4 - V_{h1} - V_{g1}$
10	$1 < V_{g1} \leq 2$ $1 < V_{h1} \leq 2$ $V_{g1} + V_{h2} \leq 3$	$d_{210/...} = 3 - V_{g1} - V_{h1}$ $d_{310/...} = V_{g1} - 1$ $d_{320/...} = V_{h1} - 1$	2	$2 < V_{g1} \leq 3$ $V_{h1} \leq 1$ $V_{g1} + V_{h2} > 3$	$d_{421/...} = 3 - V_{g1}$ $d_{411/...} = 1 - V_{h1}$ $d_{410} = V_{h1} + V_{g1} - 3$
9	$1 < V_{g1} \leq 2$ $V_{h1} \leq 1$ $V_{g1} + V_{h2} > 2$	$d_{310/...} = V_{g1} + V_{h1} - 2$ $d_{200/...} = 1 - V_{h1}$ $d_{210/...} = 2 - V_{g1}$	1	$3 < V_{g1} \leq 4$ $V_{h1} \leq 1$ $V_{g1} + V_{h2} \leq 4$	$d_{410} = V_{h1}$ $d_{400} = V_{g1} - 3$ $d_{441/...} = 4 - V_{h1} - V_{g1}$

Table 4-3: Section of region and calculation of duty cycles.

A Nearest Three Vector (NTV) modulation scheme is used in this study. Only one vector from each set of redundant vectors is selected per modulation period [4.11,4.12]. The vector is selected based on capacitor balancing and switching frequency reduction criteria. A NTV modulation strategy is considered the most suitable for use with the power converter in this study as it simplifies the capacitor balancing operation and reduces the effective switching frequency.

An alternative to NTV would be continuous modulation. Here four vectors are used per modulation cycle. The author of [4.13] notes that although continuous modulation may result in a superior waveform quality when compared to NTV, it comes at the cost of a higher effective switching frequency. It also noted that in order to achieve a similar average device switching frequency under NTV modulation, the converter switching frequency would need to be increased [4.13]. This will result in an improvement in NTV output spectrum, meaning that the adaptation of a continuous modulation strategy to achieve superior harmonic performance was futile. For these reasons a NTV modulation strategy was selected.

#### 4.5.2 Calculation of Duty Cycles and Vector Sequencing

The computational intensity of the calculation of the duty cycles for each of the three selected vectors is greatly reduced through the use of a look-up table (Table 4-3). This provides the duty ratio for each vector. The time each vector is applied for may then be found by multiplying the duty ratio by the period of the switching frequency.

In Figure 4-10 the sequence each of the vectors is applied is shown. In this instance the duty cycles of vectors 1 and 2 are halved and applied either sided of the 3<sup>rd</sup> vector [4.10]. An up/down counter is used to ensure each vector is applied for the appropriate duration. The value of the counter throughout period  $T$  is shown in red.

The sequencing of the 3 vectors may be used to minimise the number of switching events. This is discussed in Section 4.5.4.

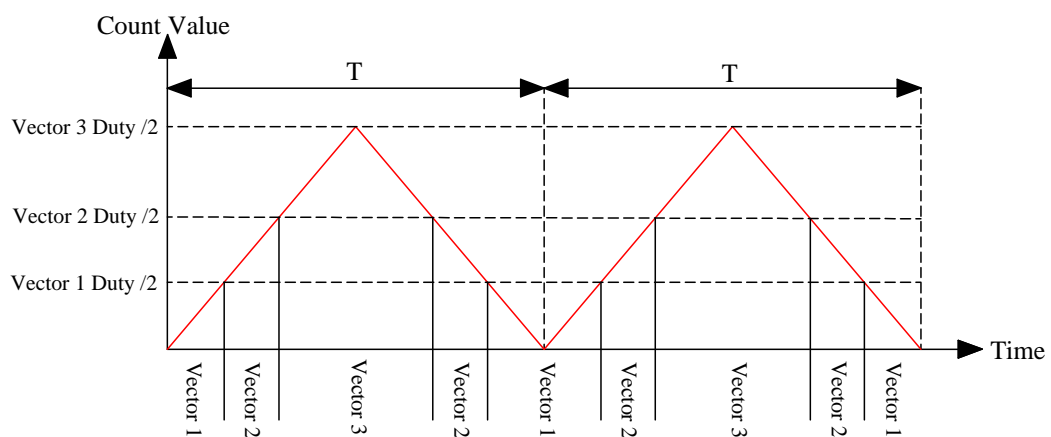


Figure 4-10: Vector sequence.

### 4.5.3 Capacitor Voltage Balancing

The selection of the optimal redundant vectors which results in a balanced DC link is achieved by minimising a quadratic function  $G$  (4.3) [4.10,4.14]. This quadratic calculates the energy in the capacitor bank, which the author of [4.15] notes reaches a minimum when all capacitor voltages are equal. Here  $C$  is the capacitance of each level in the DC link, assuming the capacitance is equal for all levels. The voltage unbalance in the  $p^{th}$  capacitor is denoted  $\Delta V_{cp}$  and is calculated using (4.4). The algorithm discussed in this section necessitates the controller to measure the voltage across each of the DC link capacitors at the start of each modulation period. This data is then used in the vector selection algorithm.

$$G = \frac{1}{2} C \sum_{p=1}^{n-1} \Delta V_{cp}^2 \quad (4.3)$$

$$\Delta V_{cp} = V_{cp} - \frac{V_{dc}}{n-1} \quad (4.4)$$

The derivative of (4.3) may be taken to yield (4.5) [4.14]. Here,  $i_{cp}$  is the current flowing in the  $p$  capacitor. To minimise (4.3), it's derivative (4.5) must be negative or zero.

$$\frac{dG}{dt} = \sum_{p=1}^{n-1} \Delta V_{cp} i_{cp} \leq 0 \quad (4.5)$$

The equation (4.5) can then be expressed in terms of the mid-point currents flowing in the various DC link taps ( $i_{mx}$ ) (4.6) [4.14,4.16]. This is important as the values of  $i_{mx}$  may be estimated for each of the redundant vectors. Equation (4.6) may be re-arranged to yield (4.7). The vector which maximises (4.7) is therefore the optimum vector from a capacitor voltages balancing perspective. The location of the mid-point and capacitor currents is shown in Figure 4-11, in the case for a six level inverter.

$$\frac{dG}{dt} = - \sum_{p=1}^{n-2} \Delta V_{cp} \left[ \sum_{x=p}^{n-2} i_{mx} \right] \leq 0 \quad (4.6)$$

$$\frac{dG}{dt} = \sum_{p=1}^{n-2} \Delta V_{cp} \left[ \sum_{x=p}^{n-2} i_{mx} \right] \geq 0 \quad (4.7)$$

If the assumption is made that the modulation period is sufficiently small that the voltage error can be considered constant throughout, then equation (4.7) may be manipulated to produce (4.8). All variables are expressed for the  $k^{\text{th}}$  modulation period. Here,  $\Delta V_{cp}(k)$  and  $\bar{i}_{mx}(k)$  is the capacitor voltage unbalance at the start of the modulation period and the averaged mid-point current over the duration of the period [4.10,4.16].

$$\frac{dG}{dt} = \sum_{p=1}^{n-2} \Delta V_{cp}(k) \left[ \sum_{x=p}^{n-2} \bar{i}_{mx}(k) \right] \geq 0 \quad (4.8)$$

So it may be used in the DSP, (4.8) must be expanded for the 5-level case ( $n=5$ ) to yield  $B$  (4.9). This may be simplified by noting that the capacitor unbalances must sum to zero (4.10), this enables (4.9) to be reduced (4.11). In the control algorithm, (4.11) must be evaluated for each possible redundant vector. The vector which maximises (4.11) is the one which most achieves capacitor balance.

$$B = \Delta V_{c1}(k)[\bar{i}_{m1}(k) + \bar{i}_{m2}(k) + \bar{i}_{m3}(k)] + \Delta V_{c2}(k)[\bar{i}_{m1}(k) + \bar{i}_{m2}(k)] \\ + \Delta V_{c3}(k)[\bar{i}_{m1}(k)] \quad (4.9)$$

$$\Delta V_{c1}(k) + \Delta V_{c2}(k) + \Delta V_{c3}(k) + \Delta V_{c4}(k) = 0 \quad (4.10)$$

$$B = \Delta V_{c1}(k)[\bar{i}_1(k)] - \Delta V_{c3}(k)[\bar{i}_2(k)] - \Delta V_{c4}(k)[\bar{i}_2(k) + \bar{i}_3(k)] \quad (4.11)$$

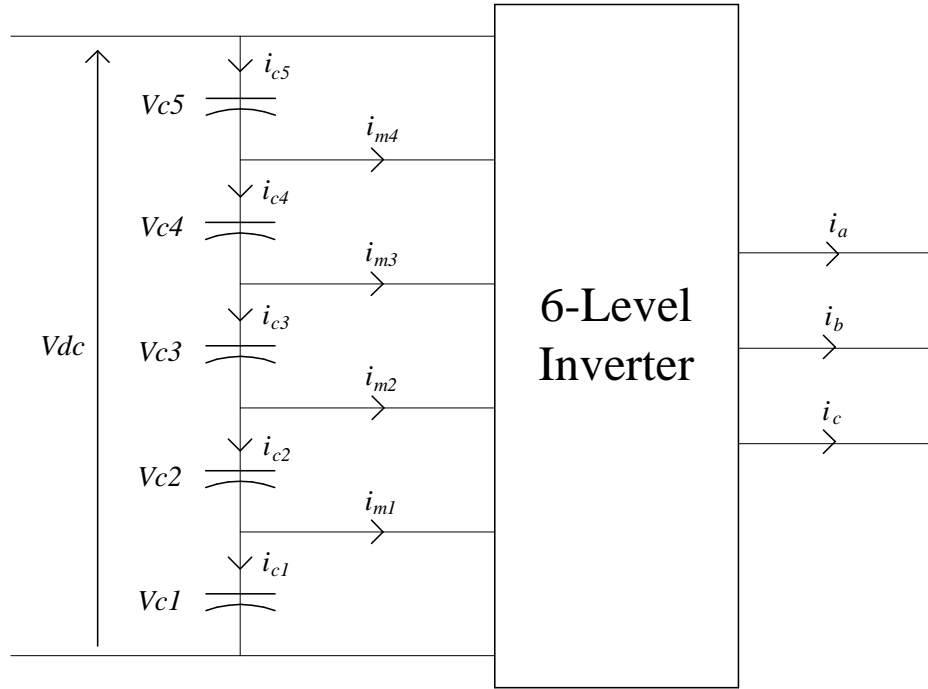


Figure 4-11: Location of capacitor and mid-point currents in a 5-level inverter.

The author of [4.11] provides a method to estimate the resultant mid-point currents for a given vector based on knowledge of the phase currents. The currents are estimated using (4.12) where  $D$  and  $S$  are two matrices.  $D$  averages the currents as a function of the examined vectors duty cycles whilst  $S$  interchanges the currents dependent upon which sector the original reference vector resides in. The derivation of  $D$  and  $S$  is considered beyond the scope of this study, however it may be found in [4.11].

$$\bar{i}_m(k) = \begin{bmatrix} \bar{i}_{m4}(k) \\ \bar{i}_{m3}(k) \\ \bar{i}_{m2}(k) \\ \bar{i}_{m1}(k) \end{bmatrix} = DS_T \begin{bmatrix} \bar{i}_d(k) \\ \bar{i}_q(k) \end{bmatrix} \quad (4.12)$$

At the start of the modulation period, the SVM discussed in Section 4.5.1 selects the nearest three vectors. For each of the redundant vectors the resultant mid-point currents are evaluated using (4.12). The calculated mid-point currents are then used to estimate the capacitor balancing function (4.11). For each redundant vector pair the one which results in the largest value of  $B$  is selected as the optimum vector.

#### 4.5.4 Device Switching Frequency Minimisation

Amongst others, the authors of [4.10,4.11,4,16] each detail methods for the reduction of the effective switching frequency in a diode-clamped inverter. The author of [4.16] utilises a cost function approach, where by poor output waveform quality may be traded against a reduction in the device switching frequency. This approach would be of use where drive efficiency/minimisation of heatsinking is a priority rather than waveform quality. This approach leads to compromises where suboptimal redundant vectors are used leading to increased DC link ripple and a degradation of the output waveform.

As this study's primary concern is the improvement of the output waveform quality through the use of a multilevel converter topology, a cost function based approach is not used. Instead the optimal vectors are selected, and the sequencing used to minimise the device switching frequency. However it must be noted this will result in sub-optimal results from a switching frequency perspective.

The objective of the controller is to minimise the number of commutations between voltage levels for each leg through the order of application of the three selected vectors. For example, assuming region 9 is selected and the vectors 432, 422 and 310 are selected as the optimal. The six possible sequences that these vectors may be applied in are shown in Table 4-4.

Sequence Number	Sequence	Commutations
1	432-422-310	4
2	432-310-422	6
3	422-310-432	6
4	422-432-310	4
5	310-422-432	4
6	310-432-422	4

Table 4-4: Vector sequences for region 1 of a 5-level inverter SV diagram.

The number of leg commutations between voltage levels is also shown in Table 4-4. Sequences two and three would be avoided as they would result in six voltage commutations. One of the remaining four sequences would therefore be selected. The choice between these four is made considering the last vector applied in the last modulation period. Of the remaining four sequences, the one which results in the smallest number of initial leg commutations at the start of the modulation period is selected.

Once the optimal sequence of vectors has been chosen they must be re-arranged using knowledge of the sextant the reference vector originally resided in. This procedure compensates for the initial reflection into the first sextant at the start of the algorithm and is achieved using a look-up table (Table 4-5). For example if the output vector from the sequence re-arrangement procedure was 432 assuming the reference was in the 5<sup>th</sup> sextant, the resultant vector to be applied in the next modulation period would be 243.

1 <sup>st</sup> Sextant	2 <sup>nd</sup> Sextant	3 <sup>rd</sup> Sextant	4 <sup>th</sup> Sextant	5 <sup>th</sup> Sextant	6 <sup>th</sup> Sextant
A	A→B	A→B	A→C	A→C	A
B	B→A	B→C	B	B→A	B→C
C	C	C→A	C→A	C→B	C→B

Table 4-5: Change output state dependant on original reference vector sextant.

#### 4.5.5 Complete Algorithm

For clarity the complete SV modulation algorithm is provided in Figure 4-12.

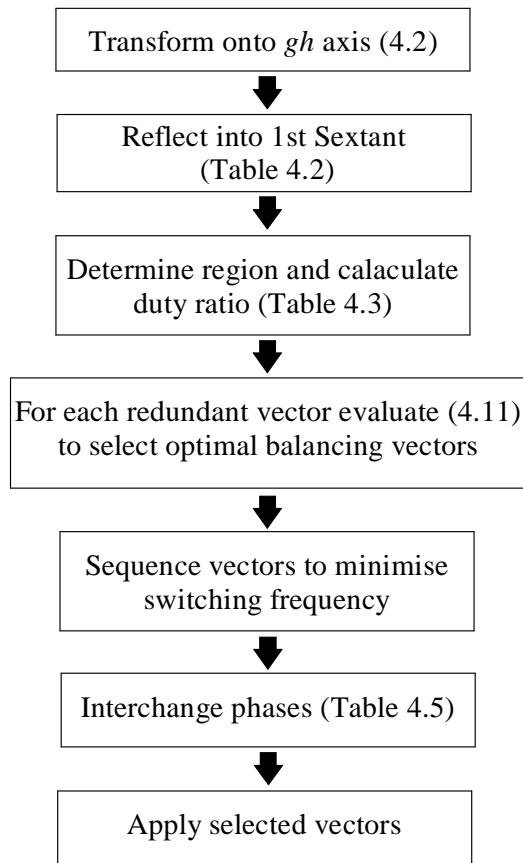


Figure 4-12: Complete SV algorithm.

## 4.6 Conclusion

In this chapter the modulation strategies commonly used to control multilevel converters have been examined. Each strategy was evaluated to determine its suitability to an aerospace S/G system. This has enabled the most applicable technique for this study to be selected.

The different modulation techniques have been classified subject to their relative switching frequencies. Fundamental switching frequency strategies such as Space Vector modulation and Selective Harmonic Elimination were quickly eliminated from this study. The low switching frequency results in a poor quality output from a harmonic perspective, which may require increased passive filtering to comply with the aerospace power quality standards. Also, the low switching frequency does not support the balancing of the DC link capacitor voltages. This would therefore either result in a poor quality output or necessitate additional circuitry to maintain the balanced DC link.

Sinusoidal PWM was then examined. SPWM may be easily applied to the control of a multilevel converter through the use of additional amplitude shifted carrier signals. The high switching frequency produces a low harmonic output, as required by this study. Also, it has been demonstrated in the literature how the algorithm may be modified to enable capacitor balance to be achieved. Unfortunately SPWM provides poor utilisation of the DC link voltage when compared to a Space Vector strategy. Using SPWM may therefore result in a larger and heavier converter than could be achieved using Space Vector control.

The Space Vector PWM modulation technique was then examined. This provides a high quality output, ability to balance the capacitor voltages and good utilisation of the DC link. Space Vector PWM was therefore chosen for use in this study. The algorithm was explained in detail with the emphasis on how it may be simplified for efficient implementation within a DSP. Special attention was given to the capacitor balancing procedure and minimisation of the converter's effective switching frequency.

## 4.7 References

- [4.1] J. Rodriguez, J. Lai, F. Z. Peng, "Multilevel Inverters: A Survey of Topologies, Controls, and Applications," *IEEE Transactions on Industrial Electronics*, Vol. 49, No. 4, pp. 724-738, August, 2002.
- [4.2] L. M. Tolbert, F. Z. Peng, T. G. Habetler, "Multilevel Converters for Large Electric Drives," *IEEE Trans. Industry Applications*, Vol. 35, pp. 36-44, 2005.
- [4.3] F. Wang, "Sine-Triangle versus Space-Vector Modulation for Three-Level PWM Voltage-Source Inverters," *IEEE Trans. Industry Applications*, Vol. 38, pp. 500-506, 2002.
- [4.4] G. Carrara, S. Gardella, M. Marchesoni, R. Salutari, G. Sciutto, "A New Multilevel PWM Method: A Theoretical Analysis," *IEEE Transactions on Industry Applications*, vol. 7, pp. 497-505, 1992.
- [4.5] B. P. McGraph, D. G. Holmes, "Multicarrier PWM Strategies for Multilevel Inverters," *IEEE Trans. Industrial Applications*, Vol. 49, No. 4, pp. 858-867, 2002.
- [4.6] Z. Pan, F. Z. Peng, "A Sinusoidal PWM Method with Voltage Balancing Capability for Diode-Clamped Five-Level Converters," *IEEE Trans. Industry Applications*, Vol. 45, No. 3, pp. 1028-1034, 2009.
- [4.7] S. Karagaba, O. Ojo, M. Abreham, "Carrier based PWM Scheme for a Three-Level Diode-Clamped Five-Phase Voltage Source Inverter Ensuring Capacitor Voltage balancing, Applied Power Electronics Conference and Exposition, Fort Worth, USA, pp 1194-1201, 2011.
- [4.8] G. P. Adam, S. J. Finney, A. M. Massoud, B. W. Williams, "Capacitor Balance Issues of the Diode-Clamped Multilevel Inverter Operated in a Quasi Two-State Mode," *IEEE Trans. Industrial Electronics*, Vol. 55, No. 8, pp. 3088-3099.
- [4.9] S. Busquets-Monge, A. Ruderman, "Carrier-Based PWM Strategies for the Comprehensive Capacitor Voltage Balance of Multilevel Multileg Diode-Clamped

Converters,” International Symposium on Industrial Electronics, Bari, Italy, pp. 688-693, 2010.

- [4.10] J. Pou, P. Rodriguez, D. Boroyevich, “Efficient Space-Vector Modulation Algorithm for Multilevel Converters with Low Switching Frequencies in the Devices,” Power Electronics Specialist Conference, Recife, Brazil, pp. 2521-2526, 2005.
- [4.11] J. Pou, “Modulation and Control of Three-Phase PWM Multilevel Converters,” Ph.D. Dissertation, Universitat Politecnica De Catalunya, 2002.
- [4.12] S. R. Minshull, “Multilevel Inverters for Driving Low Inductance Machines,” Ph.D. Thesis, University of Sheffield, 2009.
- [4.13] D. G. Holmes, T. A. Lipo, “Pulse Width Modulation for Power Converters: Principles and Practice,” Wiley-Interscience, 2003.
- [4.14] J. Pou, R. Pindado, D. Boroyevich, “Voltage-Balancing Strategies for Diode-Clamped Multilevel Converters,” Power Electronics Specialist Conference, Aachen, Germany, pp. 3988-3993, 2004.
- [4.15] M. Marchesoni, M. Mazzucchelli, F. V. Robinson, P. Tenca, “A Minimum-Energy-Based Capacitor Voltage Balancing Control Strategy for MPC Conversion Systems,”
- [4.16] S. R. Minshull, C. M. Bingham, D. A. Stone, M. P. Foster, “Frequency Reduction Schemes for Back-to-Back Connected, Diode-Clamped Multilevel Converters,” IET Power Electronics Journal, Vol. 3, No. 1, pp. 65-74, 2010.

# 5 Development of a PM Starter/Generator System

## 5.1 Introduction

In Section 2 the need to replace existing pneumatic engine starting systems with an all-electric S/G was discussed. Traditionally, the distribution bus is connected directly to the stator terminals of the generator. A CSD drive controls the output frequency and the excitation source is used to govern the grid voltage amplitude. This system is practical as firstly the generator provides no engine start function and secondly the generator output is the only electrical source upon the distribution bus, there is therefore no need to synchronise multiple sources.

In MEA aircraft the power requirements are too great to take all electrical power off one engine shaft. Instead, both the HP and LP shafts have a separate generator. Synchronisation will therefore be required between the two generator outputs if future aircraft are to persist in using AC distribution and wish to parallel generators. The simplest way of synchronising the outputs of multiple generators would be to include a power converter at the grid terminals.

As discussed in Section 2, the inclusion of a power converter at the generator output would provide aircraft manufacturers with additional benefits on top of the synchronisation of multiple generator outputs:

- The power converter provides the option of using the generator for electric engine start which is the primary goal of this study. This is a major objective of the More-Electric-Aircraft initiative as the removal of the pneumatic starting system would provide a substantial weight reduction.
- Secondly the generator speed can be allowed to vary with engine speed ensuring that the complex CSD is no longer necessary resulting in both a net weight reduction and a possible improvement in reliability.

- The next evolutionary step in the More Electric Aircraft initiative after the all-electric S/G, would be the use of an embedded machine within the engine. This would negate the need for a CSD, gearbox or engine coupling and is therefore from a weight perspective the optimum solution. However a power converter would then be required to deal with the machine output frequency which would vary from low when the engine is at idle to very high when the engine is at maximum speed.
- If the generator speed can be allowed to vary it is possible that the engine idle speed can be lowered. At present from an engine perspective idle speed is kept unnecessarily high to keep the generator at rated speed even with the CSD. A power converter with boost function and the ability to frequency change would enable idle speed to be lowered therefore saving fuel and reducing emissions.

As discussed in Section 2.2, numerous machine topologies have been proposed in the literature for future S/Gs. This study focuses only on synchronous machines. This chapter discusses the development of a PMSM S/G system, whilst in Chapter 6 the WFSM case is described.

This chapter's primary contribution is the demonstration of a multilevel converter functioning in a S/G system. The benefits of a multilevel converter in this application were discussed in Section 3. Primarily through the adoption of this technology, the distortion in the current waveform at the grid connection and in the stator will be reduced. This allows the passive filtering to be reduced therefore providing a net weight reduction. Additional benefits of this system, include a reduction in the radiated EMI which will mean less shielding is required, easing compliance with aerospace EMC standards.

The back-to-back connected, diode-clamped topology discussed in Section 3 is used. This ensures that benefits such as the reduction in current waveform distortion obtained through use of a multilevel converter are apparent at both grid and machine sides of the converter. In addition this topology provides the bi-directional power flow capability which is essential in a S/G system. Also the ability to self-balance the DC link capacitor voltages without additional circuitry is made possible by the back-to-back connection.

This chapter is organised as follows:

A basic overview of power converter vector control theory is first given. Vector control is now the industry norm in the field of three-phase power converter control as it can be efficiently implemented within a DSP. The development of the inverter's controller is first discussed. In starting mode the controller must regulate the torque produced by the S/G to ensure the turbine accelerates to idle speed. Once generation mode has been reached, the inverter's controller must regulate the DC link whilst minimising losses in both the machine and the converter.

The vector controller of the AFE is then discussed. The AFE controller is responsible for regulating the real and reactive power drawn and delivered to the grid, whilst also insuring the converter generates as little electrical distortion as possible to ensure compliance with power quality standards.

The proposed controller is then demonstrated experimentally upon a prototype converter. A conventional PMSM is used in place of an embedded machine. The test machine is then coupled to a dynamometer to provide mechanical loading.

The control of the dynamometer is then discussed. The objective of the controller is to ensure that the S/G test machine is loaded in a manner similar to a real world application. This is necessary to provide substantive results to validate the performance of the proposed system.

Results are then presented which have been obtained experimentally using the prototype hardware. The performance of the hardware is initially assessed in each mode separately. Successful operation is demonstrated with both inverters functioning satisfactory in each mode. Results are then presented showing the performance of the hardware when subjected to a full system test. The S/G is accelerated from standstill to maximum operational speed with the dynamometer providing realistic mechanical loading throughout. The experimental results show clearly that the proposed system functions as required throughout the test.

Finally, results are presented which show the performance of the converter in generation mode when the speed of the S/G is oscillating. It is crucial for the system to demonstrate performance under these conditions if it is to be used in an embedded system.

Conclusions are then drawn on the performance of the hardware and the contributions and implications of the work described in this chapter.

The work discussed in this chapter has been published in [5.1].

## **5.2 Vector Control of the Converter**

Difficulties arise when analysing and controlling AC machines as all the variables are rotating. PI regulators are often poor in tracking a sinusoidal reference therefore creating distortion upon the output. Hysteresis controllers normally result in a variable frequency distortion being added to the output signal that will require additional filtering to suppress and also complicates compliance with power quality standards. Also abc domain controllers in three-phase three wire systems do not take into account the interactions between phases which can lead to unbalance [5.2].

In synchronous machine and grid connected converter control, both the phase angle and amplitude of the stator current, hence the current vector, must be controlled for successful operation [5.3]. Vector control greatly simplifies the control of grid and machine connected inverters, through the transformation of the three-phase variables into two components on a synchronously rotating orthogonal axis reference plane. It is possible to control the real and reactive power drawn from the grid connection and the torque developed by the machine using two DC signals.

The machine and grid side controllers are now discussed separately. The interfacing of the vector controller, various converter sensors and transducers and the SVPWM algorithm is also discussed.

### **5.2.1 Machine Connected Inverter Controller**

The synchronous machine back-emf has a sinusoidal profile. It is therefore beneficial if the machine drive controller produces a sinusoidal stator current to provide a constant torque [5.4]. The first step is to transform the three-phase variables onto a stationary orthogonal

axis ( $\alpha\beta$ ) using the Clarkes transformation [5.2]. Any of the motor's three phase variables may be transformed, in Figure 5-1 the motors Magnetomotive Force (MMF) ( $F_x$ ) is transformed where  $N$  is the number of stator winding turns. The forward and inverse transformations are given in Equations (5.1) and (5.2) respectively where  $x$  is the variable to be transformed.

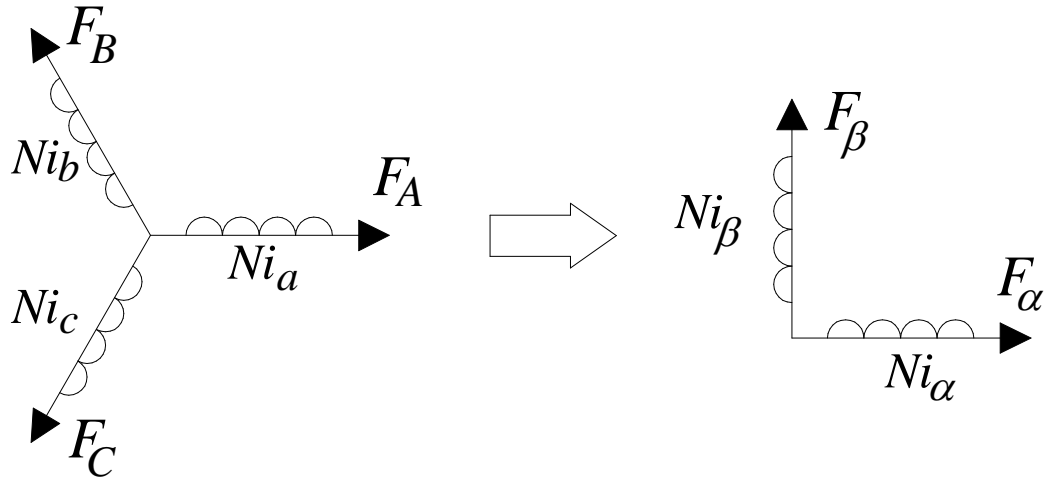


Figure 5-1: Three-axis winding transformed into two axis representation.

$$\begin{bmatrix} x_\alpha \\ x_\beta \end{bmatrix} = \frac{2}{3} \begin{bmatrix} 1 & -\frac{1}{2} & -\frac{1}{2} \\ 0 & \frac{\sqrt{3}}{2} & -\frac{\sqrt{3}}{2} \end{bmatrix} \begin{bmatrix} x_a \\ x_b \\ x_c \end{bmatrix} \quad (5.1)$$

$$\begin{bmatrix} x_a \\ x_b \\ x_c \end{bmatrix} = \begin{bmatrix} 1 & 0 \\ -\frac{1}{2} & \frac{\sqrt{3}}{2} \\ -\frac{1}{2} & -\frac{\sqrt{3}}{2} \end{bmatrix} \begin{bmatrix} x_\alpha \\ x_\beta \end{bmatrix} \quad (5.2)$$

The controller can be simplified further by interpreting all machine quantities on a reference frame that rotates synchronously with the stator fundamental frequency ( $\omega_e$ ) [5.5]. The relationship between the  $\alpha\beta$  and dq orthogonal axes is shown in Figure 5-2. Here,  $\theta$  is the angle between the  $\alpha$  and d axis, and is equal to the integral of  $\omega_e$ .

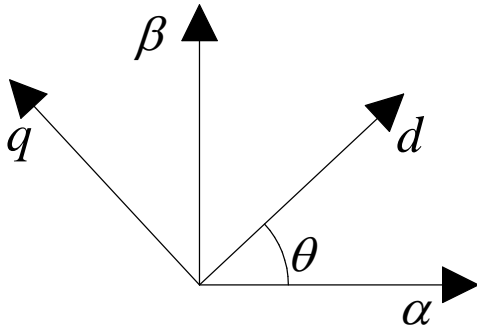


Figure 5-2: Rotating dq reference frame with respect to  $\alpha\beta$  stationary frame.

The d axis is chosen to align with the machine's rotor. The relationship between the dq axis, machine rotor and abc axis is shown in Figure 5-3. This therefore necessitates knowledge of the rotor's mechanical angle. The machines variables may be transformed into the DQ domain using Park's transformation (5.3), the inverse transform is provided in (5.4).

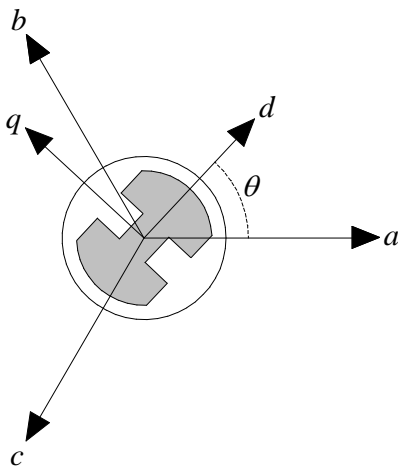


Figure 5-3: DQ axis in relationship to three-phase, salient PMSM rotor.

$$\begin{bmatrix} x_d \\ x_q \end{bmatrix} = \begin{bmatrix} \cos(\theta) & \sin(\theta) \\ -\sin(\theta) & \cos(\theta) \end{bmatrix} \begin{bmatrix} x_\alpha \\ x_\beta \end{bmatrix} \quad (5.3)$$

$$\begin{bmatrix} x_\alpha \\ x_\beta \end{bmatrix} = \begin{bmatrix} \cos(\theta) & -\sin(\theta) \\ \sin(\theta) & \cos(\theta) \end{bmatrix} \begin{bmatrix} x_d \\ x_q \end{bmatrix} \quad (5.4)$$

The transfer of the variables from abc format into the dq domain is of great benefit to the controller designer. The variables have been transformed from three, time and speed

dependant signals into a time and speed invariant vector formed by two coordinates [5.24]. This results in the transform of the three sinusoidal signals into two DC variables under steady state conditions. DC signals can be tracked more effectively by PID controllers, providing improved dynamic performance. Using DQ coordinates also enables all three-phases to modulated simultaneously, improving the level of control over real/reactive power and torque.

The equations governing the electrical behaviour of the windings in a three-phase synchronous machine are given in (5.5). Here,  $v_k$  ( $k=a,b,c$ ) is the phase voltage seen at the machine terminals and  $R$  is the stator winding resistance. It is assumed that the resistances of all phases are equal.  $L_k$  and  $M_{k,i}$  (where  $i=a,b,c$  and  $i \neq k$ ) are the phase and mutual inductances respectively. The final term in (5.5) calculates the machine back-emf. To do this, the machines speed ( $\omega_m$ ) and rotor angle ( $\theta_m$ ) must be known. In (5.5),  $p$  and  $\psi_F$  is the number of pole pairs and the total magnet flux linkage respectively [5.3,5.4,5.6].

$$\begin{bmatrix} v_a \\ v_b \\ v_c \end{bmatrix} = \begin{bmatrix} R & 0 & 0 \\ 0 & R & 0 \\ 0 & 0 & R \end{bmatrix} \begin{bmatrix} i_a \\ i_b \\ i_c \end{bmatrix} + \frac{d}{dt} \begin{bmatrix} L_a & M_{ab} & M_{ac} \\ M_{ab} & L_b & M_{bc} \\ M_{ac} & M_{bc} & L_c \end{bmatrix} \begin{bmatrix} i_a \\ i_b \\ i_c \end{bmatrix} + \begin{bmatrix} -\omega_m \psi_F \sin(p\theta_m) \\ -\omega_m \psi_F \sin(p\theta_m - 2\pi/3) \\ -\omega_m \psi_F \sin(p\theta_m + 2\pi/3) \end{bmatrix} \quad (5.5)$$

If it is assumed that  $L$  is equal in all phases (5.6), and that the mutual inductance between each phase is constant (5.7), then (5.5) may be re-written as (5.8).

$$L_a = L_b = L_c = L \quad (5.6)$$

$$M_{ab} = M_{bc} = M_{ac} = M \quad (5.7)$$

$$\begin{bmatrix} v_a \\ v_b \\ v_c \end{bmatrix} = \begin{bmatrix} R & 0 & 0 \\ 0 & R & 0 \\ 0 & 0 & R \end{bmatrix} \begin{bmatrix} i_a \\ i_b \\ i_c \end{bmatrix} + \frac{d}{dt} \begin{bmatrix} L - M & 0 & 0 \\ 0 & L - M & 0 \\ 0 & 0 & L - M \end{bmatrix} \begin{bmatrix} i_a \\ i_b \\ i_c \end{bmatrix} + \begin{bmatrix} -\omega_m \psi_F \sin(p\theta_m) \\ -\omega_m \psi_F \sin(p\theta_m - 2\pi/3) \\ -\omega_m \psi_F \sin(p\theta_m + 2\pi/3) \end{bmatrix} \quad (5.8)$$

To simplify the control of the S/G, (5.8) is transformed into the dq domain using (5.1) and (5.3) to produce (5.9). In (5.9),  $\omega_e$  is the stator fundamental electrical frequency, which is

the product of  $\omega_m$  and  $p$ .  $L_d$  and  $L_q$  is the d and q components of the synchronous reactance. In the case of a non-salient machine  $L_d$  and  $L_q$  in (5.9) may be replaced with the stator synchronous inductance ( $L_s$ ) which is defined in (5.10) [5.5].

$$\begin{bmatrix} v_d \\ v_q \end{bmatrix} = \begin{bmatrix} R & -\omega_e L_q \\ \omega_e L_d & R \end{bmatrix} \begin{bmatrix} i_d \\ i_q \end{bmatrix} + \begin{bmatrix} L_d & 0 \\ 0 & L_q \end{bmatrix} \frac{d}{dt} \begin{bmatrix} i_d \\ i_q \end{bmatrix} + \begin{bmatrix} 0 \\ K_e \omega_m \end{bmatrix} \quad (5.9)$$

$$\frac{3L_s}{2} = L - M \quad (5.10)$$

The last term in (5.9) that calculates the back-emf has been reduced to a q component. This substitution assumes that the angle used in the dq transform is correctly aligned with  $\theta_m$  multiplied by  $p$  to give the stator electrical angle  $\theta_{me}$ . If this is the case there is no direct back-emf component. The back-emf constant ( $K_e$ ) is defined in (5.11). For a PMSM,  $\psi_F$  is constant and therefore so is  $K_e$ . In the case of a WFSM,  $\psi_F$  is a function of the machine speed and excitation conditions, and can therefore no longer be assumed constant. Accommodating a fluctuating  $K_e$  into the system controller is discussed in detail in Section 6.

$$K_e = p\psi_F \quad (5.11)$$

To highlight the various voltage vectors in a motor drive, a two-level inverter connected to a model of a synchronous machine is shown in Figure 5-4. It is assumed that the DC-link supplied by the AFE is at constant amplitude. The converters output voltage vector ( $\underline{U}_{conv}$ ) and the voltage vector at the machine terminals ( $\underline{v}$ ) are defined in (5.12) and (5.13) respectively. The stator current may also be represented in vector form ( $\underline{i}$ ) as shown in equation (5.14).

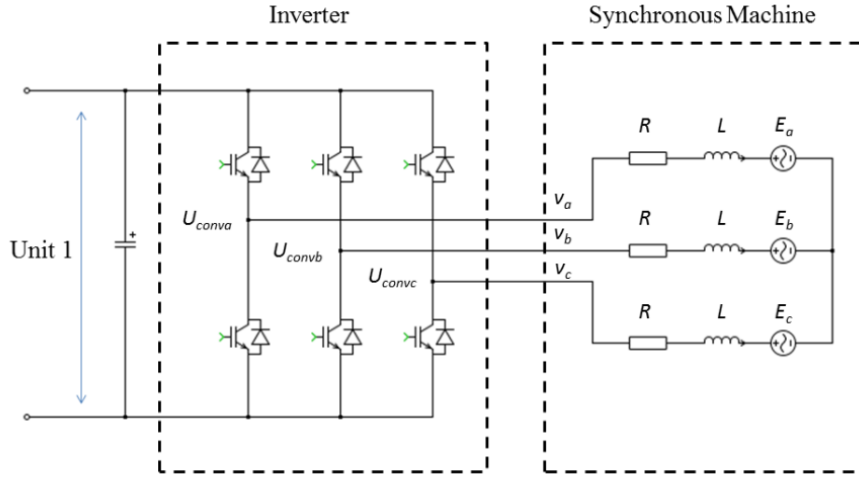


Figure 5-4: Two-level, motor connected inverter.

$$\underline{U}_{conv} = \begin{bmatrix} U_{conva} \\ U_{convb} \\ U_{convc} \end{bmatrix} \equiv \begin{bmatrix} U_{convd} \\ U_{convq} \end{bmatrix} \quad (5.12)$$

$$\underline{v} = \begin{bmatrix} v_a \\ v_b \\ v_c \end{bmatrix} \equiv \begin{bmatrix} v_d \\ v_q \end{bmatrix} \quad (5.13)$$

$$\underline{i} = \begin{bmatrix} i_a \\ i_b \\ i_c \end{bmatrix} \equiv \begin{bmatrix} i_d \\ i_q \end{bmatrix} \quad (5.14)$$

As the machine and converter terminals are connected together it is clearly apparent that  $\underline{U}_{conv} = \underline{v}$ . The vector  $\underline{U}_{conv}$  is determined by the converter switch configuration and the amplitude of the DC link, this relationship is defined in (5.15) [5.5]. The configuration of each of the inverter legs is given in  $S_k$  ( $k=a,b,c$ ), with  $\underline{S}$  being the vector representation.  $S_k$  may take the values 1 or -1.

$$\underline{U}_{conv} = \frac{2}{3} V_{dc} \begin{bmatrix} S_a \\ S_b \\ S_c \end{bmatrix} = \frac{2}{3} V_{dc} \underline{S} \quad (5.15)$$

Two current control loops are used to force  $\underline{i}$  to the reference vector  $\underline{i}^*$ . The value of the reference is dependant on the mode of operation and is discussed later in this chapter. The

current error signal is calculated and then PI controllers used to produce a converter output demand vector ( $\underline{U}_{conv}^*$ ) for implementation in the next switching cycle.  $\underline{U}_{conv}^*$  is then passed to the SVPWM algorithm discussed in Chapter 4 to determine the required switching sequence to synthesise the vector at the converter output.

One side effect of basing the controller in the dq domain is the resultant coupling between the  $i_d$  and  $i_q$  current control loops. This is apparent in (5.9). The amplitude of  $i_q$  is not solely dependent on  $v_q$  but also  $i_d$ . The same is true for the  $i_d$  control loop. To compensate for this phenomenon decoupling terms are added to  $\underline{U}_{conv}^*$ , these are given in (5.16) and (5.17). The current control loops and decoupling network for the machine connected inverter are shown in Figure 5-5.

$$\Delta U_{convd} = \omega_e L_q i_q \quad (5.16)$$

$$\Delta U_{convq} = -\omega_e L_d i_d \quad (5.17)$$

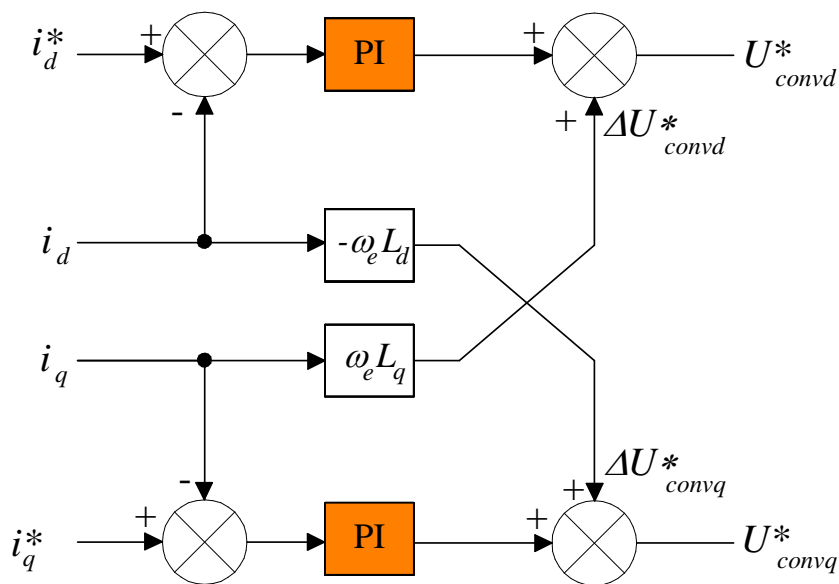


Figure 5-5: Decoupled inverter controller.

During starting mode it is important to maximise the torque produced by the S/G to ensure there is sufficient force to accelerate the turbine up to the required speed. The electrical torque ( $T_e$ ) developed by a PMSM may be calculated using (5.18). In the case of a salient machine such as an Interior Permanent Magnet Synchronous Machine (IPMSM) where

$L_q \neq L_d$ , the first part of (5.3) ( $\psi_F i_q$ ) calculates the magnetic torque and the second part ( $(L_d - L_q) i_d i_q$ ) the reluctance torque [5.3,5.7].

$$T_e = \frac{3}{2} p (\psi_F i_q + (L_d - L_q) i_d i_q) \quad (5.18)$$

In the case of a non-salient machine such as PMSM with surface mounted magnets upon the rotor,  $L_d = L_q$ , (5.18) therefore reduces to (5.19). The electrical torque developed is purely magnetic.

$$T_e = \frac{3}{2} p (\psi_F i_q) \quad (5.19)$$

Assuming a non-salient machine, it is readily apparent from (5.18) that to achieve maximum efficiency and therefore maximum torque,  $i_d$  must be minimised (ideally to zero) and  $i_q$  used to regulate machine torque. This is known as Maximum Torque Per Ampere Control (MTPAC) and results in the minimum ohmic losses in the stator [5.3,5.6]. It is also intuitive that this also maximises the system torque rating for a given inverter current rating.

In generation mode the design of the inverter's vector controller is influenced by two factors; firstly the amplitude of the DC link relative to the back-emf of the S/G and secondly the overall system efficiency.

The rms phase voltage ( $V_p$ ) at an inverter's output under SV modulation is given in (5.20) [5.8]. Here  $m$  is the modulation index, and therefore the maximum value of  $V_p$  obtainable without entering the over-modulation region is when  $m$  is unity. This means that  $V_p$  is limited to  $0.408 * V_{dc}$ .

$$V_p = \frac{1}{\sqrt{3}\sqrt{2}} m V_{dc} \quad (5.20)$$

The phase back-emf of the machine must remain below  $0.408 * V_{dc}$  to guarantee continuous and stable operation of the converter. For aerospace applications there is an impetus to minimise the converter's rated DC link voltage ( $\hat{V}_{dc}$ ). The decoupling capacitors used in the converter DC link increase in size and weight with increased  $\hat{V}_{dc}$ . The converter power density can therefore be improved by reducing  $\hat{V}_{dc}$ . This offset slightly by the fact

that as  $V_{dc}$  is increased the phase current drops. The DC link ripple therefore falls, which is also a factor when sizing DC link capacitors.

Converter control is simplified greatly if a WFSM is used. The excitation source may be used to govern the back-emf and ensure it remains below  $0.408 * \hat{V}_{dc}$ . Control is more complex in the PM case. The voltage seen at the converter terminals is now dependant on both the machine speed and the amplitude of the stator current. This is particularly problematic in an embedded machine application, as the machine speed will fluctuate with the turbines. This could mean that during periods of low electrical loading or during an engine speed surge the  $\hat{V}_{dc}$  limit is breached. This would result in damage to the converter and/or disruption to the aircraft's power network.

To overcome this problem field weakening is commonly employed in the control of PMSMs. The total flux linkage ( $\psi_T$ ) is given in (5.21) [5.6] where  $\psi_d$  and  $\psi_q$  is the flux linkage aligned and in quadrature with the rotor respectively.

$$\psi_T = \sqrt{\psi_d^2 + \psi_q^2} = \sqrt{(L_d i_d + \psi_F)^2 + (L_q i_q)^2} \quad (5.21)$$

As the permanent magnets cannot be adjusted,  $\psi_F$  is fixed, however by injecting a negative  $i_d$  into the stator current, it is possible to suppress the voltage seen at the converter terminals. This method is complicated when considering performance under converter fault conditions. This technique can be used to de-rate the DC link capacitors, whilst ensuring the machine voltage remains within the  $\hat{V}_{dc}$  limit. Field weakening does come at the cost of an increased stator current as calculated by (5.22). This will necessitate higher current rated components, which may negate some of the power density gained by reducing the capacitor ratings.

$$|\underline{i}| = \sqrt{i_d^2 + i_q^2} \quad (5.22)$$

The control of the inverter in generation mode can also be optimized to increase the overall system efficiency. Reducing losses in both the converter and machine is an advantage in the aerospace environment from a weight perspective. High losses due to low efficiency systems necessitate additional cooling. If some of the losses are eliminated the level of cooling may be reduced resulting in a system weight reduction.

The authors of [5.8,5.9] have conducted studies into how the vector controller may be optimised to reduce losses in both the PMSM and the converter. Based on (5.22) it seems intuitive that to reduce losses in the converter,  $i_d$  should be minimised therefore reducing  $\underline{i}$ . A reduction in  $\underline{i}$  will result in lower ohmic losses in both the converter and the machine. Switching losses will also be reduced in the converter. However the total losses ( $P_{loss}$ ) across the system must be considered.  $P_{loss}$  may be calculated by the summation of the machine's iron ( $P_{Fe}$ ) and copper ( $P_{Cu}$ ) losses and the total converter losses ( $P_{conv}$ ) (5.23) [5.8,5.9]. The effect on  $P_{loss}$  of varying  $i_d$  must therefore be assessed to determine the optimum solution from an efficiency perspective.

$$\min \left( \sum P_{loss} \right) = \min(P_{Fe} + P_{Cu} + P_{Conv}) \quad (5.23)$$

The total converter losses may be found through the summation of the losses of every component. For example the switching ( $P_{sw}$ ) and on state ( $P_{con}$ ) losses for one of the IGBTs may be calculated using (5.24) and (5.25) respectively [5.9,5.10]. These equations assume that the IGBTs are modulated using a SVPWM signal and the current is sinusoidal. Here  $E_{on}$ ,  $E_{off}$ ,  $V_{rated}$ ,  $I_{rated}$  and  $f_s$  represent the turn on and turn off losses at rated power, the rated voltage and current and the converter switching frequency respectively.  $V_t$ ,  $\Phi$ , and  $R_{ce}$  denote the threshold voltage, angle between  $\underline{i}$  and  $\underline{U}_{conv}$  and collector-emitter resistance respectively.

$$P_{sw} = \frac{6}{\pi} (E_{on} + E_{off}) \frac{V_{dc} |i|}{V_{rated} I_{rated}} f_s \quad (5.24)$$

$$P_{con} = \frac{1}{2} |i| V_t \left( \frac{1}{\pi} + \frac{m_x}{2\sqrt{3}} \cos \phi \right) + |i|^2 R_{ce} \left( \frac{1}{8} - \frac{2m_x}{3\pi\sqrt{3}} \cos \phi \right) \quad (5.25)$$

The calculation of  $P_{sw}$  and  $P_{con}$  must be repeated for every IGBT in the converter. This procedure is more complex in the diode-clamped multilevel topology when compared to a two-level inverter as the switches in each leg have different values of m. The losses in both the clamping and anti-parallel diodes also need be calculated. The IGBT and diode losses can then be summed to calculate  $P_{conv}$ .

The machine copper and iron loss may be calculated using (5.26) and (5.27) [5.11,5.12] respectively. In (5.27)  $\gamma$  is the saliency ratio factor and is calculated using (5.28).  $R_{Fe}$  and  $i_{Fed}$

and  $i_{Feq}$  are the iron loss resistance and iron loss D and Q components respectively. It is apparent from (5.27) that assuming a constant  $i_q$ , if  $i_d$  becomes negative, iron losses initially reduce whilst copper losses increase with increasing  $|i|$  [5.11,5.12]. This process continues until  $i_d - i_{Fed} = \sqrt{3}\psi_F/L_d$ . After which point both copper and iron losses increase as  $i_d$  becomes more negative.

$$P_{Cu} = R_s i^2 \quad (5.26)$$

$$P_{Fe} = \frac{1}{R_{Fe}} \omega_e^2 (\gamma L_d [i_q - i_{Feq}])^2 + \frac{1}{R_{Fe}} \omega_e^2 (\sqrt{3}\psi_F + L_d [i_d - i_{Fed}])^2 \quad (5.27)$$

$$\gamma = \frac{L_q}{L_d} \quad (5.28)$$

It is apparent from the analysis conducted that during generation mode the calculation of  $i_d^*$  is application specific and will be greatly influenced by the hardware. If the back-emf is approaching the limit imposed by the DC link capacitors ratings, field weakening will need to be employed. If the converter has only adequate cooling and it is therefore imperative that  $P_{conv}$  is minimised then it would be appropriate to set  $i_d^* = 0$ . If the machine is at risk of over-heating or is embedded within the engine therefore making cooling difficult, it may be beneficial to set  $i_d^* \leq 0$ , to reduce machine losses.

In this study the power rating of the machine was far greater than that of the converter. Also all testing was conducted well below the machines rated speed therefore resulting in a relatively low back-emf. As such  $i_d^*$  was set at zero to minimise converter losses. This also has the benefit of reducing the complexity of the control loop. However in a real world application a substantial analysis would need to be conducted upon the S/G system to aid the design of the inverter's controller. Also from a torque perspective, whilst the PMSM in this study does have a salient rotor, the saliency ratio is close to unity ( $L_q \approx L_d$ ). As the machine has ample available torque, for the purpose of this study, and to minimise losses in the converter,  $i_d^*$  is set to zero. There is therefore no reluctance torque component. In a real world application if it was important to maximise the available torque for a given machine and converter rating it would be necessary to have a negative  $i_d^*$ , however this is not the case here.

A block diagram of the inverter's controller in starting mode is provided in Figure 5-6. As mentioned previously the purpose of the controller is to accelerate the turbine using the S/G up to the engine ignition speed ( $\omega_i$ ), then maintain that speed whilst the combustors are ignited. When the engine has been ignited, the S/G must assist the engine in continuing to accelerate until it reaches idle speed ( $\omega_{idle}$ ) [5.13].

The rotor's electrical angle is measured using a resolver, then differentiated to determine the machine's rotational velocity. This is in turn fed into a speed control loop. The error between the demand speed and measured speed is calculated, and the error is fed into a PI block to produce a torque demand, which is used as  $i_q^*$ .

Current transducers are used to measure the stator line currents. These measurements along with the rotor angle are passed to a DQ transformation block in order to obtain  $i_d$  and  $i_q$ . These values are then passed to the two current control loops. The current dq component errors are calculated then fed into PI control blocks to generate  $U_{convd}^*$  and  $U_{convq}^*$ . These values are decoupled and then passed to the SVPWM block which was discussed in Chapter 4. In addition to  $U_{convd}^*$  and  $U_{convq}^*$ , the electrical angle and capacitor voltages are passed to the SVPWM block. This enables the SVPWM algorithm to select the appropriate switching vectors to produce  $U_{convd}^*$  and  $U_{convq}^*$  at the converter output whilst simultaneously balancing the converter capacitor voltages.

In the testing conducted in this and the subsequent wound field chapter. Close control of the machine was deemed unnecessary. Instead the controller's objective was to accelerate the S/G to the reference speed ( $\omega_i / \omega_{idle}$ ) as quickly as possible. This is similar to a real scenario where the starting systems are required by the standards to take no longer than 30 s to start the engine from standstill. As this is the case, during starting mode,  $i_q^*$  was simply set to a constant, high value. Therefore a step demand signal was used for q current component.

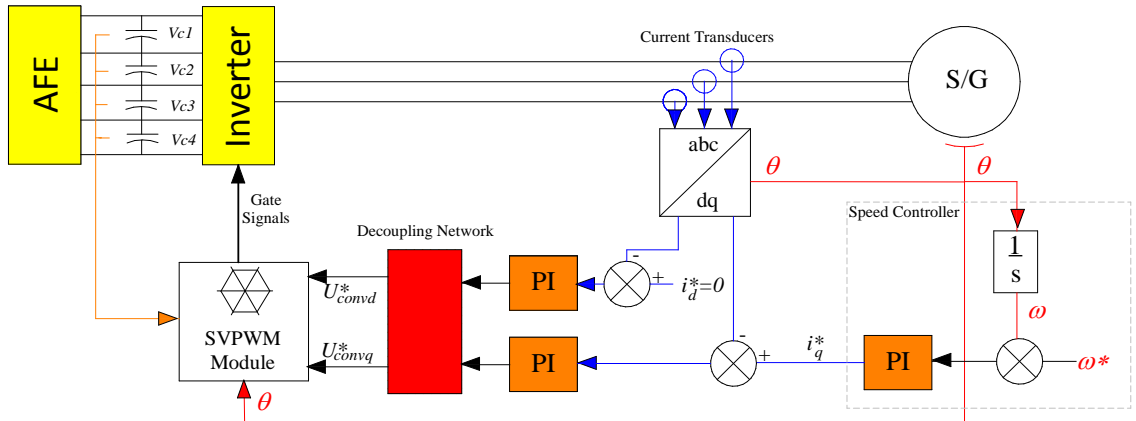


Figure 5-6: Inverter controller during starting mode.

Once the engine has been accelerated to  $\omega_{idle}$ , the controller of the inverter enters generation mode. A block diagram of the controller is provided in Figure 5-7. It is identical to that used in starting mode apart from the calculation of  $i_q^*$ . In this mode, the controller is responsible for regulating the flow of real power from the S/G to maintain a steady DC link. A voltage control loop is therefore employed to calculate the error between  $V_{dc}^*$  and  $V_{dc}$ . This error is then passed to a PI controller to produce  $i_q^*$ . For the reasons outlined earlier,  $i_d^*$  is maintained at zero to minimise power losses in the converter.

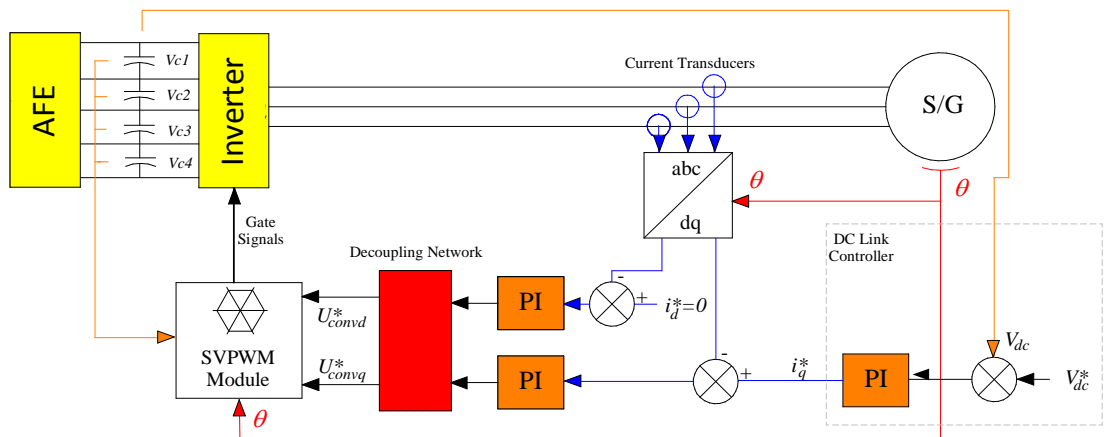


Figure 5-7: Inverter controller during generation mode.

## 5.2.2 Grid Connected Inverter Controller (AFE)

Although this chapter is concerned with the development of the vector control algorithm for a multilevel converter, the analysis of the grid connected inverter is initially focused on

a simple two-level, three phase system (Figure 5-8). This simplifies the analysis and the controller developed may be reapplied in the multilevel case.

The inclusion of the inductance ( $L$ ) at the grid interface is essential for successful operation of the inverter. It enables the inverter to function in boost mode, whilst also providing filtering to the line current and therefore improving the THD of the converter. In a practical application it would be typical to use an LC or LCL filter at the grid connection to prevent PWM injection into the grid. To simplify the controller design this was not considered at this stage.

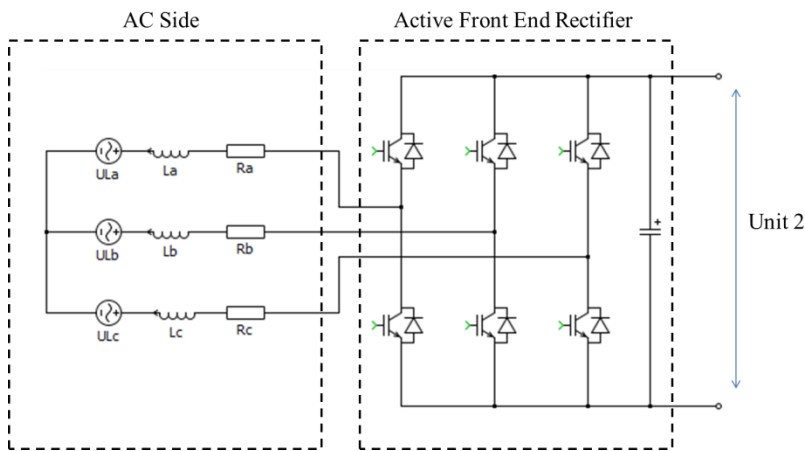


Figure 5-8: Two level, grid connected inverter.

Assuming a balanced three-phase supply, the grid voltage vector ( $\underline{U}_L$ ) is given in (5.29). Here  $U$  and  $\omega_g$  is the supply peak phase voltage and angular frequency respectively.

$$\underline{U}_L = \begin{bmatrix} U_{La} \\ U_{Lb} \\ U_{Lc} \end{bmatrix} = \begin{bmatrix} U \cos(\omega_g t) \\ U \cos\left(\omega_g t - \frac{2}{3}\pi\right) \\ U \cos\left(\omega_g t - \frac{4}{3}\pi\right) \end{bmatrix} \quad (5.29)$$

The voltage vector across the grid connection impedance is denoted ( $\underline{U}$ ) and the converter voltage vector ( $\underline{U}_{conv}$ ). These voltage vectors are related by equation (5.30), which may also be expressed in  $abc$  format (5.31). This analysis neglects the bus line reactance which would be present in a real application. This would provide an additional filtering effect,

improving waveform quality. This was omitted as there is a need to guarantee waveform quality at the point of coupling to the bus. This safeguards against equipment connected in close proximity to the converter receiving a poor quality supply.

$$\underline{U}_L = \underline{U}_J + \underline{U}_{conv} \quad (5.30)$$

$$\begin{bmatrix} U_{La} \\ U_{Lb} \\ U_{Lc} \end{bmatrix} = R \begin{bmatrix} i_a \\ i_b \\ i_c \end{bmatrix} + L \frac{d}{dt} \begin{bmatrix} i_a \\ i_b \\ i_c \end{bmatrix} + \begin{bmatrix} U_{conva} \\ U_{convb} \\ U_{convc} \end{bmatrix} \quad (5.31)$$

For the reasons outlined earlier it is preferable to keep all variables in the dq domain to simplify control. When (5.31), is transformed into the dq domain equation (5.32) is formed.

$$\begin{bmatrix} U_{Ld} \\ U_{Lq} \end{bmatrix} = \begin{bmatrix} R & -\omega_g L \\ \omega_g L & R \end{bmatrix} \begin{bmatrix} i_d \\ i_q \end{bmatrix} + \begin{bmatrix} L & 0 \\ 0 & L \end{bmatrix} \frac{d}{dt} \begin{bmatrix} i_d \\ i_q \end{bmatrix} + \begin{bmatrix} U_{convd} \\ U_{convq} \end{bmatrix} \quad (5.32)$$

It is customary to assume that the R component of the grid impedance reactors is negligible, as the voltage drop across R is normally small compared to that across the inductance [5.14]. Also if the angle used in the dq transformation is correctly aligned with the grid's electrical angle ( $\theta_e$ ), then  $U_{Lq}$  will be zero. Making these two assumptions, equation (5.32) becomes (5.33).

$$\begin{bmatrix} U_{Ld} \\ 0 \end{bmatrix} = \begin{bmatrix} 0 & -\omega_g L \\ \omega_g L & 0 \end{bmatrix} \begin{bmatrix} i_d \\ i_q \end{bmatrix} + \begin{bmatrix} L & 0 \\ 0 & L \end{bmatrix} \frac{d}{dt} \begin{bmatrix} i_d \\ i_q \end{bmatrix} + \begin{bmatrix} U_{convd} \\ U_{convq} \end{bmatrix} \quad (5.33)$$

The real ( $P_{real}$ ) and reactive ( $P_{reactive}$ ) powers delivered to the grid connected inverter may now be calculated using (5.34) and (5.35) respectively.

$$P_{real} = Re[\underline{U}_L \cdot \underline{I}] = U_{Lq} i_q + U_{Ld} i_d = U_{Ld} i_d \quad (5.34)$$

$$P_{reactive} = Im[\underline{U}_L \cdot \underline{I}] = U_{Lq} i_d - U_{Ld} i_q = U_{Ld} i_q \quad (5.35)$$

It is apparent from equations (5.34) and (5.35), that to ensure operation at unity power factor (i.e.  $P_{reactive} \approx 0$ ),  $i_q$  must be minimised. The rectifier controller in starting mode must therefore determine what voltage vector to produce at the converter output ( $\underline{U}_{conv} = U_{convd} + jvU_{convq}$ ) to minimise  $i_q$  and regulate  $V_{dc}$  using  $i_d$ .

Similarly to the motor controller, the coupled nature of the dq domain control system can be seen in equation (5.33). The  $d$  component of  $\underline{U}_l$  is partially dependant on  $i_q$ , and the  $q$  component of  $\underline{U}_l$  is partially dependant on  $i_d$ . To decouple the two current control loops  $\Delta U_{convd}$  (5.36) and  $\Delta U_{convq}$  (5.37) are added to  $U_{convd}$  and  $U_{convq}$  respectively in equation (5.33) [5.15]. The decoupled control loop to calculate  $U_{convd}$  and  $U_{convq}$  is shown in Figure 5-9.

$$\Delta U_{convd} = U_{Ld} + \omega_g L i_q \quad (5.36)$$

$$\Delta U_{convq} = -\omega_g L i_d \quad (5.37)$$

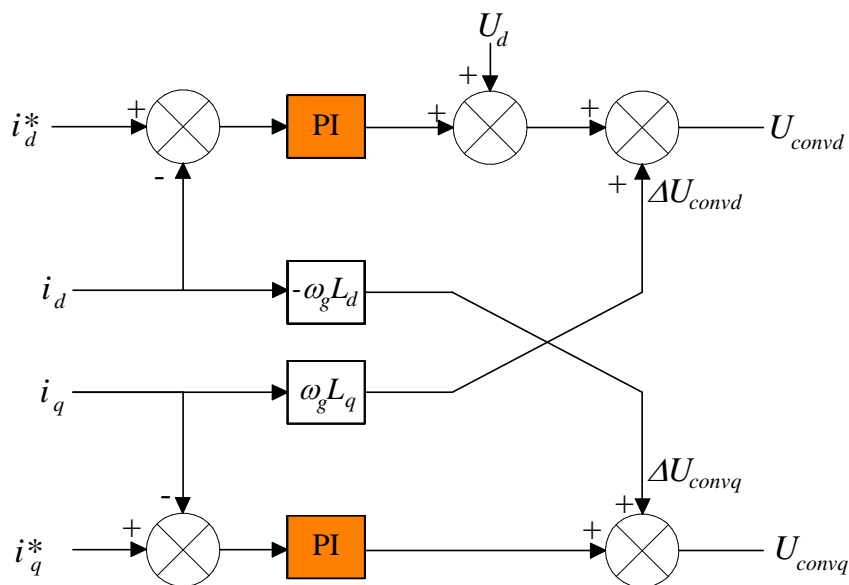


**Figure 5-9: Decoupled AFE controller.**

This DQ domain based controller relies on accurate measurements of  $i_d$  and  $i_q$ . The transformation requires the grid electrical angle ( $\theta_g$ ), which is obtained using a software based Phase Locked Loop (PLL) (Figure 5-10). The input to the PLL is  $\underline{U}_l$ , and this is measured using three voltage transducers at the grid connection. This arrangement functions well assuming a balanced three-phase grid with minimal distortion [5.16,5.17]. The grid is assumed ideal in this chapter so that a functioning system may be demonstrated. Chapter 8 discusses the modifications necessary to deal with distorted grid conditions such as that found on an aerospace AC bus.

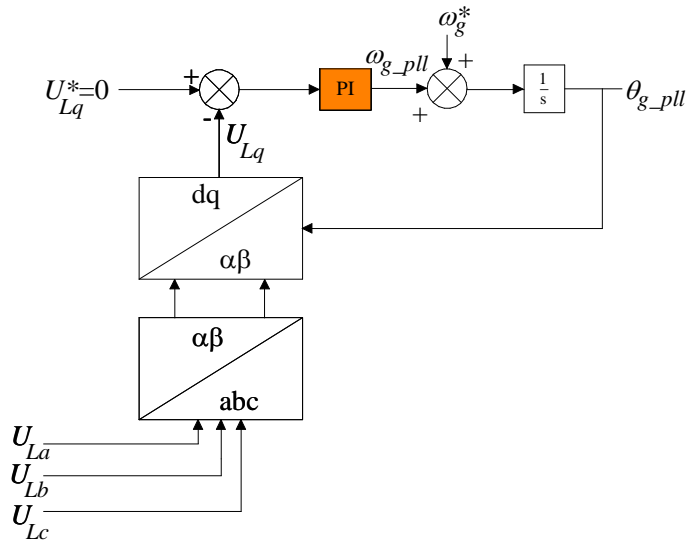


Figure 5-10: Three-phase, software based PLL.

In a basic three-phase PLL (shown in figure 5-10),  $\underline{U}_L$  is transformed first into the  $\alpha\beta$  domain then the dq domain. Assuming that ‘lock’ has been achieved,  $U_d$  and  $U_q$  will be DC values. The angular output of the PLL ( $\theta_{g\_pll}$ ) will be considered locked and in phase with the grid angle when  $U_q$  is zero [5.17]. The  $U_q$  error is calculated, then a PI controller is used to adjust  $\omega_{g\_pll}$  to bring the PLL into lock with  $\omega_g$ , therefore forcing  $U_q$  to zero. An integrator is then used to convert  $\omega_{g\_pll}$  into  $\theta_{g\_pll}$ , which is then fed back as the angular input to the dq transformation.

A block diagram of the AFE’s controller during starting mode is provided in Figure 5-11. It is similar to the controller used for the inverter, with the only major differences being the calculation of  $i_d^*$  and  $i_q^*$  and the measurement of the electrical angle.

Three voltage transducers are used to measure  $\underline{U}_L$ , these measurements are then passed to the PLL loop to determine the grid electrical angle. The grid line current measurements are obtained using three current transducers and then passed along with the grid electrical angle to the dq transformation block to calculate  $i_d$  and  $i_q$ . As discussed earlier, to ensure operation at unity power factor the reactive power is minimised using a current loop and setting  $i_q^*$  to zero. A voltage control loop is used to produce  $i_d^*$  ensuring that  $V_{dc}$  is regulated. The current control loops error outputs are then passed to the rectifier

decoupling network discussed earlier. An identical SVPWM algorithm to that in the inverter's controller is then used to determine the switch gate signals.

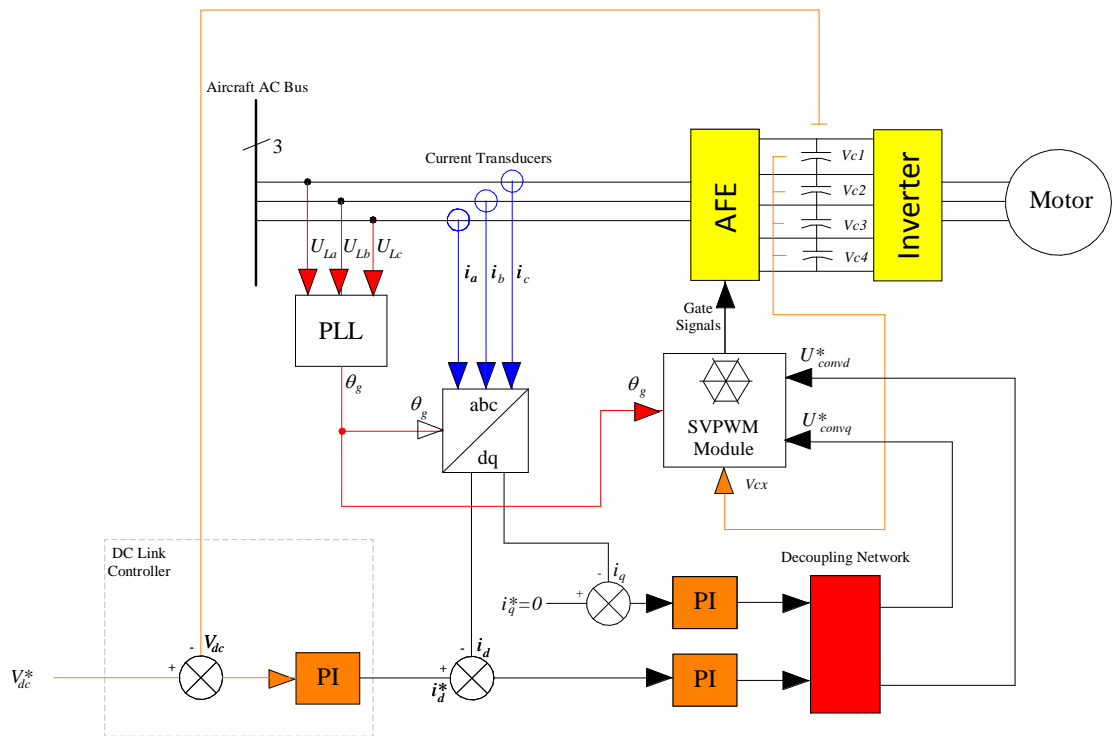


Figure 5-11: AFE controller during starting mode.

The controller of the AFE during generation mode is shown in Figure 5-12. The only difference between this and the controller used in starting mode is the calculation of  $i_d^*$ . Instead of controlling the DC link voltage,  $i_d^*$  is now used to regulate the flow of real power back into the aircraft's distribution bus. In this case the real power currently being supplied to the grid is obtained by feeding  $i_d$  and  $U_d$  into a power calculator block. This is compared against a reference power ( $P_{real}^*$ ), to produce an error which is turned into  $i_d^*$  using a PI block. This method would be appropriate if the outputs of multiple generators were fed onto the same transmission bus. A central control unit would therefore be required to produce power demand values for each generator to ensure the bus voltage remained stable.

A central control unit would therefore be required to produce power demand values for each generator to ensure the bus voltage remained stable. In future engines with multiple shaft generation, this unit may dictate the power removed from each shaft dependent

upon the flight cycle, or measured engine parameters such as velocity or temperature. Droop control would also be an alternative method to provide power sharing between multiple generation sources connected upon different shafts and supplying a common bus. However at present there is no paralleling of generation sources upon aircraft electrical systems.

If this system was applied in a situation with only one generator upon the bus, the real power control loop would need to be replaced with a voltage control loop. This would regulate  $i_d^*$  to ensure that  $\underline{U}_L$  remained within the limits of the power quality standards regardless of the electrical loading upon the distribution bus.

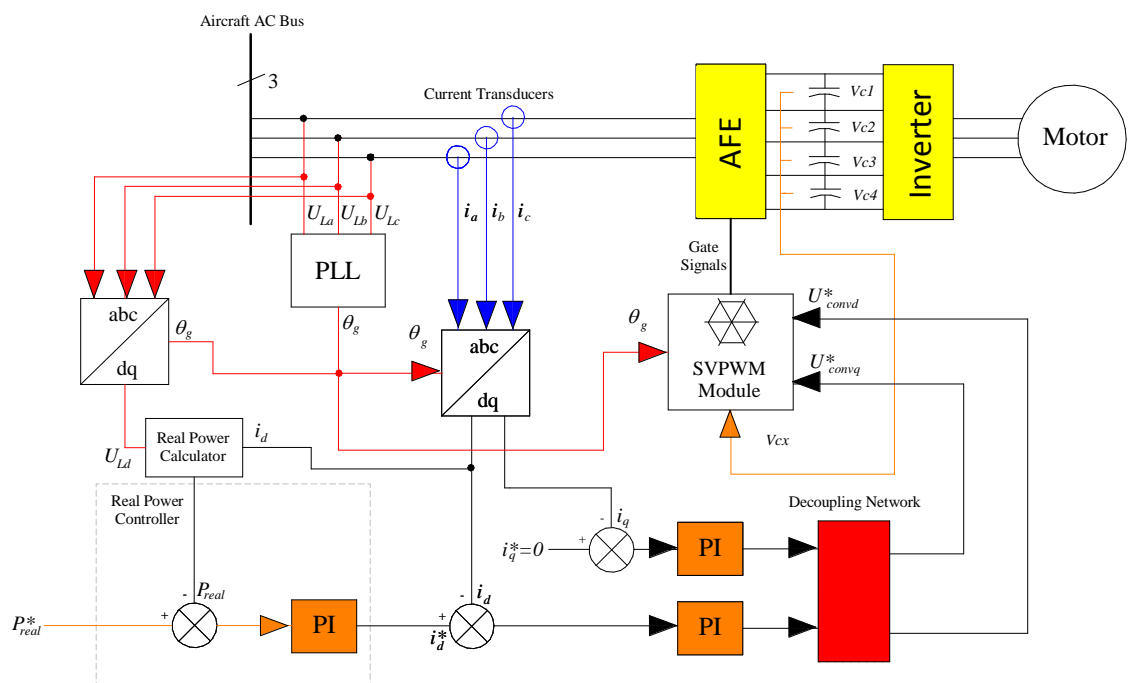


Figure 5-12: AFE controller during generation mode.

### 5.3 Test Setup

Thorough testing is essential to the efficacy of the proposed system. A brief review has therefore been conducted into how similar studies in the same field evaluated their designs. Much of the work published upon aerospace S/G systems relates to the machine design [5.18,5.19,5.20]. In these studies the designs were not generally subjected to a rigorous system test. Instead the prototype machine's performance was evaluated in starting mode and again in generating mode, with both tests conducted in isolation. The

authors of [5.18,5.19,5.20] have also tended to place more emphasis on tests highlighting performance, such as determining the maximum torque as a function of machine speed or efficiency as a function of stator current. Such limited testing is appropriate for a machine design project, as the authors attempt to show the incremental performance gain exhibited by the novel design described. However, a more extensive testing regime is required here as this study is focused on how the multilevel converter may be incorporated into the S/G system. System level tests must therefore be conducted presenting the converter's operation across a range of operating points.

To provide realistic comparisons it is desirable to mechanically load the S/G in a manner similar to the loading a gas turbine would place upon it during the operating cycle. The author of [5.13] undertook a study, looking into the testing of a complete embedded S/G system for a small Unmanned Air Vehicle (UAV). Both dynamometer and engine testing results are provided in the manuscript. The dynamometer controller is configured to produce an "assist-resist" curve. Here the dynamometer initially appears as a mechanical load, 'breaking' the S/G. Once the dynamometer has reached engine idle speed the dynamometer accelerates up to the engine maximum operation speed.

An approach similar to [5.13] was taken in this study using a dynamometer since it was not feasible to retro fit a S/G to a gas turbine and then conduct testing using fuel. The purpose of the dynamometer is to mimic the torque-speed characteristics produced by the turbine as seen by the S/G at the point of coupling. The dynamometer will therefore have two distinct modes of operation; starting and generating with a transition period between them.

The laboratory test cell in which all rotating machinery is contained is shown in Figure 5-13. A brushed DC, wound field machine dynamometer is used and is driven by a 75kW, four quadrant [5.21] Control Techniques DC drive. The dynamometer drive is controlled by a remote PC using a LabView program (Figure 5-14) (Appendix B). If an embedded system was being considered with the high rotational speeds, a brushed DC machine would not be appropriate due to the speed limitation imposed by the brushes.



Figure 5-13: Test cell.

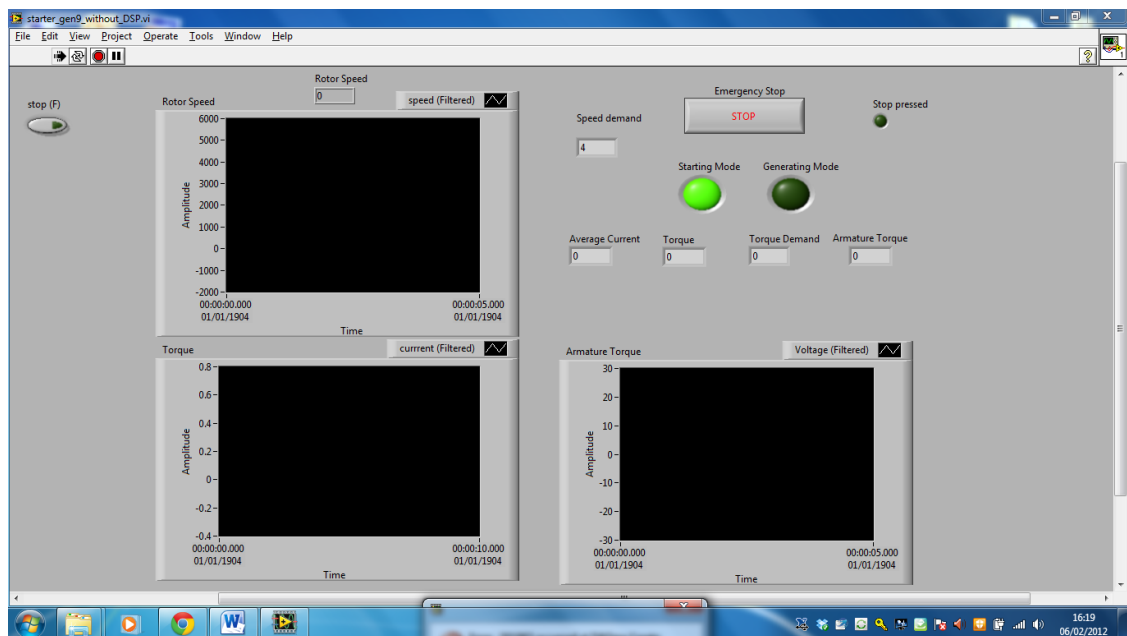


Figure 5-14: LabView control program panel.

A block diagram of the test rig is shown in Figure 5-15. The drive uses a rotary encoder to determine the dynamometer speed ( $\omega$ ) and by measuring the current, estimates the torque being produced at the S/G coupling. The torque is estimated based on the known brushed DC machine torque constant. This data is used by the MENTOR's internal speed controller and also is sent to the LabView controller using a National Instruments (NI) data acquisition card. Using this data the control program determines the mode of operation (starting or generating) then calculates a torque or speed demand. Demand signals are

then sent back to the MENTOR drive via the NI card. A detailed description of the control algorithm is now provided with each mode discussed separately.

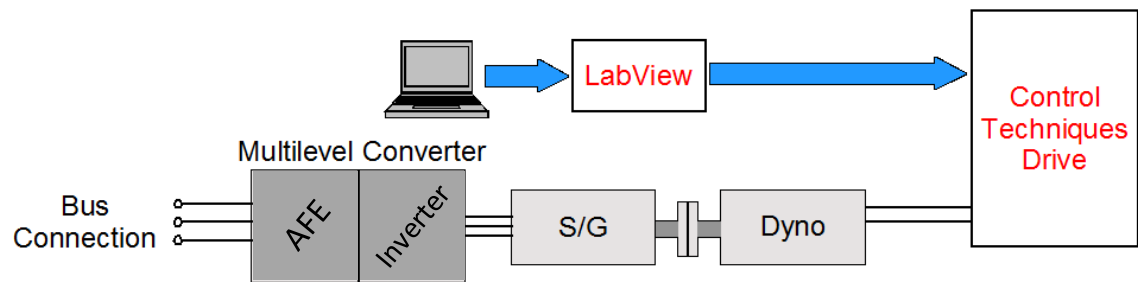


Figure 5-15: Block diagram of test rig.

In the absence of a programmable three-phase regenerative bench top supply it was necessary to connect the AFE to the utility network. A transformer was used to step down the utility voltage to the standard aerospace 115  $V_{line-line}$ . Whilst this arrangement resulted in a substantial reduction in  $\omega_g$  from 400 Hz to 50 Hz, it does not change the operating principle of the AFE's controller and therefore the results obtained are considered valid. One disadvantage of this test setup was the high level of distortion and unbalance upon the utility voltage waveform.

### Starting Mode Control

In starting mode the dynamometer is required to replicate the torque produced by the turbine as it is accelerated from standstill to the engine ignition speed ( $\omega_{idle}$ ) by the S/G. The LabView controller must therefore monitor the dynamometer speed and by using a model of the torque-speed characteristics of a turbine calculate the effective loading torque. The torque demand is then sent to the MENTOR drive for implementation.

In this study the engine during starting mode is modelled as a fan load with some additional friction coefficients. This is a considerable simplification, for instance a two spooled engine has both high (HP) and low pressure (LP) shafts both rotating at different speeds. Although they are not mechanically coupled together the exhaust gases from the HP compressor are used to rotate the LP shaft [5.22]. The relationship between engine shaft speed and the mechanical input torque from the S/G is therefore likely to be much more complex. This level of complexity is not considered necessary in this study. Taking

into account such detail would have no effect upon the operating principle of the S/G system it would simply affect the electrical sizing if this technology was to be adopted for real world application. The aim was to produce a simple S/G testing rig to allow full system testing to occur. However using a similar setup engine manufacturers could improve the realism of the test greatly by entering real engine data gained experimentally into the LabView controller. The assembled hardware should therefore be of use to future S/G projects.

In the dynamometer controller the torque-speed characteristics of the engine are simplified to a polynomial (5.38). Here  $k_f$ ,  $k_v$ ,  $k_c$  and  $k_s$  represent the fan, viscous friction, coulomb friction and sticktion constants respectively.

The relationship is plotted in Figure 5-16. Here the torque is assumed to be negative when opposed to the direction of rotation. This convention is used throughout this study.

$$T(\omega) = k_f \omega^2 + k_v \omega + k_c + k_s e^{-\tau \omega} \quad (5.38)$$

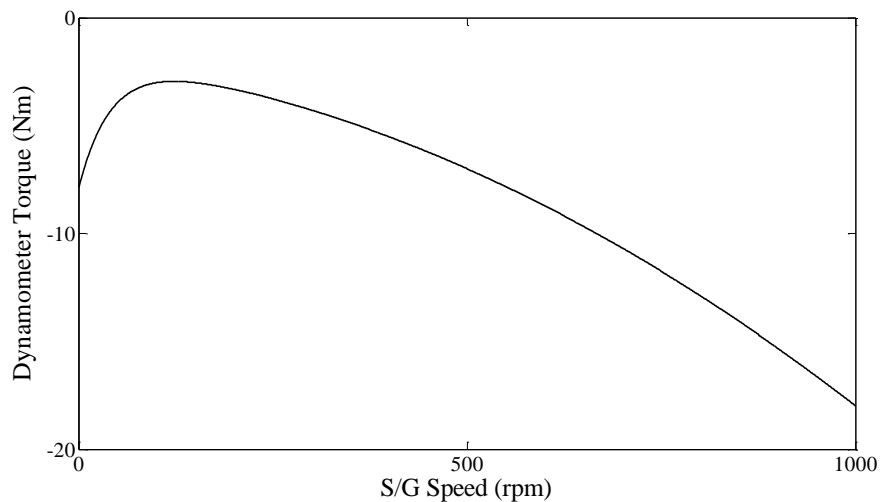


**Figure 5-16: Torque-speed profile of dynamometer during starting mode.**

As well as controlling the dynamometer the LabView program is used for all data logging. Example data channels that are logged include dynamometer speed and the  $I_d$  and  $I_q$  components for both the grid and machine connected inverters. This data is used for report generation and further converter performance analysis.

Upon achieving a speed of  $\omega_i$  the dynamometer begins to linearly reduce the loading of the S/G in accordance with an engine accelerating under a mixture of torque from the S/G and that produced by combustion as discussed in Section 2 [5.13]. This process continues with the torque eventually turning positive (indicating a shift in dynamometer operation from the fourth to the first quadrant), until the dynamometer has reached  $\omega_{idle}$ . The complete starting mode (standstill to  $\omega_{idle}$ ) torque-speed profile can be seen in Figure 5-17.

### Generating Mode Control

The dynamometer accelerates from  $\omega_{idle}$  to  $\omega_c$  in accordance with an engine being throttled for flight. The dynamometer has a maximum operation speed of approximately 5000 rpm due to the brushed DC machine topology. As has been discussed in Section 2 the operating speed of future S/Gs will depend on which shaft they are mounted to and whether the design is embedded or gearbox driven. This speed restriction may therefore represent a realistic operating speed or a scaled down laboratory test dependant on the intended S/G's application in the engine.

In generating mode the dynamometer swaps from torque control mode to speed control. The LabView controller sets the speed demand and allows the Control Techniques drive's internal speed controller to operate. The drive is programmed to maintain a constant speed in accordance with the speed demand signal irrespective of the electrical loading from the S/G. This is representative of a S/G operating cycle as the loading placed upon an engine by its generator is normally small compared to the mechanical loading caused by thrust production. The generator therefore has a negligible effect upon the engine speed. The complete dynamometer torque-speed profile for the whole test is shown in Figure 5-17.

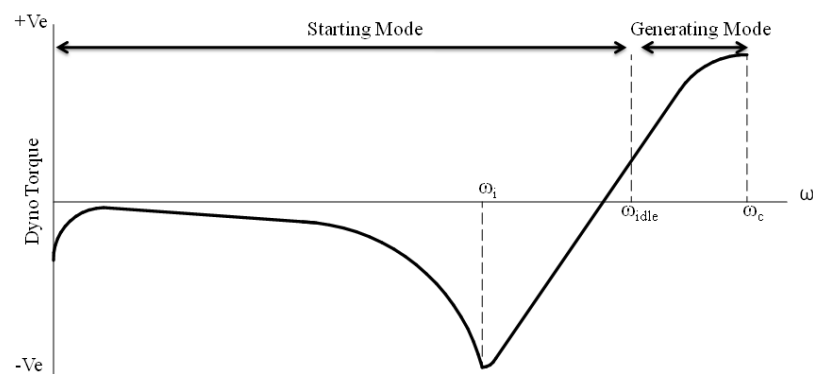


Figure 5-17: Complete dynamometer torque speed profile.

The LabView controller may also be configured to add speed perturbations upon  $\omega_c$  throughout the generating mode. This is in accordance with the varying engine shaft speed that would be expected due to engine throttling or in flight turning. Such variations in shaft speed would be passed directly to the S/G speed unless a CSD was used [5.23].

### 5.3.1 PM S/G Test Machine

In the absence of an embedded PM generator a conventional PMSM is instead used as the test S/G. The machine can be seen in Figure 5-13 and its parameters are given in Table 5-1.

Machine Parameter	Value
Rated Power	45 kW
Maximum Speed	5000 rpm
Pole Pairs	5
$L_q$	180 $\mu$ H
$L_d$	150 $\mu$ H
$k_E$	0.55 V/rad/s
$k_T$	0.83 Nm/A

Table 5-1: PMSM parameters.

## 5.4 Experimental Results

A description of the prototype converter and controller used to provide all experimental data in this study is provided in Appendix A. With a functioning power converter prototype, control system, test machine and dynamometer testing of the system could now be undertaken. The results obtained during the testing process are now presented.

### 5.4.1 Initial Testing Results

Converter performance was initially assessed in each mode separately, with starting mode being examined first. The AFE's controller maintained a constant DC link whilst the inverter drove the S/G at a defined speed. The dynamometer maintained a constant mechanical loading upon the S/G. Testing was conducted across a range of machine speeds, Figure 5-18 shows the current waveforms at a machine speed of approximately 650 rpm.

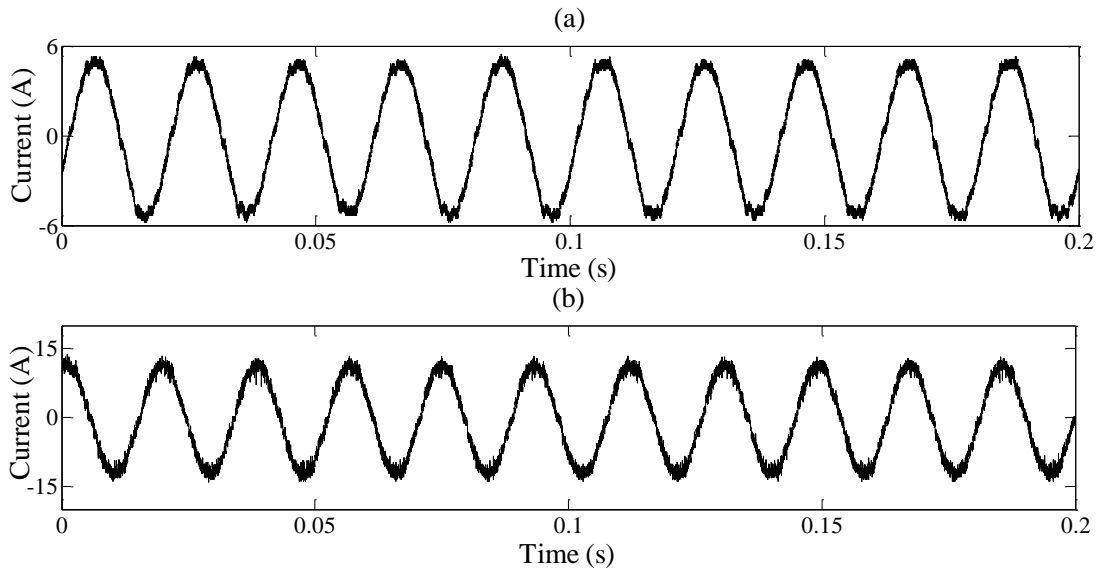


**Figure 5-18: Starting mode current waveforms (a) AFE, (b) Inverter.**

To assess performance in generation mode the dynamometer rotated the S/G at a constant defined speed, whilst the AFE regenerated current into the mains networks. This procedure was repeated across a range of speeds. Figure 5-19 provides example waveforms for both inverters. In this test the S/G was rotated at approximately 2500 rpm whilst the AFE drove 5 A<sub>rms</sub> into the grid. Note the change in time base between Figure 5-19 (a) and (b). This was necessary due to the high electrical frequency of the machine.

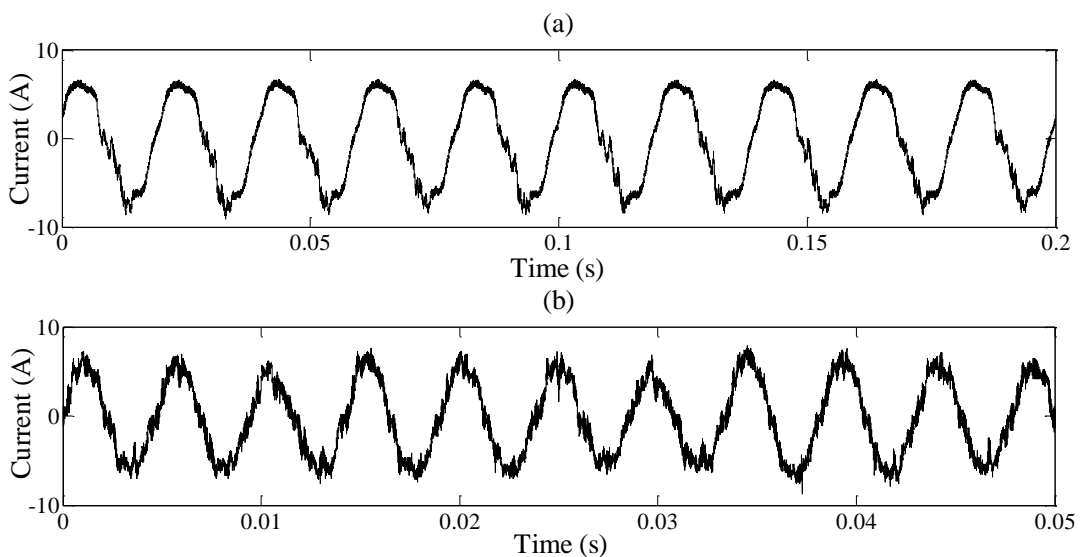


**Figure 5-19: Generating mode waveforms (a) AFE, (b) Inverter.**

As discussed in Section 2, in the case of an embedded S/G or a mechanical coupling which does not feature a CSD, the generator speed would be expected to vary with the turbines shaft speed. Assuming the S/G is a PMSM the back-emf varies with the speed. During generation mode, the inverter's controller is therefore expected to adjust the  $I_q$  demand signal as the back-emf varies to ensure the DC link's amplitude remains constant. To assess the converter's performance under varying speed conditions, a test was conducted where the generator speed was oscillated between 2500 and 3000 rpm with a period of approximately 200s. During the test the AFE drove 5 Arms into the utility terminal to ensure the converter was loaded. This is aimed at emulating an aircraft performing repeated in-flight turns. Both the generator speed and the DC link amplitude were logged and the results are presented in Figure 5-20. It is apparent from this figure that the converter's controller is working as required, ensuring the DC link remains at a constant 350 V.

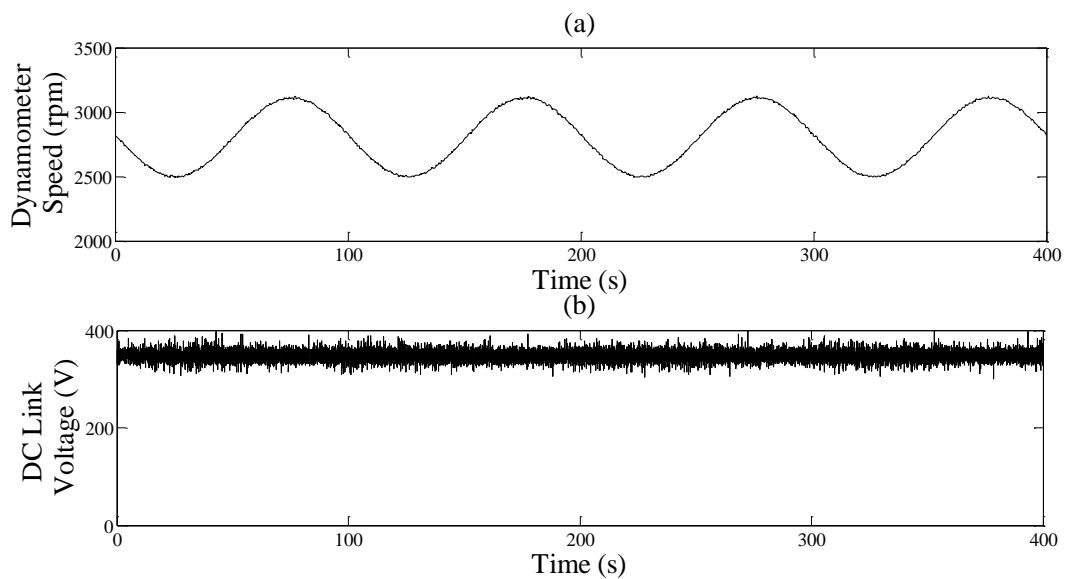


Figure 5-20: DC link under fluctuating machine speed conditions.

#### 5.4.2 Full System Testing

Having demonstrated the converter performance in each mode separately, a full system test could be undertaken. The dynamometer was operated using a torque-speed profile shown in Figure 5-17 and described in Section 5.3. Waveforms showing the dynamometer speed, dynamometer torque and the AFE and the inverter current components are provided in Figure 5-21. The dq current components were fed out of the DSP using a DAC.

This data was then logged by the LabView alongside other important signals such as dynamometer torque and speed.

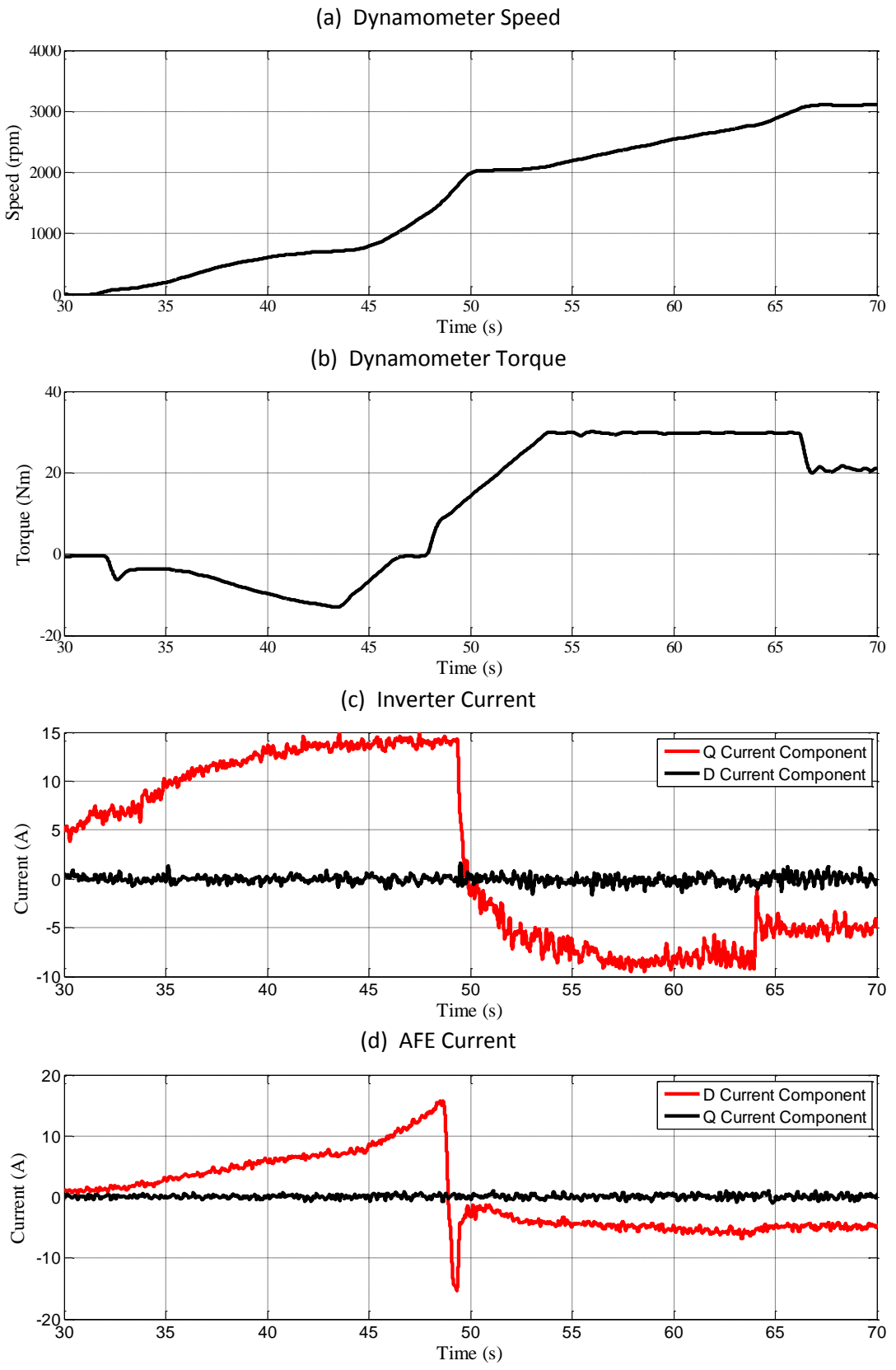


Figure 5-21: Complete test waveforms.

Based on the values of  $k_f$ ,  $k_v$ ,  $k_c$  and  $k_s$  that were selected it was necessary for the inverter to produce an  $I_q$  of  $15A_{rms}$  to accelerate the S/G up to  $\omega_i$  (= 700 rpm). This is apparent from Figure 5-21 (a) and (c), where the speed and Q current component of the inverter are shown. The torque applied by the dynamometer throughout the test is shown in Figure 5-21 (b). Upon reaching  $\omega_i$  the dynamometer linearly reduces its loading of the S/G, allowing it to accelerate up to  $\omega_{idle}$  (= 1800 rpm). At  $\omega_{idle}$  the inverter reverses the polarity of the Q current component, stopping to contribute torque for driving the S/G, instead drawing a substantial current (Figure 5-21 (c)) from the S/G to supply the DC link. This is necessary as the AFE is now driving power into the AC bus (Figure 10 (d)). The converter has therefore reversed the direction of electrical power flow. Just before  $\omega \approx \omega_{idle}$  the dynamometer makes the transition from fourth to first quadrant operation. Shortly after reaching  $\omega_{idle}$  the dynamometer accelerates towards  $\omega_c$ . Throughout this region ( $\omega_{idle}$  to  $\omega_c$ ) the AFE continues to drive current into the utility.

A blip can be seen in the dynamometer torque profile (Figure 5-21 (b)) at approximately 47 seconds. This was due to a dynamometer control limitation. To avoid ringing deadtime is imposed upon the dynamometer drive output when making transitions between operating quadrants. This results in the brief period of zero torque as the dynamometer changes the torque polarity from negative to positive. This does not compromise the performance of the converter, it simply increases the test duration.

Throughout the test the inverter maintains  $I_d$  at 0 A, as discussed earlier this reduces the losses in the S/G and is possible as the speed is so low that field weakening is not required. Conversely, the AFE ensures that  $I_q$  is minimised throughout the test guarantying operation at unity power factor.

## 5.5 Conclusion

This chapter has demonstrated how a back-to-back connected multilevel inverter can be used to drive a PMSM in an aerospace S/G system. The multilevel converter topology was adopted in this application to minimise the distortion in the current. This allows a reduction in the passive filtering at the grid connection. At the machine side, the stator winding inductance is used as the sole source of filtering therefore no additional inductance is used.

It was important to demonstrate system operation with a PMSM as this is one of the most likely machine topology candidates for use in future aerospace S/G systems. This is due to the high power density and rugged rotor structure when compared to WFSMs. The PMSM fixed back EMF constant presented a challenge for the converter due to the fluctuating voltage at the machine terminals. It has been proven experimentally how the converter during generation mode is capable of taking a variable amplitude input from the machine and producing a stable DC link. This ensures that variation in voltage at the machine side does not have an effect on the supply at the grid terminals.

To produce substantive results a dynamometer based test rig was assembled. The dynamometer was controlled to mechanically load the S/G in a similar manner to that which an engine would in real application. This enabled realistic testing to be conducted upon the system.

The converter was initially subjected to testing where performance under starting and generating mode were assessed in isolation. In starting mode the converter drove the S/G as a motor which was mechanically loaded by the dynamometer. In generating mode the converter drew electrical power from the S/G to maintain the DC link which was used to supply power at the grid connection.

The converter was then subjected to an extensive system test using the utility network as the supply. The converter initially drew current from the utility to accelerate the S/G. Once the S/G had reached engine idle speed power flow was reversed and energy driven into the utility to supply bus connected loads. The transition between the two modes was conducted in a controlled manner which is essential to avoid compromising the integrity of the supply.

Experimentation was also conducted when the machine speed was oscillating, whilst the converter drove a fixed amount of power into the utility connection. It was important that the converter demonstrated satisfactory performance under these conditions for two reasons; firstly it demonstrates the converter's ability to function under oscillating engine speed conditions which would be expected during flight, secondly it provides a good test of the performance of the converter in synchronising the electrical outputs of multiple generators onto a common distribution bus. This is likely to become a more pressing issue

in future aircraft electrical architectures as manufacturers seek to synchronise the outputs of multiple generators connected to different engine shafts.

## 5.6 References

- [5.1] R. Williams, D. A. Stone, M. P. Foster, S. R. Minshull, "Back-to-Back Connected Multilevel Converters for Aerospace Starter-Generator Applications," Power Conversion Intelligent Motion Conference, Nuremburg, Germany
- [5.2] "Field Orientated Control of 3-Phase AC-Motors," Texas Instruments Application Note, BPRA073, 1998.
- [5.3] P. Vas, "Sensorless Vector and Direct Torque Control," Oxford Science Publications, 1998.
- [5.4] P. Pillay, R. Krishnan, "Modelling, Simulation and Analysis of Permanent-Magnet Drives, Part I: The Permanent-Magnet Synchronous Motor Drive," IEEE Trans. Industry Applications, Vol. 25, No. 2, pp. 265-273.
- [5.5] P. Wipasuramonton, "Current and Sensorless Control Strategies for PM Brushless AC Drives Using a Low-Cost DSP," Ph.D. Dissertation, University of Sheffield, 2006.
- [5.6] N. Bianchi, T. M. Jahns, "Design, Analysis and Control of Interior PM Synchronous Machines," IEEE Industry Applications Society, 2004.
- [5.7] T. M. Jahns, G. B. Kliman, T. W. Neumann, "Interior Permanent-Magnet Synchronous Motors for Adjustable-Speed Drives," IEEE Trans. Industry Applications, Vol. 22, No. 4, pp. 738-747, 1986.
- [5.8] M. Chinchilla, S. Arnaltes, J. C. Burgos, "Control of Permanent-Magnet Generators Applied to Variable-Speed Wind-Energy Systems Connected to the Grid," IEEE Trans. Energy Conversion, Vol. 21, No. 1, pp. 130-135, 2006.
- [5.9] Z. Xu, D. Zhang, F. Wang, D. Boroyevich, "Unified Control for the Permanent Magnet Generator and Rectifier System," Applied Power Electronics Conference and Exposition, Fort Worth, USA, pp. 1888-1895, 2011.

- [5.10] M. H. Bierhoff, F. W. Fuchs, "Semiconductor Losses in Voltage Source and Current Source IGBT Converters Based on Analytical Derivation," Annual IEEE Power Electronics Specialists Conference, Aachen, Germany, pp. 2836-2842, 2004.
- [5.11] C. Mademlis, I. Kioskeridis, N. Margaris, "Optimal Efficiency Control Strategy for Interior Permanent Magnet Synchronous Motor Drives," IEEE Trans. Energy Conversion, Vol. 19, No. 4, pp. 715-723, 2004.
- [5.12] S. Morimoto, Y. Tong, Y. Takeda, T. Hirasa, "Loss Minimization Control of Permanent Magnet Synchronous Motor Drives," IEEE Trans. Industrial Electronics, Vol. 41, No. 5, pp. 511-517, 1994.
- [5.13] B. S. Bhangu, K. Rajashekara, "Control Strategy for Electric Starter Generators Embedded in Gas Turbine Engine for Aerospace Applications," Energy Conversion Congress and Exposition, Phoenix, USA, 2011, pp. 1461-1467.
- [5.14] M. Malinowdki, "Sensorless Control Strategies for Three-Phase PWM Rectifiers," Ph.D. Dissertation, Warsaw University of Technology, 2001.
- [5.15] B. Kwon, J. Youm, J. Lim, "A Line-Voltage-Sensorless Synchronous Rectifier," IEEE Trans. Power Electronics, Vol. 14, No. 5, pp. 966-972, 1999.
- [5.16] X. Ren-Zhong, L. Fei, "Study on the Three-Phase Software Phase-Locked Loop Based on D-Q Transformation," Asia-Pacific Power and Energy Engineering Conference, Chengdu, China, pp. 1-4, 2010.
- [5.17] P. Rodriguez, J. Pou, J. Bergas, "Decoupled Double Synchronous Reference Frame PLL for Power Converters Control," IEEE Trans. Power Electronics, Vol. 22, No. 2, pp. 584-592, 2007.
- [5.18] S. R. Jones, B. T. Drager, "Performance of a High Speed Switched Reluctance Starter/Generator System using Electronic Position Sensing," Industry Applications Society, Orlando, Florida, pp. 249-253, 1995.

- [5.19] C. A. Ferreira, S. R. Jones, W. S. Heglund, W. D. Jones, "Detailed Design of a 30-kW Switched Reluctance Starter/Generator System for a Gas Turbine Engine Application," IEEE Trans. Industry Applications, Vol. 31, No. 3, pp. 553-561, 1995.
- [5.20] E. Richter, C. Ferreira, "Performance Evaluation of a 250 kW Switched Reluctance Starter Generator", Industry Applications Society, Orlando, Florida, 434-440, 1995.
- [5.21] Control Techniques, "MENTOR II User Guide," [www.controltechniques.com](http://www.controltechniques.com): Control Techniques Drives Ltd, 2006.
- [5.22] Ronald D. Flack, "Fundamentals of Jet Propulsion with Applications," Cambridge University Press, 2005.
- [5.23] M. J. Provost, "The More Electric Aero-Engine: A General Overview from an Engine Manufacturer," Power Electronics Machines and Drives Conference, Bath, UK, 2002, pp. 246-251.

# 6 Utilisation of Wound Field Synchronous Machines

## 6.1 Introduction

The work described in this chapter was published in [6.1].

This chapter explores how the back-to-back connected multilevel converter which was demonstrated in Chapter 5 may be applied to a WFSM. This is an important area as the WFSM is the industry norm for aerospace generators [6.2] owing to the ease with which the back-EMF may be regulated and the high fault tolerance when compared to PMSM. In addition to generator applications, the WFSM topology has been used as the all-electric S/G in first generation, large civil engines. For instance a 250 kW WFSM is used as the S/G in Rolls-Royce's Trent 1000 and GE's GEnX engines [6.3]. For the system proposed in this thesis to be considered relevant, performance must therefore be demonstrated in conjunction with a WFSM.

There is limited published work on utilising a WFSM as a S/G. In [6.4] the author investigates the control of the machines exciter winding using an FPGA. The voltage at the machine terminals is measured and then compared to a reference voltage signal. The calculated error is passed as the demand signal to the controller of an inverter connected across the exciter winding. This feedback loop ensures that the machine terminal voltage is maintained at the desired level despite load fluctuations. This works novel contribution is therefore performing the task of the GCU using an FPGA. No consideration is given to controlling the excitation during starting mode.

There has been increased interest in the sensorless operation of WFSM S/Gs [6.2,6.5]. The removal of the position sensor is prioritised to reduce complexity and improve overall system reliability. These studies only focus on the control during starting mode, with the main challenge being resolving the machines rotor angle at low speeds in order to achieve full torque from standstill. If manufacturers persist with the frequency wild distribution

architecture deployed upon the A380 and B787, the power converter will only be attached to the generator during starting mode and therefore rotor position information will only be required during this period. At the commencement of generating mode, the machine terminals are connected directly to the distribution bus.

This chapter's primary contribution is therefore demonstrating the application of a multilevel converter with a WFSM in an aerospace S/G application. This study is the first to investigate how a multilevel converter and WFSM may be integrated together to form a functioning S/G system. Also this study is the first to demonstrate experimentally a full WFSM S/G system test in a laboratory.

This chapter is organised as follows:

The proposed system is initially discussed, with attention being paid to where the power converter would fit into the aircraft's distribution network. This includes a comparison of the generation and distribution network employed on older civil aircraft and modern aircraft such as the A380 and B787.

The excitation required by a WFSM in order that it may be used as a S/G is then examined. In starting mode, excitation is optimised to maximise the torque constant of the machine, whilst in generation mode, the emphasis is on producing a stable output at the machine terminals. The excitation algorithm developed may then be applied throughout testing.

The WFSM is then subjected to a similar testing program to that adopted with the PM machine discussed in Chapter 5. Results are presented illustrating performance in starting and generating mode in isolation. The findings from a full system test are then provided, where the WFSM was taken from standstill to maximum engine speed.

Conclusions are then drawn on the performance of the hardware and the contributions and implications of the work described in this chapter.

## **6.2 System Development**

A near identical vector controller to that employed in the PMSM, was used to obtain the experimental results documented in this chapter. A cross-section of the rotor of a non-

salient WFSM is provided in Figure 6-1. This shows the relationship between the rotor-mounted field windings and the DQ axis.

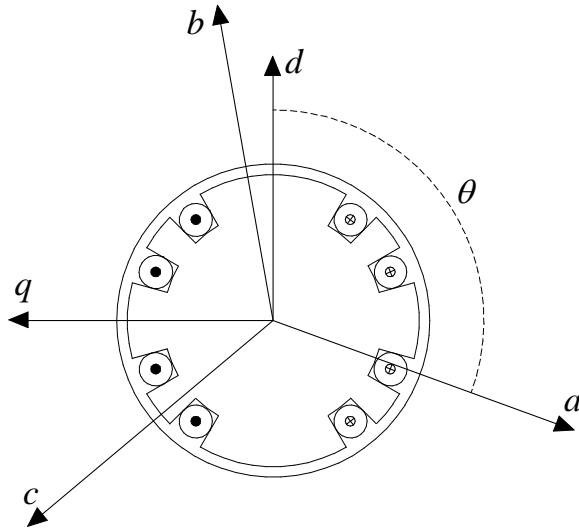


Figure 6-1: WFSM rotor.

The torque developed by a WFSM is calculated using (6.1), where  $L_{md}$  and  $i'_{fd}$  is the d component of the mutual inductance and the field current referred to the stator [6.7]. Torque can therefore be controlled using both  $i_q$  and  $i'_{fd}$ .

$$T_e = \frac{3}{2}p[L_{md}i'_{fd}]i_q \quad (6.1)$$

In Section 6.3.1 the excitation conditions which result in the maximum value of  $i'_{fd}$  and therefore maximises  $T_e$  for a given level of  $i_q$  is investigated. This means that the same maximum torque per ampere control strategy employed with the PM machine, may be used here with the WFSM.

In Section 6.3.2 the excitation is examined to determine how  $i'_{fd}$  may be used to control the back-emf. By adjusting  $i'_{fd}$  as a function of machine speed, the need for field weakening control in the converter can be avoided and the same generating mode control strategy developed for the PM machine may be used with the WFSM, whereby the emphasis is on minimising converter losses.

The location of the S/G converter within the aircraft power system must be considered. Using a WFSM as a S/G presents the option of keeping the converter connected between the machine and grid terminals permanently or alternatively disconnecting the converter once starting mode has been completed. This is not possible with a PMSM as the voltage at the terminals fluctuates with machine speed and electrical loading. Whereas the voltage at the terminals of a WFSM may be controlled using the exciter. Both converter placement options have associated benefits and disadvantages which are now discussed.

Figure 6-2 shows the system configuration necessary to include the electric start option utilising a WFSM whilst continuing to distribute the 400 Hz, 115 V<sub>line-line</sub> used on all large civil aircraft with the exception of the A380 and B787. The power converter is connected between the machine and grid terminals. In starting mode power is drawn from the APU generator and used to accelerate the engine. In generating mode the APU is disconnected from the distribution bus using BTBs. The converter draws electrical power from the S/G, this is then placed onto the distribution bus to supply electrical loads.

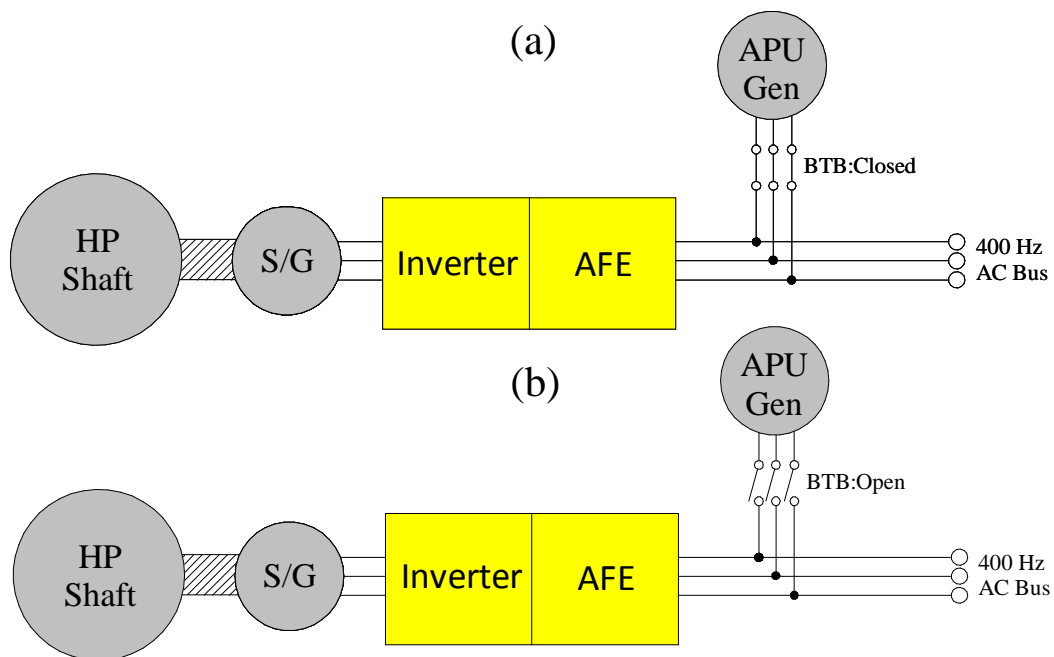


Figure 6-2: Fixed frequency S/G system (a) Starting mode, (b) Generating mode.

The disadvantage of this system is that the converter must be highly rated as all the aircraft's electrical power requirements must be supplied by it. The effect of the converter upon the aircraft's electrical reliability must also be considered if this technology was to be

applied in the real world. A fault in the converter would lead to the disruption of the distribution bus. BTBs could be used to minimise this risk facilitating the isolation of the faulty converter and the connection of the output of a functioning power converter to the disrupted bus.

The connection of the power converter between machine and grid terminals enables frequency wild generation whilst still distributing a fixed frequency, fixed amplitude supply to the aircraft's electrical loads. This has some benefits when compared to the frequency wild distribution system used in B787 for reasons which are discussed shortly.

An alternative S/G arrangement is shown in Figure 6-3. This is the system employed on the Rolls-Royce Trent 1000 when fitted in the B787. An inverter is fed from the aircraft's DC distribution bus. During starting mode BTBs connect the inverter to the S/G's terminals. The inverter then drives the S/G accelerating the engine towards idle. Upon reaching idle, the BTBs disconnect the inverter from the S/G. The S/G then operates in generating mode producing a frequency wild output that is distributed around the aircraft.

Once the engine has been started, the inverter is connected using BTBs to a second motor. This motor is used to drive the air conditioning compressor [6.7]. The sharing of the inverter between systems gives a weight saving which is beneficial to manufacturers. It also increases the electrical system reliability as during flight the distribution network is connected directly to the machine terminals. The reliability of the power converter therefore has a greatly reduced influence on the reliability of the overall electrical system when compared to the system shown in Figure 6-2.

As was discussed in Section 2 the major advantage of this arrangement is that the CSD is no longer required. This provides a weight saving and increases reliability. One major drawback is that all bus connected electrical loads must have their front ends adapted to accommodate the frequency wild variable amplitude supply. This may give a substantial weight gain when compared to the fixed frequency case.

The other disadvantage of the system shown in Figure 6-3 is that it does not facilitate the coupling of multiple generation sources upon the same bus. This would compromise the use of multiple embedded generators within the same engine. The system discussed earlier

and shown in Figure 6-2 provides easy paralleling of generation sources assuming each generator is connected to a dedicated power converter.

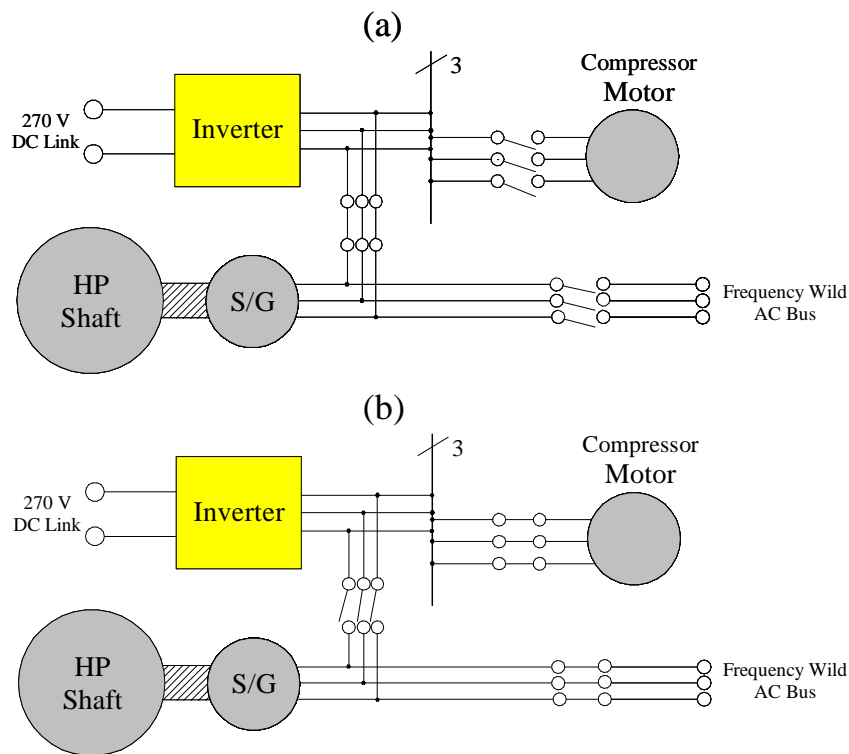


**Figure 6-3: Trent 1000 S/G system (a) Starting mode, (b) Generating mode.**

This thesis only considers the configuration shown in Figure 6-2. This is due to the reasons outlined earlier; easy paralleling of multiple electrical sources, compatibility with existing electrical loads and the possible removal of the CSD. A third alternative has been proposed in the literature whereby all aircraft electrical power is distributed using high voltage DC. The adoption of this technology would require a radical change in the existing aircraft electrical architecture and is considered beyond the scope of this thesis.

### 6.3 Exciter Mapping

As discussed in Section II, a WFSM generator must have an external excitation source to induce an electrical output upon the stator. To use a WFSM as a S/G the GCU must be replaced with a more sophisticated unit to supply differing excitation dependant on machine speed and operating mode. The excitation for each mode is investigated separately to determine the optimal conditions.

Testing was conducted upon a Lucas Aerospace 50 kW WFSM (Figure 6-4). This machine was removed from a Rolls-Royce Artouste engine (Figure 6-5). With the generator being from an engine this ensures an extremely realistic test for the proposed system. The generator was connected to the engine using a gearbox with a ratio of approximately 6 to 1 ensuring the generator operates at it's rated speed of 6000 rpm when the engine was at it's governed normal operating speed of 35,000 rpm.

Utilising this machine provides a tough challenge for the power converter, as it was never designed for operation as a motor. The torque constant at starting mode speeds is low even with maximum excitation. Table 6-1 provides the electrical parameters.

The stator winding inductance is also very low in comparison to the PMSM discussed in Section 5. This is because the WFSM was designed for a generator application whereas the PMSM was designed for use as a motor. This therefore provides a greater challenge to the multilevel converter to keep the stator current waveform distortion within acceptable limits in order to ensure the stable operation of the drive.

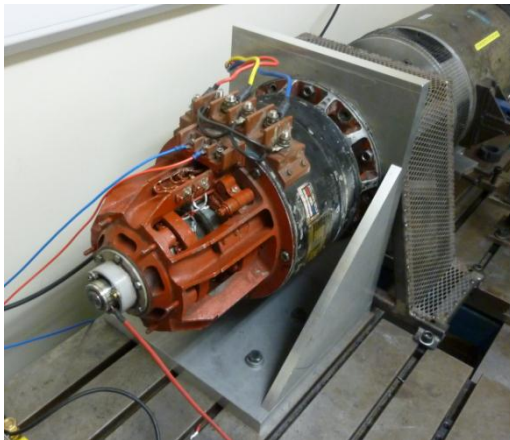


**Figure 6-4: WFSM mounted to dynamometer.**



Figure 6-5: Rolls-Royce Artouste engine.

Parameter	Value
Rated Power	50 kW
Rated Speed	6000 rpm
Pole Pairs	4
Stator Synchronous Inductance	36 $\mu$ H
Stator Winding Resistance	300 m $\Omega$
Exciter Winding Inductance	12 mH
Exciter Winding Resistance	3.3 $\Omega$

Table 6-1: WFSM electrical parameters.

At points during subsequent experimentation a low frequency harmonic appeared upon the stator current waveform of the WFSM. Upon investigation it was found that one phase of the machine has a significantly lower synchronous inductance than the other two, which were measured at the value provided in Table 6-1. The abnormal phase having a synchronous reactance of approximately two thirds of the stated value in Table 6-1. The author has come to the conclusion that the difference in inductance is probably due to an inter-winding short, which will unfortunately mean that the back-emf of that phase is also reduced compared to the other two phases. This would mean that the machine appears as an unbalanced load, which is problematic from an inverter control perspective. This would explain why a low frequency component appears in the stator current waveform, which occurs at around a quarter of the frequency of the fundamental. As there was no possibility

of obtaining a second WFSM machine it was decided to continue with testing, despite the high level of distortion that was resulted from using a damaged machine.

### 6.3.1 Excitation During Starting Mode

Normally WFSMs have a low torque constant when compared to similarly rated PM synchronous machines as the flux produced by the field winding is small compared to a PM rotor. It is therefore essential to determine the optimum excitation to make the best of the achievable torque.

Ordinarily the GCU produces a DC output relying on the relative motion between the exciter and rotor mounted windings to induce the field current. If the established aerospace WFSM is to be used as a S/G it must be capable of accelerating from standstill to  $\omega_i$ . At standstill the rotor is stationary and there is therefore no relative motion to induce a field current. To determine the speed below which DC excitation becomes ineffective the dynamometer was used to rotate the WFSM at constant speed, whilst measuring the torque produced at the point of coupling. Throughout this process a constant stator current of 10 A<sub>rms</sub> was maintained. The Torque Constant ( $T_c$ ) of the WFSM at various speeds is plotted in Figure 6-6.

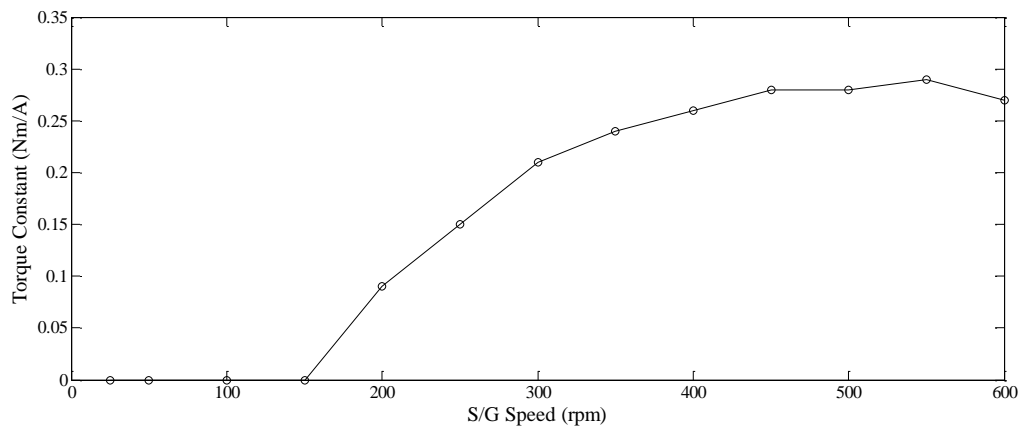
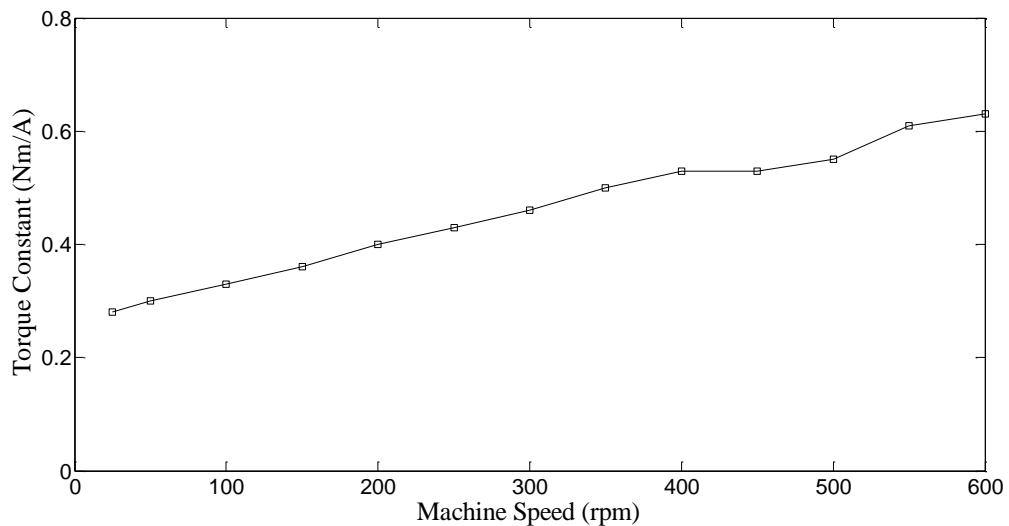


Figure 6-6: WFSM  $T_c$  under DC excitation.

No torque is produced until the WFSM has reached 150 rpm. However the  $T_c$  produced at this speed is minimal ( $< 0.05$  Nm/A). As the machine accelerates the  $T_c$  increases, reaching a plateau of 0.27 Nm/A at 450 rpm

To overcome this problem it is necessary to use an AC excitation source during starting mode. A bench top AC supply was used which is controlled by the LabView controller via a serial connection. This ensures a field current is always induced upon the rotor. To highlight this, the procedure used to generate Figure 6-6 was repeated using a 100 Hz excitation source. Due to the high impedance of the winding at 100 Hz, a 3.5 A<sub>rms</sub> excitation current was used. The results are presented in Figure 6-7.



**Figure 6-7: WFSM T<sub>c</sub> under AC excitation.**

The AC excitation has increased the T<sub>c</sub> across the speed range considerably despite the reduced excitation current. Due to a dynamometer limitation, testing could not be achieved below 25 rpm. At 25 rpm DC excitation achieved no torque whilst when using AC excitation a T<sub>c</sub> of 0.3 Nm/A resulted.

The optimum excitation frequency varies dependant on the machines speed. It is necessary to determine this relationship so that the GCU can adjust the excitation throughout the system test. The procedure used to produce Figure 6-7 was repeated but this time across the speed range 25-1000 rpm. At each speed the excitation frequency was varied between DC and 400 Hz and T<sub>c</sub> recorded. The results are plotted in Figure 6-8.

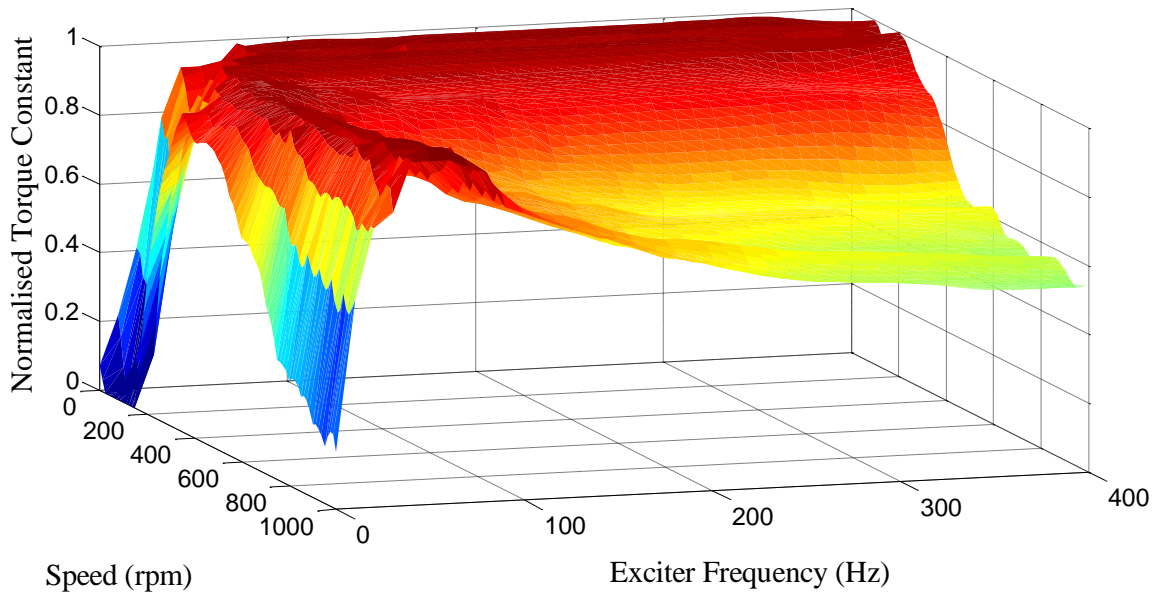


Figure 6-8: Torque Constant as a function of excitation and speed.

From the data depicted in Figure 6-8 it was possible to determine the optimum exciter frequency at each speed. These points are plotted as “Experimental Data” in Figure 6-9.

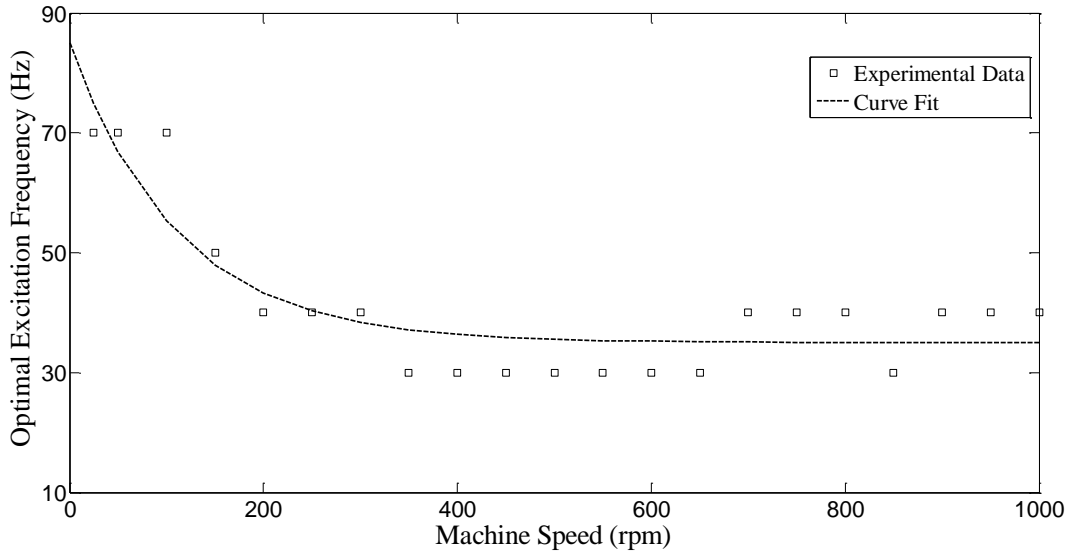


Figure 6-9: Optimum excitation frequency.

A function could then be fitted to these points which may be implemented in the GCU. Equation (6.1) was found to match the points well where  $F$  and  $\omega$  represent the optimum

frequency in Hz and the machine speed in rpm respectively. In Figure 6-9, (6.1) is also plotted so it's correlation with the experimental data can be seen.

$$F(\omega) = 50e^{-0.009\omega} + 35 \quad (6.1)$$

### 6.3.2 Excitation During Generating Mode

Once the S/G has entered generating mode, the machine will have speeded up to and beyond  $\omega_{idle}$  ( $\approx 1000$  rpm in this study), so DC excitation may be used. The field current can be adjusted to maintain a constant back-emf regardless of fluctuations in machine speed and load current. A phase back-EMF of 80 Vrms was selected as it corresponded well with the 300 V DC link, ensuring that the inverter operated in boost mode which increases converter stability.

The back-EMF is plotted in Figure 6-10 as a function of excitation current and machine speed. Saturation occurs above 8 A so it is unnecessary to test above this.

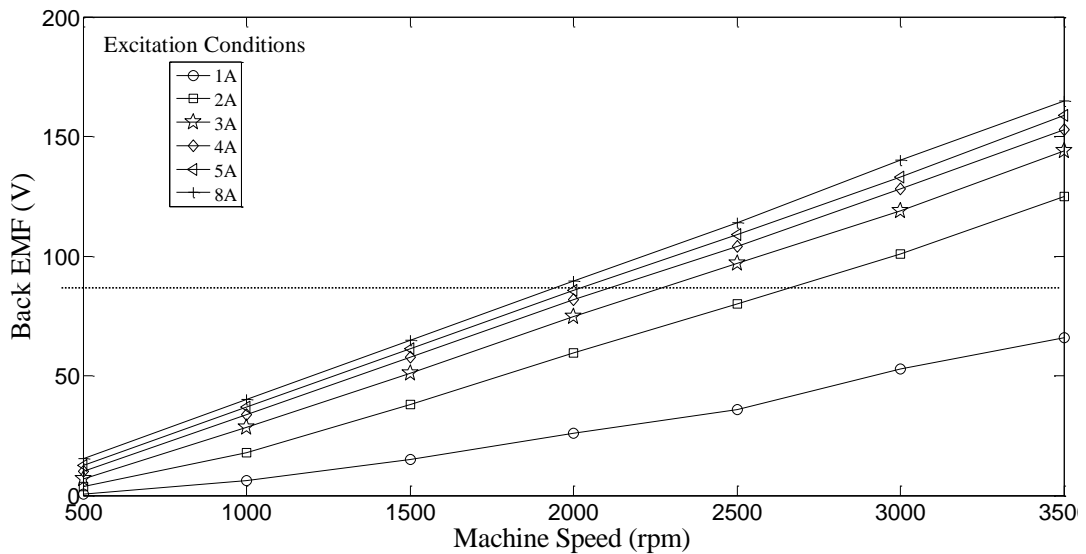


Figure 6-10: Measured back-EMF as excitation and machine speed vary.

During hardware testing, once the starting process had finished the dynamometer accelerated from  $\omega_{idle}$  up to 2500 rpm. Throughout this period a substantial current was driven into the utility network. It was found necessary to set the excitation to a constant 8 A to avoid the DC link collapsing. This is to be expected as the machine is being operated well below the nominal speed. If testing at higher speeds it is likely that the excitation

would have to be linearly reduced with the increasing back-emf to keep the converter in boost mode.

## 6.4 Test Setup

The test setup is very similar to that used with the PMSM in the previous chapter. Owing to the machine's low torque constant, the frictional parameters used during starting mode were lowered, the machine was therefore required to produce reduced amounts of torque to accelerate the S/G to  $\omega_{idle}$ . In addition to calculating the speed and torque demands for the dynamometer, the LabView controller is also tasked with calculating the optimum excitation based upon the analysis in Section 6.3. The optimum excitation is then sent to a power amplifier connected across the S/G exciter winding. This approach negates the need for a purpose-built GCU. The LabView control program used in this chapter is included in Appendix C. A block diagram of the test rig used in this chapter is provided in Figure 6-11.

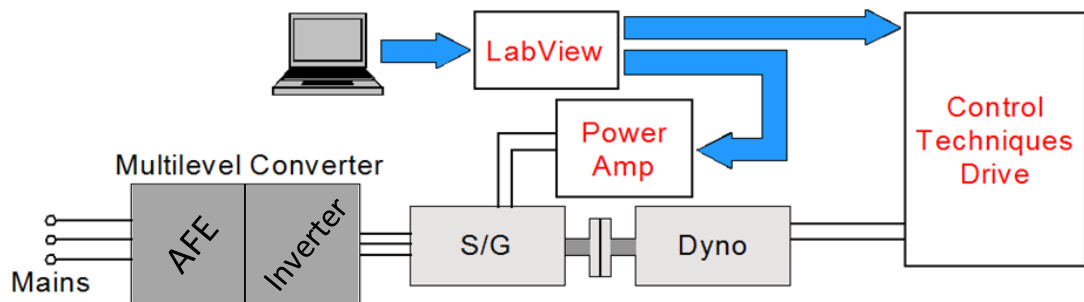
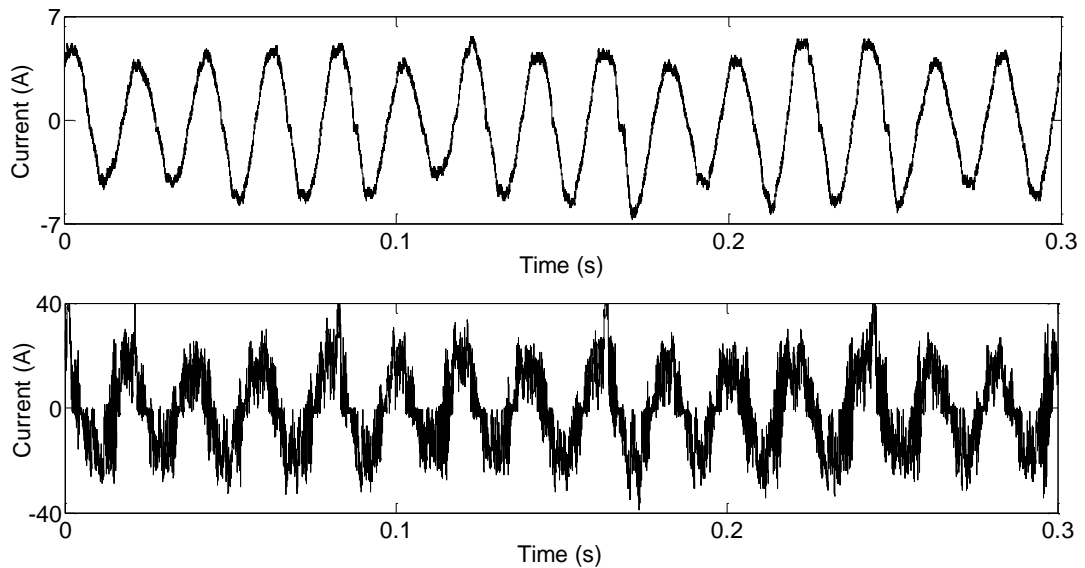


Figure 6-11: Experimental test setup.

## 6.5 Results

In starting mode the power converter drove the S/G whilst it was mechanically loaded by the dynamometer. The dynamometer operated with a torque speed profile similar to that used with the PMSM in Chapter 5. As a 400 Hz regenerative supply was not available the utility network was used to represent the aircraft's AC bus. This was connected to the AFE terminals. The results are presented in Figure 6-12.



**Figure 6-12: Starting mode waveforms, Upper waveform- AFE, Lower waveform- Inverter.**

The converter functioned correctly; the AFE maintained a constant DC link whilst the inverter drove the machine to the required speed. The lower waveform exhibits the high levels of current ripple expected from a low inductance machine.

The results of generation mode testing are now presented. Upon reaching  $\omega_{idle}$  (set to 700 rpm), the dynamometer accelerated up to  $\omega_c$ . Throughout this process the AFE drove approximately 5 A<sub>rms</sub> into the AC bus. Current waveforms are provided in Figure 6-13. The upper plot shows the current flowing into the utility network and the lower shows the current drawn from the S/G to maintain the DC link.

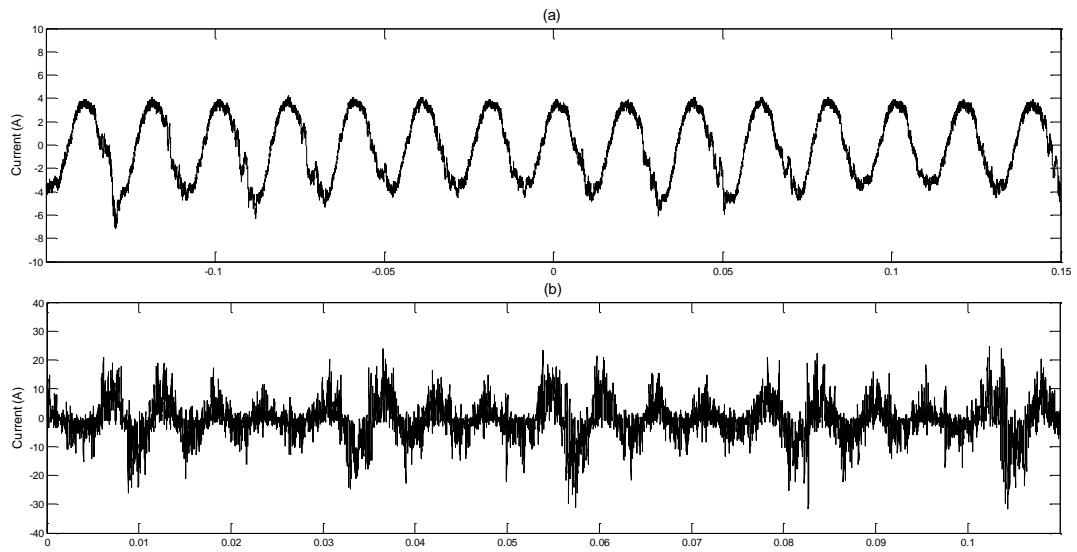
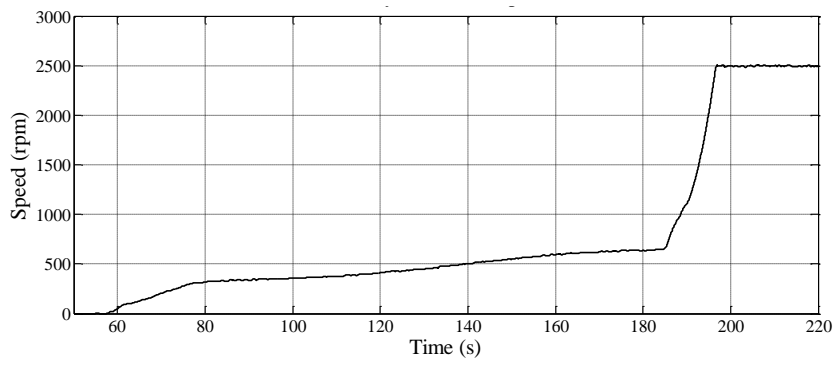


**Figure 6-13: Generating mode waveforms (a) AFE, (b) Inverter.**

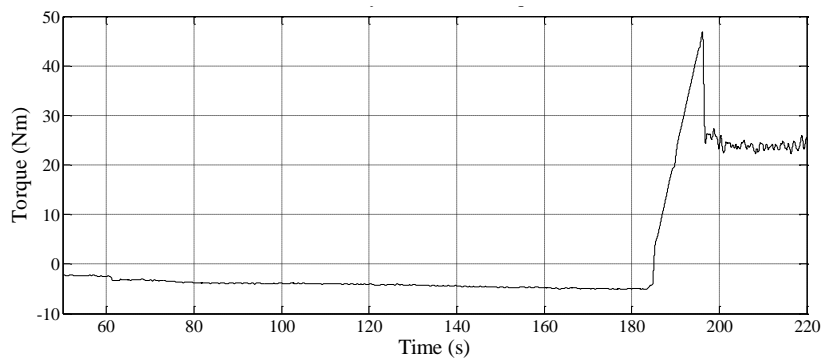
Testing in generation mode was successful; the inverter produced a stable DC link at the required amplitude with all levels balanced whilst the AFE regenerated current into the utility network.

With the converter functioning in both modes of operation, a full system test could be conducted.. The test takes the WFSM from standstill to  $\omega_c$ . The results are presented in Figure 6-14.

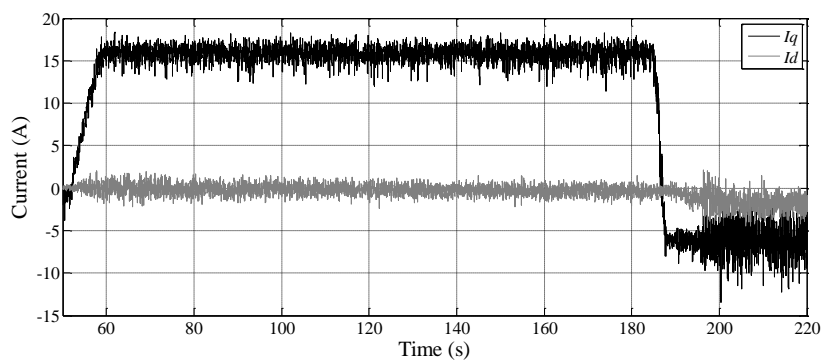
(a) Dynamometer Speed



(b) Dynamometer Torque



(c) Inverter Current



(d) AFE Current

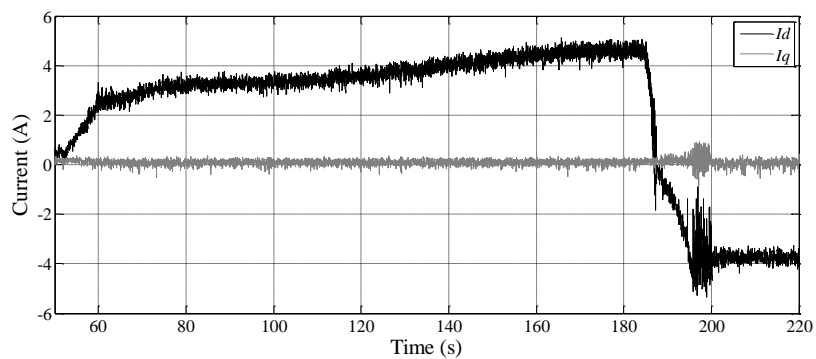


Figure 6-14: Full S/G profile testing.

In this test  $\omega_{idle}$  was set to 650 rpm. The values of  $k_f, k_v, k_c$  and  $k_s$  selected in the dynamometer controller requires the inverter to produce an  $I_q$  of  $15A_{rms}$  to accelerate the WFSM up to  $\omega_{idle}$ . This is apparent from the dynamometer speed (Figure 6-14 (a)) and the inverter's current (Figure 6-14 (c)) plots. During starting mode the utility connected AFE linearly increases  $I_d$  as the WFSM accelerates. This is to be expected as the stator current remains constant ( $15A_{rms}$ ) throughout the test but the back-emf increases linearly with speed. Therefore the electrical power supplied to the WFSM is increasing with speed. The AFE must therefore draw an increasing current from the utility network to supply the inverter.

Upon the WFSM achieving a speed of  $\omega_{idle}$ , the inverter's  $I_q$  and the AFE's  $I_d$  both reverse polarity. This indicates the transition between starting and generating mode as the converter reverses electrical power flow. Throughout the test the AFE's  $I_q$  and the inverter's  $I_d$  components are maintained at zero. As discussed in Chapter 5 this ensures the inverter operates with maximum torque per ampere, whilst the AFE appears as a unity power factor load.

The torque produced by the dynamometer throughout the test is shown in Figure 6-14 (b). Between standstill and  $\omega_{idle}$  the torque is negative as it loads the WFSM; upon reaching  $\omega_{idle}$  the torque becomes highly positive as it starts to accelerate the WFSM towards  $\omega_c$ , reminiscent of a turbine after ignition being throttled for takeoff. Upon reaching  $\omega_c$  the torque of the dynamometer is modulated to maintain a constant speed.

Throughout the test both controllers functioned well ensuring the DC link was maintained at the specified level with all levels balanced.

## 6.6 Conclusion

This chapter has demonstrated how a back-to-back connected multilevel inverter can be used to drive an aerospace WFSM in a S/G system. The multilevel converter topology was adopted in this application to minimise the distortion in the current waveform. This reduces the THD at the grid connection, which will aid the compliance with power quality standards. At the machine side, the stator winding inductance is used as the sole source of filtering therefore no additional inductance is used. Additional inductance would reduce the power factor of the machine, increasing the size of the machine and the converter.

It was important to demonstrate system operation with a WFSM as this the industry standard machine topology for use in aerospace generator applications due to the easy control of the voltage at the machine terminals and high fault tolerance. It has been proven experimentally how the converter during generation mode is capable of taking a variable amplitude, variable frequency input from the machine and producing a stable DC link. This ensures that variation in voltage at the machine side does not have an effect on the supply at the grid terminals.

To produce substantive results the same dynamometer based test rig assembled for the work documented in Chapter 5 was used. The dynamometer was controlled to mechanically load the S/G in a similar manner to that which an engine would in real application. This enabled realistic testing to be conducted upon the system.

The excitation requirements of the machine were investigated experimentally. In starting mode the excitation necessary to maximise the available torque was examined. This will be essential in a real world application as there is often a need to produce a high level of torque from standstill to overcome the sticktion. In the field this has been found to be especially true when starting the engine in a cold environment as the lubricating oil is at it's most viscous. The optimal exciter source frequency was mapped with regards to torque produced as a function of machine speed. This enables the GCU to adjust the excitation throughout the starting procedure as the engine accelerates.

Once the engine has reached idle speed, the excitation winding is connected to a DC source. The effect of the excitation source DC amplitude upon the voltage seen at the machine terminals was examined experimentally. This means the GCU can adjust the excitation as a function of machine speed and the electrical loading to safeguard the stability of the converter. The starting and generating mode excitation rules were then incorporated into the LabView dynamometer controller, which sends the required excitation to a power amplifier connected across the exciter winding terminals.

The WFSM was subjected to a similar testing regime to that used in Chapter 5. Initially the converter performance under starting and generating mode was assessed in isolation. In starting mode the converter drove the S/G as a motor which was mechanically loaded by the dynamometer. In generating mode the converter drew electrical power from the S/G to maintain the DC link which was used to supply power at the grid connection.

The converter was then subjected to an extensive system test using the utility network as the supply. The converter initially drew current from utility to accelerate the S/G. Once the S/G had reached engine idle speed power flow was reversed and energy driven into the utility to supply bus connected loads. The transition between the two modes was conducted in a controlled manner which is essential to avoid compromising the integrity of the supply.

## 6.7 References

- [6.1] R. H. Williams, D. A. Stone, M. P. Foster, S. R. Minshull, "Utilizing Existing Aircraft Wound Field Generators for Starter-Generators," 8<sup>th</sup> International Conference on Power Electronics, Jeju, South Korea, pp. 691-696, 2011.
- [6.2] A. Maalouf, S. L. Ballois, L. Idkhajine, "Sensorless Control of Brushless Exciter Synchronous Starter Generator Using Extended Kalman Filter," 35<sup>th</sup> Annual Conference on Industrial Electronics, Porto, Portugal, pp. 2581-2586, 2009.
- [6.3] S. Jordan, J. Apsley, "Diode Rectification of Multiphase Synchronous Generators for Aircraft Applications," Energy Conversion Congress and Exposition, Phoenix, USA, pp. 3208-3215, 2011.
- [6.4] A. Maalouf, M. W. Naouar, E. Monmasson, "Digital Control of a Brushless Excitation Synchronous Starter/Generator in the Generation Mode," 34<sup>th</sup> Annual Conference on Industrial Electronics, Orlando, Florida, USA, pp.1155-1160, 2008.
- [6.5] A. Griffo, D. Drury, T. Sawata, P. H. Mellor, "Sensorless Starting of a Wound Field Synchronous Starter/Generator for Aerospace Applications," IEEE Transactions on Industrial Electronics, Accepted for publication June 2009.
- [6.6] A. K. Jain, V. T. Ranganathan, "Modelling and Field Orientated Control of Salient Pole Wound Field Synchronous Machine in Stator Flux Coordinates," IEEE Trans, Industrial Electronics, Vol. 58, No. 3, pp. 960-970, 2011.
- [6.7] "Boeing 787: Hamilton Sundstrand Content," Product Fact Sheet, Hamilton Sundstrand, [www.hamiltonsundstrand.com](http://www.hamiltonsundstrand.com).

# 7 Implementation of Predictive Current Control

## 7.1 Introduction

One of the primary objectives of this study is to investigate how to reduce the harmonic content of a power converters current waveform. So far only possible changes to the converter topology have been considered as a means to reducing the harmonics. It has been demonstrated in the literature, that significant increases in harmonic performance can also be achieved by improving the control strategy.

There is a wide range of different current control techniques that appear in the literature aimed at reducing harmonics in the output waveform. One of the most developed concepts is predictive control. Although predictive control is a broad area most techniques can be grouped into three major classes [7.1, 7.2]; Hysteresis Based Predictive Control, Trajectory Based Predictive Control and Model Predictive Control.

### **Hysteresis Based Predictive Control**

Hysteresis based control in its simplest form, is commonly referred to as the “bang-bang controller,” and is formed using three comparators incorporating a hysteresis band for a three-phase inverter application. Each comparator is tasked with producing the gate signal for one of the inverter phases. If the phase A current  $i_a$  becomes smaller than the reference current  $i_a^*$  by an amount equal to the hysteresis band ( $H$ ), the comparator reacts by selecting the phase A positive switching vector [7.2]. The opposite is true if  $i_a$  is greater than  $i_a^*$  by a margin of  $H$ . This ensures that the actual current always remains within the boundaries of the hysteresis band. A block diagram of a three-phase motor drive utilising a hysteresis current controller is provided in Figure 7-1.

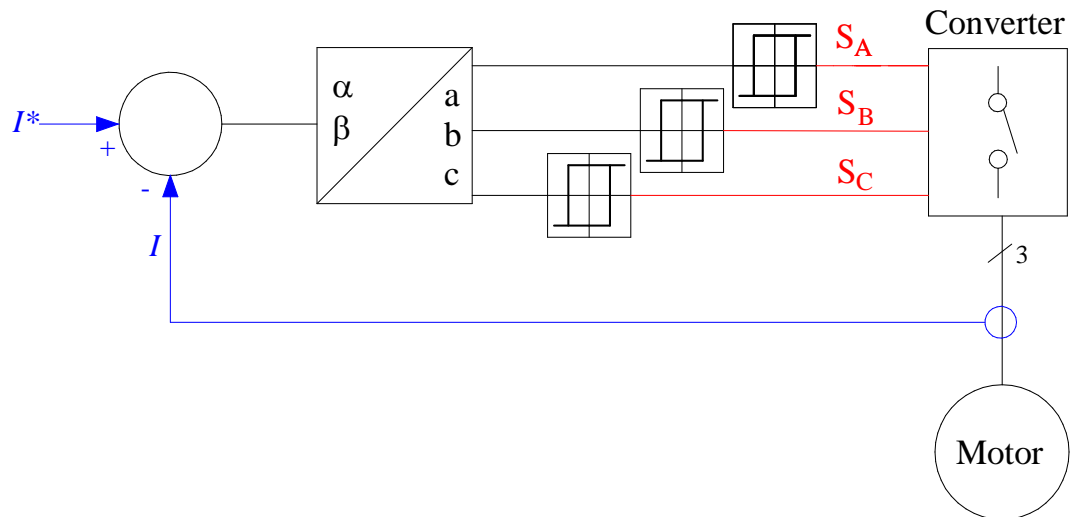


Figure 7-1: Hysteresis controller.

The authors of [7.3] are accredited [7.1,7.4] with performing the first study into adjusting the conventional bang-bang algorithm to incorporate predictive control, to form Hysteresis Based Predictive Control (HBPC). Figure 7-2 [7.1,7.4] highlights the operating principle of HBPC.

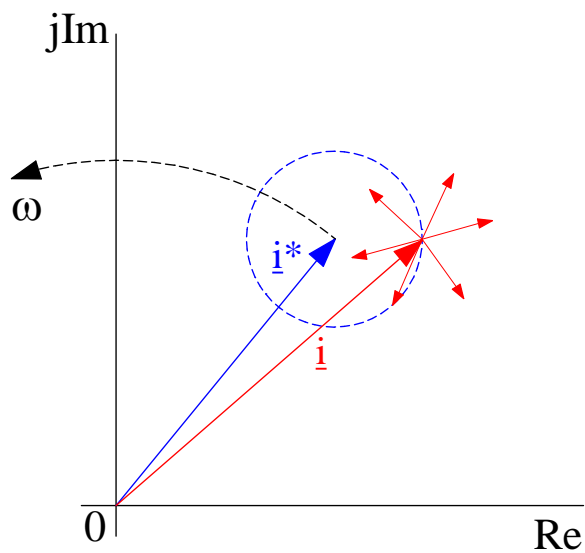


Figure 7-2: Hysteresis control, reference vector and corresponding boundary circle.

The reference current vector  $\underline{i}^*$  is plotted along with its corresponding hysteresis boundary circle upon an Argand diagram. The reference vector rotates around the diagram with a

frequency equal to its fundamental frequency ( $\omega$ ). The objective of the controller is to ensure that the measured current vector ( $\underline{i}$ ), is always located within the boundary circle of  $\underline{i}^*$ . The next switching state is calculated when  $\underline{i}$  touches the boundary circle of  $\underline{i}^*$ . The effect on the trajectory of  $\underline{i}$  is calculated for all possible converter switching states. This is represented in Figure 7-2 by the smaller red arrows emanating from  $\underline{i}$ . A mathematical model of the load is used to produce these predictions. The switching vector that results in  $\underline{i}$  being within the boundary circle of  $\underline{i}^*$  for the longest period is then selected. This minimises the converter switching frequency [7.1,7.3,7.4].

Implementation of HBPC therefore results in a variable switching frequency. A variable switching frequency is problematic as it often results in unpredictable harmonic performance when compared to constant switching frequency systems. It has also been documented that a variable switching frequency may result in unwanted resonant behaviour [7.4].

### **Trajectory Based Predictive Control**

A number of different control algorithms may be classified under the title trajectory based predictive control including Direct Self Control [7.5], Direct Torque Control and Direct Speed Control (DSC) [7.4,7.5]. However it must be noted that many of these methods also share characteristics with hysteresis controllers [7.4]. DSC in a drive application is used as an example to highlight the basic operating principles of trajectory based predictive controllers.

Most power converter controllers such as the Field Orientated Controller (FOC) described in Section 4 utilise separate control loops to regulate the stator current. The motor speed is controlled by an additional control loop “wrapped” round the current controller, which regulates the current demand signal in order to control the speed. Conversely, DSC attempts to directly control speed, by predicting the effect of the converters switching vectors on the motors acceleration [7.4]. At each switching instant the speed is measured and the error calculated. The effect of each switching vector upon the motors speed is then predicted, and the vector that most minimises the error selected.

## Model Predictive Control

Trajectory and hysteresis based predictive controllers only use the current system values to calculate the next switching vector. In contrast, Model Predictive Control (MPC) utilises previous measurements, in order to calculate the optimal switching vector not only for the next cycle, but for future cycles over a defined horizon [7.1,7.7]. At the heart of the MPC algorithm is a discrete-time model of the system to be controlled, this model is evaluated subject to a cost function  $g()$ . The system model can therefore be repeatedly evaluated to determine the switching vector that minimises  $g()$ . Using this technique the optimal switching vector may be determined for implementation in the next cycle. A block diagram of a MPC is provided in Figure 7-3 [7.7].

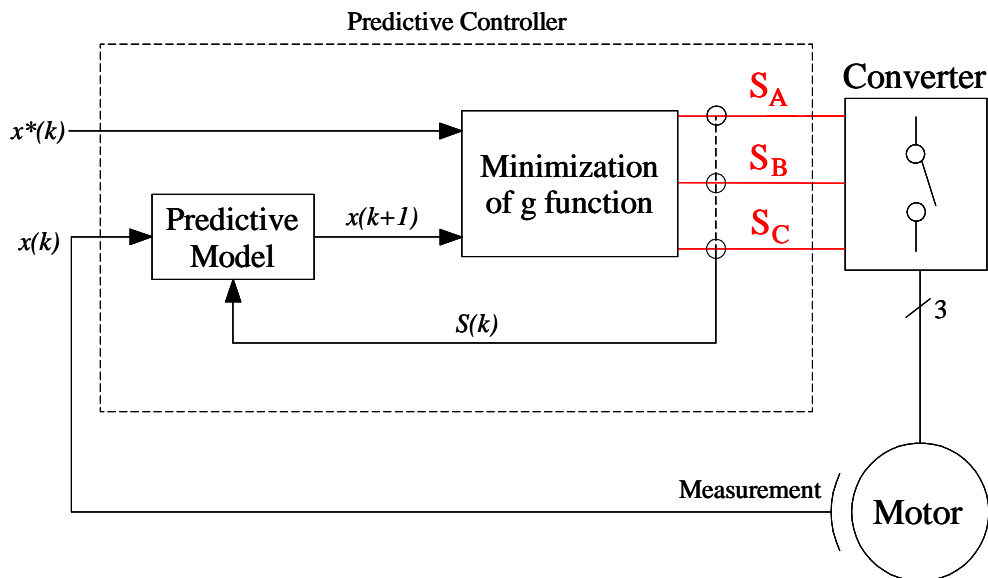


Figure 7-3: Model Predictive Controller block diagram.

One common application of MPC is the current control of a motor drive. In Section 4, it is described how in a FOC, two decoupled PI feedback loops may be used to force  $i_d$  and  $i_q$  to their respective reference values  $i_d^*$  and  $i_q^*$ . In MPC this task could be achieved by using (7.1) [7.8] as  $g()$  in the algorithm. In (7.1)  $i_d^p$  and  $i_q^p$  are the predicted D and Q stator current components. For each switching vector  $i_d^p$  and  $i_q^p$  must be calculated and  $g()$  re-evaluated. The switching vector that results in the smallest value of  $g()$  will thus result in the smallest

discrepancy between the actual current and demand and is therefore the optimal vector to apply in the next switching cycle.

$$g = |i_d^*(k+1) - i_d^p(k+1)| + |i_q^*(k+1) - i_q^p(k+1)| \quad (7.1)$$

This example demonstrates MPC in its simplest form. Where the objective of  $g()$  is solely to minimise the current error. It has been documented in the literature how MPC is particularly well suited to more complex control applications, where the optimization function must take into account the effect of the switching vector on multiple variables. The author of [7.4] provides a good example of a more complex MPC application. The control of an induction machine using MPC is discussed, the optimisation algorithm must therefore consider both the machines torque and flux. Where two or more variables are to be controlled, weighting functions are commonly used to prioritise the control of more critical variables [7.9].

## 7.2 Application of Predictive Control to Multilevel Converters

The use of predictive control with multilevel converters is becoming increasingly well documented in the literature. Authors have reported applying predictive controllers to the neutral-point-clamped [7.10], diode-clamped [7.9], flying capacitor [7.11] and cascaded H-bridge [7.12] topologies.

Much of this work investigates how MPC may be used to control the converter output current whilst simultaneously balancing the DC capacitor voltages [7.4,7.9,7.11] in both the diode-clamped and capacitor clamped topologies. A term may also be included in the cost function to help reduce the number of switch commutations. Capacitor balance is achieved using redundant switching vectors, as described in Section 4. An example cost function for a neutral-point-clamped converter is given in (7.2) [7.4]. Where  $V_1^p$ ,  $V_2^p$ , and  $n^p$  represent the predicted capacitor voltages and number of switch commutations respectively. Weighting factors  $A$  and  $B$  are used to balance the action of the cost function to ensure that the control of any one variable does not become too dominant.

$$g = |i_d^* - i_d^p(k+1)| + |i_q^* - i_q^p(k+1)| + A|V_1^p(k+1) - V_2^p(k+1)| + Bn^p \quad (7.2)$$

### 7.3 Control Algorithm Development

The objective of this section is to develop a control algorithm incorporating predictive control, which when applied to the control of the inverter, produces a reduction in the THD of the stator current waveform when compared to conventional linear PI controllers. From a control perspective a S/G system is complicated due to the two distinct modes of operation. In starting mode the speed is low resulting in a low back-emf, which can result in a high level of THD. During generating mode the machine speed is high as is the back-emf. There are also relatively few switching cycles per fundamental period. It is therefore hard to tune a conventional FOC to perform well in both modes of operation. The controller documented in this study attempts to overcome this problem using prior knowledge of the load machine and the effect of excitation on the torque and back-emf constants to form a model of the system. This model is then utilized within the controller to predict the likely optimal switching vectors to reduce the current error. In short it is a method of attempting to ensure the controller is adequately tuned to minimize the THD regardless of the mode of operation or the S/G's speed.

At the heart of the algorithm is a model of the load. This is derived from the three phase equations for a synchronous machine, which are given in (7.3). Here  $R_s$ ,  $L_s$ ,  $\omega_m$ ,  $\theta_e$  and  $\lambda_m$  represent winding resistance, synchronous inductance, machine angular velocity, electrical angle and machine flux linkage respectively.

$$\begin{bmatrix} V_a \\ V_b \\ V_c \end{bmatrix} = \begin{bmatrix} R_s & 0 & 0 \\ 0 & R_s & 0 \\ 0 & 0 & R_s \end{bmatrix} \begin{bmatrix} I_a \\ I_b \\ I_c \end{bmatrix} + \begin{bmatrix} L_s & 0 & 0 \\ 0 & L_s & 0 \\ 0 & 0 & L_s \end{bmatrix} \frac{d}{dt} \begin{bmatrix} I_a \\ I_b \\ I_c \end{bmatrix} + \begin{bmatrix} -\omega_m \lambda_m \sin(\theta_e) \\ -\omega_m \lambda_m \sin(\theta_e - 2\pi/3) \\ -\omega_m \lambda_m \sin(\theta_e - 4\pi/3) \end{bmatrix} \quad (7.3)$$

Equation (7.3) may be transformed into the DQ domain to yield (7.4) [7.13].  $L_d$  and  $L_q$  represent the D and Q components of the synchronous inductance, whilst  $K_e$  is the back-emf constant of the machine.

$$\begin{bmatrix} V_d \\ V_q \end{bmatrix} = \begin{bmatrix} R_s & -\omega_e L_q \\ \omega_e L_d & R_s \end{bmatrix} \begin{bmatrix} I_d \\ I_q \end{bmatrix} + \begin{bmatrix} L_d & 0 \\ 0 & L_q \end{bmatrix} \frac{d}{dt} \begin{bmatrix} I_d \\ I_q \end{bmatrix} + \begin{bmatrix} 0 \\ K_e \omega_m \end{bmatrix} \quad (7.4)$$

So that (7.4) may be efficiently implemented within the digital signal processor (DSP) it is first transformed into its discrete-time form (7.6) and (7.7) [7.8,7.14]. To do this the derivative in (7.4) is approximated using (7.5) [7.8], where  $T_s$  is the sampling period.

$$\frac{dI}{dt} \approx \frac{I(k) - I(k-1)}{T_s} \quad (7.5)$$

$$V_q(k) = R_s I_q(k) + \frac{L_q}{T_s} [I_q(k) - I_q(k-1)] + L_d \omega_e(k) I_d(k) + K_e \omega_m(k) \quad (7.6)$$

$$V_d(k) = R_s I_d(k) + \frac{L_d}{T_s} [I_d(k) - I_d(k-1)] - L_q \omega_e(k) I_q(k) \quad (7.7)$$

Equations (7.6) and (7.7) can be modified for use in a predictive current controller by shifting the equation one discrete time step forward [7.8,7.15], and re-arranging the equation so that they predict the current in the next switching cycle ( $I_q^p(k+1)$ ).

$$I_q^p(k+1) = \left[ \frac{1}{R_s + \frac{L_q}{T_s}} \right] \left[ V_q(k+1) + \frac{L_q}{T_s} I_q(k) - L_d \omega_e(k+1) I_d(k+1) - K_e \omega_m(k+1) \right] \quad (7.8)$$

$$I_d^p(k+1) = \left[ \frac{1}{R_s + \frac{L_d}{T_s}} \right] \left[ V_d(k+1) + \frac{L_d}{T_s} I_d(k) + L_q \omega_e(k+1) I_q(k+1) \right] \quad (7.9)$$

These functions may be utilised in MPC to evaluate the effect of each switching vector on the predicted current in the next cycle. For each switching vector the resulting values of  $V_d(k+1)$  and  $V_q(k+1)$  may be calculated using (7.10) [7.16]. Where  $S_{ij}$  ( $i=a,b,c$  and  $j=1,2,\dots,8$ ) represents the state ( $S_{ij} = 0,1$ ) of the  $j^{\text{th}}$  switch in the  $i^{\text{th}}$  phase. Equations (7.8) and (7.9) may then be re-evaluated for each vector and the calculated values of  $I_q^p(k+1)$  and  $I_d^p(k+1)$  inserted into a cost function such as (7.1).

$$\begin{bmatrix} V_a \\ V_b \\ V_c \end{bmatrix} = \begin{bmatrix} S_{a1} & \cdots & S_{a8} \\ \vdots & \ddots & \vdots \\ S_{c1} & \cdots & S_{c8} \end{bmatrix} \begin{bmatrix} V_{c4} \\ V_{c3} \\ V_{c2} \\ V_{c1} \end{bmatrix} \quad (7.10)$$

Although this technique will select the optimum vector, a subtly different approach was used in this study in order to take advantage of the existing SVPWM techniques discussed in Section 4. Equations (7.6) and (7.7) were still shifted forward one time step, however the predicted current term  $I(k+1)$ , was replaced with the demand value  $I^*(k+1)$ . The equations therefore calculate the necessary converter output voltage ( $V_d$  and  $V_q$ ) to apply next time step ( $k+1$ ), in order to force the current  $I(k+1)$  to the demand value  $I^*(k+1)$ .

The outer control loop that regulates torque/DC link voltage, calculating  $I^*(k+1)$ , is of sufficiently lower bandwidth than the current controller that it can be assumed that  $I^*(k+1)=I^*(k)$ . This assumption can be made as high performance closed loop speed control was not used in starting mode and there was a large amount of DC link capacitance to damp the performance of the voltage loop controller. It is also assumed that the substitution  $\omega_m(k+1) \approx \omega_m(k)$  is valid as the S/G speed is low. If these two assumptions are not true, the future values of these variables could easily be extrapolated from previous values based on the rate of change. These operations result in equations (7.11) and (7.12).

$$V_q(k+1) = R_s I_q^*(k) + \frac{L_q}{T_s} [I_q^*(k) - I_q(k)] + L_d \omega_e(k) I_d^*(k) + K_e \omega_m(k) \quad (7.11)$$

$$V_d(k+1) = R_s I_d^*(k) + \frac{L_d}{T_s} [I_d^*(k) - I_d(k)] - L_q \omega_e(k) I_q^*(k+1) \quad (7.12)$$

The  $K_e \omega_m(k)$  term in (7.11) compensates for the back-emf of the S/G. In the case of a PMSM,  $K_e$  can be assumed constant regardless of the machine speed. The load machine used in this chapter was however a WFSM. This machine topology was chosen because for the reasons discussed in Chapter 2, it the machine topology of choice for aerospace manufacturers, and therefore provides a realistic test for the system. This machine also has a very low inductance stator, therefore making it a stiff challenge for the converter controller to minimise the current THD. The need to excite the WFSM was discussed in Section 6. In the case of a WFSM,  $K_e$  is no longer a constant, but is instead a function of both machine speed and the excitation source. When this control algorithm was implemented in hardware, the dsp has to be provided with prior knowledge of the

excitation provided to the WFSM to accurately predict  $K_e$ . The inverter therefore measures the machine speed, determines the mode of operation, then based on knowledge of the excitation applied at that speed and in that mode, estimates  $K_e$  for use in (7.11). If this system was implemented in an aircraft, it would necessitate a communications link between the GCU and the power converter controller.

Instead of calculating the optimum switching vector, equations (7.11) and (7.12) calculate the voltage vector that is predicted to reduce the current error to zero. This technique is preferred as the SVPWM already has the ability to synthesize any space vector at the converter output, whilst ensuring all capacitor voltages remain balanced. After calculation  $V_d(k+1)$  and  $V_q(k+1)$  are therefore passed to the modulator for implementation in the next times step.

It should also be noted that, although not shown in (7.8) and (7.9), an integrator term is included in the controller to remove steady state errors between the actual and demand current vectors. This is necessary to compensate for inaccuracies in the model parameters, and also because the model assumes the converter is constructed from ideal components with no parasitics or deadtime delays [7.17]. It goes beyond the scope of this current work, but these parasitics could be included into the model at a later date. A block diagram of the complete controller is provided in Figure 7-4.

In [7.15] the author conducted a study into compensating for converter non-linearities and motor parameter inaccuracies. The method uses the same model discussed in this study, but with some additional terms added in place of the integrator. High frequency and low frequency errors are compensated for separately, increasing system stability. This method would be of use in a real-world application, where motor parameters are either not-known or changeable. This would be particularly applicable to the control of an embedded S/G, due to the large temperature operating range and resulting parameter value fluctuations.

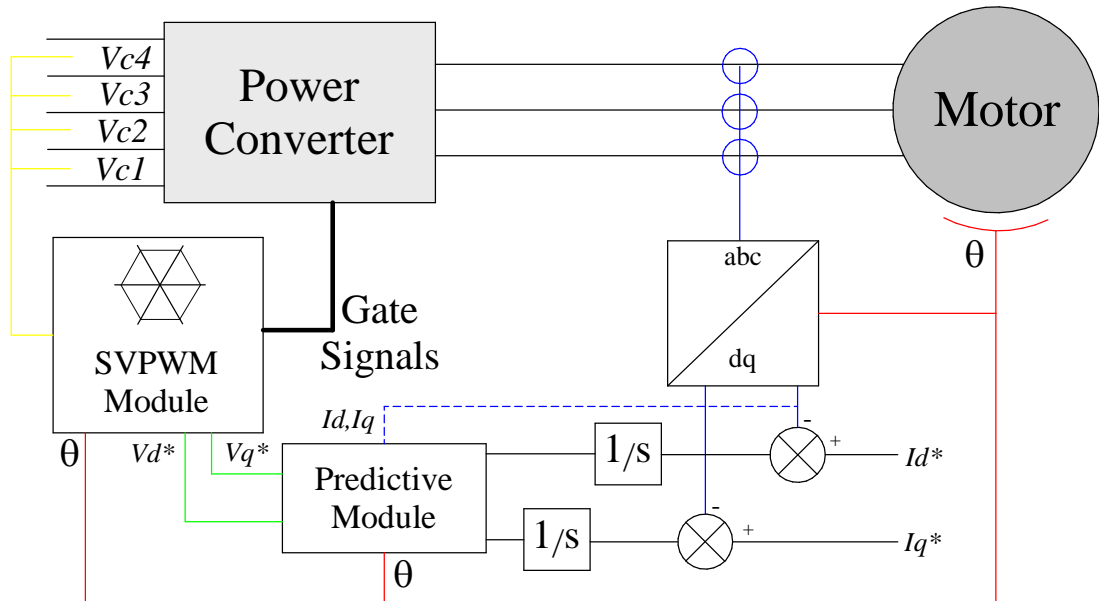


Figure 7-4: Control system block diagram.

## 7.4 Results

Results for starting mode and generating mode are presented separately. In each case both the conventional FOC and the predictive controller are subjected to the same testing conditions so comparisons may be drawn. A power analyser was connected between the converter and machine terminals to provide current measurements.

### Starting Mode

To test the controllers' performance in starting mode, the converter drove the S/G, which was mechanically loaded by the dynamometer. The controller was instructed to maintain a stator current of  $7A_{rms}$ . Current waveforms were obtained using a probe with a bandwidth of 50 MHz. This procedure was repeated for both control strategies. Waveforms are provided in Figure 7-5, which show the resultant stator current when the S/G was rotating at 500 rpm. The upper plot shows the current when the converter was operating using conventional FOC, whilst the lower waveform is that achieved using the predictive controller. The harmonic spectrum of each plot is provided in Figure 7-6.

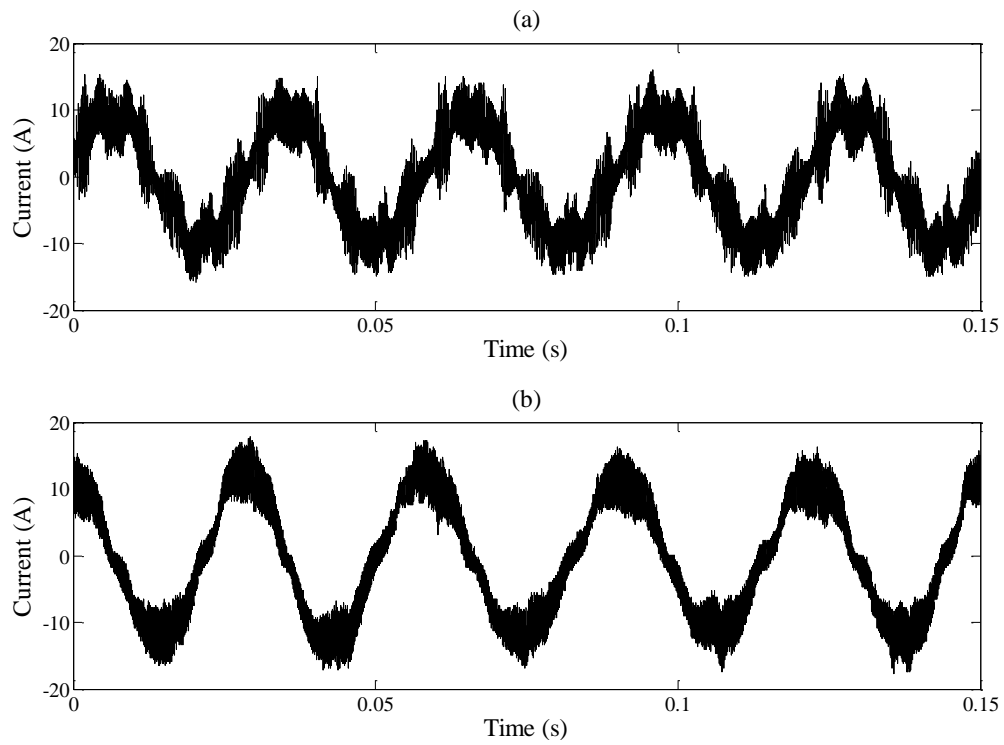


Figure 7-5: Starting mode stator current, (a) Conventional control, (b) Predictive control.

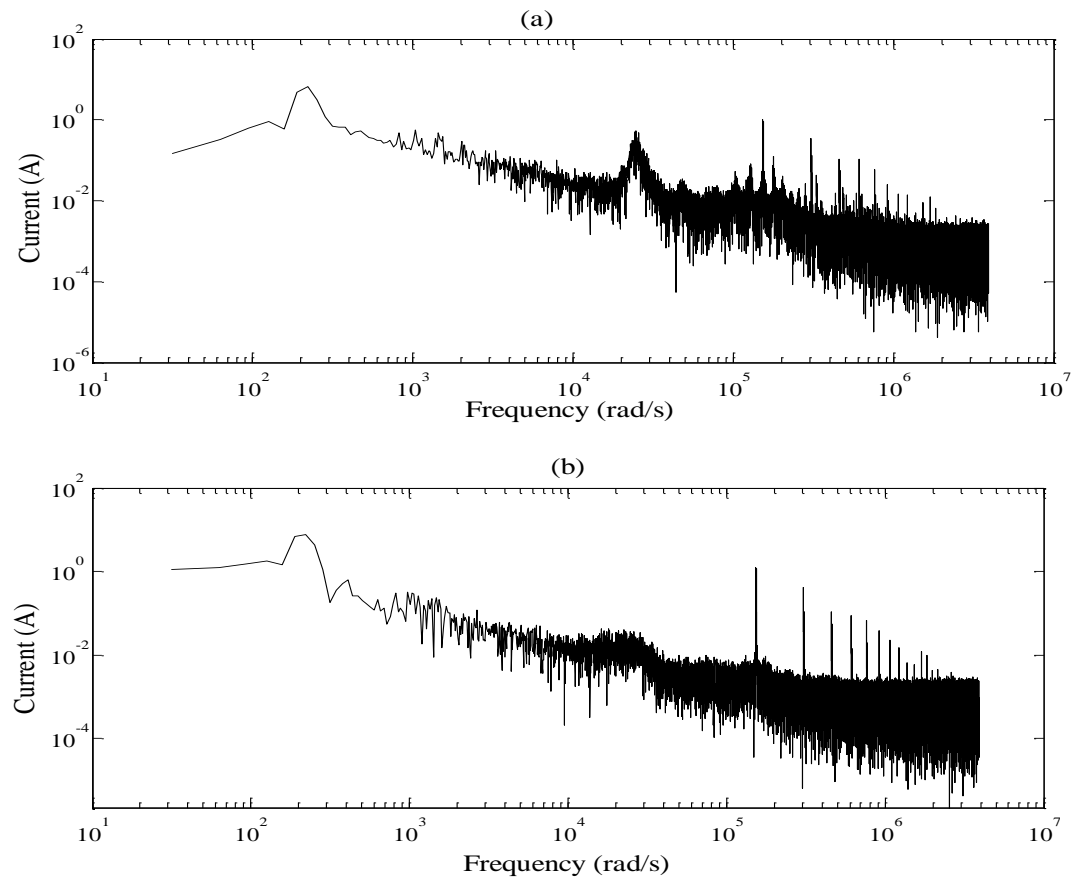


Figure 7-6: Starting mode current spectrum (a) Conventional control, (b) Predictive Control

The implementation of predictive control provides a significant reduction in the THD of the stator current during starting mode. For the waveforms in Figure 7-5, the THD recorded by the power analyser was 40% and 17% for the conventional controller and predictive controller respectively. A large reduction in THD using the predictive controller was apparent across the speed range. The speed was varied between 100 and 700 rpm, whilst the power converter drove a stator current of 8 A<sub>rms</sub> into the S/G. The THD of the current waveform was recorded for both controllers. The results are plotted in Figure 7-7.

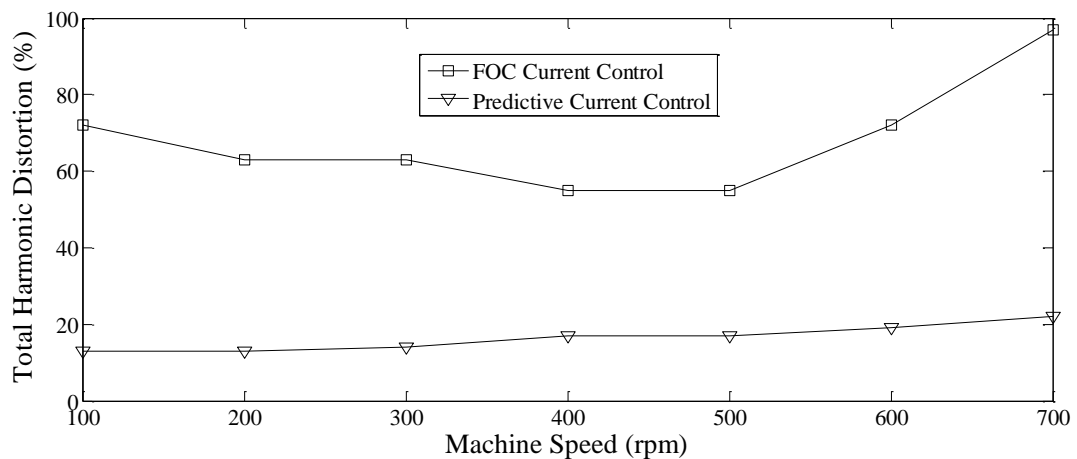
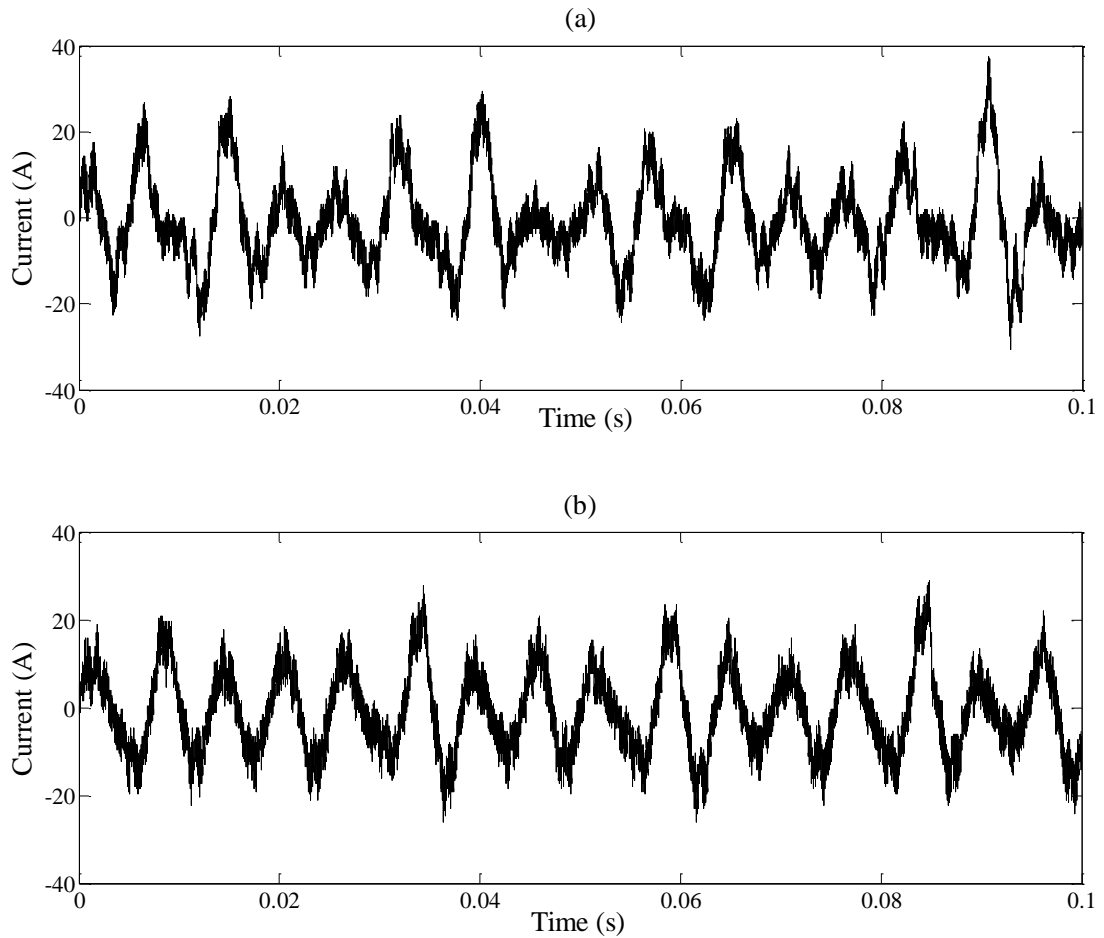


Figure 7-7: THD measured as a function of machine speed.

### Generating Mode

A similar procedure was used to examine the performance in generating mode. The dynamometer rotated the S/G at a constant 2500 rpm ( $\omega_c$ ), whilst the controller of the AFE was used to regulate the flow of electrical power into the utility network. In Figure 7-8 the stator current waveforms are provided from one test where the flow of power into the utility was adjusted such that a stator current of 9.5 A<sub>rms</sub> resulted.



**Figure 7-8: Generating mode waveforms, (a) Conventional control, (b) Predictive control.**

The THD was measured at 75% and 43% for the FOC and predictive controllers respectively. The predictive controller is therefore providing a significant reduction of the THD during generation mode. To further quantify the improvement offered by the predictive controller, the current at the grid connection was varied between 1 and 5 A, whilst the dynamometer maintained a constant speed of  $\omega_c$ . This test therefore assesses the controller performance as a function of the real power delivered to the utility. The results are provided in Figure 7-9.

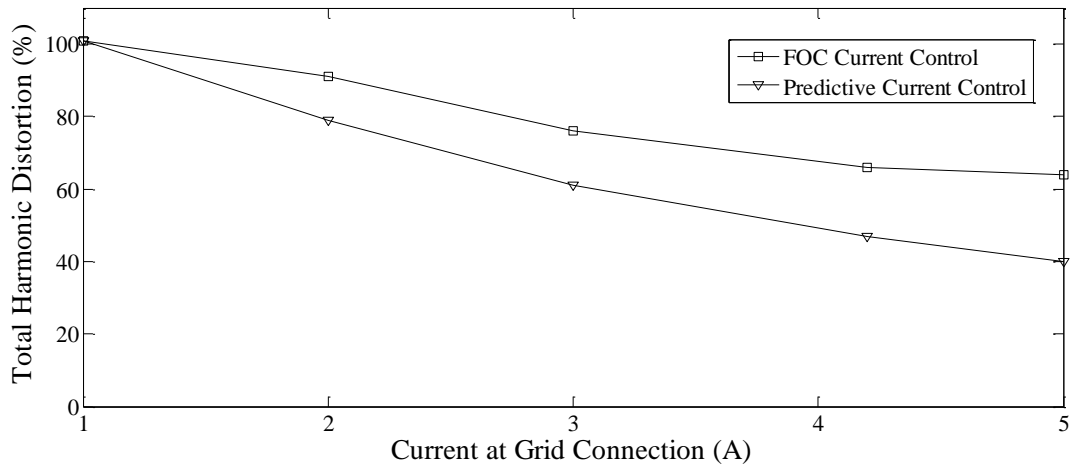


**Figure 7-9: THD measured in the stator as a function of current driven into the utility network.**

The predictive control reduces the THD of the stator current for the majority of the range tested. The THD for both controllers improves as the utility current is increased. This is to be expected as the stator current's fundamental component increases linearly with the power that is delivered to the utility in order to maintain a constant DC link. As the fundamental component increases, the majority of the other harmonics tend to remain at a constant amplitude. The THD is therefore seen to fall as it is the ratio of the fundamental component to the sum of all harmonics.

At low levels of utility current both controllers operate at a high level of THD. This is to be expected as the fundamental components amplitude has dropped so low that the other harmonics particularly those around the converter switching frequency become the more dominant constituent part of the current waveform. In this region neither controller shows a clear advantage over the other.

## 7.5 Conclusion

This chapter has described how predictive control based on a model of the converter and load machine is applied to a multilevel converter operating in an aerospace S/G system. This combination of controller and converter topology ensures that the THD measured in the S/G's stator current waveform is kept low.

The predictive controller is compared to the industry standard FOC and is found to perform favourably, providing a significant reduction to the measured THD in both starting and generating modes, across a range of speeds and current levels. As this method utilizes for its backbone the same SV modulator as the FOC, it has the same advantages such as easy implementation within a DSP, and a fixed switching frequency. Utilising the SV modulator also simplifies the design of the predictive current controller, as capacitor balancing does not need to be considered.

The developed algorithm assumes that all parameter values are known and accurate. The model also assumes that the power converter has no dead-time delays or parasitic components. These assumptions are made to simplify the developed model, however they lead to some steady-state errors between the predicted stator current and the actual measured current. An integrator is used to trim the control algorithm, and remove the error. The model accuracy and system performance could be improved if parasitic components were included in the model at a later date.

## 7.6 References

- [7.1] R. Kennel, A. Linder, "Predictive Control of Inverter Supplied Electrical Drives," Power Electronics Specialist Conference, Galway, Ireland, pp. 761-766, 2000.
- [7.2] P. Wipasuramonton, "Current and Sensorless Control Strategies for PM Brushless AC Drives Using a Low-Cost DSP," Ph.D. Dissertation, University of Sheffield, 2006.
- [7.3] J. Holtz, S. Stadtfeld, "A Predictive Controller for the Stator Current Vector of AC-Machines fed from a Switched Voltage Source," Conf. Record IPEC, Tokyo, Japan, pp. 1665-1675, 1983.
- [7.4] P. Cortes, M. P. Kazmierkowski, R. M. Kennel, "Predictive Control in Power Electronics and Drives," IEEE Trans. Industrial Electronics, Vol. 55. No. 12, pp. 4312-4324, 2008.
- [7.5] M. Depenbrock, "Direct Self-Control (DSC) of Inverter-Fed Induction Machine," IEEE Trans. Power Electronics, Vol. 3, No. 4, pp. 420-429, 1988.
- [7.6] I. Takahashi, T. Noguchi, "A New Quick Response and High Efficiency Control Strategy of an Induction Motor," IEEE Trans. Industrial Applications, Vol. 22, No. 5, pp. 820-827, 1986.
- [7.7] P. Cortes, J. Rodriguez, R. Vargas, U. Ammann, "Cost Function-Based Predictive Control for Power Converters," 32<sup>nd</sup> IEEE Annual Conference on Industrial Electronics, Paris, France, pp. 2268-2273, 2006.
- [7.8] J. Rodriguez, J. Pontt, C. A. Silva, "Predictive Current Control of a Voltage Source Inverter," IEEE Trans. Industrial Applications, Vol. 54, No. 1, pp. 495-503, 2007.
- [7.9] S. A. Verne, M. I. Valla, "Predictive Control of a Back to Back Motor Drive Based on Diode Clamped Multilevel Converters," Proc. 36<sup>th</sup> Annual Conference on IEEE Industrial Electronics Society, Glendale, AZ, USA, 2010, pp. 2972-2977.

- [7.10] R. Vargas, P. Cortes, U. Ammann, "Predictive Control of a Three-Phase Neutral-Point-Clamped Inverter," *IEEE Trans. Industrial Electronics*, Vol. 54, pp. 2697-2704, October, 2007.
- [7.11] E. I. Silva, B. P. McGraph, D. E. Quevedo, G. C. Goodwin, "Predictive Control of a Flying Capacitor Converter," *Proc. American Control Conference*, New York, USA, pp. 3763-3768, 2007.
- [7.12] P. Cortes, A. Wilson, S. Kouro, J. Rodriguez, H. Abu-Rub, "Model Predictive Control of Multilevel Cascaded H-Bridge Inverters," *IEEE Trans. Industrial Electronics*, Vol. 58, Nu. 8, pp. 2691-2699, 2010.
- [7.13] N. Bianchi, T. M. Jahns, "Design, Analysis and Control of Interior PM Synchronous Machines," *IEEE Industry Applications Society*, 2004.
- [7.14] H. Moon, H. Kim, M. Youn, "A Discrete-Time Predictive Current Control for PMSM," *IEEE Trans. Power Electronics*, Vol. 18, pp. 464-472, 2003.
- [7.15] P. Wipasuramontorn, Z. Q. Zhu, D. Howe, "Predictive Current Control with Current-Error Correction for PM Brushless AC Drives," *IEEE Trans. Industry Applications*, Vol. 42, No. 4, pp. 1071-1097, 2006.
- [7.16] J. Pou, "Modulation and Control of Three-Phase PWM Multilevel Converters," Ph.D. Dissertation, Universitat Politecnica De Catalunya, 2002.
- [7.17] H. Le-Huy, K. Slimani, P. Viarouge, "Analysis and Implementation of a Real-Time Predictive Current Controller for Permanent-Magnet Synchronous Servo Drives," *Conference Record of the Industry Applications Society Annual Meeting*, Dearborn, USA, pp. 996-1002, 1991.

# 8 Grid Interface

## 8.1 Introduction

Up to this point the control of the grid connected inverter has been greatly simplified, using the assumption that the grid is a balanced three-phase source with minimal distortion. This however is rarely true and some form of pollution/distortion is normally present in all AC systems, be it the utility network or an aircraft's distribution bus.

In Section 2 the aerospace power quality standards were introduced. These standards dictate the allowable levels of distortion upon an aerospace distribution bus. All bus connected apparatus must continue to function under grid distortion up to the limits specified within the power standards.

The control of the grid connected front end of a power converter will have the greatest influence on the ability of that converter to comply with these standards. It is therefore essential as this stage to examine the control of the AFE to see how it can be made more resilient and robust to the grid conditions it would encounter in a real world application.

This chapter is organised as follows:

Common grid interface control techniques and the associated advantages and limitations of each are initially discussed. A grid synchronisation technique which has the benefit of operating well under distorted grid conditions but also the potential to increase converter reliability is then described. Emphasis is placed on how it may be best adapted for use with the multilevel *S/G* system developed in this study.

The results of simulations are then provided which demonstrate the performance of the AFE using the new grid synchronisation technique under a range of operating conditions. Attention is focused on converter performance under the unbalanced phase conditions likely to be encountered upon an aircraft distribution bus.

The grid synchronisation technique is then applied to the control of the AFE in hardware with the emphasis still on performance during unbalanced conditions. The results obtained experimentally are presented and analysed.

Conclusions are then drawn on the performance of the system and the contributions and implications of the work described in this chapter.

The work described in this chapter was published in [8.1].

## 8.2 Grid Interface Techniques

The most common method used to control the reactive and real power in an active front rectifier is Voltage Orientated Control (VOC) [8.2]. This is the method that has been employed in the control of the AFE throughout this study. VOC functions by ensuring that the vector representation of the current drawn by the rectifier ( $\underline{i}$ ) (8.1) is aligned with the grid voltage vector ( $\underline{v}$ ) (8.2).

$$\underline{i} = i_d + ji_q \quad (8.1)$$

$$\underline{v} = v_d + jv_q \quad (8.2)$$

This is achieved by first aligning a revolving reference frame with  $\underline{v}$ , then using two current control loops to regulate the D and Q components such that  $i_q$  is minimised. Assuming the current control loops are well configured, VOC offers good performance both statically and dynamically [8.2,8.3]. VOC also allows a constant switching frequency to be used which is beneficial from a harmonic perspective, and is compatible with advanced modulation strategies such as SVPWM. The use of SVPWM is essential to this project due to the modifications made to enable it to balance the DC link capacitor voltages as discussed in Section 4. The major disadvantage of VOC is poor performance under distorted grid conditions.

A major disadvantage of VOC is that its ability to control active and reactive power is entirely dependent on the two current control loops [8.4]. In contrast, Direct Power Control (DPC) seeks to control active and reactive power directly using an optimal switching vector

look up-table. Before each switching cycle the reactive and active powers are measured and then compared to the demand values to calculate the error. The error along with the grid angle is then fed into the look-up table to select the switching vector for implementation in the next PWM period.

The major drawback from an aerospace perspective is that DPC results in a variable switching frequency. This can generate a high level of harmonic distortion with a large bandwidth in the grid current waveform. This could necessitate additional filtering to ensure compliance with the aerospace power quality standards.

From a multilevel control perspective DPC has the major disadvantage of not utilising a SVPWM modulation block. The SVPWM block is essential in this project to ensure the DC link voltages are balanced and therefore guarantee a high quality output waveform. There is a limited amount of published material [8.5] regarding the application of DPC to a multilevel converter whilst incorporating DC link capacitor voltage balance. However it is the author's opinion that this has so far only been demonstrated upon the NPC topology. There appears to be no published material relating to capacitor balance achieved using DPC in the five level diode clamped topology.

Regardless of the control strategy used, determining the grid angle is critical to successful operation of the power converter. This information is used to calculate and implement the switching vectors for the power devices, measure and control the active and reactive power and also transform three-phase variables into different reference frames to simplify control operations [8.6]. Inaccurate grid angle information would therefore cause disruption to the converter which could cause instability/collapse of the aircraft distribution network.

Common types of distortion encountered on AC buses are line-notching, phase unbalance, line dips and frequency variations [8.6]. Aircraft electrical systems are required to be resilient to grid distortion provided the distortion is within stated limits as governed by the power quality standards [8.7]. The method used to determine the grid angle must therefore continue to function under distorted conditions.

The grid angle in the VOC in the AFE is obtained using three voltage transducers which measure the phase voltage waveforms. The phase voltage signals are then used as the

input to a three-phase, software based PLL to extract the grid angle. It has been well documented how a basic software-based PLL can be adversely affected by grid distortion leading to a poor quality representation of the grid angle [8.8]. There is a large amount of published work on how a conventional software-based PLL can be modified to make it more resilient to distorted grid conditions [8.6,8.8,8.9]. These methods normally involve adding additional compensating terms into the PLL's PI controller to ensure the grid angle output is of high quality despite the presence of distortion upon the input.

An alternative approach to VOC to avoid the inherent difficulties of synchronising with the grid voltage is Virtual Flux Orientated Control (VFOC). Here the controller is instead synchronised with the rotor of a virtual machine at the grid terminal. It has been demonstrated that using this technique it is possible to eliminate phase voltage sensors from the controller. This not only has the advantage of making the system more immune to distorted grid conditions, but importantly from an aerospace power system perspective, may increase overall system reliability. The increase in reliability is because three key components have been eliminated. Under VOC, if one or more of the voltage transducers were damaged the power converter would no longer function. For these reason the VFOC technique was selected for implementation upon the AFE.

### **8.3 Virtual Flux Estimation**

There has been a large amount of work [8.2,8.3,8.10] upon the replacement of grid connected AC voltage sensors with a Virtual Flux (VF) estimator. The VF algorithm is formed by making the assumption that the voltage seen at the grid connection is due to a virtual motor [8.3]. Parameters like the filtering inductance and stray resistance, now relate to the electrical characteristics of the virtual motor's stator. This is shown in Figure 8-1.

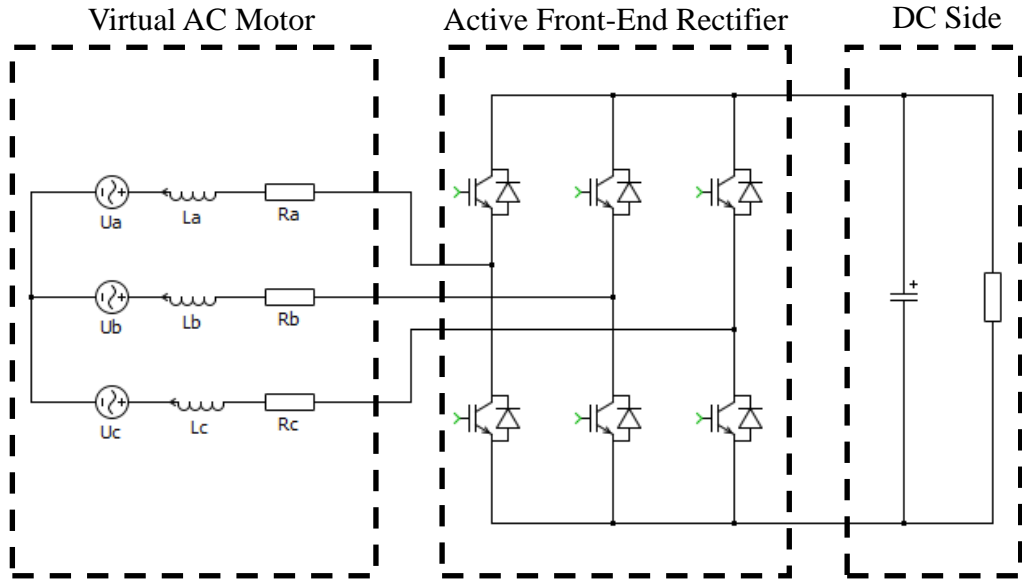


Figure 8-1: Virtual flux block diagram.

If the utility connection is interpreted as a virtual motor, a virtual flux ( $\psi_L$ ) may be considered to exist, which induces the line-line voltages ( $U_L$ ) seen at the converter terminals. The integration of the line-line voltage vector must therefore result in the virtual flux vector (8.1) [8.10].

$$\underline{\psi}_L = \begin{bmatrix} \psi_{L\alpha} \\ \psi_{L\beta} \end{bmatrix} = \int \underline{U}_L dt = \begin{bmatrix} \int U_{L\alpha} dt \\ \int U_{L\beta} dt \end{bmatrix} \quad (8.1)$$

The voltage at the converter terminals consists of the voltage drop across the line impedance and the converter terminal voltage ( $\underline{U}_{conv}$ ). This is expressed in (8.2).

$$\underline{U}_L = R \underline{i}_L + L \frac{d}{dt} \underline{i}_L + \underline{U}_{conv} \quad (8.2)$$

In the case of the two-level inverter,  $\psi_{L\alpha}$  and  $\psi_{L\beta}$  may be estimated (8.3 and 8.4) [8.2] after each switching cycle, using knowledge of the switch duty cycle ( $D_a$ ,  $D_b$ , and  $D_c$ ) and the current measurements. Here it is assumed that  $R$  is negligible.

$$\psi_{L\alpha} = \int \left( \sqrt{\frac{2}{3}} V_{dc} (D_a - \frac{1}{2}(D_b + D_c)) \right) dt + L i_{L\alpha} \quad (8.3)$$

$$\psi_{L\beta} = \int \left( \frac{1}{\sqrt{2}} V_{ac} (D_b - D_c) \right) dt + Li_{L\beta} \quad (8.4)$$

## 8.4 Implementation of VF Estimator with Space Vector Modulator

Equations (8.3) and (8.4) may be modified for implementation within a DSP so they may be used to estimate the grid angle. The angle may then be passed to the vector controller for use in the DQ transforms and to the SV modulator to select the appropriate switching vectors.

Equations (8.3) and (8.4) rely on knowledge of the switching duty cycles to estimate the alpha-beta components of  $\underline{U}_{conv}$  ( $\underline{U}_{conv\alpha}$  and  $\underline{U}_{conv\beta}$ ). As the controller for the converter is based around a SV modulator,  $U_{conv\alpha}$  and  $U_{conv\beta}$  can easily be extracted from this algorithm. This reduces the processing load as it is now not necessary to evaluate  $U_{conv\alpha}$  and  $U_{conv\beta}$  from the switching vector. Equations (8.3) and (8.4) therefore reduce to (8.5) and (8.6) respectively. The integrating term has the advantage of making the controller inherently stable under distorted or noisy grid conditions [8.3].

$$\psi_{L\alpha} = \int U_{conv\alpha} dt + Li_{L\alpha} \quad (8.5)$$

$$\psi_{L\beta} = \int U_{conv\beta} dt + Li_{L\beta} \quad (8.6)$$

It is impractical to evaluate the integral term of (8.5) and (8.6) within the DSP. Pure integrator terms result in drift and initial value problems which quickly lead to the integrator being driven into saturation [8.11, 8.12]. Assuming that  $U_{conv\alpha}$  and  $U_{conv\beta}$  are sinusoidal, the integral of these terms would be a phase-shifted, scaled sinusoid.

To overcome the problems associated with the integral term, it can be replaced with a first order low pass filter [8.11]. The corner frequency ( $\omega_c$ ) of the filter is chosen to produce a 90° phase shift between the input and output at the grid frequency. Assuming that an appropriate scaling factor is chosen, the filter therefore produces approximately the same output as an ideal integrator. This technique is only suitable for application to systems with a fixed frequency. It is considered relevant in this study as the assumption is made that

electrical power is distributed around the aircraft at a constant 400 Hz with only minor frequency deviations. The authors of [8.11,8.12] provide modified integrator schemes suitable for use in variable frequency systems. Such works would need to be consulted if the proposed S/G system were to be applied in frequency wild networks such as those present upon the A380 and B787.

After estimating  $\underline{\psi}_L$ , the rotor angle of the virtual machine ( $\theta_{VF}$ ) may be calculated using (8.5). When (8.5) is implemented in software provision must be made to prevent a potential divide by zero. It is important to note that  $\underline{\psi}_L$  lags the grid voltage vector by 90° [8.13], the programmer must shift the angle of  $\theta_{VF}$  before use in the coordinate transform equations in order to use the same FOC described earlier. Alternatively the angle shift can be accommodated by adjusting the current control loops such that  $I_d$  is zero and  $I_q$  is used to regulate the flow of real power.

$$\theta_{VF} = \tan^{-1} \left( \frac{\psi_{L\beta}}{\psi_{L\alpha}} \right) \quad (8.5)$$

The grid angle is then passed to a PLL. This ensures that the electrical angle passed to the SVM and the coordinate transforms is a high quality, constant frequency signal [8.13,8.14]. Without the PLL, voltage transients such as spikes and dips could propagate to  $\theta_{VF}$  and disrupt the converter's operation.

A block diagram of the control system for the front end rectifier operating during starting mode, incorporating a VF estimator is shown in Figure 8-2.

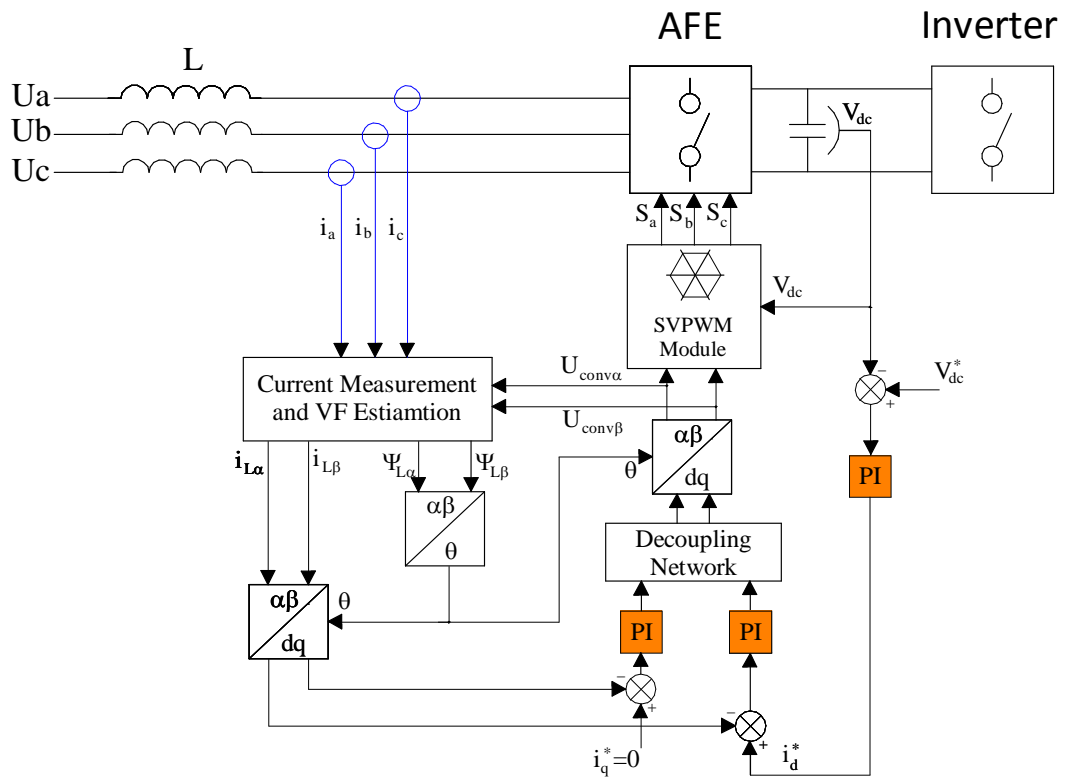


Figure 8-2: AFE controller incorporating VF estimator.

## 8.5 Simulation Results

The proposed VF estimator was first assessed in simulation so that the system may be tuned before being applied in hardware. Producing a functioning simulation model also enabled tests to be conducted upon the system which were not possible in hardware. For instance, the bench top AC programmable supply which was used to represent the aircraft's AC network did not support regenerative power flow. For this reason only operation in starting mode could be assessed in hardware. However it was possible to assess the performance of the VF estimator during generating mode in simulation.

Simulations were conducted at a power rating of approximately 5 kW, which coincides with the rating of a typical UAV S/G [8.15]. The simulation model is provided in Appendix D. Only the grid connected inverter was simulated, this is because the presence of the inverter does not affect the operation of the AFE, but would increase the simulation time. The performance of the system during starting and generating mode was assessed with both balanced and distorted grid conditions.

### 8.5.1 Balanced Grid Conditions

The converter was initially simulated operating under ideal grid conditions, with a balanced, 115 V<sub>line-line</sub>, 400 Hz supply.  $V_{dc}^*$  was set at 270 V with a 2 kW load across the DC link capacitors to model the inverter. The choke inductance for all simulations was set at 400  $\mu$ H. The logged variables from these simulations are displayed graphically below.

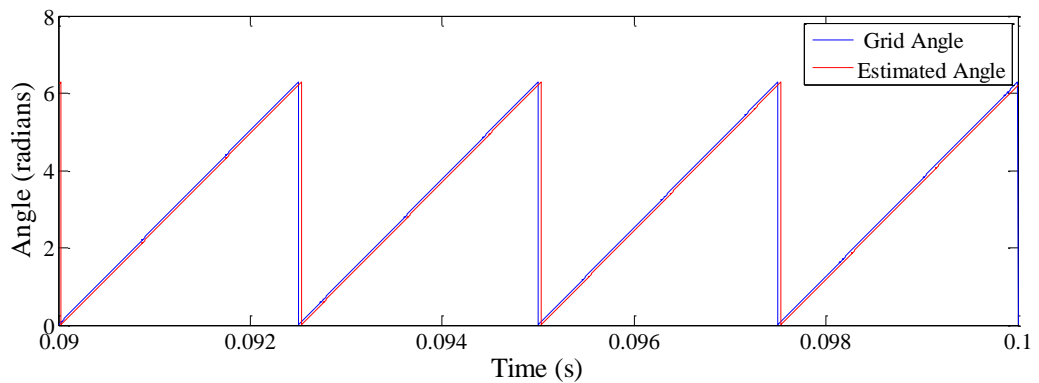


Figure 8-3: Estimated and actual grid angle under balanced conditions during starting mode.

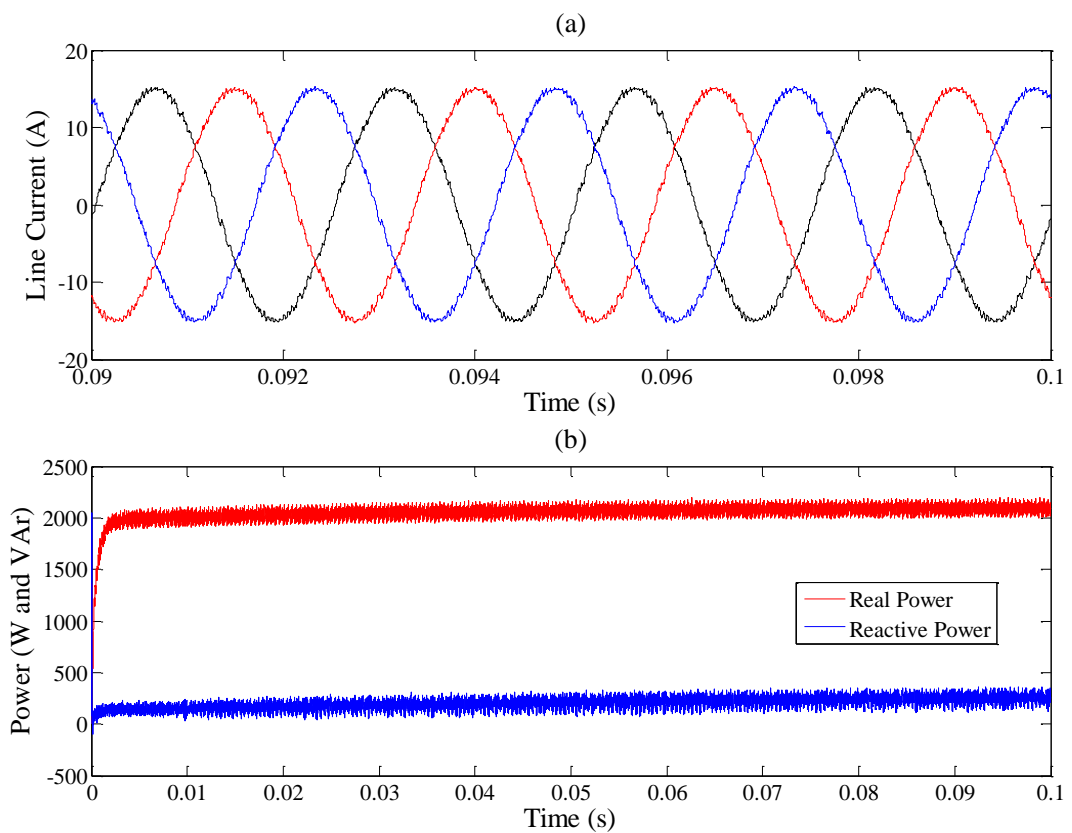
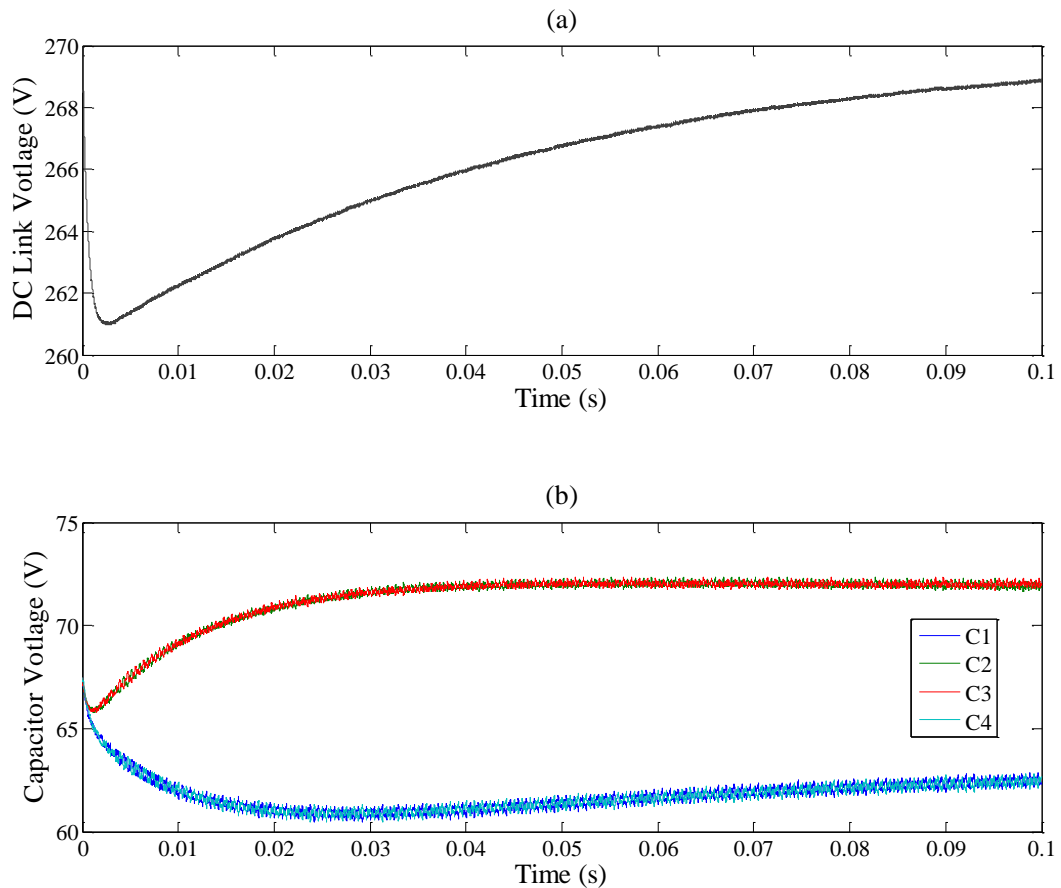


Figure 8-4: Starting mode (a) Line current waveforms, (b) Real and reactive power.



**Figure 8-5 Starting mode (a) DC link voltage, (b) Capacitor voltages.**

The actual grid angle and the angle calculated by the VF estimator are shown in Figure 8-3. It is immediately apparent that the VF estimator is functioning well with only a small error between the actual and estimated grid angle. With an accurate estimation of the grid angle, the converter vector controller functions almost identically to when its grid angle is derived from three voltage transducers providing the input to a PLL. The converter draws a sinusoidal current waveform (Figure 8-4 (a)) with minimal distortion with a power factor close to unity (0.99). The operation at unity power factor ensures that only minimal reactive power is drawn from the grid (Figure 8-4 (b)). The DC link (Figure 8-5 (a)) is maintained at close to  $V_{DC}^*$ . The individual capacitor voltages are shown in (Figure 8-5 (b)). It is apparent that some unbalance exists in the DC link. This is not a reflection on the VF estimator. As discussed in Section 4, when only one three-phase diode-clamped inverter is used, capacitor balance can only be achieved using redundant switching vectors provided the modulation index remains below 0.5. The unbalance shown Figure 8-5 would therefore not occur if the inverter was simulated in unison with the AFE.

The converter was then simulated during generating mode. The load connected across the DC link was replaced with four DC sources each with an amplitude of  $V_{dc}^*/4$ . These sources therefore represent the inverter during generation mode. This also ensures that the capacitor balance problem displayed in Figure 8-5 does not occur in this test. The logged variables from these simulations are displayed graphically below.

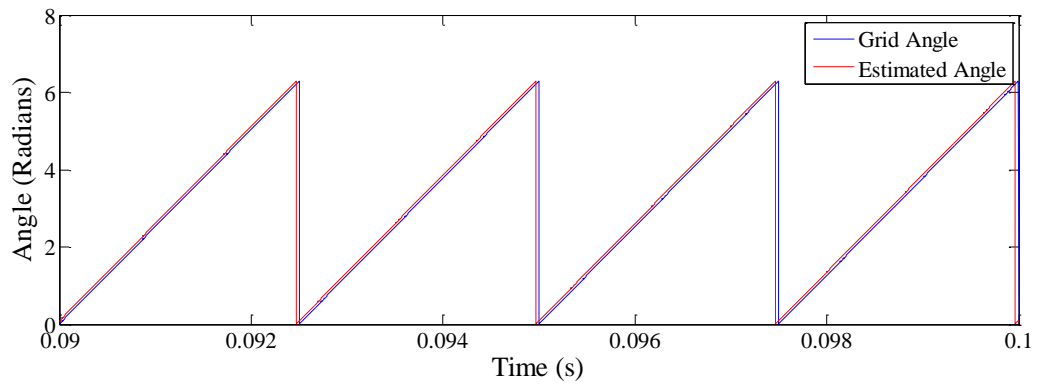


Figure 8-6: Estimated and actual grid angle under balanced conditions during generating mode.

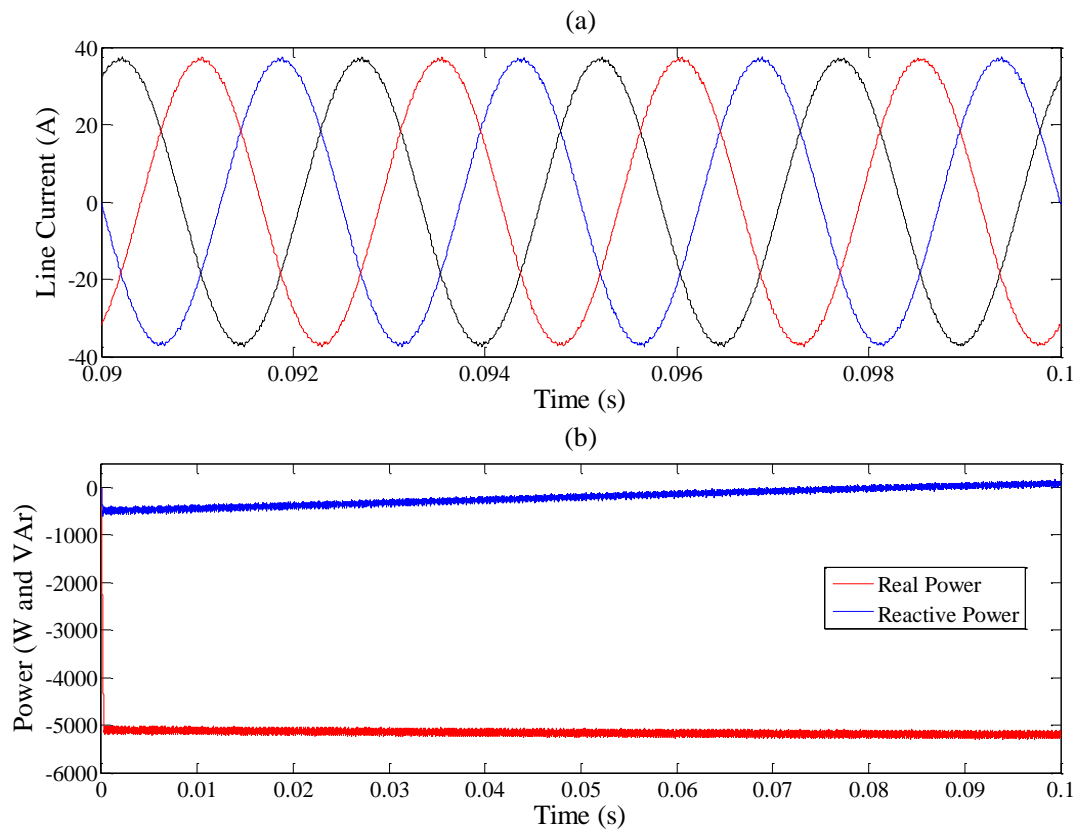


Figure 8-7: Generating mode (a) Line current waveforms, (b) Real and reactive power.

It is apparent from Figure 8-6, showing the estimated and actual grid angle, that the controller is functioning satisfactorily with only minimal error. The controller is therefore functioning well, driving a sinusoidal current (Figure 8-7 (a)) with minimal distortion into the supply. This results in approximately 5 kW of real power (Figure 8-7 (b)) being delivered to the grid, with only a small amount of reactive power.

### 8.5.2 Unbalanced Grid Conditions

Having verified performance under ideal grid conditions, the models were re-simulated under distorted grid conditions. A grid voltage (Figure 8-8) was used with a 5% phase unbalance from the normal 115 V<sub>line-line</sub> supply used in previous simulations. This is in line with the maximum permitted phase unbalance on an aerospace distribution bus as governed by [8.7]. This is therefore the worst case scenario from a power converter control perspective. The logged variables from these simulations are presented graphically below.

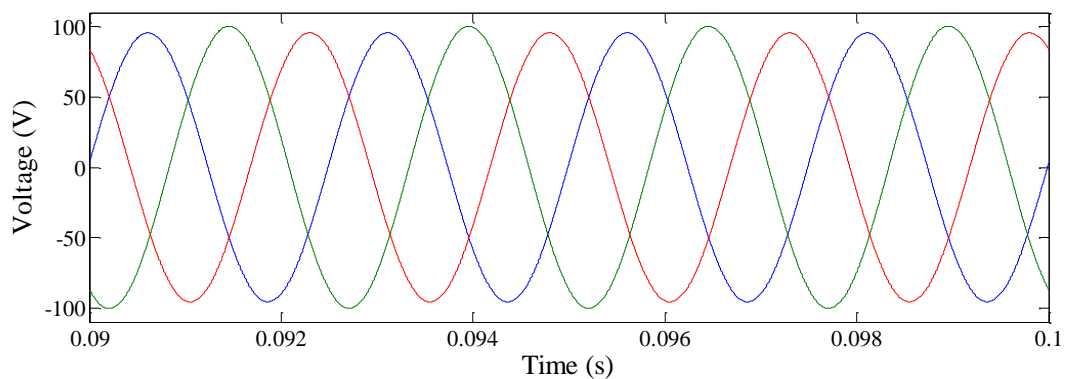


Figure 8-8: Distorted grid voltage waveform during starting mode.

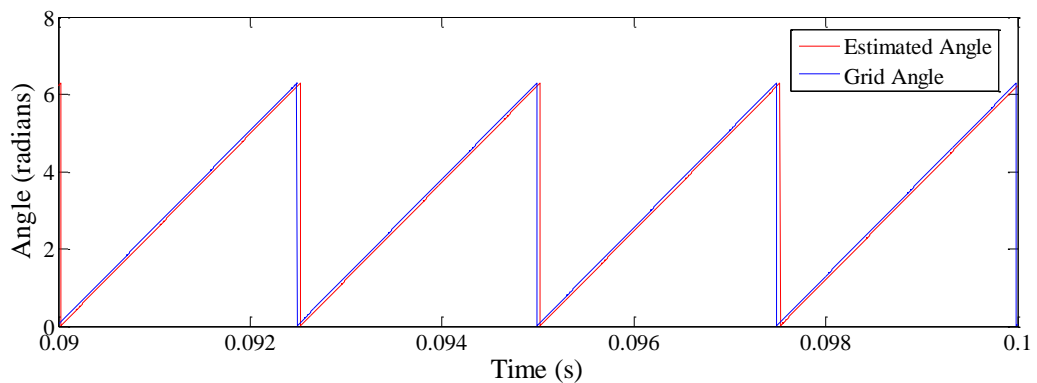


Figure 8-9: Estimated and actual grid angle under distorted conditions during starting mode.

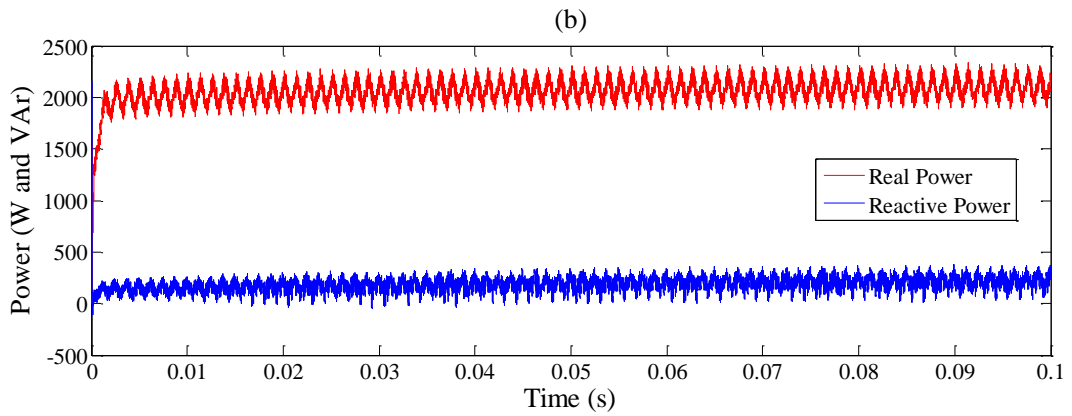
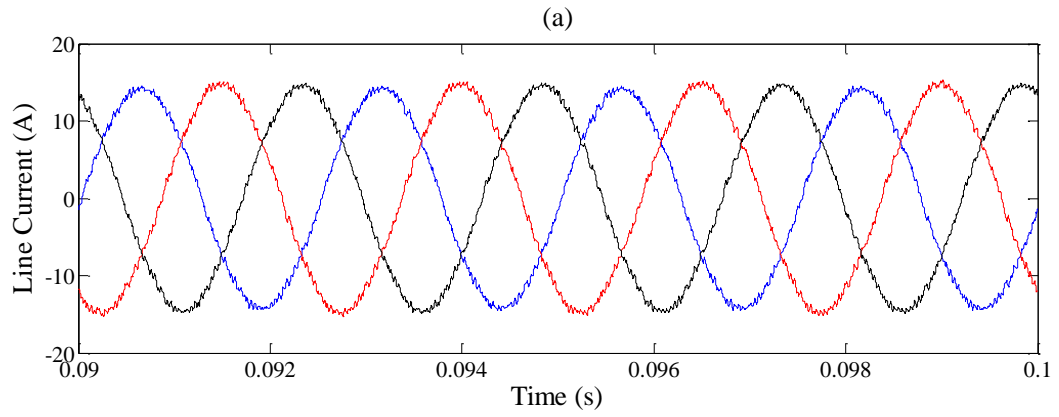


Figure 8-10: Starting mode (a) Line current waveforms, (b) Real and reactive power.

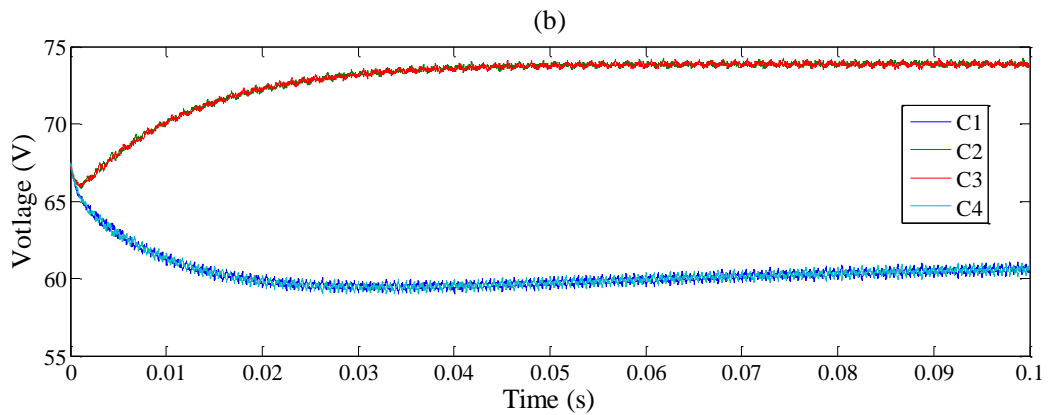
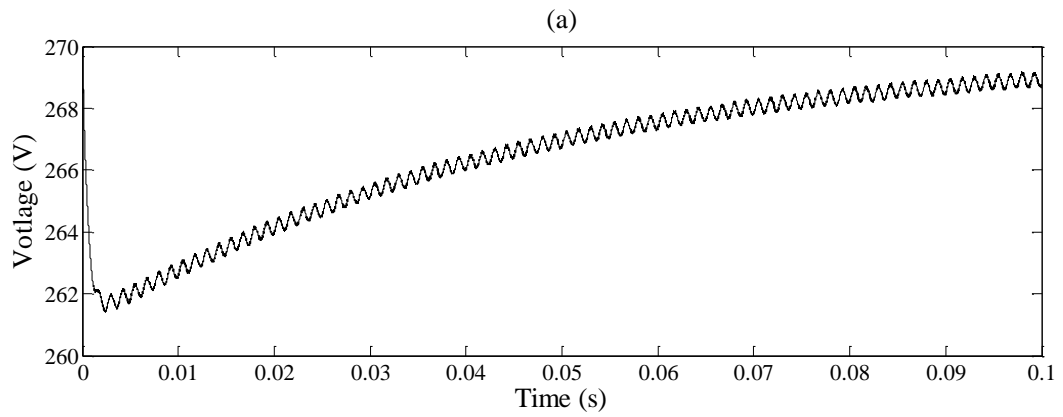


Figure 8-11: Starting mode (a) DC link voltage, (b) Capacitor voltages.

It is apparent from the plots of estimated and actual grid angle Figure 8-9 that the VF estimator is unaffected by the distorted grid conditions with only a small angle error. The average error angle was estimated from the power factor. The power factor was calculated based on the real and reactive power data shown in Figure 8-10. The resultant angular error was calculated to be  $7.125^\circ$ .

The converter still produces the required DC link voltage (Figure 8-11) and minimises the reactive power drawn from the grid (Figure 8-10). There is however a noticeable ripple upon the voltage and also the real power drawn from the grid. This has a frequency of 800 Hz. This is due to the entire phase imbalance being applied to phase B. There is therefore a slight increase in the current drawn from the supply whenever phase B is at its maxima or minima.

It is apparent from Figure 8-10 (a) that the distorted grid has resulted in an unbalance in the three phase currents. During starting mode the converter appears as a load upon the aircraft's distribution network. The maximum permissible load unbalance is dictated by the power quality standards and is stated as a function of the total three-phase load. In this application the converter is assumed to be a 5 kVA load, meaning the load distortion must be less than or equal to approximately 440 VA to comply with [8.7]. The rms current values were measured at 10.3 A, 10.8 A and 10.7 A for phases A, B and C respectively. The phase powers were then calculated taking into account the unbalance in the voltage waveforms. The load unbalance could then be calculated as the difference between the smallest and largest phase powers. This was found to be 65 VA, which is well below the specified limit.

The above calculations make the assumption that during generating mode the converter produces 5 kW to supply the aircraft's electrical loads, whilst in starting mode only 2 kW is required to ignite the engine. The converter would therefore need to be re-simulated before application in the real world if this assumption upon power levels was not true as the relative load unbalance limits would change.

The performance under distorted grid conditions during generating mode was then simulated. The results are presented below.

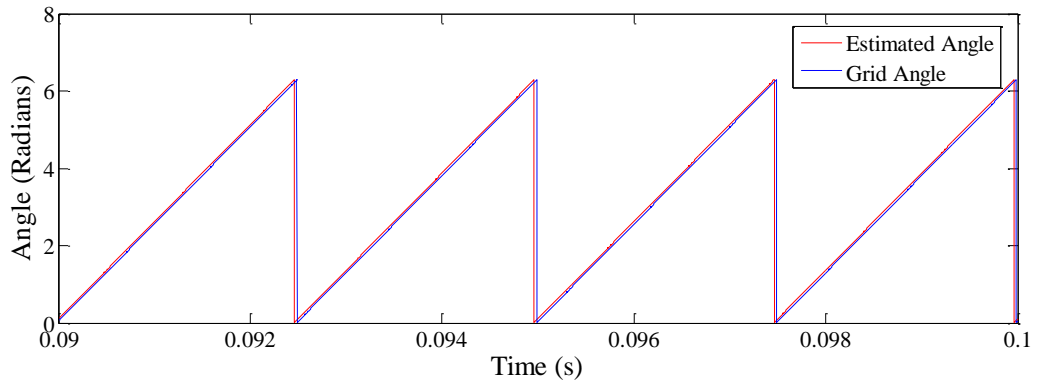


Figure 8-12: Estimated and actual grid angle under distorted conditions during generating mode.

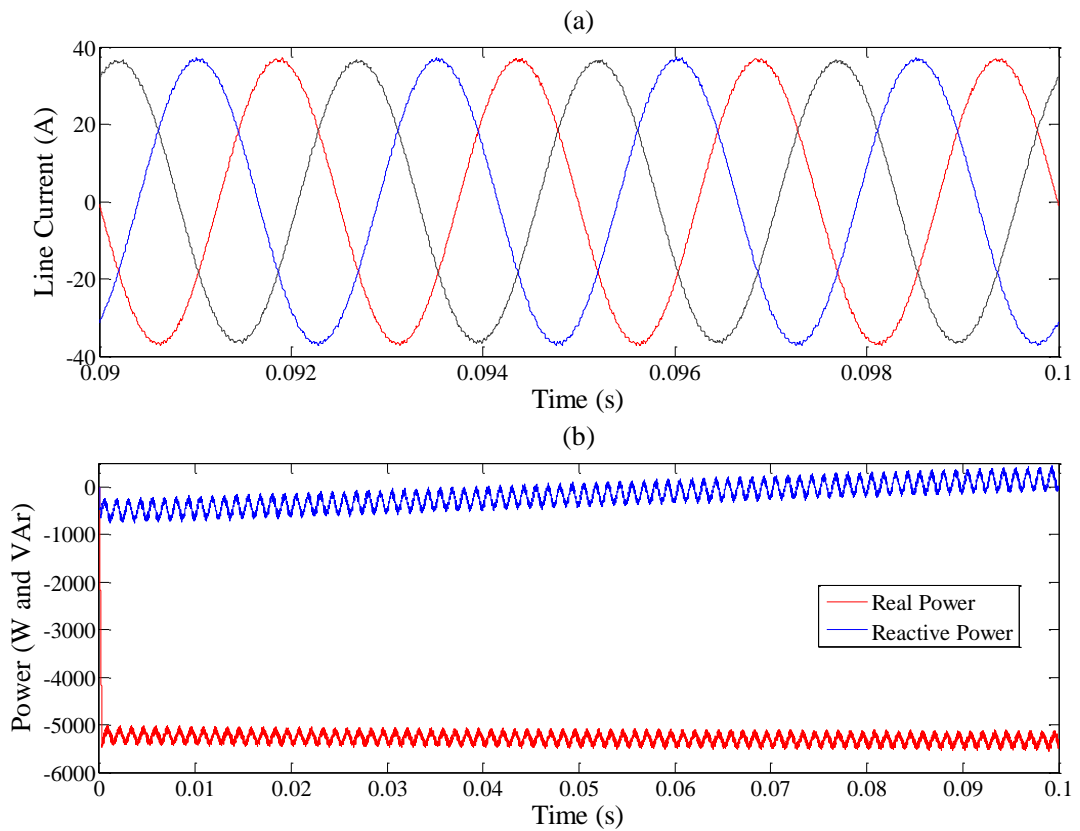


Figure 8-13: Generating mode (a) Line current waveforms, (b) Real and reactive power.

The results during generating mode are near identical to those obtained during starting mode. With minimal error between the estimated and actual grid angle (Figure 8-12), but with an 800 Hz ripple imposed on the real and reactive power driven into the grid (Figure 8-13 (b)).

## 8.6 Experimental Results

The system demonstrated in simulation in Section 8.5 was then implemented in hardware to provide experimental results. The code used to implement the VF estimator within the DSP is provided in Appendix E.

It was necessary to use a programmable bench top power supply rather than the utility network at the converter grid connection. Firstly this provides a more realistic 400 Hz supply and secondly the supply allows control over the level of grid distortion unlike the utility where the distortion fluctuates dependant on other users/loads upon the network. As discussed earlier, only starting mode could be assessed in hardware as the supply did not have regenerative capabilities.

### 8.6.1 Balanced Phase Conditions

The system was initially tested with a 400 Hz, 115 V<sub>line-line</sub> balanced supply, with  $V_{DC}^*$  set at 200 V. The inverter was used to load the AFE by driving current into the WFSM. This also ensures that balance is achieved upon the DC link alleviating the problems encountered in Section 8.5. The results obtained during experimentation are displayed graphically below.

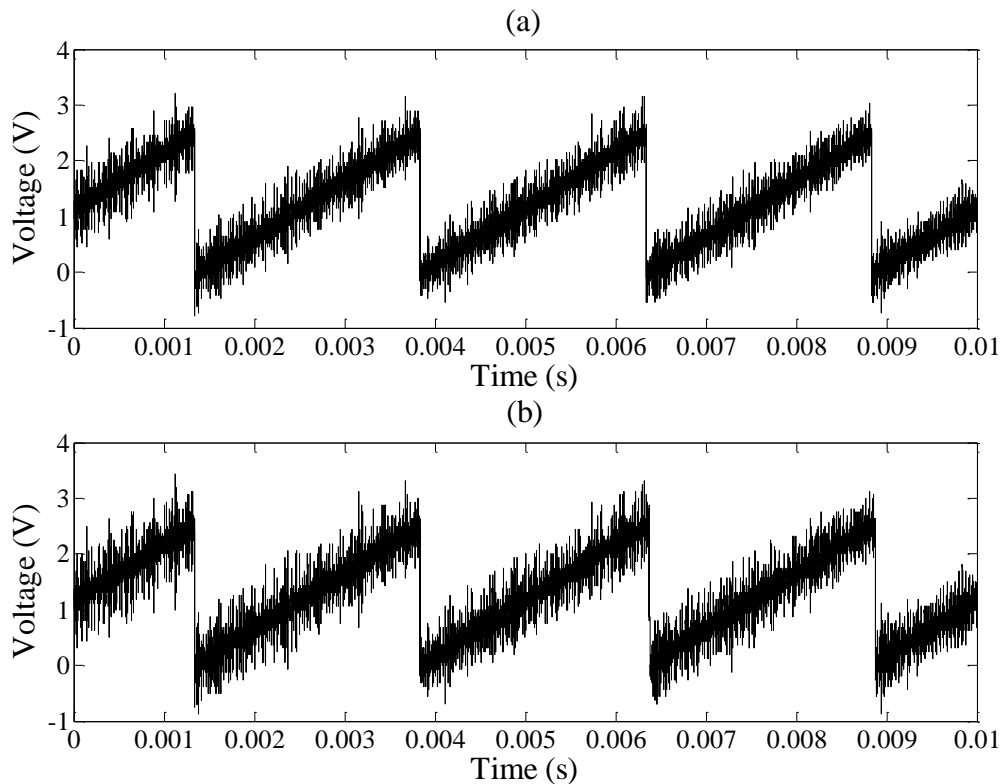
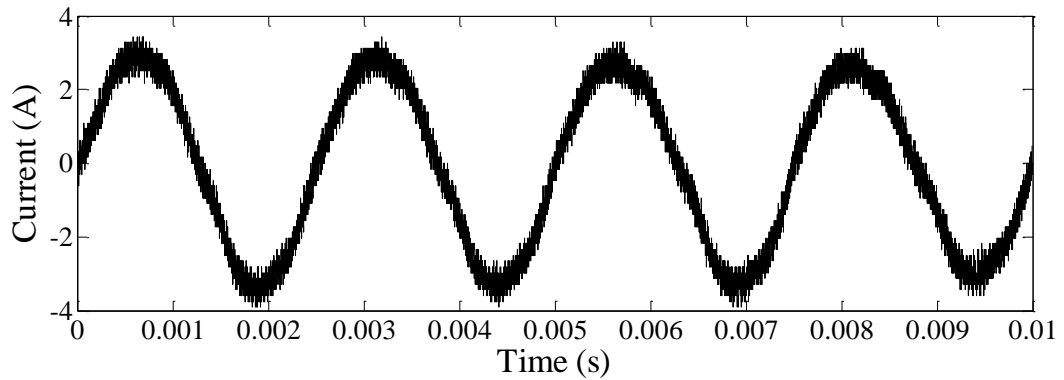


Figure 8-14: Grid angle (a) Estimated, (b) Actual.



**Figure 8-15: Current drawn from the grid.**

The VF estimator appears to be functioning well with very little discrepancy between the estimated and actual grid angle (Figure 8-14). The grid angles were fed out of the DSP using a DAC. This explains why the grid waveforms in Figure 8-14 vary between approximately 0 and 2.5 V rather than 0 and  $2\pi$  radians as in the simulation results. The absolute amplitude of either of the waveforms in Figure 8-14 is therefore incorrect due to the DAC's scaling factor. However the waveform shape and the relative phase between the estimated and actual plots are of significance. It is the author's opinion that the noise present on both signals displayed in Figure 8-14 is due to radiated EMI rather than distortion upon the angle signals within the DSP.

The current drawn from the supply is shown in Figure 8-15. With the grid angle being accurately obtained using the VF estimator the controller functioned near identically to in Sections 5 and 6 where the grid angle was measured from the phase voltages.

### 8.6.2 Distorted Phase Conditions

The hardware's performance under distorted grid condition was then examined. Similarly to the simulations in Section 8.5 an unbalance of 5 % was added in line with the power quality standards. The results are displayed graphically below.

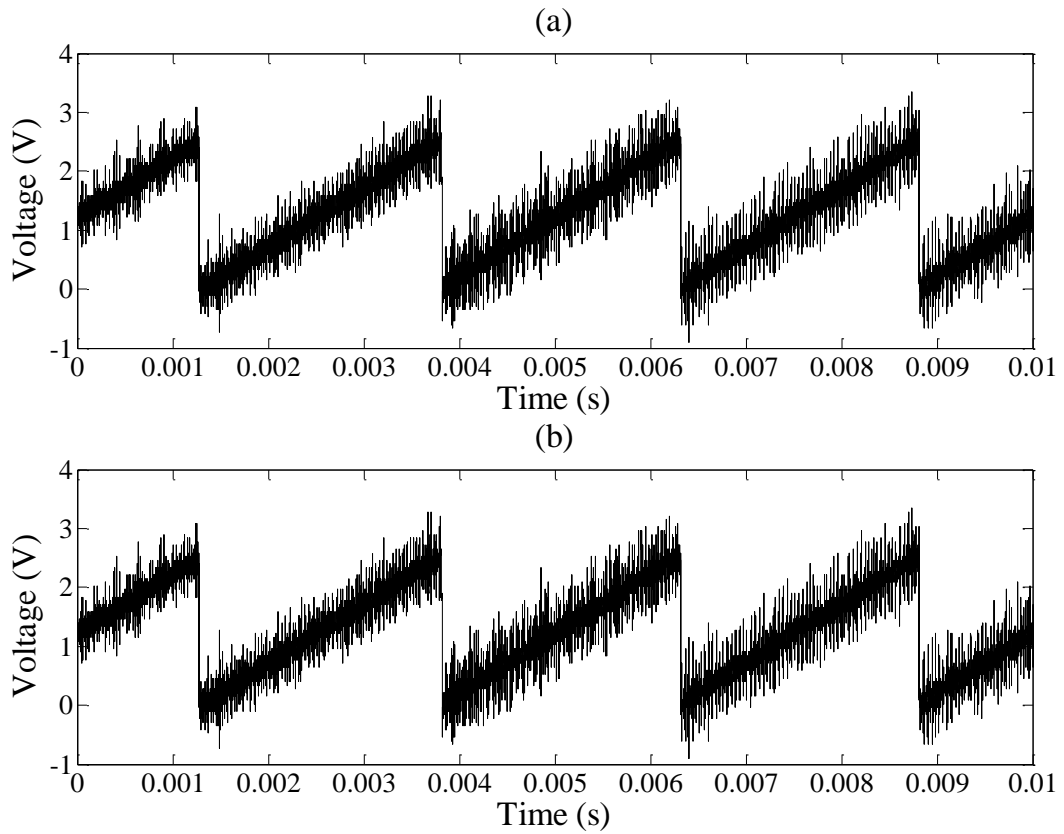


Figure 8-16: Grid angle under distorted conditions (a) Estimated, (b) Actual.

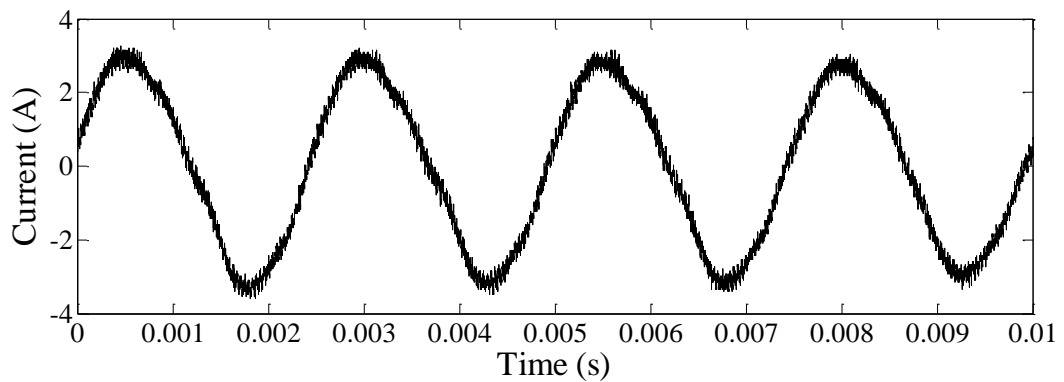


Figure 8-17: Current drawn from grid under distorted grid conditions.

The unbalance has had little effect upon the VF estimator as the error between the estimated and measured grid angle (Figure 8-16) is similar to that obtained under balanced conditions. As such the converter continues to draw a sinusoidal current waveform (Figure 8-17) to maintain the DC link voltage.

## 8.7 Conclusion

The focus on this chapter has been front-end rectifier control techniques, with the emphasis placed on making the control of the AFE more resilient to the kind of distortion it would be expected to encounter upon a real aircraft bus. One of the major complications of grid connected converter control under distorted conditions is grid synchronisation.

In Chapter 5 the three phase voltages are measured using transducers, the data is then passed to a software-based PLL to obtain the electrical angle which in turn is used in a VOC. This method is particularly susceptible to synchronisation problems. A brief review of the various solutions to this problem which have been documented in the literature was undertaken; the methods reviewed included advanced PLL modifications, direct power control and virtual flux orientated control.

Virtual flux orientated control was selected as the most appropriate solution for this application as it's ability to perform well under heavy grid distortion was well documented in the literature. Also virtual flux orientation control was easy to integrate with the existing SVPWM algorithm and resulted in a constant switching frequency, both of which from this study's perspective are advantageous over the direct power control technique. In addition the use of virtual flux orientated control presented the opportunity to remove the three voltage transducers from the converter which could result in an increase in reliability in a real world application.

The virtual flux estimator was first tested in simulation in conjunction with a model of the AFE. Performance was assessed in both starting and generating mode, under ideal and unbalanced grid conditions. The performance of the model was judged on how well the converter functioned, for example, if the DC link was maintained at the required amplitude and/or the required amount of real power was delivered/drawn from the grid. Performance was also assessed by comparing the actual grid angle and that estimated.

Once performance had been demonstrated in simulation, the virtual flux estimator was integrated into the hardware prototype. Experimentation was conducted under ideal and distorted supply conditions to produce substantive results to prove the performance of the controller. Due to a hardware limitation, testing could only be conducted in starting mode.

## 8.8 References

- [8.1] R.H. Williams, D. A. Stone, M. P. Foster, S. R. Minshull, "The Use of Virtual Flux Estimation in Aerospace Starter-Generator Systems," International Symposium on Power Electronics, Electrical Drives, Automation and Motion, Sorrento, Italy, pp. 1-5, 2012.
- [8.2] M. Malinowski, M. Jasinski, M. P. Kazmierkowski, "Simple Direct Power Control of Three-Phase PWM Rectifier Using Space-Vector Modulation (DPC-SVM)," IEEE Trans. Industrial Electronics, Vol. 51, No. 2, pp. 447-454, 2004.
- [8.3] M. Malinowski, M. Kazmierkowski, A. M. Trzynadlowski, "A Comparative Study of Control Techniques for PWM Rectifiers in AC Adjustable Speed Drives," IEEE Trans. Power Electronics, Vol. 18, No. 6, pp. 1390-1396.
- [8.4] L. Xu, D. Zhi, "Direct Power Control of Grid Connected Voltage Source Converters," Power Engineering Society General Meeting, Tampa, USA, pp. 1-6, 2007.
- [8.5] J. Eloy-Garcia, S. Arnaltes, J. L. Rodriguez-Amenedo, "Extended Direct Power Control for Multilevel Inverters Including DC Link Middle Point Voltage Control," IET Electric Power Applications, Vol. 1, No. 4, pp. 571-580, 2007.
- [8.6] V. Kaura, V. Blasko, "Operation of a Phase Locked Loop System under Distorted Utility Conditions," IEEE Trans. on Industry Applications, Vol. 33. No. 1, pp. 58-63, 2007.
- [8.7] Department of Defence Interface Standard: Aircraft Electrical Power Characteristics, MIL-STD-704F, 2004.
- [8.8] R. Xu, F. Liu, X. Zhu, "Study on the Three-Phase Software Phase-Locked Loop Based on DQ Transformation," Asia-Pacific Power and Energy Engineering Conference, Chengdu, China, pp. 1-4, 2010.
- [8.9] S. R. Naidu, W. Mascarenhas, D. A. Fernandes, "A Software Phase-Locked Loop for Unbalanced and Distorted Utility Conditions," International Conference on Power Systems Technology, Singapore, China, pp. 999-1004, 2004.

- [8.10] M. Malinowski, M. Kazmierkowski, S. Hansen, F. Blaabjerg, G. D. Marques, "Virtual Flux Based Direct Power Control of Three-Phase PWM Rectifiers," IEEE Trans. Industry Applications, Vol. 37, No. 4, pp. 1019-1027.
- [8.11] J. Hu, B. Wu, "New Integration Algorithm for Estimating Motor Flux over a Wide Speed Range," IEEE Trans. Power Electronics, Vol. 13, No. 5, pp. 969-977, 1998.
- [8.12] M. Cirrincione, M. Pucci, G. Cirrincione, G. Capolino, "A New Adaptive Integration Methodology for Estimating Flux in Induction Machine Drives," IEEE Trans. Power Electronics, Vol. 19, No. 1, pp. 25-34, 2004.
- [8.13] M. Malinowski, "Sensorless Control Strategies for Three-Phase PWM Rectifiers," Ph.D. Dissertation, Warsaw University of Technology, 2001.
- [8.14] A. M. Razali, M. A. Rahman, "Grid Voltage Sensorless Control Method for Front-End PWM Rectifier Connected to the Voltage Source Inverter," Newfoundland Electrical and Computer Engineering Conference, St John's, Canada, 2011.
- [8.15] B. S. Bhangu, K. Rajashekara, "Control Strategy for Electric Starter Generators Embedded in Gas Turbine Engine for Aerospace Applications," Energy Conversion Congress and Exposition, Phoenix, USA, pp. 1461-1467, 2011.

## 9 Conclusion

This thesis has explored how a multilevel inverter may be applied to an aerospace gas turbine S/G system. S/Gs are typically low inductance machines due to the low number of windings. A low number of windings is used to reduce losses during generation mode, regulate the back-emf at the high rotational speeds and to increase the overall machine power density.

When driving low inductance machines with conventional two-level inverters a high level of harmonic distortion is typically displayed in the current waveform. This results in increased losses in both the machine and power converter necessitating additional cooling/heatsinking, which results in a weight penalty. Furthermore the high current ripple imposed on the current fundamental waveforms may require both the machine windings and the power converter to have an increased current rating to ensure the operational limits are not breached. The poor quality waveform also leads to an increased production of common-mode voltages upon the converter output which can lead to the destruction of the machine's winding insulation and bearings. The use of a two level active-front end is also detrimental to the performance of the converter, drawing a non-sinusoidal current from the supply during starting mode and producing a poor voltage waveform during generation mode if appropriate measures are not taken.

The poor performance of the two-level inverter is typically corrected through additional choke inductance and/or increasing the device switching frequency. Unfortunately both methods result in an increase in the system weight which is undesirable in an aerospace application.

The limitation of the two-level inverter may be overcome through the use of a multilevel converter. The stepped output produces a higher quality waveform at both the machine and grid terminals. This in some applications negates the need for large amounts of passive filtering or a high switching frequency. The multilevel converter also reduces common-

mode voltages, which helps to increase the life expectancy of the machines bearing and winding insulation.

The most common multilevel topologies were initially reviewed to assess which was the most suitable for this application. The back-to-back, five level, diode-clamped topology was eventually selected for a number of reasons. The resultant improvement in waveform quality is seen at both the machine and grid side of the converter. This helps compliance with aerospace power quality standards whilst reducing the amount of radiated and conducted EMI. This configuration also supports bidirectional power flow which is essential in a S/G system. The back-to-back connection of the two multilevel inverters provides the opportunity to self-balance the DC link levels without the need for additional circuitry. This ensures the converter produces a high quality output regardless of the operating conditions and minimises the system weight.

The selected converter topology was first applied to a PMSM S/G system. This is important as the PMSM is likely to be the machine topology of choice for future aircraft S/G systems due to the high power density and rugged rotor structure. The control of the converter was examined in detail to enable it to operate in both modes of operation. The controller was applied to a prototype inverter to provide substantive hardware results. A dynamometer test rig was assembled to mechanically load the S/G. The dynamometer controller was used to ensure that the torque-speed profile produced by the dynamometer is similar to that a S/G in a real application would see at the point of coupling to the engine.

The performance of the rig was initially assessed in both starting and generating mode in isolation. In starting mode the AFE drew a sinusoidal current from the grid to maintain the DC link voltage at the specified level whilst the inverter drove a sinusoidal current into the machine stator which was mechanically loaded by the dynamometer. In generating mode the inverter drew electrical power from the S/G which was now rotating at constant speed to maintain the DC link. The AFE drove a defined current into the utility network.

A complete system test was then conducted taking the S/G from standstill to the maximum operational speed. In starting mode the dynamometer operated as a fan load representing a heavily simplified model of a gas turbine. Once idle speed has been attained, the dynamometer reverses the polarity of the torque upon the S/G accelerating it towards the maximum operating speed. The converter demonstrated a satisfactory level of

performance throughout the system test. A steady DC link voltage was maintained at the required level across both modes of operation regardless of the torque produced or the speed of the S/G. The converter performance was also verified in generating mode under fluctuating speed conditions. This was necessary to represent in-flight turning/engine throttling in a real world application.

The application of this system to a WFSM S/G was then investigated. The WFSM is the machine topology of choice for large civil aerospace generators and S/Gs. In order to use the WFSM in starting mode it was necessary to investigate the excitation conditions to maximise the available torque. Once the required excitation conditions had been determined these were implemented using a power amplifier connected across the excitation windings and controlled by the dynamometer controller. A similar testing procedure to that used with the PMSM was conducted. Performance was initially assessed in each mode in isolation before a full system test was conducted. The converter demonstrated the required level of performance in each test and it can therefore be concluded that this topology may warrant further investigation for use as an alternative to conventional two level inverters in future WFSM S/Gs.

Control methods which may yield a further improvement in harmonic performance were then investigated. From a control perspective a low inductance WFSM operating over a wide speed range provides a challenge even for a multilevel converter controller to provide a satisfactory level of harmonic performance. Predictive control strategies were examined whereby a model of the machine load is used to predict the effect of each converter switching vector upon the stator current waveform. The vector which results in the smallest error between the reference and actual current vectors may therefore be selected giving an improvement in the waveform quality when compared to conventional FOC utilising PI control loops.

A review of the literature concerning predictive control was conducted to determine the most suitable technique for this application. Predictive control was then instigated in the machine connected inverter's DSP. A power analyser was used to measure the THD of the stator current waveform and therefore provide an accurate assessment of the predictive controller's performance. Measurements were conducted in both starting and generating mode and across a range of operating conditions.

The proposed predictive controller was found to provide a substantial reduction in the level of THD in the machine current waveform during both modes of operation. During starting mode the THD was found to be reduced across the full starting mode speed range. In generating mode the performance of the controller was examined as the power drawn from the generator was varied. At the low power levels this testing was conducted at the performance of the predictive controller was found to improve linearly with the power rating.

In the final part of this study grid interfacing techniques for S/Gs were examined. With aircraft power levels continuing to rise making it necessary to have multiple generators, the paralleling of generator outputs onto a single distribution bus is likely to become increasingly important. Conventionally power converters use Voltage Orientated Control whereby the grid angle is derived using voltage transducers upon each phase, which provide the inputs to a three-phase PLL. This arrangement offers poor performance under distorted grid conditions, which can lead to a false measurement of the grid angle. This in turn results in a poor quality output from the converter. The voltage transducers must also be considered a possible failure mechanism. For instance if one was damaged the PLL would no longer be able to lock to the grid angle leading to the possible collapse of the converter output.

Instead a Virtual Flux Orientated controller was considered for this study. Here the grid voltage is considered to have been induced by the flux of a virtual motor connected across the grid terminals. Using knowledge of the grid connection impedance and the converter output vector applied across the terminals it is possible to estimate the virtual flux. This rotor angle of the virtual machine can then be calculated providing the converter with synchronisation to the grid whilst eliminating the voltage transducers.

The elimination of the voltage transducers has the effect of making this technique substantially more resilient to grid side distortion when compared to Voltage Orientated Control. It is likely that the converter Mean-Time-to-Failure will also be improved as three possible failure mechanisms have been eliminated.

The proposed controller was implemented in both simulation and software. As the AC supply used during testing did not have regenerative capabilities testing in hardware could

only be conducted upon starting mode. Both modes of operation could be assessed in simulation.

Results are presented obtained from simulation and experimentally showing the satisfactory performance of the Virtual Flux controller under both ideal and distorted grid conditions. The level of grid distortion applied was in line with that required by the power quality standards. In each case the error between the actual grid angle and that estimated was minimal. This enabled the SV modulator to function as normal despite the distorted grid conditions.

## 10 Future Work

Aircraft electrical systems are typically four wire. The fourth wire is necessary to minimise the effect of unbalanced loads upon the supply phase voltage balance. In this study a three wire system was assumed. Further work is required to examine how best the topology may be modified to provide the fourth wire. There are numerous options available including, the use of a zig-zag transformer, fourth leg or the connection of the fourth wire to the DC link midpoint. In addition to changes in the topology, the effect on the modulation technique must be examined. For instance the connection of a fourth wire to the midpoint of the DC link is likely to have some effect on the balancing of the capacitor voltages. This needs to be investigated when appraising the various methods of providing the additional wire.

The work described in Chapter 8 concerning the grid interfacing of the power converter could be enhanced through simulation work incorporating a realistic distribution bus and loads. For instance the simulation could incorporate both linear and non-linear loads such as de-icing systems and an electrical actuator drive. The model could be further improved by including the cable impedance. A model of this accuracy would require a substantial amount of technical information from both the airframer and the various system providers. A model of this accuracy would be required to realistically assess the performance of the proposed grid synchronisation. This level of detail would also be necessary for the system to gain accreditation.

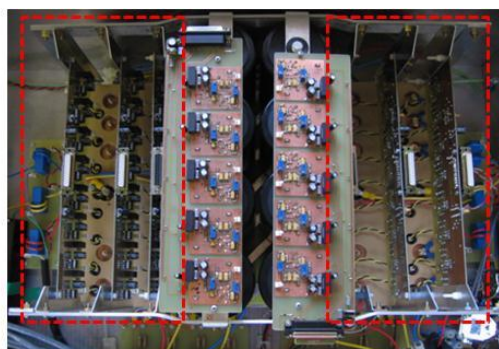
Aircraft electrical systems are typically sized by the fault/overload conditions rather than at the nominal operating conditions. To produce an accurate weight estimate for this converter the operation under fault conditions would need to be examined. This would provide sufficient detail for an accurate weight estimate to be conducted to size the multilevel topology for a realistic application. A weight comparison could then be made between the proposed multilevel topology and a conventional two-level inverter.

## Appendix A

All the experimental data provided in this thesis was attained using a test rig of approximately 5-10 kW rating. The rig was developed in a previous study [1], then modified for use in this system. Modifications included:

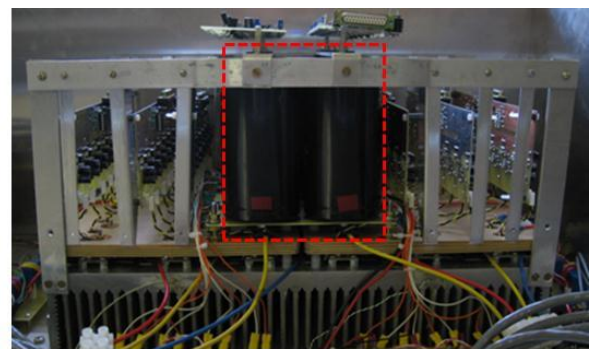
- Replacement off all active devices to higher rated parts.
- Modification of all power stage PCBs to increase maximum current carrying capacity.
- Rewrite of control software for use in a *S/G* system, including custom communications protocol between inverter's to coordinate power flow direction.
- Up rating of switchgear over-current protection.

The converter and gate drive boards are shown in Figure 0-1. The key components are summarised in Table 0-1.



Rectifier Gate  
Drive Boards

Inverter Gate  
Drive Boards



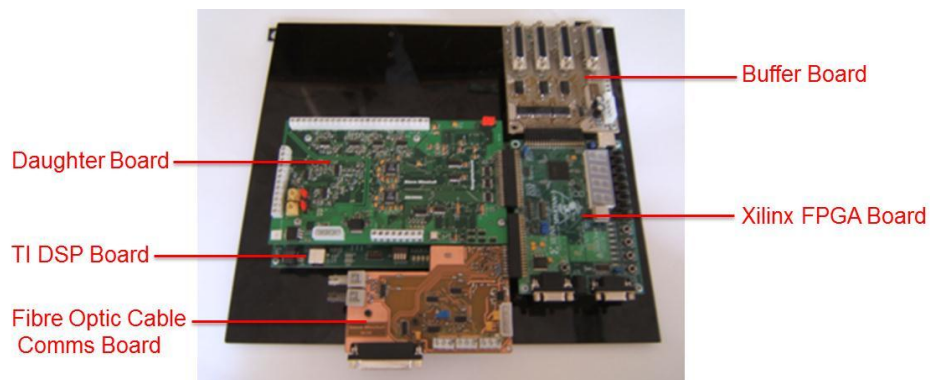
DC Link Capacitor Bank

Figure 0-1: Test rig.

Component:	Manufacturer Part Number:
IGBT:	International Rectifier: GA200SA60U
Clamping Diodes:	International Rectifier
Capacitors:	BHC-Components: ALS31332NP450

**Table 0-1: Converter components.**

The control board developed in [1] was also utilised in this study and is shown in Figure 0-2. Two control boards are used, one for each inverter. The control software executes upon a Texas Instruments floating point TMS320C6713 DSP. A daughter-board is mounted above the DSP. The daughter-board provides the peripherals such as signal-conditioning, ADCs and DACs. Owing to the large number of IGBTs a Xilinx Spartan 3 FPGA was used to generate the gate signals. The duty cycle and switching vector is calculated in the DSP and is then passed to the FPGA for implementation. A communications board is also connected to the FPGA which provides a fibre optic link between control boards to permit communication. For instance in this rig, the inverter dictates the mode of operation. This is then communicated to the AFE. The switching and ADC sampling frequency used throughout this study was 24 kHz.

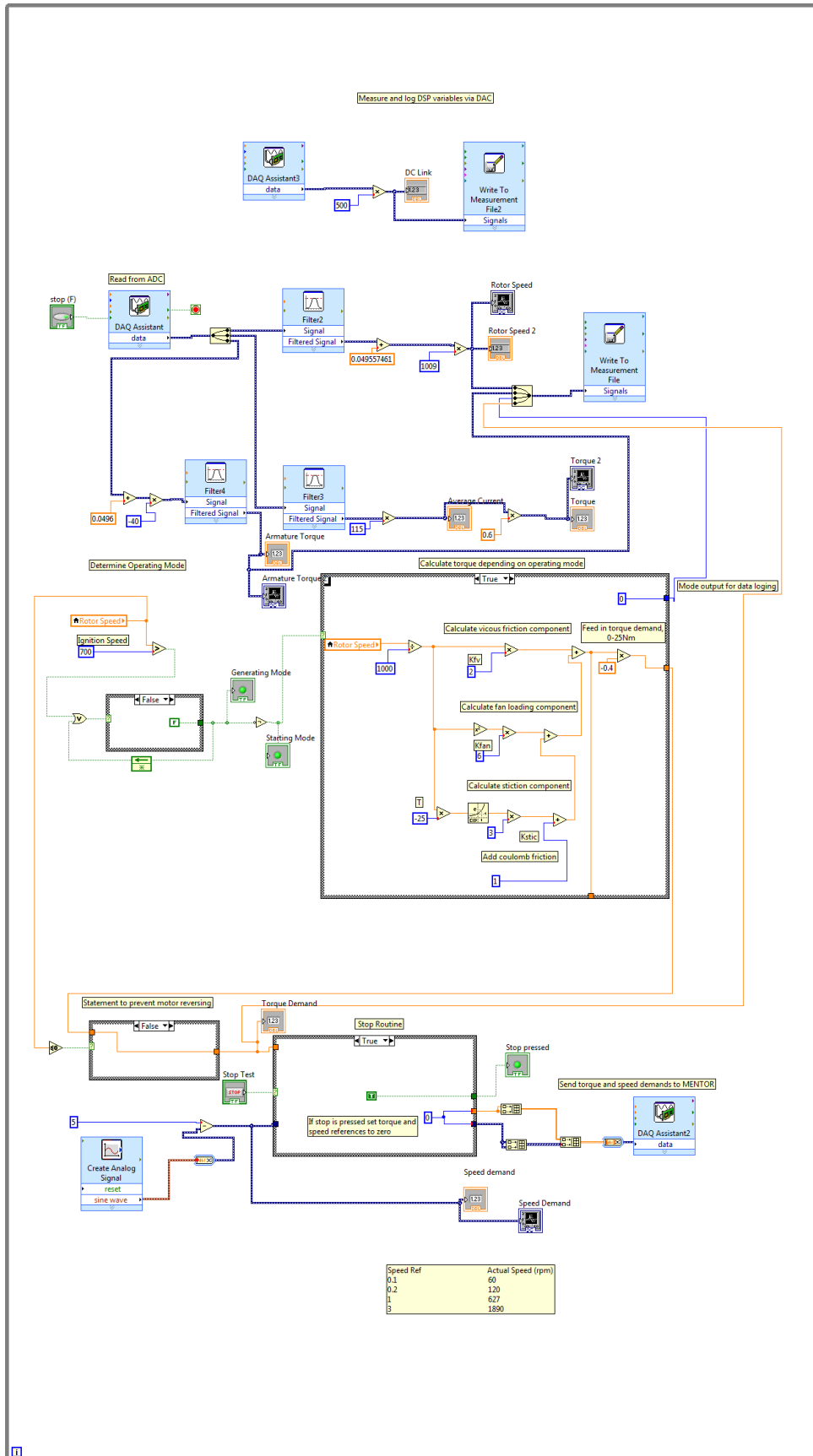


**Figure 0-2: Control board.**

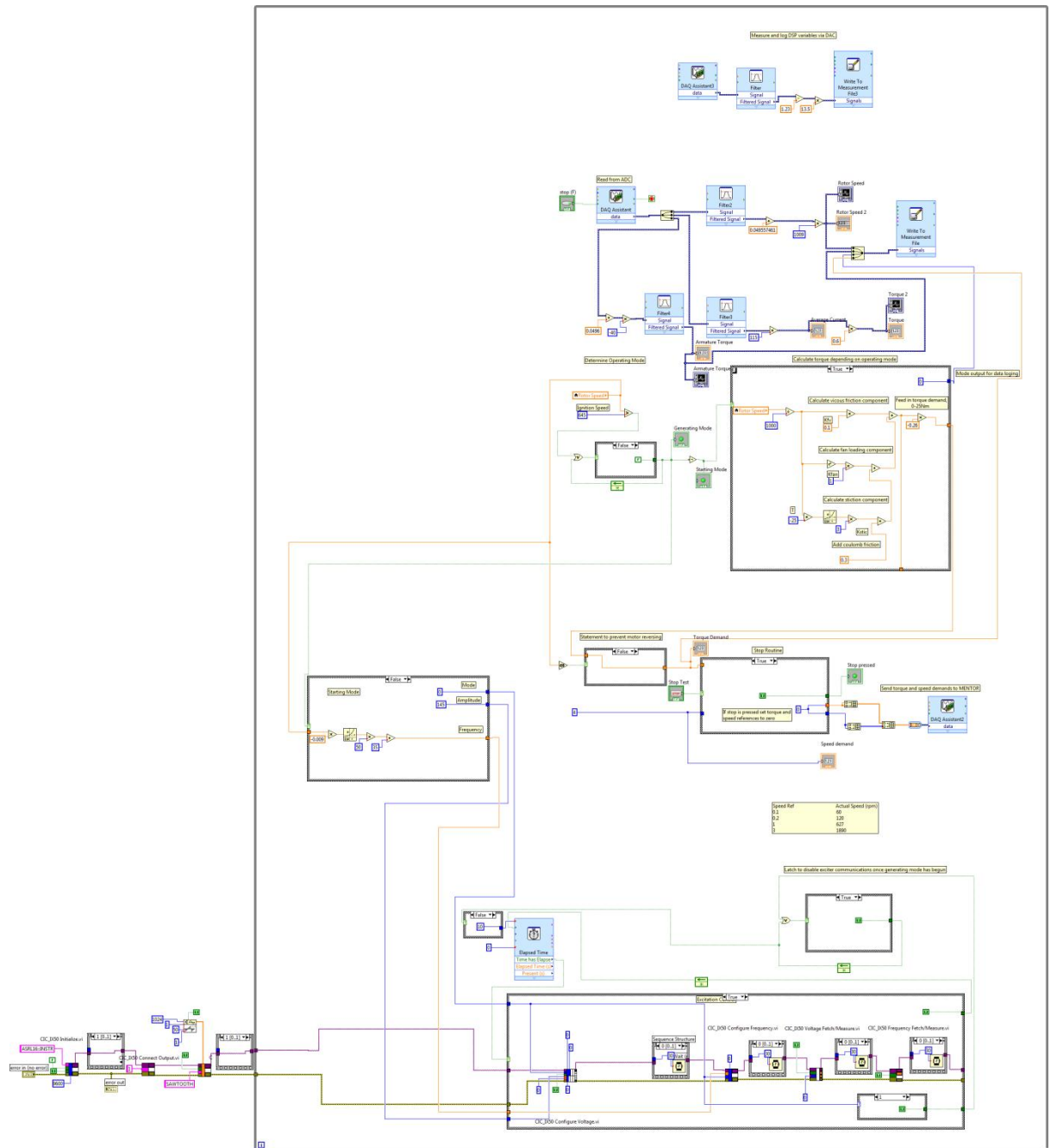
## References

- [1] S. R. Minshall, "Multilevel Inverters for Driving Low Inductance Machines," Ph.D. Thesis, University of Sheffield, 2009.

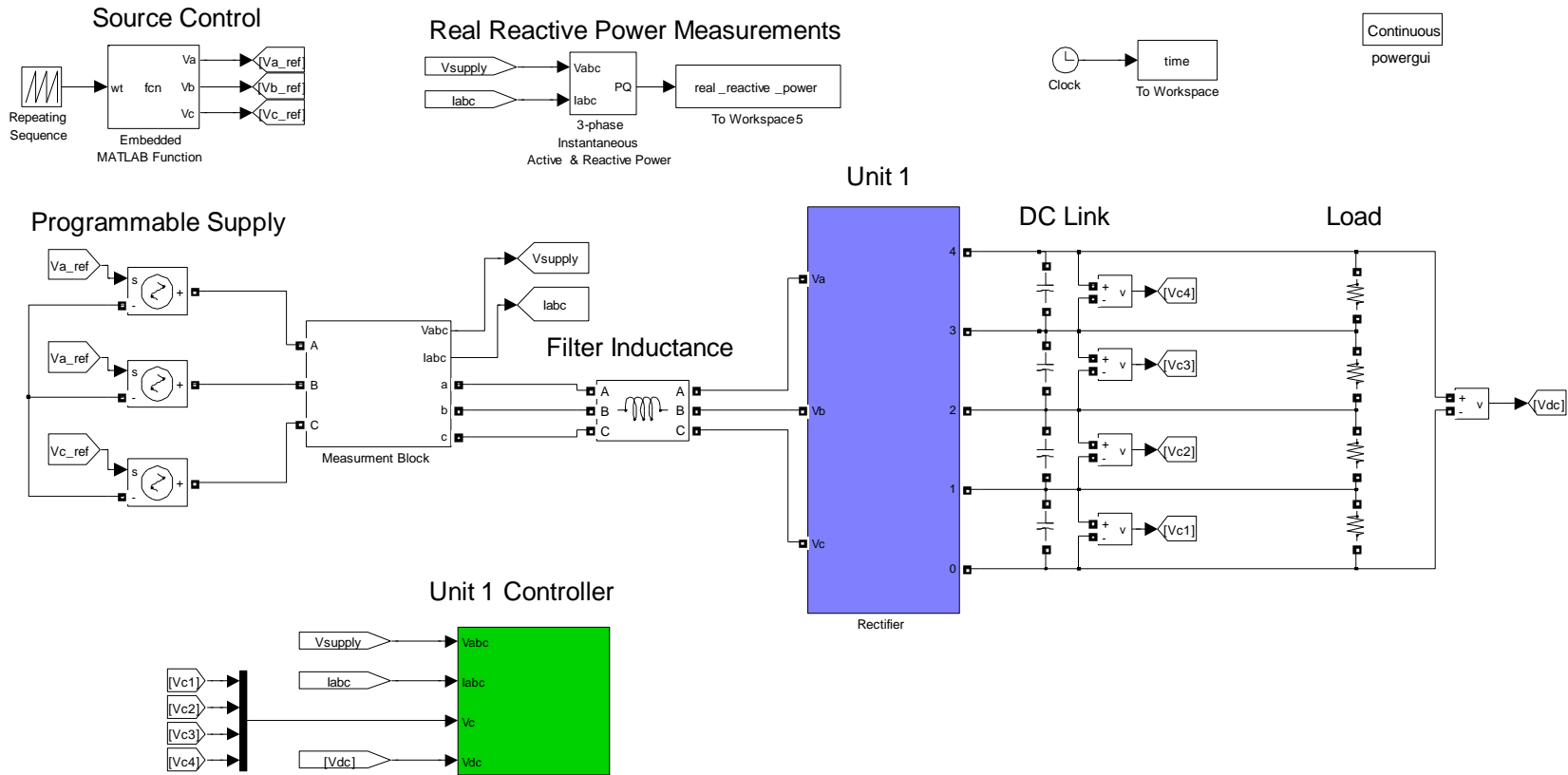
# Appendix B



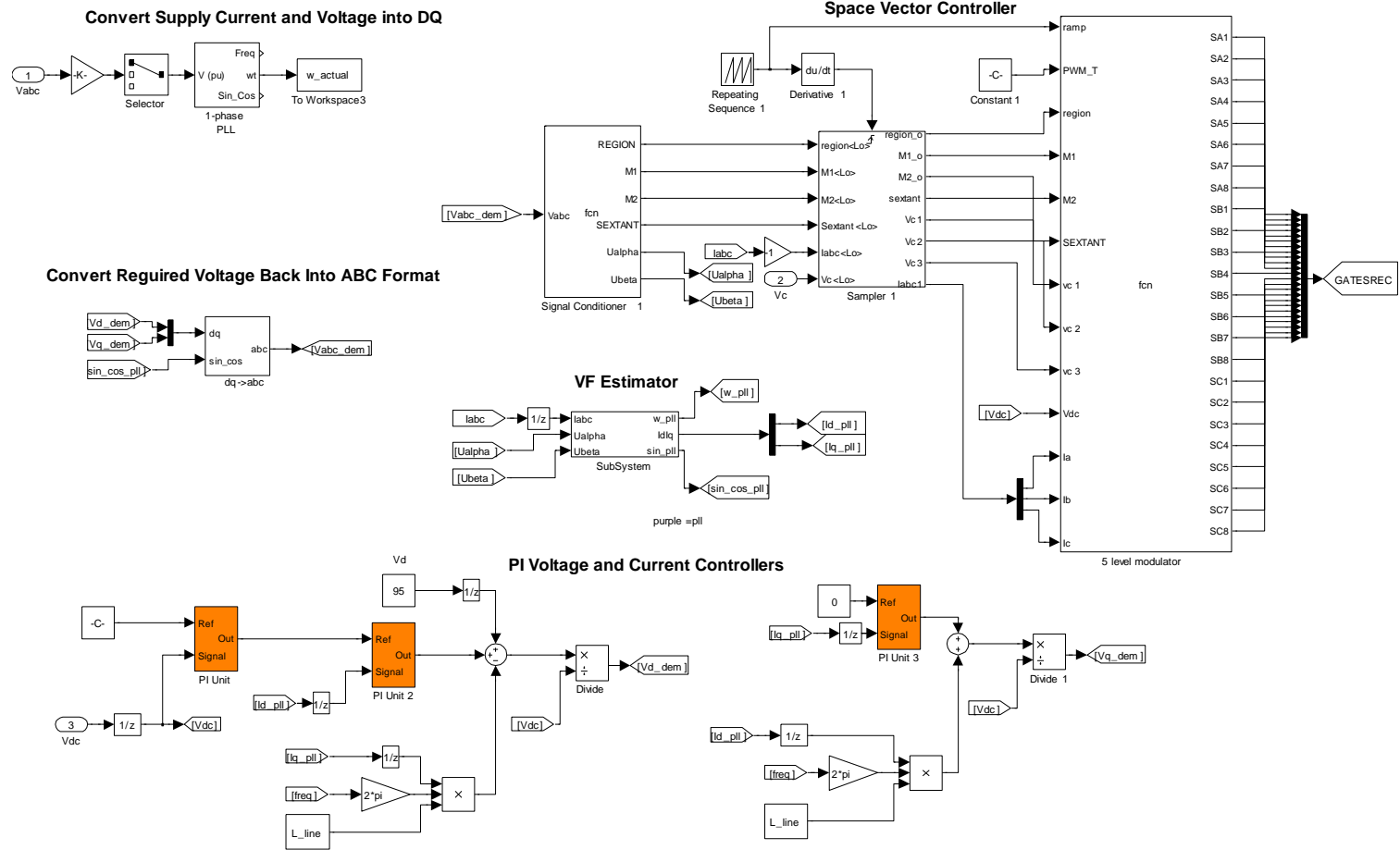
# Appendix C



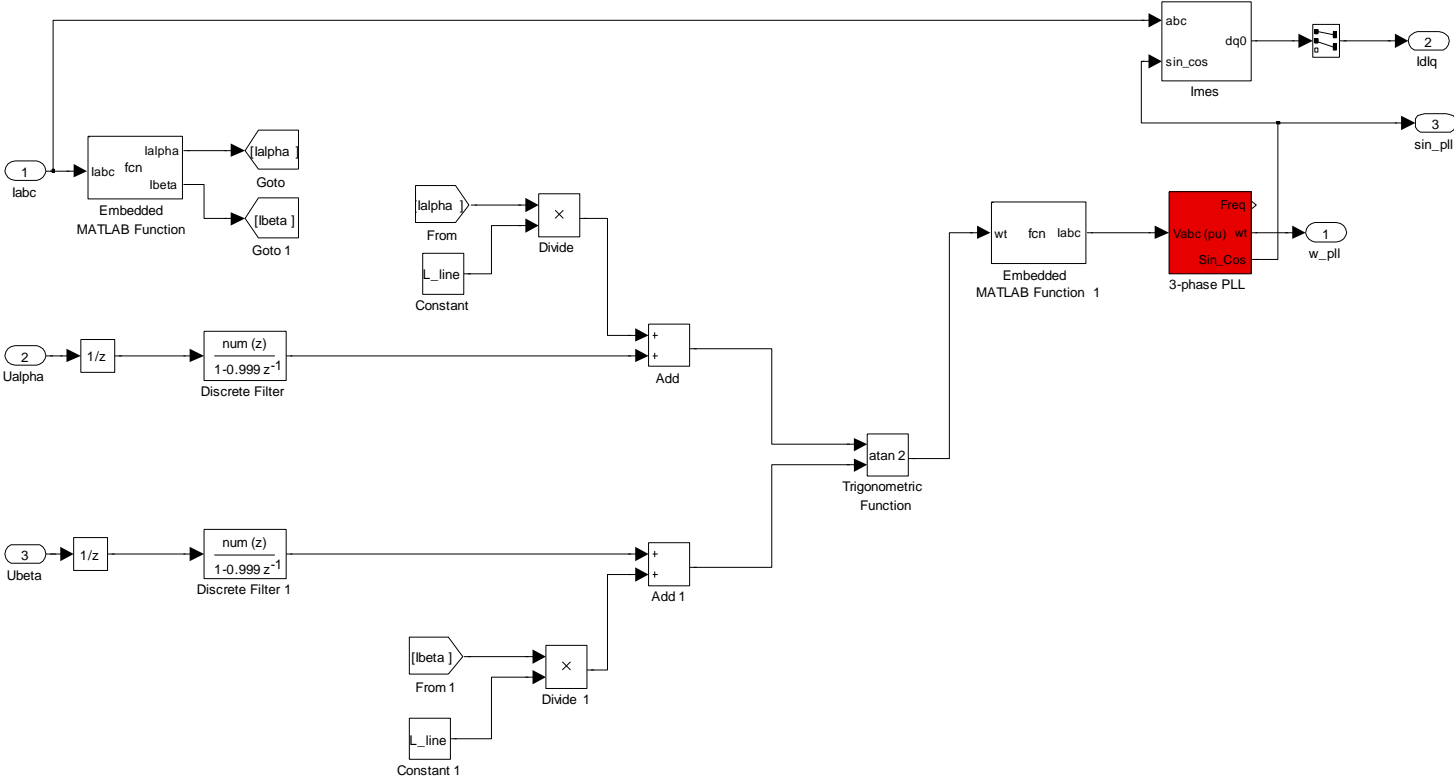
# Appendix D



# AFE Controller Block



# VF Estimator Block



## Appendix E

```
//////////Virtual Flux Grid angle estimation//////////

Ualpha3=Ualpha2*0.9;

Ualpha2=Ualpha;

Ubeta3=Ubeta2*0.9;

Ubeta2=Ubeta;

//Estimate converter output in the last switching cycle

Ualpha=(Vd_dem*cosf(position_pll_mod))-(Vq_dem*sinf(position_pll_mod));

Ubeta=(Vd_dem*sinf(position_pll_mod))+(Vq_dem*cosf(position_pll_mod));

//Pass Ualpha and beta through LPF to perform integration

//4Hz LP

Ualpha_integral=0.999*Ualpha_integral_old+0.00052332*Ualpha+0.00052332*Ualpha_old
;

Ualpha_integral_old=Ualpha_integral;

Ualpha_old=Ualpha;

//4Hz LP

Ubeta_integral=0.999*Ubeta_integral_old+0.00052332*Ubeta+0.00052332*Ubeta_old;

Ubeta_integral_old=Ubeta_integral;

Ubeta_old=Ubeta;

//Calculate current alpha-beta components

Ialpha = (0.666 * Ia) - (0.333 * (Ib + Ic));

Ibeta = 0.577 * (Ib - Ic);

//Calculate virtual flux by adding voltage drop across line inductance

flux_alpha=Ualpha_integral+0.0008*Ialpha;
```

```

flux_beta=Ubeta_integral+0.0008*Ibeta;

position_VF=(atan2f(flux_beta,flux_alpha));
//////////////////////////////////PLL//////////////////////////////////
//Produce virtual ABC supply voltage signals
VF_phaseA=40*sinf(position_VF+0.754)*(-1);
VF_phaseB=40*sinf(position_VF-2.0944+0.74)*(-1);
VF_phaseC=40*sinf(position_VF-4.1888+0.74)*(-1);
Valpha_supply_VF = (0.666 * VF_phaseA) - (0.333 * (VF_phaseB + VF_phaseC));
Vbeta_supply_VF = 0.577 * (VF_phaseB-VF_phaseC);
sin_pos_pll = sinf(position_pll);
cos_pos_pll = cosf(position_pll);
Vq_supply_pll = -(Valpha_supply_VF * sin_pos_pll) + (Vbeta_supply_VF * cos_pos_pll);
//Pi controller
    prop_pll = 100 * -Vq_supply_pll;
    int_pll = 50 * ((4.096e-5 * -Vq_supply_pll) + int_pll_old);
    if (int_pll > 5000){
        int_pll = 5000;
    }
    else if (int_pll < 1200){
        int_pll = 1200;
    }
    else {
        int_pll = int_pll;
    }

```

```

int_pll_old = int_pll;
w_pll = prop_pll + int_pll;

position_pll = (((4.096e-5) * (w_pll)) + position_pll_old); //integrator
if (position_pll > 6.28318){
    position_pll = position_pll - 6.28318;
}
else if (position_pll < -6.28318){
    position_pll = position_pll + 6.28318;
}
else{
    position_pll = position_pll;
}
position_pll_old = position_pll;
position_pll_mod=position_pll-3.14159;
//Position fudge factors
position_pll_mod=position_pll_mod+(3.1426*1);
if (position_pll_mod>3.1416)
    position_pll_mod=position_pll_mod-(2*3.1426);

```